# Turbulent mixing in photodissociation regions

Inaugural-Dissertation
zur
Erlangung des Doktorgrades
der Mathematisch-Naturwissenschaftlichen Fakultät
der Universität zu Köln

vorgelegt von

**Aleena Baby**
aus
Thrikkaipatta, India

I. Physikalisches Institut
Universität zu Köln
January 25, 2024

---


| | |
|---|---|
| Berichterstatter: | Priv.-Doz. Dr. Volker Ossenkopf-Okada |
| (Gutachter) | Prof. Dr. Peter Schilke |
| Vorsitzende : | Prof. Dr. Berenike Maier |
| Beisitzer: | Priv.-Doz. Dr. Markus Röllig |

**Abstract**

Molecular clouds are dynamic environments where species are transported through random motions. To fully understand the physical conditions within these clouds, it is essential to quantify this transport. This study focused on the diffusion effects in the multi-fluid gas of photodissociation regions (PDRs) by considering turbulent, molecular, and thermal diffusion. To model the diffusion effects in a PDR, the KOSMA-$\tau$ PDR model is used. The KOSMA-$\tau$ PDR model simultaneously solves the chemistry, level populations, and energy balance in a spherical geometry. This model included energy balance, cosmic ray ionization, CO and $H_2$ self-shielding, photodestruction process, $H_2$ formation, gas-dust interactions, and dust surface chemistry.

This model derived the limits of the coherence length of turbulent diffusion and the total diffusion coefficient as a function of the radius of the cloud. By examining the impact of diffusion flows on chemical processes within the PDRs, this study found that diffusion can increase surface temperature and modify chemical pathways compared to a scenario without diffusion. The diffusion flows facilitate the transportation of $H_2$ and CO molecules from lower temperature to higher temperature regions. As a consequence, $H-H_2$ transition and $C^+-C-CO$ transition shift towards the surface, in contrast to a situation where diffusion is absent. This diffusion-induced shift substantially influences the chemistry of the PDR. The chemistry of electrons, $H, H_2, C^+, C, CO, CH, CH^+, O$, and OH show a significant impact when diffusion is added. $C, C^+, CS^+$, and $HCO^+$, and their isotopologues, show changes ($\geq 10\%$) in the integrated intensities. The integrated line intensity ratio of $^{13}CO\,(1 \rightarrow 0)/\,^{12}CO(1 \rightarrow 0)$, $[^{12}CII]/^{12}CO(1 \rightarrow 0)$ and $[^{12}CI]/^{12}CO(1 \rightarrow 0)$ shows $\leq 30\%$ change when diffusion is added. Observations with telescopes such as ALMA or JWST can verify these changes in the intensity of specific organic molecules, allowing for investigating non-stationary chemistry effects resulting from the diffusion of gas in the PDR.

To my parents, Baby Thomas and Celine, and their sleepless nights!

# Aknowledgements

I would like to express my gratitude to my supervisor PD. Dr. Volker Ossenkopf-Okada for his guidance and encouragement throughout my Ph.D. His mentorship has not only made me a better researcher but also a better person. I also thank PD. Dr. Markus Röllig for his assistance, valuable suggestions (both academic and personal), and input. Thank you for the intense debugging sessions. Without his support, this modeling work would not have been possible. I am extremely grateful to Prof. Dr. Jürgen Stutzki for creating this terrific group together and Prof. Dr. Dominik Riechers for continuing the support. I would like to extend my sincere thanks to members of my thesis advisory committee, Prof. Dr. Frank Bigiel and Prof. Dr. Peter Schilke, for their valuable suggestions and to Prof. Dr. Berenike Maier for chairing my thesis committee.

I am deeply indebted to my officemate Craig Yanitski for the hours-long discussions about PDRs, diffusion, clumps, and life. Thank you for the Spotify playlists. If I know how to add a comma correctly, it is because of him. I would also like to thank Dr. Slawa Kabanovic and Dr. Cristian Guevera for helping me whenever needed. Words cannot express my gratitude to Dr. Slawa Kabanovic enough for his support while dealing with the German administration. Without his intervention, I would have been homeless and penniless in the last months.

I would like to thank Dr. Yoko Okada for her support and guidance, which helped me navigate through my professional life. I would also like to thank Dr. Veena V.S. and Roya Hamedani Golshan for their support, suggestions, and guidance. For their advice, criticism, and support throughout my time at the University of Cologne, I would like to thank Dr. Juan Luis, Dr. Christof Buchbender, Dr. Robert Simon, Dr. Ronan Higgins, Dr. Nicola Schneider, Parit Mehta, Daniel Viera, Jonathan Clarke, Arron Beyer, and other group members. I would definitely miss the lunch table discussions and Feierabend bier. I would be remiss in not mentioning Bettina Krause, Steffi Simon, and Dr. Petra Neubauer-Guenther for their unconditional support. I acknowledge SFB 956 and BCGS for their support.

Thanks should also go to Dr. Phuong Glaser and my IFS peers (2022-2023 batch) for supporting and guiding me through the last years of my Ph.D. I am extremely grateful to Dr. Dorottya Szécsi (Institute of Astronomy, Faculty of Physics, Astronomy, and Informatics, Nicolaus Copernicus University, Poland) for mentoring me through IFS mentoring program. I appreciate your help in

making my dreams a reality. Your guidance and shared experiences have been priceless.

I would like to thank Prof. Avinash Deshpande for his motivation and support. Thanks for taking me under your wing. I would like to thank my teachers, Prof. G. Muralidharan (Professor, Gandhigram Rural Institute, Tamil Nadu), Dr. Biju KG (Head of the Department, WMO Arts and Science College, Muttil, Kerala), Rafi K.E, and Hashim N.K (Assistant professor, WMO arts and science college, Muttil, Kerala) without whom my dreams would not have fulfilled. Thank you for seeing my potential and helping me harness it.

I thank Mrs. K. Yuva Priya for her invaluable support, unconditional love, and motivation (especially after every Ph.D. entrance exam result). I would like to express my sincere gratitude to my friends, Dr. Persis Misquitta, Dr. Harshita Bhatt, Dr. Shashwata Ganguly, Akhil Jaini (Indian Insitute of Astrophysics, Bengaluru, India), Hrishikesh Shetagonkar (University of Würzburg, Germany), Yash Bhusare (National Center for Radio astrophysics, NCRA-TIFR, India), Gowri Nanda, and Vineetha Viswanathan for their unwavering support, insightful remarks, and love throughout my Ph.D. and beyond. Thanks for being my unpaid therapists. I would also like to express my gratitude to Purvi Gupta and her cat Fifi for welcoming me into their home. In the final days of my writing, they have been a tremendous help.

I am grateful to my husband, Tins Jose, for his support through this stressful time. Thanks for being calm amidst the storm and managing everything, which helped me focus on my thesis. His jokes certainly made my gloomy days better. I thank my brother Nubin Baby for his support and for fighting with anyone who asks whether I am still studying (sadly, this is the last degree. So I might have to find a job!). Thanks for reminding me why I started the Ph.D. every now and then. I also thank my extended family, both in Europe and India, who have supported me through their prayers, well wishes, and occasional home-cooked meals.

Last, I want to thank my parents for devoting their sleep, sweat, and time to making my aspirations come true. Their commitment paved the way for my journey. Thank you for upholding such high standards. Without the lunch boxes and teas, you gave up, I would not have made it this far.

Finally, I thank myself. I thank the twelve-year-old me for dreaming of this day, the nineteen-year-old me for making the right choices, and twentyone year old me for fighting inside and outside battles. Thanks for staying up late, cramming books, walking kilometers to school, and giving up on every chocolate and egg puff for a book. Thanks for using the opportunities and making plans and road maps without backups. I hope this journey inspires thousands of young people

from Wayanad to go above and beyond to follow their dreams.

# Contents

# Chapter 1

# Introduction

The interstellar medium (ISM) is a complex system encompassing diffuse gas clouds and small (nanometer to micrometer range) dust particles with many processes to consider (Ferrière 2001; Wakelam et al. 2017). The interstellar clouds are divided into (Draine 2011) dark clouds (cold molecular gas, temperature $\sim$ 10 - 20 K), diffuse clouds (cold atomic gas, temperature $\sim$ 100 K), and translucent clouds (atomic and molecular clouds). The remaining interstellar matter constitutes: mostly neutral warm (T $\sim 10^4$K ) atomic, warm ionized, and hot (T $\sim 10^6$K ) ionized gas, spread between the clouds (Ferrière 2001). ISM-specific volumetric heating functions and radiative cooling determine the equilibrium of the neutral ISM. Molecular clouds are multiphase (Klessen & Glover 2016), and the initial models assumed that different phases were in pressure equilibrium with each other (Ferrière 2001). The balance between gravitational potential energy and kinetic energy is crucial for the evolution of molecular clouds, despite the effects of magnetic fields, external pressure, and other parameters (Sun et al. 2018). This balance is explained using the virial theorem, which states that the cloud will maintain equilibrium if the gravitational potential energy is twice the internal thermal energy. The impact of virial parameter $\alpha_{\rm vir}$ on the star formation is explored by many authors (e.g., McKee & Zweibel 1992; Padoan & Nordlund 2011).

The recent observations of HI (Wang et al. 2020) show that interstellar turbulence mixes the cold neutral medium (CNM) and warm neutral medium (WNM). Turbulent motions in the interstellar medium (ISM) can mix gas, dust, and other quantities over various spatial scales. This mixing impacts the chemical, dynamic, and structural evolution of the ISM. In recent years, studies (e.g. Ballesteros-Paredes et al. 2006) have revealed that turbulence is a rudimentary component in molecular clouds that determines the properties such as star formation rates, morphology, lifetimes, etc.

Turbulence consists of eddies of different sizes. The larger eddies can also

contain smaller eddies. The energy is transferred to the smaller eddies when the large eddies are unstable and break up (Larson 1981). The energy transfer from the larger eddies to the successively smaller eddies is called an energy cascade, which continues until the eddy motion is stable and molecular viscosity effectively dissipates the kinetic energy. Eventually, this hierarchy produces structures on tiny enough scales that molecule diffusion or other forms of dissipation become significant. The turbulent eddies grow so small that they become random thermal motion, and their kinetic energy converts to heat, which can be radiated away (Mac Low & Klessen 2004; Klessen & Glover 2016). The dissipation of turbulent energy can affect the fragmentation of the molecular clouds, influencing the mass distribution.

The three Larson (Larson 1981) scaling equations have supplied the fundamental observational limits on molecular cloud dynamics for nearly thirty years. Larson established a power-law scaling between velocity dispersion, $\sigma_v$, and cloud size, L, with an index of 0.38, using data from the literature at the time; an inverse link between the mean density of the cloud,$\langle n_{MC} \rangle$, and L, and the relationship $2GM_MC/\sigma_v^2 L \approx 1$. Traditional interpretations of these scaling relationships lead to the following conclusions: (a) molecular clouds are turbulent structures; (b) there is no significant variation in the mass surface density throughout molecular clouds; and (c) there is an equipartition between the gravitational and kinetic energy densities.

Stutzki et al. (1998) used wavelet analysis to characterize the velocity field in the interstellar cloud. Mac Low & Ossenkopf (2000) tried to characterize the interstellar turbulence using the $\Delta$- variance method. One of the interesting findings from their work is that the magnetic fields influence the energy transfer to lower scales from larger scales and tend to destroy the fractal structure. The interstellar turbulence also leads to large density fluctuations across different spatial scales, from large-scale filaments to small-scale clumps. These dense filaments and clumps can provide favorable conditions for gravitational collapse and subsequent star formation.

Turbulent diffusion is crucial in promoting the formation or destruction of chemical species, and it affects the chemical composition and local condition of the molecular cloud, which in turn impacts star formation efficiency. Dust grains act as catalysts for forming molecules, increasing the efficiency of chemical reactions. The diffusion coefficients associated with turbulent motions affect the transport of magnetic fields, momentum, and chemical species within the ISM, influencing the dynamics of the molecular cloud and the formation of protostellar disks. Turbulence causes the diffusion process to be more efficient at smaller scales. Molecular clouds are the primary constituents that establish how the

star formation process unfolds within galaxies (McKee & Ostriker 2007). Hence, investigating the dynamical state of molecular clouds is vital in the understanding of star formation in galactic (e.g., Sun et al. 2018) and extra-galactic scales (e.g., Kaufman et al. 1999). There are many studies (e.g., Xie et al. 1995; Willacy et al. 2002; Levrier et al. 2012) conducted previously to explain turbulent mixing and diffusion.

Photodissociation regions (PDRs) contain most of the atomic and molecular gas in a galaxy and are influenced by far-UV radiation, which drives the chemistry and heating of the PDR. The dynamics of these regions depend on the molecules or atoms present and the interaction with them and photons. The gas composition in the PDR will give rise to absorption and emission lines due to various chemical reactions. Molecular lines in these regions have broad profiles implying the presence of supersonic motions of cloud material. Line emissions from PDRs can help guide our understanding of the local conditions and unanswered questions on star formation and feedback.

The impact of turbulence on the chemical structure of interstellar clouds has been explored from several angles. The study by Xie et al. (1995) investigated a sphere with isothermal properties, characterized by a gas temperature of $T_{\rm gas} = 10\,K$, and radius of 1.11 pc. The study employed a model incorporating 87 distinct species that underwent formation and destruction via 1100 reactions, which included cosmic ray ionization, photodestruction processes, and CO self-shielding. Notwithstanding, the model lacked the incorporation of isotopes, interactions between gas and dust, $H_2$ self-shielding, or $H_2$ formation and energy balance. They reported significant modification in the abundance of some species, such as C, $C^+$, $H_2O$, $O_2$, and O. In their investigations,Yate & Millar (2003) expanded upon these findings by integrating adsorption on the grains. In contrast to the study conducted by Xie et al. (1995), this research employed a more extensive chemical network consisting of 127 species and 1669 reactions, excluding nitrogen and all the negative ions apart from electrons. Their research found that introducing diffusive mixing in relatively modest quantities can delay the freeze-out process at the center of the cloud. This is attributed to the inward diffusion from the edges of the cloud. They also tested the influence of sticking parameters on diffusion coefficients.

The research conducted by Willacy et al. (2002) incorporating the turbulent diffusion together with $H_2$ and CO self-shielding with gas-grain interaction showed that HI is highly sensitive to the diffusion process and can be used as a tracer. They also showed that the ratio C/CO and H/ $H_2$ show the diffusion effects. The inclusion of freezeout in the diffusion model has been observed to be sufficient in explaining the presence of O, C, CO, $H_2O$, and $O_2$ (Willacy et al.

2002). According to Bell et al. (2011), turbulent mixing affects the chemistry of deuterium within molecular clouds. This investigation found that diffusion causes an increase in ionization fraction and a decrease in the freezing of heavy molecules, leading to a reduction in the efficiency of deuteration. Their analysis also found that the turbulent mixing expanded the atomic region, which helped explore the observed atomic D/H ratio.

Using a post-processing technique, Levrier et al. (2012) investigated the chemical structure of turbulent photo-dominated areas (PDRs) and discovered that the abundances of several molecules (e.g., $H_2$, CO, CH, and CN) deviate significantly from a homogeneous PDR model. The research conducted by Lesaffre et al. (2007) employed a plane-parallel model to examine the interaction between a cold neutral medium and a warm neutral medium with varying temperatures. This paper integrated the concepts of energy balance, cosmic ray ionization, and photodissociation of $H_2$. However, they did not consider the CO self-shielding. This study contains 138 reactions, encompassing isotopes, gas-dust interactions, $H_2$ self-shielding, and $H_2$ formation. With their research, they concluded that the turbulent diffusion could help in interpreting the warm $H_2$, formation of $CH^+$, and presence of ${H_3}^+$. They also found that molecular production in the cloud is increased, increasing the abundance of $OH, H_2O, CO, CH^+$, and ${H_3}^+$. In contrast to the study by Bell et al. (2011), Lesaffre et al. (2007) found that the turbulence mixing expands the molecular region. Many other studies like Offner et al. (2013); Glover & Mac Low (2007); Glover et al. (2010); Valdivia et al. (2016) included the magnetic field into consideration.

The dynamic process on a large scale determines the local properties (temperature, densities, etc.) of different phases of ISM (Chevance et al. 2020). To comprehend the large-scale dynamics of the ISM, one needs a profound knowledge of the underlying microphysics. This study aims to quantitatively understand how dynamic mixing between different layers of PDRs influences local conditions. Diffusion coefficients quantify the rate at which material is transported and mixed by turbulent motions. Mixing between different layers of PDRs can shed light on understanding the molecular clouds and ISM better (Lesaffre et al. 2007). The molecular line observations can assist in understanding the influence of material transport in the ISM (Shu et al. 1987; Blake 1988). Typically turbulence is traced by $^{12}CO$ (Szűcs et al. 2014). However, $^{12}CO$ is optically thick, making it less useful throughout the cloud (Xie 1997; Peñaloza et al. 2018). The isotopologues $^{13}CO$ or $C^{18}O$ can be used. In low-density regions of the PDR, the CO is mostly photodissociated and left with $C^+$ whereas, in the high-density regions, CO will freeze out onto the dust grains. This chemical inhomogeneity makes using CO as a good tracer at low-density PDRs challenging. So it is necessary to understand

which species could be used as tracers.

The key objective of this thesis is to integrate the dynamics and chemistry of the photodissociation region (PDR) in order to comprehend the effects of diffusion on local conditions, such as gas temperature, abundance profiles, and the chemistry of different species. This study aims to determine the boundaries of the mixing length scales and diffusion coefficients and explore other molecular tracers. These investigations will contribute to a better understanding of the local conditions of the ISM.

# Chapter 2

# Photodissociation Regions

Energy radiated by stars in star-forming galaxies significantly impacts their surroundings. The energy absorbed by atoms and molecules may be re-radiated at longer wavelengths (Draine 1978). A significant fraction of the absorbed energy changes the temperature of the region, and the formation and destruction of various species, especially $H_2$. The regions where chemistry or heating is dominated by far-UV radiation are called photodissociation regions or PDRs (Sternberg & Dalgarno 1995). These regions are also called photon-dominated regions. However, calling a photon-dominated region would bring ambiguity into a listener's mind because the interstellar region is photon-dominated. Therefore, this thesis exclusively uses the term photodissociation regions.

PDR contains most of the ISM, which caught astronomers' attention in the last forty years (Tielens & Hollenbach 1985). The introduction of different telescopes and advancement in computational modeling helps a lot in the studies of these regions. With the observations made by telescopes like Herschel (Fischer et al. 2004; Pilbratt et al. 2010) and SOFIA(Young et al. 2012), galactic scales of a few parsecs are resolved. ALMA and JWST will map the extra-galactic observations, which could explain the extra-galactic PDRs. The upcoming FYST/CCAT prime will also contribute significantly to PDR research. This chapter provides a comprehensive overview of the structure and chemical composition of PDRs and the astronomical conventions and terminology used in this thesis.

## 2.1 Absorption, emission, and Einstein's coefficients

Electrons can transition between the energy levels by absorbing or emitting quanta of energy. The lowest energy state is the ground state of the electron. The amount of photons needed to excite or de-excite an electron varies based

on the energy difference between levels. Absorption happens when electrons absorb energy, causing them to move to a higher energy state. On the other hand, emission occurs when an electron releases energy and returns to a lower energy state. Conversely, atoms emit light when heated or excited at high energy levels. Consider an absorber $X$ at level $l$ is irradiated with a photon of energy $E_u - E_l$ then,

$$\mathrm{X}_l + \mathrm{h}\nu \longrightarrow \mathrm{X}_u, \qquad h\nu = E_u - E_l. \tag{2.1}$$

If the level $l$ has a number density $n_l$, the absorption rate of photons is proportional to the density of photons with sufficient energy and the number density $n_l$.

$$\left(\frac{dn_u}{dt}\right)_{l\to u} = -\left(\frac{dn_u}{dt}\right)_{l\to u} = n_l B_{lu} u_\nu, \qquad \nu = \frac{E_u - E_l}{h}. \tag{2.2}$$

The proportionality constant $B_{lu}$ is the *Einstein* B *coefficient* for the transition $l \to u$. An absorber X in the excited level $u$ can emit radiation and reach a lower level $l$ via spontaneous or stimulated emission.

$$\text{spontaneous emission} : \mathrm{X}_u \to {}^{+}\mathrm{X}_l{}^{+}\mathrm{h}\nu, \qquad \nu = \frac{E_u - E_l}{h} \tag{2.3}$$

$$\text{stimulated emission} : \mathrm{X}_u + \mathrm{h}\nu \to {}^{+}\mathrm{X}_l + 2\,\mathrm{h}\nu, \qquad \nu = \frac{E_u - E_l}{h} \tag{2.4}$$

Spontaneous emission is independent of the presence of a radiation field. Therefore, the probability for spontaneous emission per unit volume is $A_l$ *Einsteins A coefficient* (Draine 2011).

## 2.2 Lines and observations

Absorption will occur when the incident radiation has energy greater than or equal to the energy gap between the two levels of an atom or molecule. Emission occurs when an atom or molecule emits radiation equal to the difference between the two levels. The emission and absorption of different species in the interstellar medium help an astronomer observe and interpret the region. The absorption spectrum is observed against a continuum source behind the target. The light emitted by the source will be absorbed by the target. The missing lines in the continuum spectra will help to understand the absorption. The transition between different energy levels of an atom or molecule is governed by selection rules. The electric dipole transitions follow the following rules (Draine 2011).

1. orbital angular momentum quantum number: $\Delta \mathrm{L} = 0, \pm 1$
2. total angular momentum quantum number:$\Delta \mathrm{J} = 0, \pm 1$. However, $\mathrm{J} = 0 \to 0$

is forbidden

3. spin angular momentum quantum number does not change:$\Delta S = 0$

4. $\Delta l = \pm 1$

5. Parity must change

The electric dipole transitions are allowed transitions. The transitions which follow all the rules except the spin angular momentum are semi-forbidden. The transitions which do not follow the spin angular momentum and fail to fulfill at least one of the rules from above are forbidden.

While writing the lines and their ionization, astronomers follow certain conventions. If an atom or molecule is neutral, then "I" will be written. For a singly ionized atom/molecule, "II" and doubly ionized atom/molecule, "III" will be written. For example, atomic hydrogen would be HI, and atomic carbon would be written as CI. $C^+$ would be written as CII. A forbidden line will be written inside a square bracket, e.g.: [CII]. A line that is semi-forbidden would be written, e.g., CI] Semi-forbidden lines are $10^6$ times weaker than the allowed transitions, and forbidden lines are $10^2 - 10^6$ times weaker than the semi-forbidden lines (Draine 2011). In a high-density region, the excited states would be depopulated by collision reactions. However, in the lower density regions like interstellar medium, collisions are sufficiently infrequent, and excited states would depopulate via forbidden transitions. Hence, these forbidden lines are essential in astrophysics.

## 2.3 Composition of the PDR

The composition of the interstellar medium (ISM) is complex and consists of various components. The primary constituents of the ISM include dust, gas, interstellar radiation fields, and cosmic rays (Draine 2011). Among these, dust accounts for only 1% of the total mass of the ISM (Herbst 1995). Hydrogen and helium gases account for 70% and 28% of the total gas mass, respectively (Klessen & Glover 2016). Other elements contribute to the remaining 2%. Even though the ionized gas contributes less than 25% of the total gas mass, it occupies the majority of the volume of the ISM. The regions dominated by neutral atomic gas (H, He) or molecular gas ($H_2$) contributes more to the total mass of the ISM (Klessen & Glover 2016). The interaction of gas and dust with the interstellar radiation field determines the chemical and thermal state of the gas. Cosmic rays comprise 99% nuclei (protons, alpha, and metal nuclei) and 1% electrons, making them high-energy, relativistic particles Klessen & Glover (2016).

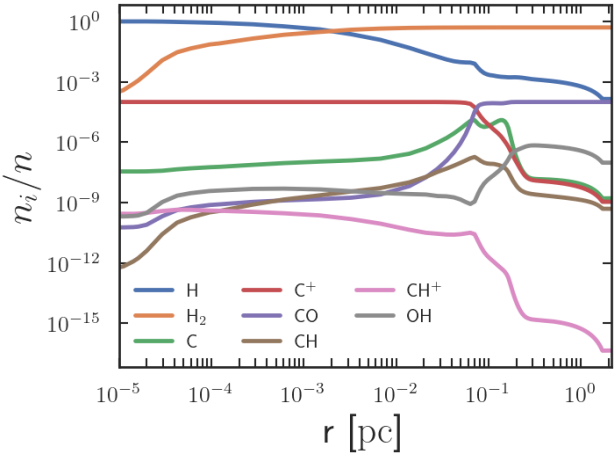


Figure 2.1: Fractional density profile of species in a PDR using KOSMA-$\tau$PDR model. Model parameters: table [3.1].

Although not yet discussed, polycyclic aromatic hydrocarbons (PAHs) are a crucial constituent of PDR. They are large organic molecules with one or more benzene rings (Klessen & Glover 2016). The absorption rate of PAHs is small. However, the effect of photons on the internal energy of the molecule is significant. The photon absorption puts the molecule in an excited state, which subsequently undergoes infrared transitions to return to its ground state. Therefore, it exhibits dominance over shorter wavelengths. For further details, refer to Bakes & Tielens (1998); Fuente et al. (2003); Arab et al. (2012); Hollenbach et al. (2012); Röllig et al. (2013); Klessen & Glover (2016). PAHs are a good tracer of the formation of massive stars due to their dependence on the strength of the UV radiation field.

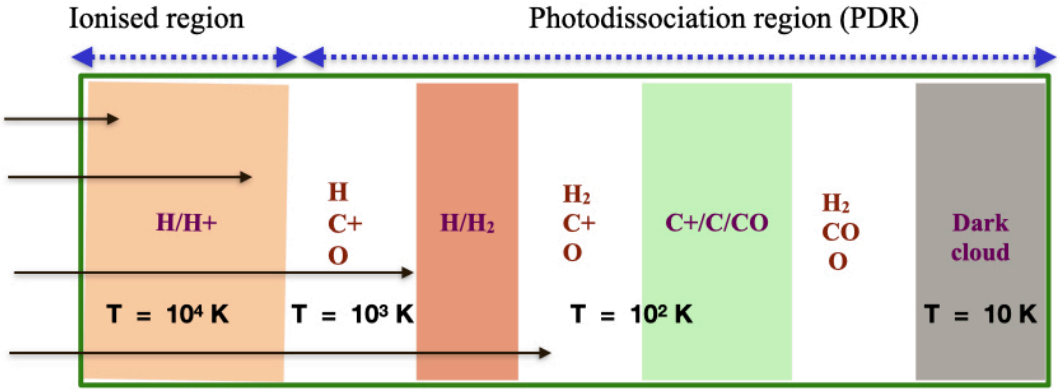


Figure 2.2: A simplified PDR structure sandwiched between the HII region and dark cloud (adapted from Hollenbach & Tielens 1999; Wolfire et al. 2022). Here the star is assumed to be on the left side.

## 2.4 Structure of a PDR

The formation of stars involves the collapse of dense and cold molecular gas due to gravity. When massive stars reach the main sequence, they emit high-energy ultraviolet radiation while still surrounded by dense gas. Figure [2.2] depicts a

one-dimensional photodissociation region that is adjacent to the ionized (HII) region as a function of the hydrogen column density. The OB stars (on the left side of Figure [2.2]) emit radiation that ionizes the surrounding areas, creating the HII region (Draine 2011). This high-energy ultraviolet radiation causes photodissociation and photoionization of nearby molecules, increasing the number of free particles and the gas temperature to $\sim 10^4$ K. Consequently, the thermal pressure increases, and the surrounding low-pressure region is pushed away by the high-pressure region (Draine 2011). The ionization front is the boundary between the ionized and neutral regions. Ionization fronts are classified into D-type and R-type (Maillard et al. 2021). A shock wave precedes the former, whereas the latter is not. The region between the ionization front and the dark cloud is called PDR, and the boundary close to the ionization front is the dissociation front. A dark cloud is an opaque molecular core where the chemistry has no changes due to FUV radiation. Cosmic rays dominate the chemistry and the heating in the dark cloud (Kaufman et al. 1999).

In the atomic region, $\sim 50\%$ of the mass of the cloud will be in atomic hydrogen. Whereas in the molecular region, $\sim$ 50% of the mass of the hydrogen would be in the molecular form (Draine 2011). The transition between the atomic and molecular regions is crucial in the chemistry of the photodissociation region because the formation or destruction of many molecules has reactions with $H_2$ as an intermediate step (Maillard et al. 2021). Figure [2.1] illustrates the fractional abundance of different species as a function of distance from the surface of the cloud. Neutral H, He, O and singly ionized metals such as $Si^+$, $C^+$, and $Fe^+$ comprises the gas in the outer layers of the PDR structure.

Self-shielding is a phenomenon when the photoexcitation transitions become optically thick, preventing the photoexcited molecule in question from being directly exposed to light (Draine 2011).

Figure [2.3] depicts the heating and cooling rates for the selected reactions in the PDR. Photoelectric heating (Draine 1978) contributes mainly to the heating rates, while the [CII] and [OI] lines contribute to the cooling rates. The gas cools by line radiation, whereas the dust cools by continuum radiation, making the gas temperature higher than the dust temperature. Due to dust opacity, FUV radiation declines deeper in the cloud. Most of the cloud will be converted into molecular hydrogen approximately around an $A_v$ of 2 (the precise value of $A_v$ depends on $G_0/n$ (Draine 2011)). Around an $A_v$ $2-4$, $C^+$ is recombined to form C and then form CO. The region between $H_2$ formation and CO formation is called *CO-poor* or *CO-dark* molecular gas (Glover et al. 2010). In these regions, the [CI] and [CII] lines are the top contributors to the cooling rates. Around an

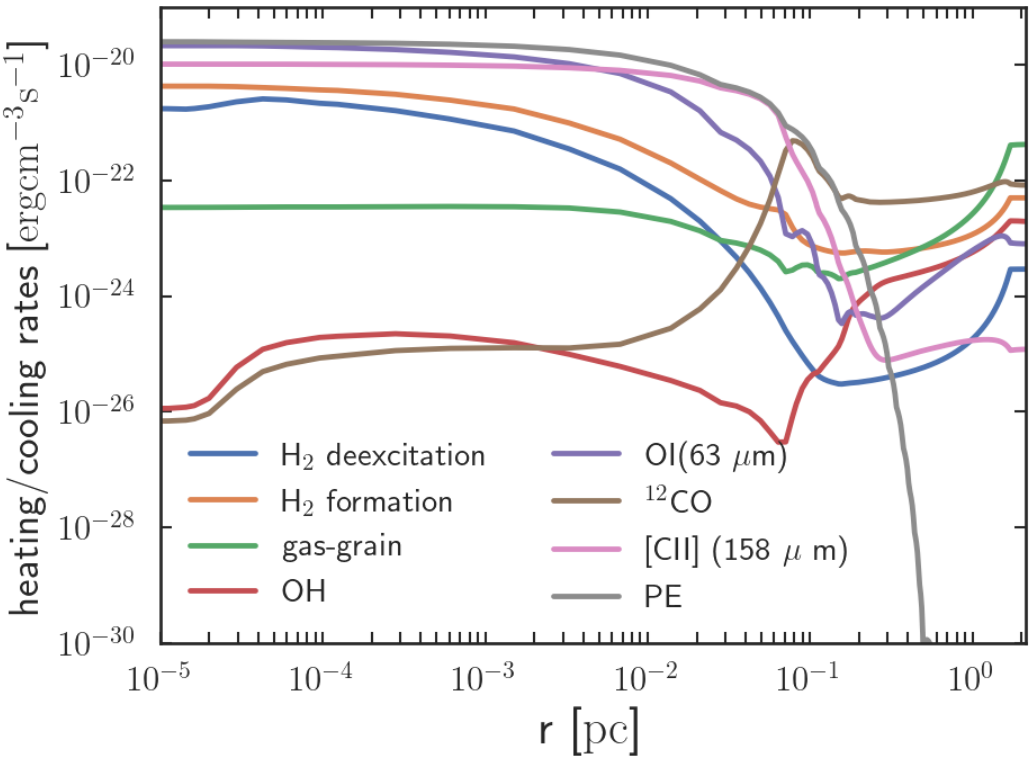


Figure 2.3: Heating and cooling rates in a PDR modeled using the KOSMA-$\tau$ PDR model. Model parameters: table [3.1].

$A_v$ of 10, dissociation of $O_2$ is no longer substantial (Draine 2011). The cooling of the gas is facilitated through the rotational transition of CO, while its heating is attributed to the ionization caused by cosmic rays. C, CO, O, and $H_2O$ are the predominant cooling reactants of the molecular gas in the ISM. However, the relative abundances of various coolants can modify the total cooling rates. In the PDR, $H_2$ formation and cosmic rays are the predominant heating mechanisms. For more details about the heating and cooling mechanisms, see Draine (1978); Hollenbach (1988); Bakes & Tielens (1994); Pan & Padoan (2009); Kazandjian et al. (2012).

## 2.5 Chemistry of PDRs

Molecular clouds are rich in chemistry. The Cologne Database for Molecular Spectroscopy (CDMS) has about 270 molecules detected. The local conditions influence the chemistry of the PDR and vice versa. Every molecule is created or destroyed through a series of chemical reactions, which can be summarized into chemical networks. For example, Figure [2.4] shows hydrogen, oxygen, and carbon chemical networks. This separation into different networks is for clarity;

in reality, the chemistry is not separable but rather intertwined. Many species like $H_2$, CO, and $HCO^+$ appear in multiple chemical networks. Every reaction is characterized by a reaction coefficient which is defined as the number of reactions per $cm^3$ and per second. A detailed explanation of different chemical networks refers to Sternberg & Dalgarno (1995).

The temperature and radiation field notably influences the chemistry of the PDR. Moreover, the coexistence of diverse species explains the evolution of the star-forming region and the formation of molecular clouds. When we look into the chemistry of PDR, a significant fraction depends on $H_2$ formation and destruction. The availability of $H_2$ leads to the formation of other species. At low temperatures, primarily exothermic reactions are found with a potential barrier to overcome (activation barrier). But at higher temperatures, such as in shocks or PDR, endothermic reactions occur.

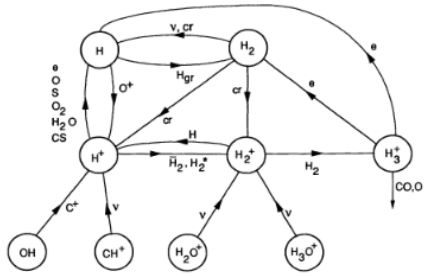

(a) Hydrogen

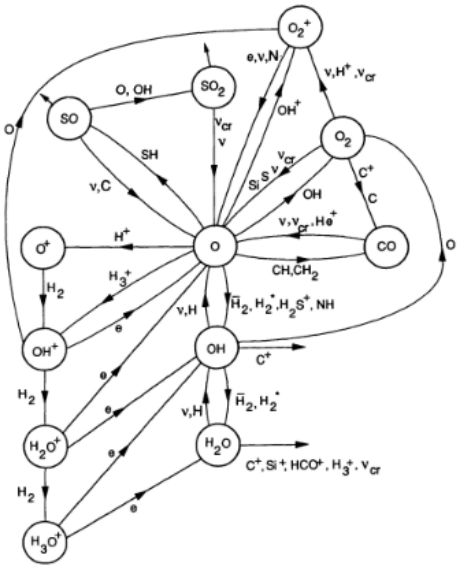

(b) Oxygen

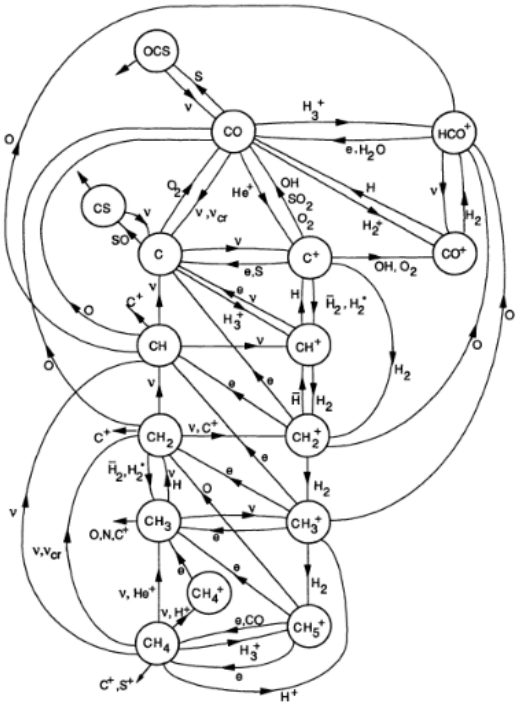

(c) Carbon

Figure 2.4: Chemical networks of oxygen, hydrogen, and carbon. Taken from Sternberg & Dalgarno (1995)

The important chemical reactions are summarised as follows. A detailed explanation is provided in Sternberg & Dalgarno (1995); Draine (2011).

1. **Photoionization:** $\mathrm{AB} + \mathrm{h}\nu \longrightarrow \mathrm{AB}^+ + \mathrm{e}^-$
   The successful occurrence of this reaction necessitates that the energy possessed by the incident photon is either equivalent to or surpasses the energy threshold required for ionization. The ionization energy of $H_2$ is measured to be 15.43eV, which explains the absence of photoionization of $H_2$ in HI regions (Draine 2011). For example:

$$\mathrm{C} + \mathrm{h}\nu \longrightarrow \mathrm{C}^+ + \mathrm{e}^- \qquad\qquad \mathrm{S} + \mathrm{h}\nu \longrightarrow \mathrm{S}^+ + \mathrm{e}^-$$

2. **Photodissociation:** $\mathrm{AB} + \mathrm{h}\nu \longrightarrow \mathrm{A} + \mathrm{B}$
   Molecular clouds contain primarily neutral molecules. Hence, neutral reactions are necessary and frequent. Even though the neutral-neutral reaction is exothermic, there is often an energy barrier to overcome. For example:

$$\mathrm{OH} + \mathrm{h}\nu \longrightarrow \mathrm{O} + \mathrm{H} \qquad\qquad \mathrm{CH}^+ + \mathrm{h}\nu \longrightarrow \mathrm{C} + \mathrm{H}^+ \tag{2.5}$$

3. **Ion-neutral exchange:** $\mathrm{AB}^+ + \mathrm{C} \longrightarrow \mathrm{AC}^+ + \mathrm{B}$
   This reaction occurs rapidly and is essential in molecular cloud chemistry because the energy barriers are non-existent for these exothermic reactions, even at low temperatures. Also, because of the induced-dipole interaction, ion-neutral rate coefficients are substantial. For example:

$$\mathrm{OH} + \mathrm{h}\nu \longrightarrow \mathrm{O} + \mathrm{H} \qquad\qquad \mathrm{CH}^+ + \mathrm{h}\nu \longrightarrow \mathrm{C} + \mathrm{H}^+ \tag{2.6}$$

4. **Neutral-neutral exchange:** $\mathrm{AB} + \mathrm{C} \longrightarrow \mathrm{AC} + \mathrm{B}$
   Frequent exchanges of neutral particles are commonly observed within molecular clouds, primarily due to the high abundance of neutral species within these environments. For example:

$$\mathrm{OH} + \mathrm{H} \longrightarrow \mathrm{O} + \mathrm{H}_2. \tag{2.7}$$

5. **Radiative association reactions:**

$$\mathrm{A} + \mathrm{B} \underset{k_\mathrm{d}}{\overset{k_\mathrm{f}}{\longleftrightarrow}} (\mathrm{AB})^\star \xrightarrow{k_\mathrm{r}} \mathrm{AB} + \mathrm{h}\nu, \tag{2.8}$$

   where $k_\mathrm{f}$, $k_\mathrm{d}$, and $k_\mathrm{r}$ are the reaction rate coefficients. A photon is emitted from the excited complex, $(AB)^\star$, which is created by this reaction. If the photon is not emitted, the complex will fly apart at a vibrational speed of $\sim 10^{-14}$ s.

The most prevalent molecule in the Universe, molecular hydrogen, dominates

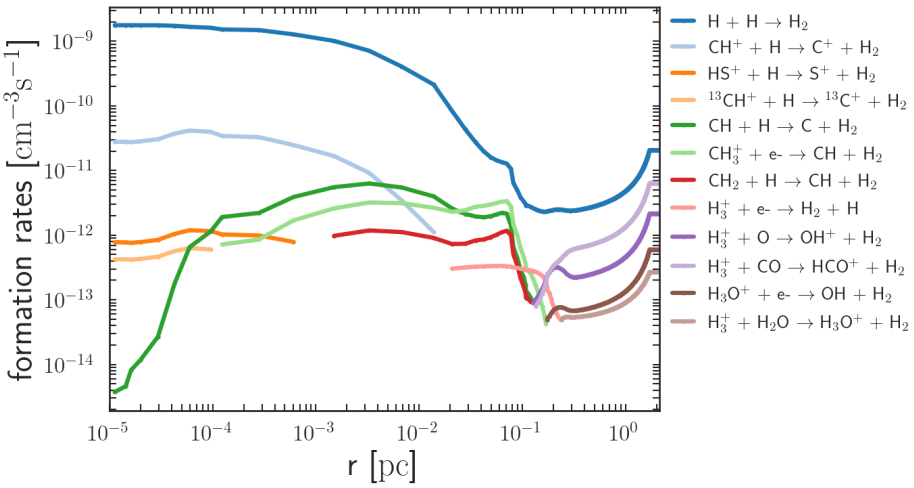


(a) formation reaction rates

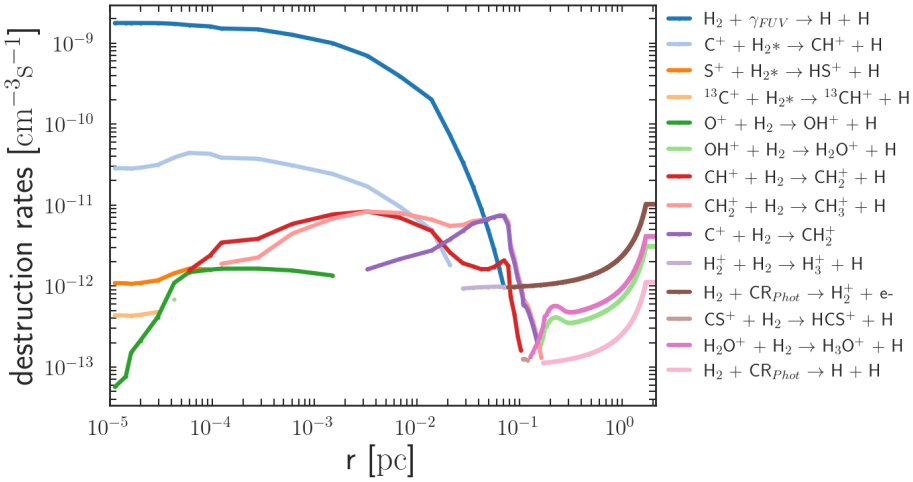


(b) destruction reaction rates

Figure 2.5: Formation and destruction reactions of $H_2$ using KOSMA-$\tau$ PDR model. Model parameters: table [3.1].

the mass budget of interstellar gas, especially in areas where stars are forming. Figure [2.5] shows the five biggest contributors to the formation and destruction reactions of $H_2$. Because it is so prevalent, molecular hydrogen is essential for the emergence of other molecular species. A crucial intermediate step in the chemical pathway toward many simple abundant interstellar substances is ion-molecule interactions involving molecular hydrogen followed by dissociative recombination (Cazaux & Tielens 2004). As the primary collision partner in dense clouds, molecular hydrogen controls the excitation and, by extension, the cooling of the gas. Also, molecular hydrogen can significantly cool, particularly in hot gas areas. The formation of $H_2$ is mainly via grain catalysis, and destruction is via photodissociation ($H_2 + h\nu \rightarrow H + H$ and kinetic energy).

When a star illuminates a gas cloud, some chemical reactions with an activa-

tion barrier can occur. For example,

$$C^+ + H_2 + 0.4\,\text{eV} \longrightarrow CH + H,$$

or in terms of energy $\Delta E/k = 4600$ K (Valdivia et al. 2017). This reaction happens only at higher temperatures which reduce the availability of the species $CH^+$ and CH on the surface of photodissociation regions. Due to the low density of the molecular cloud, the timescale of the chemical reactions is of the order of $10^6 - 10^7$ years, whereas the lifetime of the cloud is $10^7 - 10^8$ years (Draine 2011). For a cloud with a surface density of $n = 10^4 \text{cm}^{-3}$, the collision time scale is of the order of months.

# Chapter 3

# PDR Modelling

Astrochemical models of ISM have been available for the last fifty years. Due to the development of computational and observational techniques in the past forty years, there has been a tremendous improvement in the complexity of the models. The initial PDR models were created to explain the observed fine-structure emission (Gierens et al. 1992). Some of them are further developed and used to explain different observational data. As the computational infrastructure developed, models became more complex, from plane parallel to spherical, 1D to 3D, and complex chemical and dynamic structures.

The plane parallel PDR model consists of layers that are parallel to each other, as seen in the Meudon PDR code (Le Petit et al. 2006). Depending on the needs, the model can have either uni-directional illumination (Figure [3.1a]) or bi-directional illumination (Figure [3.1b]). The Meudon PDR model focuses on the precise treatment of chemical and physical processes, including hundreds of different species with surface and gas phase reactions. A spherical PDR structure typically features isotropic illumination (Figure [3.1b]), as in KOSMA-$\tau$ PDR model (Stoerzer et al. 1996; Röllig & Ossenkopf-Okada 2022, and references therein). The KOSMA-$\tau$ PDR model is extended to 3D using the clumpy approach (Cu-

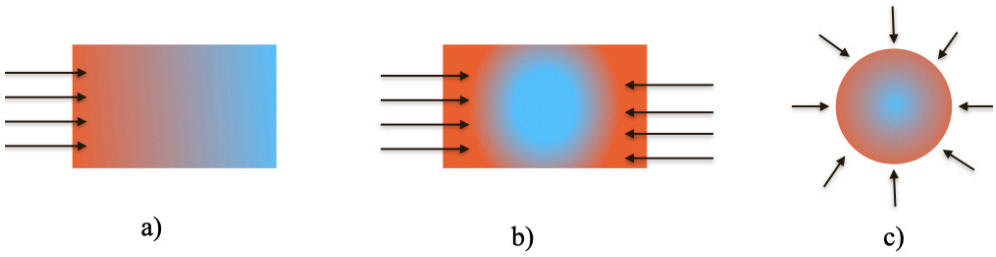


Figure 3.1: Geometry of the PDR model, plane-parallel geometry with rays (black arrows) coming from only a) one side and b) from both sides and c) spherical geometry with isotropic illumination. The color gradient shows that temperature is high at the surface and decreases as it moves to the center.

Table 3.1: Reference model parameters

| parameter | values | units |
|---|---|---|
| radius, $r$ | 2.13 | pc |
| surface density, $n_{\rm surf}$ | $10^4$ | $\rm cm^{-3}$ |
| mass of the clump, $M$ | $10^4$ | $\rm M_\odot$ |
| UV field, $\chi$ | 100 | Draine field |
| density profile, $\xi$ | $0, 1.5$ | |
| gas temperature, $T_{\rm gas}$ | 50, 70, 120 or non-uniform (Figure [3.5]) | K |
| dust temperature, $T_{\rm dust}$ | 20 or non-uniform (Figure [3.5]) | K |
| cosmic ray ionisation rate, $\zeta_{\rm CR}$ | $2.5 \times 10^{-16}$ | $\rm s^{-1}$ |

bick et al. 2008; Andree-Labsch et al. 2017; Yanitski et al. 2023).

Other PDR models are CLOUDY (spectral synthesis code which simulates the conditions in the interstellar matter Ferland et al. 2013, 2017), UCL_PDR (1D, time-dependent PDR model, Bell et al. 2005; Priestley et al. 2017; Bell et al. 2006), and 3D-PDR (3D extension of UCL_PDR). PDR Toolbox (Pound & Wolfire 2008; Kaufman et al. 2006; Pound & Wolfire 2011) is an open-source tool that provides an exhaustive set of computed models to understand observations. With the new development in computational power, MHD models (Glover et al. 2010; Kritsuk et al. 2017; Bisbas et al. 2012) are also solving PDR physics using small chemical networks. Röllig et al. (2007) was the first to attempt to benchmark the various PDR models. The main parameters to consider in the modeling are:

- radius/mass of the cloud ($r$)
- cloud density ($n_{\rm surf}$) or pressure
- radiation field ($\chi$)
- temperature ($T$)
- grain scattering properties
- $\rm H_2$ formation rate coefficient
- geometry/ clumpiness
- chemical reactions and gas phase abundances
- magnetic field

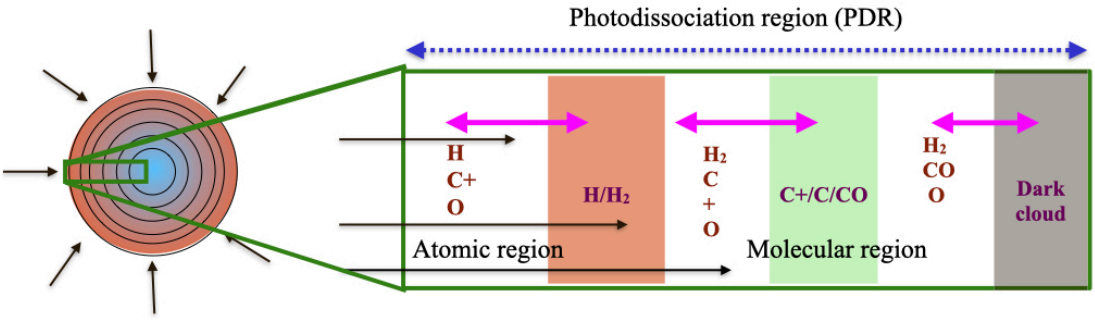


Figure 3.2: A slice of the KOSMA-$\tau$ PDR model cloud showing the PDR structure with diffusion. The FUV field passes through the cloud (black arrows), which ionizes and dissociates the region. The different molecules in the cloud are transported through it, as represented by the double-headed arrows.

## 3.1 KOSMA-$\tau$ PDR Model

Every PDR model must solve differential equations in a self-consistent way in a chosen geometry for gas temperature, radiation field, and abundance of different species. KOSMA-$\tau$ PDR model uses spherical geometry with isotropic illumination (Röllig et al. 2007). As you move from the surface of the cloud to the center, the UV field reduces the intensity, as species will absorb and re-radiate it. As a result, the temperature is higher at the surface of the cloud than at the center of the clump. The core of the cloud has a radius of 20% of the size of the clump.

A 1D PDR configuration in spherical coordinates uses an isotropic FUV radiation field with radiation from all sides (Figure [3.2]). Due to the significant scattering of interstellar dust in the FUV band, this assumption is reasonably accurate for the average ambient FUV field in the Galaxy and for local FUV sources if the PDR is embedded in a diffuse medium (Röllig & Ossenkopf-Okada 2022). The strength of the radiation field $\chi$ is in the units of Draine fields $\chi_D = 2.6 \times 10^{-3}\,\mathrm{ergs\,cm^{-2}\,s^{-1}}$ (integrated between 91.2nm and 200nm) (Draine 1978). The KOSMA-$\tau$ PDR model uses modular chemistry (Röllig & Ossenkopf-Okada 2022), i.e., you can add or remove a species with at least one destruction and formation reaction. Every point in the spherical shell calculates the abundance, temperature, and UV field density by solving a series of chemical equations, energy balance, and level populations. Since these components are interdependent, an iterative method is required to solve the differential equations (Figure [3.1.2]). These results are stored in the HDF file format.

### 3.1.1 Mass and surface density of the clump

The radial density profile of the clump is (Gierens et al. 1992; Cubick et al. 2008; Röllig & Ossenkopf 2013; Röllig & Ossenkopf-Okada 2022)

$$n(r) = n_{\rm surf} \begin{cases} \left(\frac{r}{R}\right)^{-\xi}, & \text{for } R_{\rm core}R \leqslant r \leqslant R \\ R_{\rm core}^{-\xi}, & r \leqslant R_{\rm core}R, \end{cases} \tag{3.1}$$

where $n_{\rm surf}$ is the total hydrogen nucleus number density($n_{\rm surf} = n_{\rm H,surf} + 2n_{\rm H_2,surf}$) at the surface of the clump and $R_{\rm core}$ is the radius of the core of the clump. When $\xi$ is zero, the clump will have a constant density $n_{\rm surf}$ irrespective of $r$. However, in a realistic cloud model, the density of the cloud is depth ($r$) dependent (Gierens et al. 1992). The molecular cloud can be considered as the dens core with a diffused PDR envelope, as shown in Figure [3.3].

The mass of the clump (Gierens et al. 1992) is calculated as follows,

$$M \approx 8.41629 \times 10^{-58} M_{\odot} \left[ \frac{12 n_{\rm surf} \pi R^3}{9 - 3\xi} - \frac{4n\pi R^3 R_{\rm core}^{3-\xi}}{9 - 3\xi} \right] \tag{3.2}$$

If we consider a sphere of constant density ($\xi = 0$) and $R_{\rm core} = 20\% R$, then th equation [3.2] will be,

$$M \approx 3.52541 \times 10^{-57} n_{\rm surf} R^3 \ M_{\odot}. \tag{3.3}$$

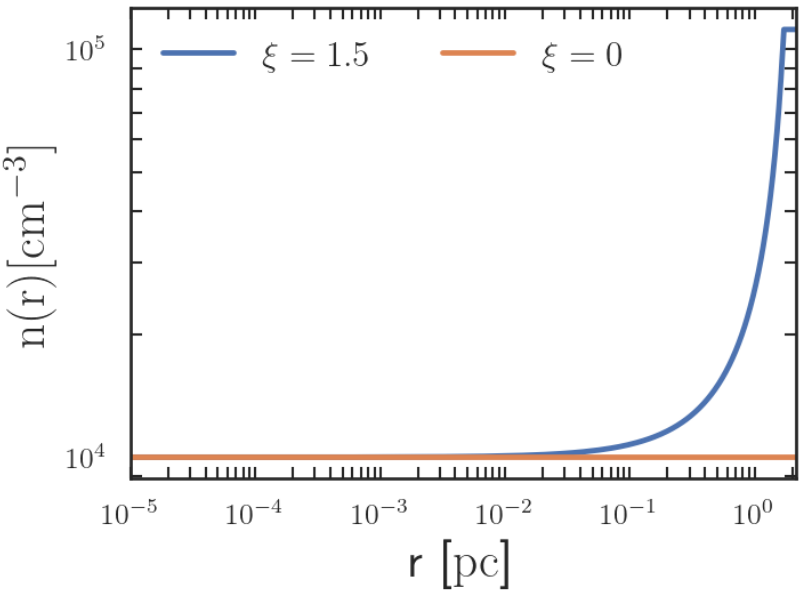


Figure 3.3: The radial density profile as a function of distance from the surface of the clump. Model parameters: table [3.1]

| |
|---|
| $e^-$, H, $H_2$, $H^+$, $H_2^+$, $H_3^+$, $He^+$, He, $O^+$, O, $C^+$, C, $^{13}C^+$, $^{13}C$, $OH^+$, OH, $O_2$, $CO^+$, CO, $CH^+$, CH, $^{13}CO^+$, $^{13}CO$, $13\,CH^+$, $^{13}CH$, $HCO^+$, $H_2O^+$, $H_2O$, $H^{13}CO^+$, $CH_2^+$, $^{13}CH_2^+$, $H_3O^+$, $CH_2$, $CH_3^+$, $SO_2$, $SO^+$, SO, $S^+$, S, $OCS^+$, OCS, $HS^+$, HS, $HCS^+$, $H_2S^+$, $CS^+$, CS, $^{18}O^+$, $^{18}O$, $O^{18}O$, $H_3^{18}O^+$, $H_2^{18}O^+$, $H_2^{18}O$, $^{18}OH^+$, $^{18}OH$, $HC^{18}O^+$, $H^{13}C^{18}O^+$, $C^{18}O^+$, $C^{18}O$, $^{13}C^{18}O^+$ |

Table 3.2: List of 61 species used in this PDR model.

### 3.1.2 Numerical iteration scheme

The numerical iteration scheme of the KOSMA-$\tau$ PDR model is shown in Figure [3.4]. The iteration scheme is summarised here, and for a detailed explanation, refer to Röllig & Ossenkopf-Okada (2022). KOSMA-$\tau$ PDR model uses a pre-processed dust model as an input. The dust properties are calculated by assuming a size distribution and composition as given by Weingartner & Draine (2001) or Mathis et al. (1977). For this model, the Mathis et al. (1977) dust model is used, and for more detailed explanations of dust models in KOSMA-$\tau$ PDR model, refer to Röllig et al. (2013).

The iterative scheme starts with an initial guess of the radiation field, temperature, and abundance. During a local iteration, the model will try to balance chemical, heating, and cooling rates to calculate the abundance and temperature. Once chemical and energy balance is achieved (local iteration), the position of the next shell will be determined. The spatial positions are neither fixed nor are they input parameters. Using the Bulirsch-Stoer algorithm (Bulirsch & Stoer 1964) KOSMA-$\tau$ computes the position of the subsequent shell from the current shell (Röllig & Ossenkopf-Okada 2022). With this adaptive mesh refinement (AMR) technique, the H$-$H$_2$ transition and atomic carbon to CO transition are sufficiently resolved numerically.

The Bulirsch-Stoer algorithm (Bulirsch & Stoer 1964) solves differential equations numerically. This modified Euler technique approximates the solution to a differential equation using a series of increasingly fine grids and then extrapolates to locate the solution on the finest grid. This enables the algorithm to attain higher precision compared to previous techniques that employ a single grid. The algorithm is named after its designers, Jürgen Bulirsch and Roland Stoer.

Every global iteration contains multiple spatial loops (shells), which are spatial

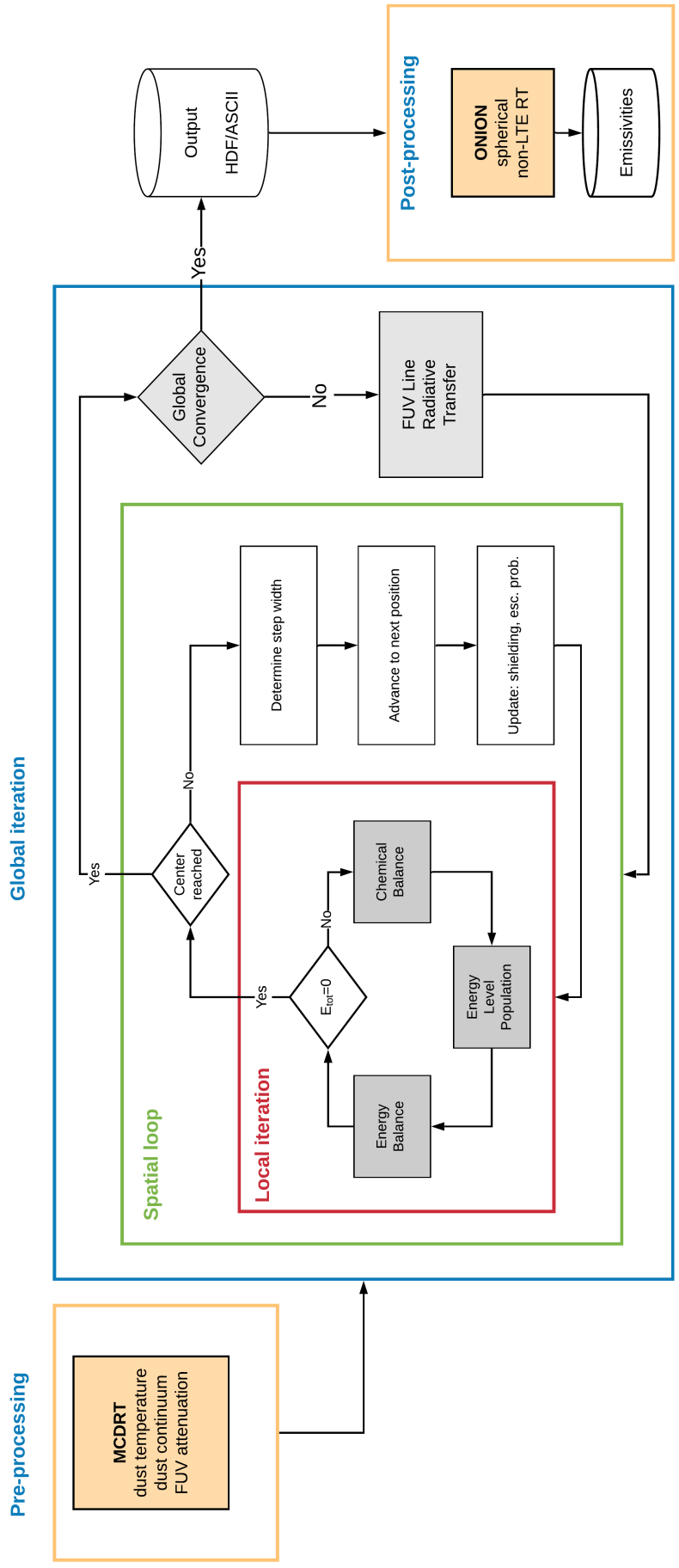


Figure 3.4: Numerical iteration scheme of KOSMA-$\tau$ PDR model (Röllig & Ossenkopf-Okada 2022). Every global iteration contains multiple spatial iterations (shells) to cover the entire radius of the spherical clump.

positions from the surface of the cloud to the center. Once the center of the cloud is reached, the model will try to solve the radiative transfer equations (Figure [3.4]) to obtain photodissociation rates, FUV intensity, and other parameters. All the positions in the cloud are non-locally coupled through this solution. As a result, the local physical conditions computed in the local iterations are updated based on the solution to the radiative transfer solutions. The heating and cooling rates will be calculated from the revised absorption and emission of IR and UV photons, which will change the local abundances. KOSMA-$\tau$ uses the final column density of all the species as a measure to test the global convergence. Once the global convergence is attained, the model will write abundance, column densities, temperatures, and other properties of the modeled cloud into an HDF file. Figure [2.1] shows the resultant abundance of selected species. Some of the KOSMA-$\tau$ PDR model output is available in ASCII format, all in HDF4 or HDF5.

The Bulirsch-Stoer algorithm can be used as an adaptive mesh refining technique. It can automatically adjust the size and resolution of the grids used to approximate the solution to a differential equation. This is done by comparing the results obtained from different grids and refining the grid in areas where the solution is not well-approximated. This allows the algorithm to achieve higher accuracy with fewer calculations and makes it helpful in solving problems with complex or changing solutions (Press et al. 2007).

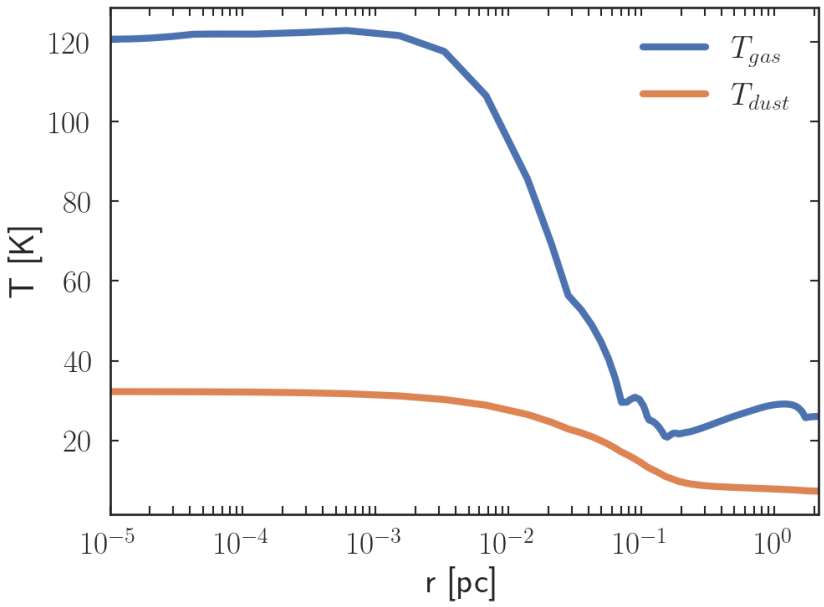


Figure 3.5: The gas and dust temperature profile of the modeled clump. Model parameters: table [3.1].

| ID | h/c | Process |
|---|---|---|
| 1 | h/c | Collisional de-excitation of vibrationally excited $H_2$ |
| 2 | h | Photodissociation heating of $H_2$ |
| 3 | h | $H_2$–formation heating using 1/3 of the binding energy of 4.48 eV |
| 4 | c | [O I] $^3P_1 \rightarrow {}^3P_2$(63 µm) line cooling |
| 5 | c | [O I] $^3P_0 \rightarrow {}^3P_2$(44 µm) line cooling (negligible) |
| 6 | c | [O II] $^3P_0 \rightarrow {}^3P_1$(146 µm) line cooling |
| 7 | h | Cosmic ray heating (Glassgold et al. 2012) |
| 8 | h/c | Grain photoelectric (PE) heating (minus recombination) |
| 9 | c | $^{12}$CO line cooling (J = 0-49) |
| 10 | c | [C II] $^2P_{3/2} \rightarrow {}^2P_{1/2}$ (158 µm) line cooling |
| 12 | c | [C I] $^3P_2 \rightarrow {}^3P_0$ line cooling |
| 11 | c | [C I] $^3P_1 \rightarrow {}^3P_0$ line cooling |
| 13 | c | [C I] $^3P_2 \rightarrow {}^3P_1$ line cooling |
| 15 | c | $^{13}$CO line cooling (J = 0-49) |
| 14 | c | [Si II] $^2P_{3/2} \rightarrow {}^2P_{1/2}(35\mu m)$ line cooling |
| 16 | c | [H I] Lyman-$\alpha$ cooling (Spitzer 1978) |
| 17 | c | $H_2O$ line cooling (Neufeld & Melnick 1987) |
| 18 | h/c | Gas-grain collisions |
| 19 | c | OH line cooling (including lowest 16 energy levels) |
| 20 | c | [OI] 6300$\AA$ cooling (Bakes & Tielens 1994) |
| 21 | c | $H_2$ photodissociation kinetic cooling (Lepp & Shull 1983) |
| 22 | h | Carbon photoionization heating (Tielens & Hollenbach 1985) |

Table 3.3: The heating and cooling reactions used in the KOSMA-$\tau$ PDR model. Taken from Röllig & Ossenkopf-Okada (2022).

### 3.1.3 Thermal balance

The evaluation of temperature is done at every position in the shell (see Figure [3.5]) by solving heating and cooling reactions.

$$E_{tot}(T)_s^S = \sum_h \Gamma_h(c_s^S) - \sum_c \Lambda_k(c_s^S) = 0, \tag{3.4}$$

where $c_s^S$ denotes the local conditions at global iteration $S$ and position $s$. $\Gamma_h$ denotes all the heating reactions and $\Lambda_k$ denotes the cooling reactions. The table [3.3] provides a list of heating and cooling rates. The heating and cooling rates depend on the position of the shell in the PDR, as shown in Figure [2.3]. The

solution of equation [3.4] determines the temperature at which all the heating and cooling processes add up to zero. A detailed explanation of the temperature solution is given in Röllig & Ossenkopf-Okada (2022).

Equation [3.4] clearly shows that the thermal balance depends on the local conditions and is linked to the chemical balance. Once the diffusion terms are added, the thermal balance also should be maintained to attain a stable temperature solution and steady state. However, the resulting chemical vector with diffusion would differ from that without diffusion.

### 3.1.4 Chemical balance

A detailed explanation of the chemistry solver in the KOSMA-$\tau$ is given in Röllig & Ossenkopf-Okada (2022). A comprehensive summary is given below. The chemical pathways through which the species are formed or destroyed significantly depend on the local FUV intensity, gas-phase abundance, gas and dust temperatures, etc., and vary with depth. The chemical reactions are discussed in §[2.5]. The density of every species $i$ is calculated by solving the formation and destruction reactions rates. The formation and destruction of species $i$ at a spatial position $s$ is,

$$\mathbb{F}_i^s = \frac{dn_i^s}{dt} = \sum_{j,j'} k_{jj'} n_j n_{j'} + \sum_t n_t \tilde{\zeta_{it}} - n_i \left( \tilde{\zeta_i} + \sum_q n_q k_{qi} \right) + \left[ \frac{\partial n_i^s}{\partial t} \right]_{\rm d} \quad (3.5)$$

where $n_j$,$n_{j'}$, and $n_q$ are the number densities of species that participated in the formation or destruction. On the right-hand side, the first two terms represent the formation of species $i$ by the interaction of species $j$ and species $j$' and the formation of the species $i$ by the cosmic ray process and/or photoprocess of the species $t$, respectively. The second-to-last term represents the sum of the destruction reactions of species $i$ via photo-process ($\tilde{\zeta}$) and two body collisions. The final term is the formation/destruction via diffusion transport. If the diffusion flux gradient is greater than zero, it is a formation reaction, and a negative value is a destruction reaction. An example of non-diffusive chemical reactions (formation and destruction) of $H_2$ is shown in Figure [2.5]. A detailed explanation of the calculation of the diffusion transport is given in the §[4.4].

The chemistry of the KOSMA-$\tau$ PDR model has been updated to include the grain surface reactions (Röllig & Ossenkopf-Okada 2022). The gas-phase chemistry is also extended to include additional accretion and desorption reactions.

Hence, eq.[3.5] becomes,

$$\mathbb{F}_i^s = \frac{dn_i^s}{dt} = \sum_{j,j'} k_{jj'} n_j n_{j'} + \sum_t n_t \tilde{\zeta_{it}} - n_i \left( \tilde{\zeta_i} + \sum_q n_q k_{qi} \right) + \left[ \frac{\partial n_i^s}{\partial t} \right]_{\rm d} - k_{acc,i} n_i + K_{des,i} n_{surf,i} \quad (3.6)$$

The lowercase $k$ and uppercase $K$ distinguish between chemical reaction rate coefficients other than diffusion and diffusion reaction rate coefficients, respectively. Using eq.[3.6] we can write,

$$\mathbb{F}_i^s = \frac{dn_i^s}{dt} = \mathbb{F}_{i,c}^s + \mathbb{F}_{\rm d} \quad (3.7)$$

where,

$$\mathbb{F}_{i,c}^s = \sum_{j,j'} k_{jj'} n_j n_{j'} + \sum_t n_t \tilde{\zeta_{it}} - n_i \left( \tilde{\zeta_i} + \sum_q n_q k_{qi} \right) - k_{acc,i} n_i + K_{des,i} n_{surf,i}, \quad (3.8)$$

$$\mathbb{F}_{i,{\rm d}}^s = \left[ \frac{\partial n_i^s}{\partial t} \right]_{\rm d}. \quad (3.9)$$

Here $\mathbb{F}_{\rm c}$ denotes the chemical reactions other than diffusion and $\mathbb{F}_{\rm d}$ denotes the contribution from diffusion.

Diffusion rate for species $i$ at a spatial position $s$ is written as,

$$\left[ \frac{\partial n_i^s}{\partial t} \right]_{\rm d} = \frac{\partial \phi_i^s}{\partial x} = \frac{\partial \phi_{turb}}{\partial x} + \frac{\partial \phi_{mol}}{\partial x} + \frac{\partial \phi_{thermal}}{\partial x} \quad (3.10)$$

where $\phi_{turb}, \phi_{\rm mol}$, and $\phi_{\rm thermal}$ are total, turbulent, molecular, and thermal diffusion flux, respectively. The §[4.4] gives a detailed explanation of diffusion rates.

A Newton-Raphson method with a Jacobi matrix can be used to solve the partial differential equations iteratively (Röllig & Ossenkopf-Okada 2022). Using this method, KOSMA-$\tau$ computes an equilibrium solution to eq.[3.6].

$$\mathbb{F}_i^s = \frac{dn_i^s}{dt} \quad (3.11)$$

The Jacobi matrix $\mathbb{Q}$ is a square matrix of size $NSP \times NSP$ where $NSP$ is the total number of species in the model. The Jacobi matrix contains the partial derivatives of the system of equations with respect to the density of the species $(n_i^s)$ at the shell where the solution is evaluated. The locally convergent method will converge for a starting point sufficiently close to the root. The Jacobi matrix

elements are,

$$\mathbb{Q}(i,j) = -\frac{d\mathbb{F}_i^s}{dn_i^s} = -\frac{d\mathbb{F}_{i,\mathrm{c}}^s}{dn_i^s} - \frac{d\mathbb{F}_{i,d}^s}{dn_i^s} = \mathbb{Q}_{\mathrm{c}}^s(i,j) + \mathbb{Q}_{i,\mathrm{d}}^s \tag{3.12}$$

where, $i$ and $j$ denotes species, and

$$\mathbb{Q}_{\mathrm{c}}^s(i,j) = -\frac{d\mathbb{F}_{i,\mathrm{c}}^s}{dn_i^s}, \qquad \mathbb{Q}_{i_{\mathrm{d}}}^s = \frac{d\mathbb{F}_{i_{\mathrm{d}}}^s}{dn_i^s}. \tag{3.13}$$

Here, $\mathbb{Q}(i,j), \mathbb{Q}_{\mathrm{c}}^s(i,j)$ and $\mathbb{Q}_{i_{\mathrm{d}}}^s$ corresponds to the Jacobi matrix, contributions to the Jacobi matrix from chemical reactions other than diffusion, and contributions to Jacobi matrix from diffusion, respectively. The derivative of $\mathbb{F}_i^s$ is taken with respect to every species to populate $\mathbb{Q}$. If $\mathbb{F}_i^s$ does not depend on $n_j^s$ (through formation or destruction), then the corresponding Jacobi matrix element will be $\mathbb{Q}(i,j) = 0$.

The improved solution, $n_i^{new}$, is computed from an approximate solution (old) or an initial guess, $n_i^{old}$ in the next step:

$$\sum_j -\mathbb{Q}_{i,j}^{old} \left(n(j)^{new} - n(j)^{old}\right) = \mathbb{F}_i^{old}. \tag{3.14}$$

which results in a linearised system of the form $\mathbb{Q} \cdot \delta n = \mathbb{F}$. More details about the solution scheme are given in Röllig & Ossenkopf-Okada (2022).

# Chapter 4

# Diffusion

> Big whirls have little whirls which feed on their velocity;
> And little whirls have lesser whirls
> And so on to viscosity in the molecular sense.
>
> *L.F. Richardson*

Two fundamental material transport processes are diffusion and advection. Consider a river. There are two outcomes if a bottle of dye is thrown into the river's middle. Advection occurs when the river's flow transports the dye downstream. In addition, the color will move from the center to the edges. Diffusion spreads dye from a concentrated point to a less concentrated region. Dye molecule advection occurs exclusively in one direction (direction of river flow). The dye will spread faster if the river contains eddy currents. In this case, turbulence in all directions causes eddy currents, which regulate the dye diffusion rather than random movements.

According to Fick's law (Fick 1855), the flow of ink is proportional to the spatial changes in the concentration, i.e., the flux $\phi = -\frac{\partial C}{\partial x^s}$ where $C$ is the concentration, and $x$ is the spatial position. The negative sign indicates that the flow would be from the region of higher concentration to the lower concentration. This study considers turbulent, thermal, and molecular diffusion. The rate of change of abundance with respect to time will equal the rate of change of diffusion flux. Therefore, diffusion rates are,

$$\left[\frac{\partial n}{\partial t}\right]_d = \frac{\partial \phi}{\partial x} = \frac{\partial \phi_{turb}}{\partial x} + \frac{\partial \phi_{mol}}{\partial x} + \frac{\partial \phi_{thermal}}{\partial x} \tag{4.1}$$

where, $\phi, \phi_{turb}, \phi_{\text{mol}}$, and $\phi_{\text{thermal}}$ are total, turbulent, molecular, and thermal diffusion flux respectively. The flow would be from higher concentration to lower

concentration.

Transport of species or thermal energy can be by the random motion of species or the turbulent eddies. From eq.[4.1] diffusion rate of species $i$ at position $s$ is,

$$\left[\frac{\partial n_i^s}{\partial t}\right]_d = \frac{\partial \phi_i^s}{\partial x^s} = \frac{\partial \phi_{turb}}{\partial x^s} + \frac{\partial \phi_{mol}}{\partial x^s} + \frac{\partial \phi_{thermal}}{\partial x^s} \tag{4.2}$$

The diffusion flux of species $i$ at position $s$ is (Chapman 1958),

$$\phi_{\rm i} = -K_{\rm turb}\frac{\partial n_i^s}{\partial x^s} - K_{\rm mol}\frac{\partial n_i^s}{\partial x^s} + n_\Sigma K_{\rm therm}\left(\frac{1}{T^s}\frac{\partial T^s}{\partial x^s}\right) \tag{4.3}$$

$$= -K\left(f\frac{\partial n_i^s}{\partial x} + g\frac{\partial n_i^s}{\partial x}\right) + K_{\rm therm}\ n_\Sigma\left(\frac{1}{T^s}\frac{\partial T^s}{\partial x^s}\right) \tag{4.4}$$

$$= -K\ d_{12} + K_{\rm therm} n_\Sigma\left(\frac{1}{T^s}\frac{\partial T^s}{\partial x^s}\right)\ , \tag{4.5}$$

where $f$, and $g$ are the respective weights for turbulent and molecular diffusion. $n_\Sigma$ is the total particle number density cm$^{-3}$.

$$d_{12} = \left(f\frac{\partial n_i}{\partial x^s} + g\frac{\partial n_i}{\partial x^s}\right) \tag{4.6}$$

$d_{12}$ is proportional to the diffusive motion (both turbulent and molecular) of molecules of the gas components in a multi-component gas medium.

## 4.1 Molecular diffusion

To investigate the molecular and thermal diffusion coefficient in a multi-fluid plasma, we consider species moving over a length scale equal to the mean free path with thermal velocity. Molecular diffusion coefficient

$$K_{\rm mol} = V_i\lambda \tag{4.7}$$

where, $\lambda = 1/\sigma n$ is the mean free path (the gas is assumed to be atomic, $\sigma = 10^{-15}$cm$^2$ Lesaffre et al. 2007) in the neutral medium, $n_i$ is the number density of the species and n is the total number density of particles cm$^{-3}$ and

$$V_i = \sqrt{\frac{5kT^s}{3\mu}}, \tag{4.8}$$

where $T^s$ is the temperature at the spatial position $s$, and $\mu$ is the molecular weight of the species. Figure [4.1] displays the molecular velocity for selected species. Figure [4.2] shows the molecular diffusion coefficient of atomic and molec-

ular hydrogen. The molecular diffusion flux can be written as,

$$\phi_{mol}(\mathrm{cm^{-2}\,s^{-1}}) = K_{\mathrm{mol}}\,\frac{\partial n_i}{\partial x^s} = \sqrt{\frac{5kT_i}{3\mu_i}}\,\frac{1}{\sigma n}\,\frac{\partial n_i}{\partial x^s} \tag{4.9}$$

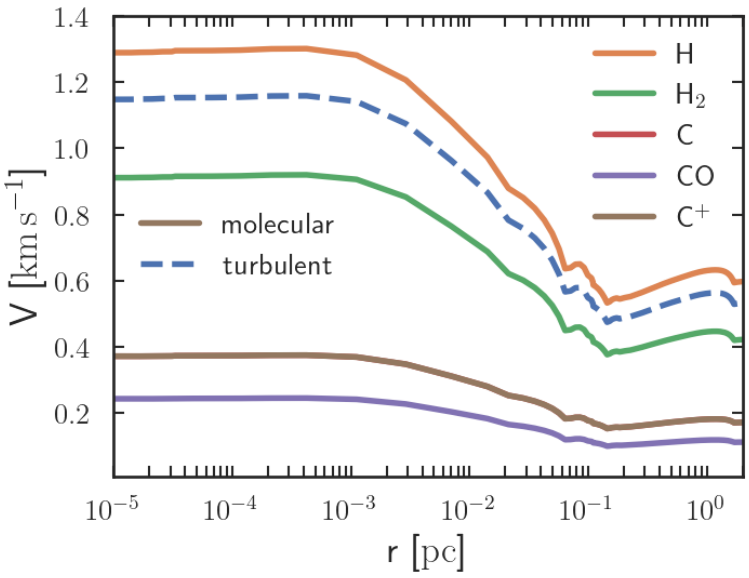


Figure 4.1: Turbulent ($v_t$) and molecular diffusion ($v_i$) velocities of different species. The turbulent velocity (dashed line) is the same for all species (eq. [4.23]), whereas molecular diffusion velocities are calculated using eq.[4.8]. Model parameters: table [3.1] with $\xi = 1.5$.

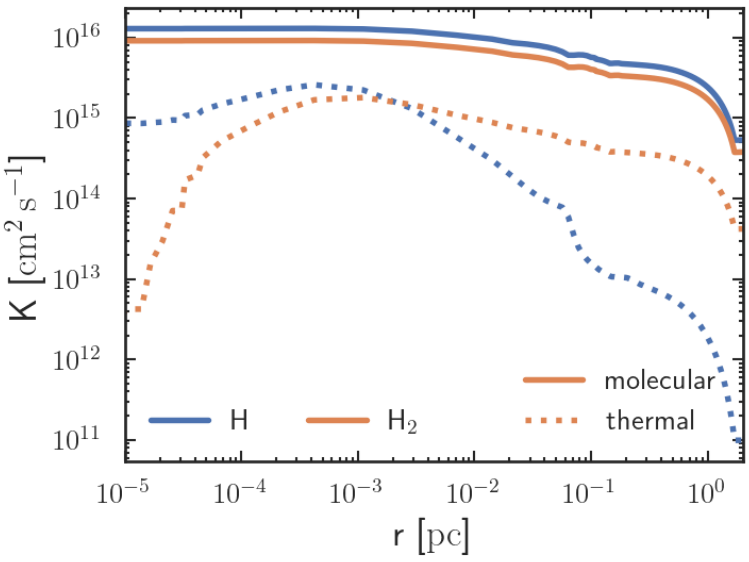


Figure 4.2: Molecular and thermal diffusion coefficients for atomic and molecular hydrogen. Model parameters: table [3.1] with $\xi = 1.5$ with nonuniform temperature (Figure [3.5]).

## 4.2 Thermal diffusion

The relative mobility of different gases in a mixture of gases in a temperature gradient medium causes thermal diffusion. Typically, lighter/smaller species migrate from a cold to a hot location (negative thermal diffusion). In contrast, heavier/larger molecules move from a hot to a cold region (positive thermal diffusion). When the masses of two molecules are comparable, the bigger molecules shift to the colder region. As a result of this transportation, a composition gradient is formed, which is balanced by remixing to achieve a stable state (Kincaid et al. 1986). As a result of thermal diffusion, ions and electrons move depending on their size. This separation can create a small electric field in an ionized gas medium (S. Chapman 1916). The electric field will keep the electrons with the ions, resulting in an electrically neutral gas almost everywhere. This bounding of electrons with ions reduces the contribution of thermal diffusion to the total diffusion in a medium. S. Chapman (1916) and Enskog (1917) predicted the thermal diffusion in gases and were later confirmed by the experiments of Chapman & Dootson (1917).

Consider a binary gas mixture, with the number densities per unit volume of the two gas components 1 and 2 being $n_1$ and $n_2$. In a binary mixture, thermal diffusion flux between the two gas components could be written as (Chapman 1940),

$$\phi_{therm}(\mathrm{cm^{-2}\,s^{-1}}) = -n_\Sigma K_{\mathrm{therm}} \left(\frac{1}{T}\frac{\partial T}{\partial x^s}\right) \tag{4.10}$$

where $n_\Sigma = n_1 + n_2$, and $T$ is the gas temperature in Kelvin.

$$\phi_{therm} = -n_\Sigma K k_T \left(\frac{1}{T}\frac{\partial T}{\partial x^s}\right) \tag{4.11}$$

Without external forces, $K = K_{\mathrm{mol}}$ (Sydney & Cowling. 1954). The thermal diffusion ratio

$$k_T = \frac{K_{\mathrm{therm}}}{K} = \frac{K_{\mathrm{therm}}}{K_{\mathrm{mol}}} \tag{4.12}$$

and is proportional to the product of the two densities. Thermal diffusion factor $\alpha$ (Chapman 1940) is

$$k_T = \alpha \frac{n_1 n_2}{n_\Sigma^2}, \tag{4.13}$$

Hence,

$$K_{\mathrm{therm}} = K_{\mathrm{mol}} \alpha \frac{n_1 n_2}{n_\Sigma^2} \tag{4.14}$$

$$\phi_{therm}[\mathrm{cm^{-2}s^{-1}}] = -n_\Sigma \left(K_{\mathrm{mol}} \alpha \frac{n_1 n_2}{n_\Sigma^2}\right) \left(\frac{1}{T}\frac{\partial T}{\partial x^s}\right) \tag{4.15}$$

Thermal diffusion depends on the mass and structure variation between the

species.

### Choice of $\alpha$

Thermal diffusion in a gaseous mixture depends on the 'thermal diffusion factor' ($\alpha$). To understand the diffusion in a non-uniform temperature region, the value of $\alpha$ should be evaluated. Finding an $\alpha$ value that explains the condition in the molecular cloud is complex due to the lack of precise theory. Most thermal diffusion calculations consider a fully ionized or partially ionized medium with a binary mixture of gases, where the molecular cloud contains multiple gas components of various sizes, masses, and degrees of ionization.

For a fully ionized medium a limiting value of $\alpha_{ie}$ is (Chapman 1958, (p.356))

$$\alpha_{ie} = \frac{-3(Z+1)}{2.6 + 0.8\sqrt{2}/Z} \tag{4.16}$$

which is a dimensionless quantity. Here $Z$ is the charge number. The minus sign indicates that the ions tend to move to the hotter region. Since molecular clouds primarily consist of neutral particles, eq.[4.16] does not apply.

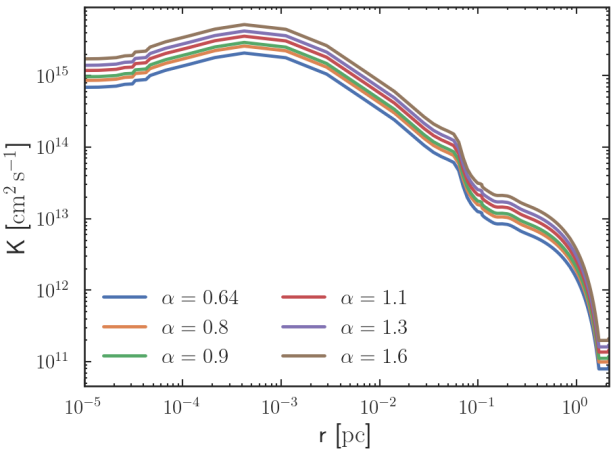


Figure 4.3: Thermal diffusion coefficient at different $\alpha$ values for H. The $\alpha$ values are chosen between 0.64 and 1.6 to show the behavior of the thermal diffusion coefficient. Model parameters: table [3.1] with $\xi = 1.5$ with nonuniform temperature (Figure [3.5]).

Values of $\alpha$ for a gas mixture of neutral particles are lower than the numerical values of $\alpha_{ie}$ from eq.[4.16](Chapman 1958). For a neutral gaseous mixture, $\alpha$ is less than unity, and in a simple ionized gas, $\alpha$ is in the order of $Z + 1$ (Chapman 1958). Since the effect of thermal diffusion for ions is more prominent than neutral species, an approximated value of $\alpha = 0.64$ can be adopted (Chapman 1958) This is the most significant observed value (helium-radon mixture). In conclusion, for a molecular cloud, the value of $\alpha$ might vary between 0.64 and 1.6 (fully ionized medium with $Z = 1$). Figure [4.3] shows the difference in thermal diffusion coefficients. Since the molecular cloud predominantly comprises neutral gas, we assumed $\alpha = 0.80$. For experimental versus the theoretical study of $\alpha$ values, see Chapman (1958); Văsaru (1967); Chapman & Dootson (1917).

Thermal diffusion coefficient between a species ($n_1 = n_i$) and the rest of the fluid ($n_2 = n_\Sigma - n_i$) is,

$$K_{\rm therm} = K_{\rm mol}\alpha\frac{n_1 n_2}{n_\Sigma^2} = K_{\rm mol}\alpha\frac{n_i(n_\Sigma - n_i)}{n_\Sigma^2} \tag{4.17}$$

Figure [4.2] shows the thermal diffusion coefficient of atomic and molecular hydrogen. Diffusion rates would be,

$$\frac{\partial\phi_{\rm therm}}{\partial x^s}({\rm cm^{-3}s^{-1}}) = -n_\Sigma K_{\rm mol}\alpha\frac{n_i(n-n_i)}{n_\Sigma^2}\frac{\partial}{\partial x^s}\left(\frac{1}{T}\frac{\partial T}{\partial x^s}\right) \tag{4.18}$$

$$-n_\Sigma K_{\rm mol}\alpha\frac{(n-n_i)}{n_\Sigma^2}\left(\frac{1}{T}\frac{\partial T}{\partial x^s}\right) \tag{4.19}$$

$$= -n_\Sigma K_{\rm mol}\alpha\frac{n_i(n-n_i)}{n_\Sigma^2}\left[\frac{-1}{T^2}\left(\frac{\partial T}{\partial x^s}\right)^2 + \frac{1}{T}\frac{\partial^2 T}{\partial x^2} + \frac{1}{n_i}\left(\frac{1}{T}\frac{\partial T}{\partial x^s}\right)\right] \tag{4.20}$$

## 4.3 Turbulent diffusion

Interstellar turbulence is distinct from Kolmogorov turbulence in numerous ways (Kritsuk et al. 2017). Kolmogorov turbulence (Kolmogorov 1991a,b,c) is both homogeneous and isotropic, whereas interstellar turbulence is neither. The gas is highly compressible and magnetized. Understanding the effects of turbulence in the dense and colder parts is vital in understanding the relationship between turbulence and star formation. To explain the interaction between different fluid parcels in a turbulent situation, a mixing-length theory is used.

**Mixing length theory** (Prandtl 1904) is a theoretical framework used in fluid dynamics to describe the motion of a fluid near a boundary. Ludwig Prandtl first developed it in 1904, and has since been used to model various phenomena in fluid dynamics, such as airflow over an airplane wing.
In mixing length theory, the motion of a fluid near a boundary is described by a **mixing length**, which measures the distance over which the fluid mixes and diffuses. This mixing length is typically assumed to be proportional to the distance from the boundary and is often used to model turbulent flow behavior in fluids.
One of the critical assumptions of mixing length theory is that the fluid near a boundary can be treated as a series of layers, each of which mixes and diffuses independently of the others. This allows for a relatively simple mathematical treatment of the fluid motion and is a valid approximation in many cases.

According to the mixing length theory, a fluid parcel moves a distance of $L$ be-

fore it disperses into the neighboring fluid. In a mixing length theory, every fluid particle is considered to be moving with a velocity compared to the background. After traveling a length of $L$, it will merge back into the background fluid.

The molecular cloud has an uneven distribution of different types of gases. Variations in the fractional abundance result from a nonlinear turbulent process that causes the gas components to move with the same velocity, denoted by $V_t$. The variation in abundance is approximated as the product of the composition gradient $d(n_i/n)/dx$ in the direction $x$ and the mixing length $L$, $\delta n_i \approx -L\frac{d(n_i/n)}{dx}$, where $n_i/n$ is the fractional number density of species $i$. The net transport flux of the tracer $i$ in the $x$-direction can be written as (Xie et al. 1995)

$$\phi_{turb}(\mathrm{cm^{-2}\,s^{-1}}) = n < V_t \delta n_i >= -n\ K_{\mathrm{turb}}\ \frac{d(n_i/n)}{dx} = -K_{\mathrm{turb}}\ \frac{dn_i}{dx} \tag{4.21}$$

where, turbulent diffusion coefficient $K_{\mathrm{turb}}$ is defined as

$$K_{\mathrm{turb}} =< V_t L > \tag{4.22}$$

and n is the total number density of particles $\mathrm{cm^{-3}}$.

The observations (Zuckerman & Evans 1974) of molecular clouds found evidence of supersonic turbulence. The empirical size-line width relationship (Larson 1981) suggests that the turbulence will decay with decreasing scales. This implies that at small scales, subsonic motions can be detected (Gong et al. 2022). For a region with a temperature of 100K, the thermal velocity would be $\sim$ $1\,\mathrm{kms^{-1}}$. Suppose we assumed a coherence length, $L = 0.1 - 0.5\,\mathrm{pc}$, (Xie et al. 1995; Ossenkopf & Low 2002) and transonic turbulence with velocity $\sim 1\mathrm{kms^{-1}}$ then the resultant turbulent diffusion coefficient is of the order of $K_{\mathrm{turb}} = 10^{22} - 10^{23}\mathrm{cm^2 s^{-1}}$. The limits of diffusion coefficients are discussed in the session §[4.4].

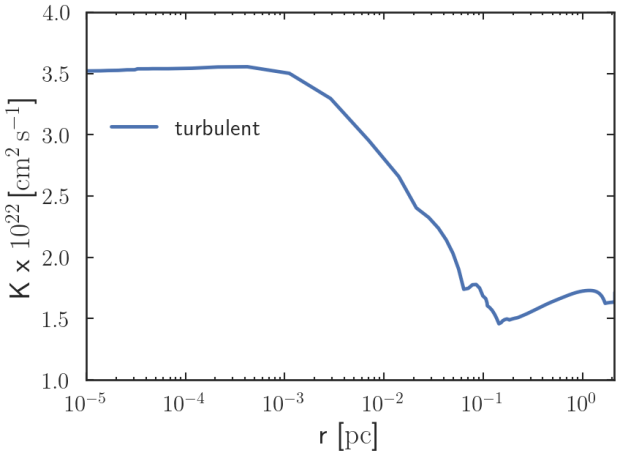


Figure 4.4: Turbulent diffusion coefficient for a coherence length of 0.1 pc. Model parameters: table [3.1] with $\xi = 1.5$ with nonuniform temperature (Figure [3.5]).

Line width and coherence length relationship in dense cores are explored by Goodman et al. (1998). The observations (for example, (Gong et al. 2022)) sug-

gest that the turbulent velocity varies over the cloud. Hence, instead of constant turbulent velocity, the local sound speed is considered the turbulent velocity, which varies over the cloud as a function of temperature. Here the turbulent velocity is constant over the mixing length scale. This would incorporate the local conditions into the turbulence. Also, the ratio between thermal pressure and turbulent pressure will be constant. The turbulent velocity,

$$V_t = \sqrt{\frac{5kT^s}{3\mu}} \tag{4.23}$$

The choice of molecular weight $\mu$ largely depends on the origin of the turbulence, which is beyond this thesis. The observations and simulations show that the large-scale turbulence cascades down to the smaller scales. The ingestion of turbulence from the large scale where the gas is mostly atomic would lead to the assumption that molecular weight is $\mu = 1.26 m_{\rm H} = 2.11 \times 10^{-24}$g (typical for purely atomic gas Klessen & Glover 2016).

## 4.4 Limits of diffusion coefficients

The total diffusion rate is,

$$\begin{aligned}\left[\frac{\partial n}{\partial t}\right]_d = \frac{\partial \phi}{\partial x^s} &= \frac{\partial \phi_{turb}}{\partial x^s} + \frac{\partial \phi_{mol}}{\partial x^s} + \frac{\partial \phi_{thermal}}{\partial x^s} \\ &= -K_{\rm turb}\frac{\partial^2 n_i}{\partial x^2} - K_{\rm mol}\frac{\partial^2 n_i}{\partial x^2} + n_\Sigma K_{\rm therm}\frac{\partial}{\partial x^s}\left(\frac{1}{T}\frac{\partial T}{\partial x^s}\right) \\ &= -K\left[f\frac{\partial^2 n_i}{\partial x^2} - g\frac{\partial^2 n_i}{\partial x^2} + h n_\Sigma \frac{\partial}{\partial x^s}\left(\frac{1}{T}\frac{\partial T}{\partial x^s}\right)\right]\end{aligned} \tag{4.24}$$

where f, g, and h are respective weights for turbulent, molecular, and thermal diffusion, and $K$is the total diffusion coefficient. Relating the mixing length ($L$) to observations is challenging, which limits the accurate expression of the total diffusion coefficient. However, from the eq.[4.7], eq.[4.14], and eq.[4.22] and the observations of turbulence in molecular clouds, a rough estimation of the total diffusion coefficient is possible.

For a temperature of 30 K, molecular diffusion velocity (eq.[4.8]) and diffusion coefficient (eq.[4.7]) for hydrogen is,

$$V_i\,({\rm cms^{-1}}) \;=\; \sqrt{\frac{5 \times 1.3806488 \times 10^{-16} \times 30\,{\rm gcm^2 s^{-2}}}{3 \times 1.6733 \times 10^{-24}\,{\rm g}}} \;=\; 6.423 \times 10^4 \tag{4.25}$$

$$K_{\rm mol}\,({\rm cm^2 s^{-1}}) = \frac{6.423\times10^4\ cms^{-1}}{10^{-15}{\rm cm^2}\times10^4{\rm cm^{-3}}} \sim 6\times10^{15}. \tag{4.26}$$

For CO, $V_i = 0.117\times10^5\,({\rm cms^{-1}})$ (molecular weight $\mu = 30$ and T $= 30\,K$).

For molecular hydrogen, let us consider $\frac{n_i(n-n_i)}{n^2} = 0.49$, then

$$K_{\rm therm}\,({\rm cm^2 s^{-1}}) = K_{\rm mol}\,\alpha\,\frac{n_i(n_\Sigma - n_i)}{n_\Sigma^2} = 10^{15}\times0.8\times0.49 \sim 3\times10^{14} \tag{4.27}$$

Even though the thermal diffusion coefficient is smaller than the molecular diffusion coefficient, the diffusion rate is comparable (Figure. 4.6).

For a gas temperature of 120 K the turbulent velocity (eq.[4.23]) and turbulent diffusion coefficient (eq.[4.22]),

$$V_{\rm turb}\,({\rm cms^{-1}}) = \sqrt{\frac{5\times1.3806488\times10^{-16}\times120\,{\rm gcm^2 s^{-2}}}{3\times2.11\times10^{-24}\,{\rm g}}} = 1.14\times10^5 \tag{4.28}$$

For a coherence length of $L = 0.1\,{\rm pc} = 3.085\times10^{17}{\rm cm}$ (Xie et al. 1995),

$$K_{\rm turb}\,({\rm cm^2 s^{-1}}) = 1.14\times10^5\,cms^{-1}\times3.085\times10^{17}cm \sim 10^{22} \tag{4.29}$$

For a coherence length of $L = 0.3\,{\rm pc}$, $K_{\rm turb}\,({\rm cm^2 s^{-1}}) \sim 10^{23}{\rm cm^2\,s^{-1}}$. For a gas temperature of 30 K the turbulent velocity $V_{\rm turb} = 0.5\times10^5\,{\rm cms^{-1}}$ resulting in a turbulent diffusion coefficient of $K_{\rm turb} = 0.5\times10^5\times3.085\times10^{17} \sim 10^{22}\,{\rm cm^2 s^{-1}}$. Due to the lack of exact values of the turbulent length scale, we have to assume turbulent diffusion as the higher end. Hence, it is safe to conclude that the highest value of the total diffusion coefficient, $K$, is $\sim 10^{23}cm^2s^{-1}$.

The lowest limit of diffusion coefficient depends on the fraction $\frac{n_i\times(n_\Sigma-n_i)}{n_\Sigma^2}$. For dominant species like H and $H_2$, the fraction $\frac{n_i\times(n_\Sigma-n_i)}{n_\Sigma^2}$ and the thermal diffusion coefficient is higher whereas, for species like C and $C^+$ the fraction $\frac{n_i\times(n_\Sigma-n_i)}{n_\Sigma^2}$ is lower; hence the thermal diffusion coefficient (Figure 4.2). For less abundant species like $H_2S^+$, the density fraction $\frac{n_i\times(n_\Sigma-n_i)}{n_\Sigma^2}$ shows spikes as illustrated in Figure [4.5a]. This fraction is too low in the region $r \geq 10^{-2}\,{\rm pc}$, which is equivalent to zero numerically. Hence, for less abundant species, $n_\Sigma - n_i \approx n_\Sigma$. Hence, the fraction is approximated as $\frac{n_i\times(n_\Sigma-n_i)}{n_\Sigma^2} \approx \frac{n_i}{n_\Sigma}$ for less abundant species. The behavior of the fraction is shown in Figure [4.5b]. The fraction values less than $10^{-20}$ are ignored because they will not impact the chemistry of the species.

The variation of different diffusion coefficients as a function of distance from the surface of the cloud is shown in Figures [4.2-4.4]. A coherence length of $L = 3.068\times10^{17}\,cm = 0.1\,{\rm pc}$ is used for plotting. However, using the scaling relations ($L \leq 10\%R$), coherence length can vary up to 0.213 pc (the radius of

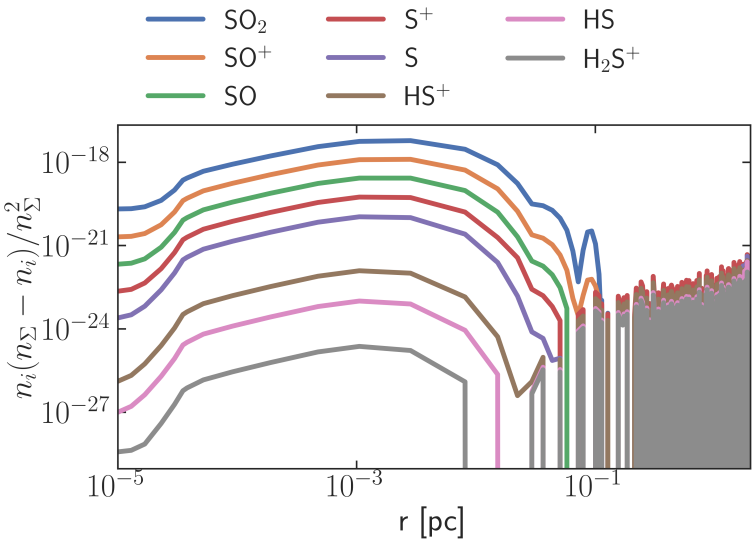


(a) less abundant species without approx

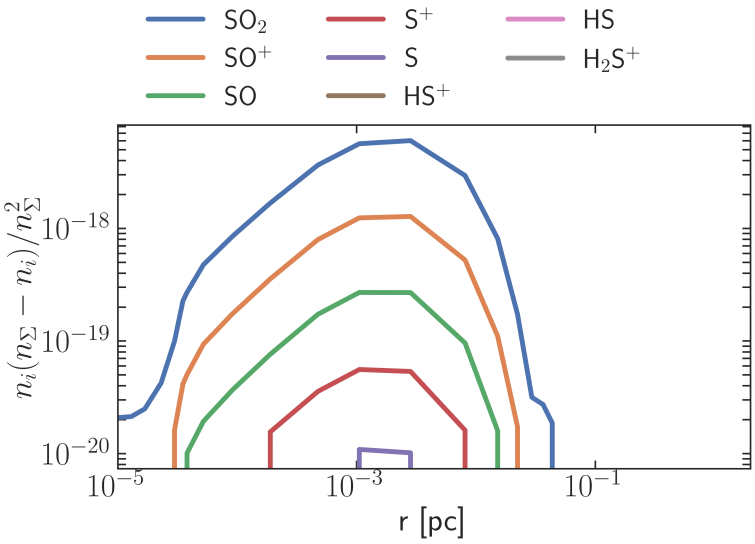


(b) less abundant species with approx

Figure 4.5: Behaviour of the density fraction $\frac{n_i \times (n_\Sigma - n_i)}{n_\Sigma^2}$ for less abundant species. Model parameters: table [3.1] with $\xi = 1.5$ with nonuniform temperature (Figure [3.5]). Coherence length, $L = 0.1\,\mathrm{pc}$, is used.

the model cloud is 2.13 pc). More results on different coherence lengths and the resultant change in the chemistry are explored in the §[6]. The turbulent diffusion coefficient does not change with species; however, the diffusion rate changes (Figure [4.6]). Figure [4.6] shows total diffusion rates and contribution from turbulent, molecular, and thermal diffusion rates for H. The wiggles in the diffusion rates are explored in §[5.5.1].

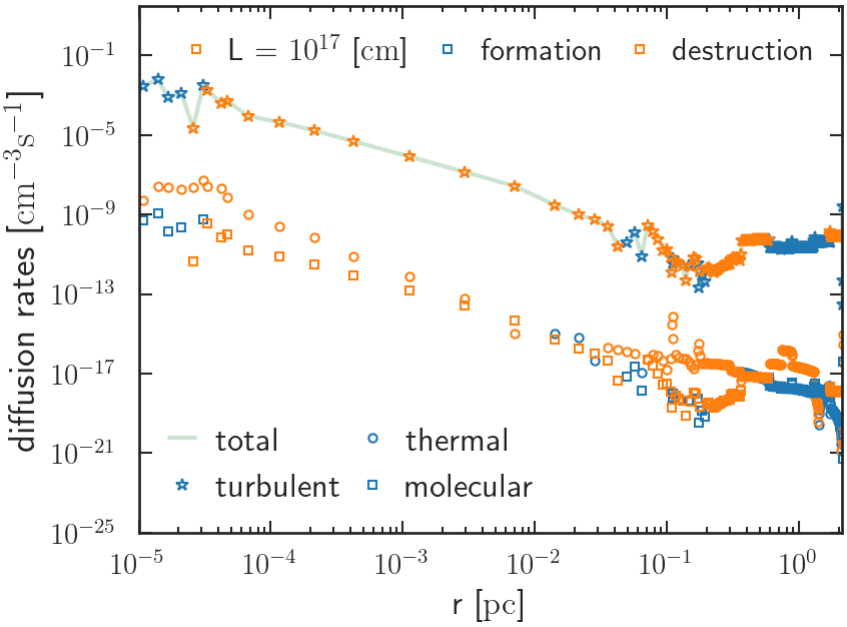


Figure 4.6: Total (green line), turbulent (star), thermal (circle), and molecular (square) diffusion rates of atomic hydrogen as a function of distance from the cloud surface. The positive (blue) and negative (orange) values are shown. Thermal and molecular diffusion contributes almost similarly. Turbulent diffusion contributes significantly to the total diffusion rates. Model parameters: table [3.1] with $\xi = 1.5$ with nonuniform temperature (Figure [3.5]).

# Chapter 5

# Implementation of the diffusion model

The movement of particles between nearby regions is referred to as diffusion. The diffusion model considers the density of adjacent spatial points to determine diffusion rates. Suppose the resulting diffusion flux gradient is positive. In that case, the reaction is called a formation reaction, whereas a negative gradient indicates that the species from the current spatial position is destroyed by diffusion. We used 61 species which are formed and destroyed through 812 reactions during the modeling. Diffusion is added to the chemical solver (eq.[3.6]). In the KOSMA-$\tau$ PDR model, the chemistry and physics are calculated from the surface of the cloud to the center of the cloud. In the thesis, the following or subsequent shell or shell on the right-hand side corresponds to the neighboring shell, which is closer to the cloud's center than the current shell. The previous or the shell on the left-hand side corresponds to the neighboring shell closer to the cloud's surface than the current shell.

The diffusion of species depends on the physical properties of the neighboring shells. To calculate the amount of diffusion in each shell, both inflow and outflow, we must know the position of the shells, temperature, and density of each species in the neighboring shells. As discussed in the §[3] with the AMR technique, the subsequent position is only determined once the thermal and chemical balance is attained. Hence, we must extrapolate the following position from the current shell to calculate the diffusion rates.

To numerically solve ordinary or partial differential equations, the finite difference method can be used (Singh & Bhadauria 2009) by replacing the derivatives with appropriate finite difference approximations. By increasing the number of points used to obtain the solution, the accuracy of the solution can be increased. However, this requires a tedious amount of mathematical calculations. The diffusion-advection equation and solving them has been studied by many

in different contexts other than astronomy over several decades, for example, Roberts (1961); Gruzinov et al. (1990); Thongmoon & Mckibbin (2006); Cheng & Cheng (2005); Hutomo et al. (2019). Cheng & Cheng (2005) provides an overview of the finite difference methods used for solving the diffusion-advection equation.

Most studies consider the entire system to solve the diffusion-advection scenarios at discrete time intervals while post-processing the chemistry. In this study, diffusion and chemistry are solved together in a steady-state scenario. By solving the diffusion equation with the chemistry, we can evaluate the impact of diffusion on the chemistry.

A detailed explanation of the calculation of the next position, evaluation of the diffusion flux, and addition of diffusion rates to the chemical rates are provided in this chapter. A summary of the chemistry solver in KOSMA-$\tau$ PDR model is given in §[3.1.4].

## 5.1 Boundary conditions

The material transport rate via diffusion-advection for an individual species from eq.[4.2],

$$\left[\frac{\partial n_i}{\partial t}\right]_{\rm d} = -\frac{\partial \phi_i}{\partial x} = -\frac{\partial \phi_{\rm turb}}{\partial x} - \frac{\partial \phi_{\rm mol}}{\partial x} + \frac{\partial \phi_{\rm thermal}}{\partial x} + \frac{\partial \phi_{\rm adv}}{\partial x} \tag{5.1}$$

where $\phi_{\rm i}$, $\phi_{\rm turb}$, $\phi_{\rm mol}$, $\phi_{\rm therm}$, and $\phi_{\rm adv}$ are total, turbulent, molecular, thermal diffusion, and advective flux, respectively.

In steady state, $\frac{dn}{dt} = 0$. Hence,

$$(\cdots) = \frac{\partial \phi_{turb}}{\partial x} + \frac{\partial \phi_{mol}}{\partial x} - \frac{\partial \phi_{thermal}}{\partial x} + \frac{\partial \phi_{\rm adv}}{\partial x} \qquad 0 \leq r \leq R \tag{5.2}$$

where $(\cdots)$ denotes the other chemical reactions from eq.[3.6]. The diffusion equation is a partial differential equation; to solve such an equation, the boundary conditions should be specified. The two types of boundary conditions are:

1 Dirichlet boundary conditions (Cheng & Cheng 2005): When resolving the underlying ordinary differential equation (ODE) or partial differential equation (PDE), Dirichlet boundary conditions specify what numerical value of the variable at the domain border should take. Solving a Dirichlet issue entails determining the function of the governing partial differential equation at the variable-determined domain boundary. The pressure or velocity parameters are frequently enforced in fluid dynamics on the domain border. For example, while addressing fluid dynamics issues for a viscous fluid

with no-slip and no-penetration criteria, the component of velocity at the boundary should be zero according to the Dirichlet boundary condition.

$$n(x = 0, t = 0) = n_0(x) \qquad n(x = R, t = 0) = n_L(x) \tag{5.3}$$

2 Neumann's boundary conditions (Cheng & Cheng 2005; Thongmoon & Mckibbin 2006) : The Neumann (or second-type) boundary condition is named after Carl Neumann in mathematics. The condition determines the derivative values applied at the domain boundary when enforced on an ordinary or partial differential equation.

$$\frac{\partial n}{\partial x}(x = 0, t = 0) = \left.\frac{\partial n}{\partial x}\right|_{x=x_0} \qquad \frac{\partial n}{\partial x}(x = R, t = 0) = \left.\frac{\partial n}{\partial x}\right|_{x=R} \tag{5.4}$$

We use Neumann's boundary condition to prescribe the flux entering through the boundary.

$$\frac{\partial n}{\partial t} + v_{adv}\frac{\partial n}{\partial x} = K\frac{\partial^2 n}{\partial x^2} \tag{5.5}$$

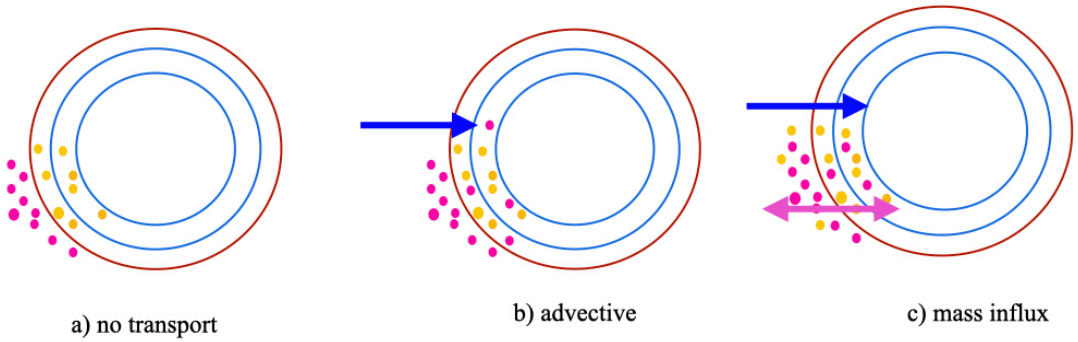


Figure 5.1: Material transport from the surface of the cloud (yellow circles) to the surroundings (pink circles). The movement of the particles is shown with arrows (blue arrows show advective movement, and the pink arrow shows diffusive movement.). Advection is unidirectional, and diffusion is bi-directional, as denoted by arrow heads.

Several combinations of boundary conditions are possible for a PDR, as illustrated in Figure [5.1]. We consider three main material transport at the surface boundary: no material transport (Figure [5.1a]) from or to the surrounding medium (the cloud is in equilibrium with the surroundings), advective transport (Figure [5.1b]), or mass influx (Figure [5.1c]) due to diffusion. Advective transport is uni-directional. The mass influx scenario is bidirectional; mass loss from the surface to the surroundings and inflow of material from the surroundings to the surface. At the center of the cloud ($x = R$), the density is assumed to be the constant.

For a finite region, the boundary conditions will be (Thongmoon & Mckibbin 2006),

$$\text{Case 1} : n(x,0) = n(x), \quad n(x=0,t) = n_0, \quad n(R,t) = n_R, \tag{5.6}$$

$$\text{Case 2} : n(x,0) = n(x), \quad n(x=0,t) = n_0, \quad \frac{\partial n}{\partial x}(0,t) = 0, \tag{5.7}$$

and

$$\text{Case 3} : n(x,0) = n(x), \quad n(x=0,t) = n_0, \quad m(0,t) = \left( n v_{adv} - \frac{\partial n}{\partial x} \right)(0,t) = constant, \tag{5.8}$$

where $n_0$ and $n_R$ are constant number densities at the boundary ($x = 0$ at the surface and $x = R$ at the center of the spherical cloud), the $m(0,t)$ denotes the mass flux, including both advective and diffusive components. Case 1 corresponds to a constant number density at $x = 0$ and $x = R$. Case 2 shows an advective inflow only at the surface ($x = 0$), and Case 3 shows a fixed constant mass influx at the surface ($x = 0$). All cases have constant number density at $x = R$.

In order to solve the advection-diffusion equation, it is necessary to obtain information about the subsequent spatial position in relation to the current point using interpolation. Additionally, two more boundary conditions are required to construct cubic splines at each step. The natural cubic splines requires to fulfill the condition $\frac{\partial^2 n}{\partial x^2} = 0$ on the interpolants at points $x = 0$ and $x = R$ (Thongmoon & Mckibbin 2006). How do the boundary conditions change as a result of this requirement?

For all cases $\dfrac{\partial n}{\partial t}(0,t) = 0$ at $x = 0$. Thus, using eq. [5.5-5.8],

$$v_{adv} \frac{\partial n}{\partial x} - K \frac{\partial^2 n}{\partial x^2} = 0 \text{ at } x = 0, \quad \frac{\partial m}{\partial x}(0,t) = 0 \tag{5.9}$$

This implies that mass flux from the left side of the boundary is equal to the right side of the boundary ($m(0,t)_{left} = m(0,t)_{right}$). Because $n = n_0$ at $x = 0_{right}$ (Thongmoon & Mckibbin 2006) this means that $\frac{\partial n}{\partial x} = 0|_{x=0_{right}}$ and $\frac{\partial^2 n}{\partial x^2} = 0|_{x=0_{right}}$. However, $m = v_{adv} n$ at $x = 0_{left}$. In conclusion, Case 1 and Case 2 could use natural cubic spline but not Case 3. While considering the mass influx in a PDR, natural cubic spline methods do not help to solve the diffusion-advection equation. Hence it is advised to use any other method for the interpolation in case 3. Thongmoon & Mckibbin (2006) found that finite difference methods give better point-wise solutions to diffusion-advection than spline methods. In this study, only case 1 is used. Methods for the advection and mass influx are

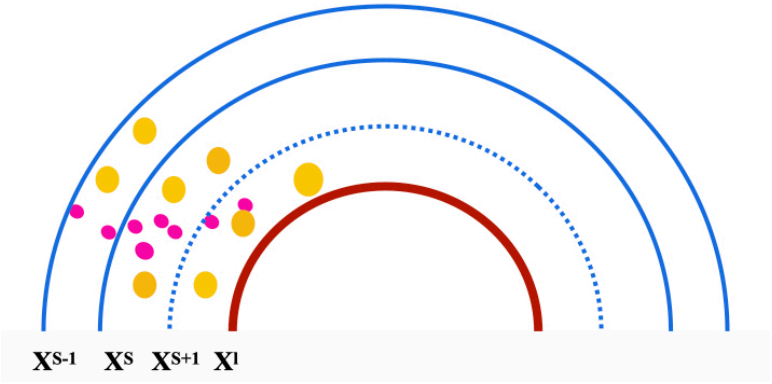


Figure 5.2: Three-point interpolation scheme used in this modeling.Three consecutive shells $s-1$, $s$, and $s+1$ at depth $x^{s-1}$, $x^s$, and $x^{s+1}$. The value of $x^l$ is the closest position to $x^s$ taken from the last computational global iteration. The position, density of species, and temperature at point $x^{s+1}$ are calculated using interpolation. Yellow and pink circles indicate two different species here.

developed during the study. However, it needs extensive study to complete.

## 5.2 Interpolation

A numerical scheme of the KOSMA-$\tau$ PDR model is shown in the Figure [3.4] and explained in §[3.1.2]. Each global iteration contains multiple spatial iteration loops (shells or spatial positions) that span over the entire radius of the cloud. The spatial positions are not fixed or predetermined. Instead, after solving chemical rate equations of every species in a shell using an adaptive mesh refinement method (Röllig & Ossenkopf-Okada 2022), the KOSMA-$\tau$ code will compute the subsequent spatial position (along $r$ direction towards the center of the cloud) in a global iteration. We use the interpolation technique to construct a new data point in position, density, and temperature and later solve the diffusion rate equations. As discussed in §[5.1], using a cubic spline is not advisable to calculate the mass influx. Since the diffusion rates crucially depend on the interpolated density and temperature, finding a different interpolation routine is necessary. Considering the unequal intervals in the KOSMA-$\tau$ PDR model, Lagrange's interpolation method can be used. The diffusion chemistry on the shell under consideration is only affected by the nearby shells, reducing the interpolation to a three-point interpolation.

Consider three consecutive shells, $s-1$, $s$, and, $s+1$, with densities of $i^{th}$ species $n_i^{s-1}$, $n_i^s$, and, $n_i^{s+1}$ and depth $x^{s-1}$, $x^s$ and, $x^{s+1}$. To compute the diffusion, we must know the position of shells, $s-1$, $s$, and $s+1$. The position of $s+1$ and the temperature and densities at $x^{s+1}$ are yet to be determined. We locate a shell $x^l$ that is the closest shell to $x^s (x^s \leq x^l)$ in the last global iteration and interpolate

the temperature and densities of the shell $x^{s+1}$ which is positioned between $x^s$ and $x^l$ (Figure [5.2]) such that $x^{s-1} < x^s < x^{s+1} < x^l$. The spatial position $x^{s+1}$ can be determined using different extrapolation methods. One potential way is to linearly extrapolate the position from the last spatial position such that the widths are equal (method 1: $x^s - x^{s-1} = x^{s+1} - x^s$). In KOSMA-$\tau$, the shells might not be at equal distances. Consequently, this method of calculating $x^{s+1}$ can result in errors. An improved way to calculate the position (method 2) based on method 1 is

$$x^{s+1} = x^s + \frac{\sum_{u=2}^{s}(x^u - x^{u-1})}{s}. \tag{5.10}$$

This implies that an average of the width of the previous shells is added to the current shell. This method is less biased than the previous method. However, the results are not accurate enough.

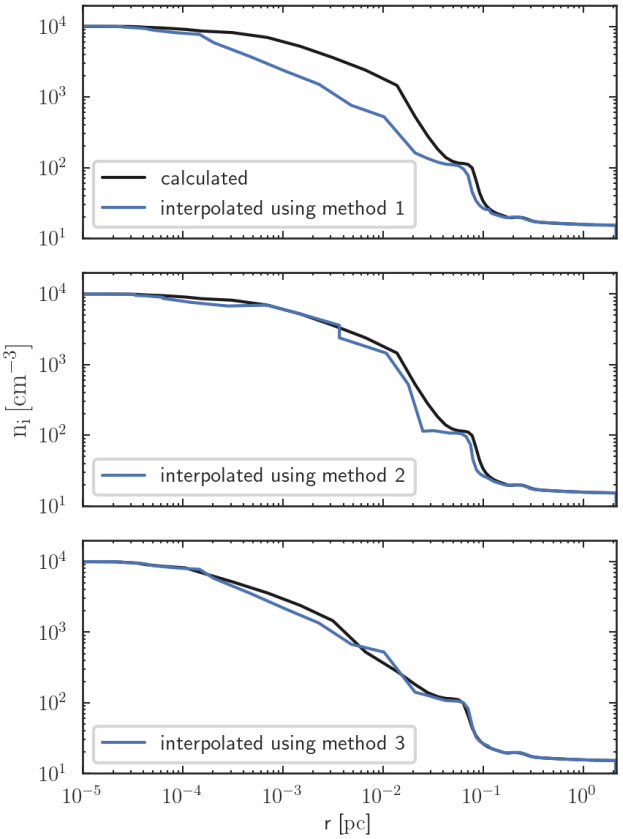


Figure 5.3: Interpolated density profiles and the evaluated densities compared to the KOSMA-$\tau$ PDR model density profile. Method 3 reproduces the calculated density profile accurately compared to the other methods. Model parameters: table [3.1].

Another way (method 3) is to locate a position $x^p$ close to the current shell from the last global iteration such that $x^{s-1} \leq x^s \leq x^p$ and use it as $x^{s+1}$. The density and temperature of the current iteration will be interpolated to the point $x^{s+1}(= x^p)$. The difference between the position of the shells does not change significantly from one global iteration to the other. Figure [5.3] shows the result of interpolation using the three methods mentioned above. The density profiles are interpolated using the three-point Lagrange method described below. The densities of less available species, such as $^{13}C^{18}O^+$, $HCS^+$, and $H_2{}^+$, vary significantly from the calculated values, regardless of the method used, compared to the more abundant species. Hence, other numerical methods like flux limiter functions are introduced, as explained in §[5.5] to limit the error

in interpolation and diffusion rates.

Lagrange's finite difference formula for unequal intervals (Singh & Bhadauria 2009) can be used to interpolate the densities and temperature. Using Lagrange's interpolation formula, a function f(x) with $(b+1)$ nodes is written as,

$$f(x) = \sum_{m=0}^{b} l_m(x) f_m \tag{5.11}$$

where, $f_m$ is $f(x_m)$ and

$$l_m(x) = \frac{\pi(x)}{(x - x_m)\dfrac{d\pi(x_m)}{dx}} \tag{5.12}$$

where,

$$\pi(x) = (x - x_0)(x - x_1)(x - x_2)\ldots(x - x_b). \tag{5.13}$$

The error in truncation could be written as,

$$E_b(x) = \frac{\pi(x)}{(b+1)!} f^{b+1}(\psi) \tag{5.14}$$

$f^{b+1}(\psi)$ is the $(\mathrm{b}+1)^{\mathrm{th}}$ derivative of $f(\psi)$, while $\psi$ lies between the interval $[x_0, x_b]$. The interval $[x_0, x_b]$ is divided into b unequally spaced $(h_1, h_2, h_3, \ldots h_b)$ intervals, such that

$$x_b = x_0 + \sum_{t=1}^{b} h_t \tag{5.15}$$

For a three-point system, Lagrange's second-order interpolation formula is,

$$l_1 = \frac{(x - x_1)(x - x_2)}{(x_1 - x_0)(x_2 - x_0)}, \quad l_2 = -\frac{(x - x_0)(x - x_2)}{(x_1 - x_0)(x_2 - x_1)}$$
$$l_3 = \frac{(x - x_0)(x - x_1)}{(x_2 - x_0)(x_2 - x_1)} \tag{5.16}$$

$$f(x) = l_1 f(x_0) + l_2 f(x_1) + l_3 f(x_2) \tag{5.17}$$

$$f'(x) = \frac{(x - x_1) + (x - x_2)}{(x_1 - x_0)(x_2 - x_0)} f_0 - \frac{(x - x_0) + (x - x_2)}{(x_1 - x_0)(x_2 - x_1)} f_1$$
$$+ \frac{(x - x_0) + (x - x_1)}{(x_2 - x_0)(x_2 - x_1)} f_2 \tag{5.18}$$

$$f''(x) = \frac{2f_0}{(x_1 - x_0)(x_2 - x_1)} - \frac{2f_1}{(x_1 - x_0)(x_2 - x_1)} + \frac{2f_2}{(x_2 - x_0)(x_2 - x_1)} \quad (5.19)$$

Using eq.[5.17] the density of tracer $i$ in the shell $s+1$ would be,

$$n_i^{s+1}(x^{s+1}) = p_1\ n_i^{s-1} + p_2\ n_i^s + p_3\ n_i^l \quad (5.20)$$

where the coefficients $p_1, p_2$ and $p_3$ are

$$p_1 = \frac{(x^{s+1} - x^s)(x^{s+1} - x^l)}{(x^s - x^{s-1})(x^l - x^{s-1})} \qquad p_2 = -\frac{(x^{s+1} - x^{s-1})(x^l - x^{s+1})}{(x^s - x^{s-1})(x^l - x^s)}$$
$$p_3 = \frac{(x^{s+1} - x^{s-1})(x^{s+1} - x^s)}{(x^l - x^{s-1})(x^l - x^s)} \quad (5.21)$$

The error in calculating the interpolated value will be,

$$E_2(x) = \frac{\pi(x)}{3!} f'''(\psi) = \frac{(x - x_0)(x - x_1)(x - x_2)}{6} f'''(\psi) \quad (5.22)$$

The computation still introduces inconsistencies. More details on minimizing the errors are given in the following subsections.

**Algorithm 1:** Interpolation scheme

**Data:** $f_{last}, f_{current}, X_{last}, X_{current}$

// $f_{last}$ and $f_{current}$ are arrays of either temperature or number density or column density from the previous global iteration and current iteration, respectively

// $X_{last}$ and $X_{current}$ are arrays of position values from the previous global iteration and current iteration, respectively

**Result:** y

// y is an array of either temperature or number density or column density that is interpolated to position $x^{s+1}$

position index, M = locate ($X_{last}$,$x^s$) // locate nearest neighbor greater than the current position $x^s$ from the previous global iteration.

$x^l = X_{last}[M]$ $f^l = f_{last}[M]$

calculate coefficient for interpolation, $p_1, p_2$, and $p_3$ (eq.[5.21])

**for** *species i* **do**

| calculate $y(x^{s+1}) = p_1 f^{s-1} + p_2 f^s + p_3 f^l$

**end**

## 5.3 Evaluation of gradient

The second-order derivative of the density and temperature is needed to calculate the diffusion rates. Depending on the accuracy needed, multiple methods exist to calculate the second-order derivative numerically. For example, using the central difference method, the second order derivative of density at point $s$ is,

$$\left.\frac{\partial^2 n}{\partial x^2}\right|_s = \frac{n^{s-1} - 2n^s + n^{s+1}}{(x^s - x^{s-1})(x^{s+1} - x^s)} \tag{5.23}$$

where, $n^{s+1}$, $n^s$, and $n^{s-1}$ are densities at positions $x^{s+1}$, $x^s$, and $x^{s-1}$ ($x^{s-1} \leq x^s \leq x^{s+1}$). Other methods are,

$$\left.\frac{\partial^2 n}{\partial x^2}\right|_s = \begin{cases} \dfrac{n^{s+2} - 2n^{s+1} + n^s}{(x^{s+2} - x^{s+1})(x^{s+1} - x^s)} & \text{(second order forward)} \\ \dfrac{n^s - 2n^{s-1} + n^{s-2}}{(x^s - x^{s-1})(x^{s-1} - x^{s-2})} & \text{(second order backward)} \end{cases} \tag{5.24}$$

where, $x^{s-2} < x^{s-1} < x^s < x^{s+1} < x^{s+2}$ and $n^{s-2}, n^{s-1}, n^s, n^{s+1}$, and $n^{s+2}$ are corresponding densities.

Using the three-point Lagrange's interpolation formula for unequal intervals, the first (eq. [5.18]) and second (eq. [5.19]) derivatives of tracer $i$ in the shell $s$ is,

$$\begin{aligned} \frac{\partial n_i^s}{\partial x^s} = &\frac{(x^s - x^{s+1})}{(x^s - x^{s-1})(x^{s+1} - x^{s-1})} n_i^{s-1} \\ &- \frac{2x^s - x^{s-1} - x^{s+1}}{(x^s - x^{s-1})(x^{s+1} - x^s)} n_i^s + \frac{(x^s - x^{s-1})}{(x^{s+1} - x^{s-1})(x^{s+1} - x^s)} n_i^{s+1} \end{aligned} \tag{5.25}$$

$$\begin{aligned} \frac{\partial^2 n_i^s(x)}{\partial x^2} = &\frac{2n_i^{s-1}}{(x^s - x^{s-1})(x^{s+1} - x^{s-1})} \\ &- \frac{2n_i^s}{(x^s - x^{s-1})(x^{s+1} - x^s)} + \frac{2n_i^{s+1}}{(x^{s+1} - x^{s-1})(x^{s+1} - x^s)} \end{aligned} \tag{5.26}$$

Figure [5.4] depicts the second-order derivative of density calculated using the forward, backward, central, and three-point Lagrange methods. The number density (not the fractional density) is plotted using a black line. Figure [5.4] demonstrates that the forward and backward difference schemes exhibit significant wiggles. Deeper in the cloud, both the central and three-point method provides a stable result, while the forward and backward difference methods exhibit abrupt changes (Figure [5.4]). Consequently, it is fair to conclude that

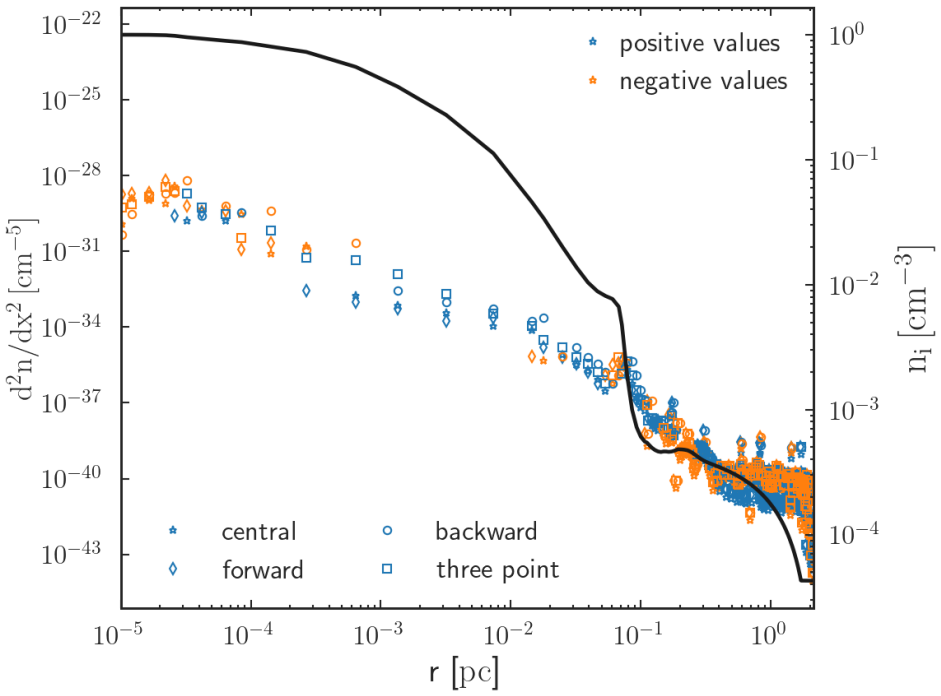


Figure 5.4: The second order derivative of the number density of H evaluated using central, forward, backward differences, and Lagrange's three-point method. Positive (blue) and negative (orange) values are plotted. The number density of the species is indicated using a black line. Each dot shows the spatial position in the code. Model parameters: table [3.1] with non-uniform temperature (Figure [3.5]) and $\xi = 1.5$.

forward and backward difference methods are less suitable for calculating the second-order density derivative. Similarly, the second-order derivative of temperature also shows that three-point and central difference methods are well suited for calculating the second-order derivative of temperature (Figure [5.5]).

As depicted in Figure [5.4], it is evident that the sudden variations are noticeable deeper in the cloud, where the grid points are comparatively more closely spaced. Figure [5.6] depicts the second-order derivative with a nearly constant density profile. The second-order derivatives exhibit wiggles even though the number density profile appears adequately smooth. A straight green line is drawn along with the number density (black circles) to show that the density values calculated are not constant. As in Figure [5.6], these changes in the number density around a mean value generate minor oscillations in the second-order derivative, which are practically zero. These fluctuations are due to the numerical precision and not due to the physics. When one of the neighboring shells is closer than the other(between 1.1 and 1.2pc in Figure [5.7]), the central difference method shows abrupt changes in the second-order derivative compared to the three-point Lagrange's method.

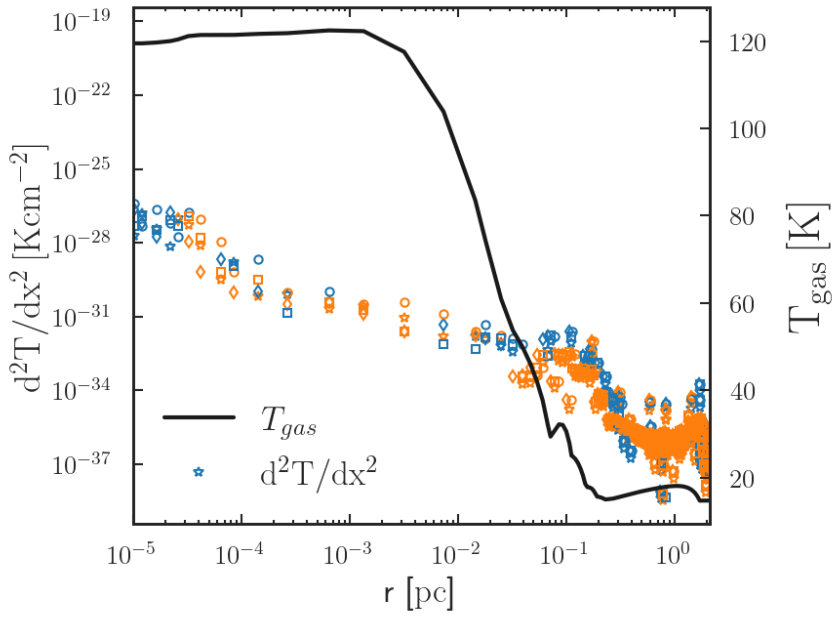


Figure 5.5: Second-order derivative of temperature calculated using forward, backward, central differences, and three-point methods. The temperature profile is shown using the black line. Model parameters and labels are the same as in the Figure [5.4].

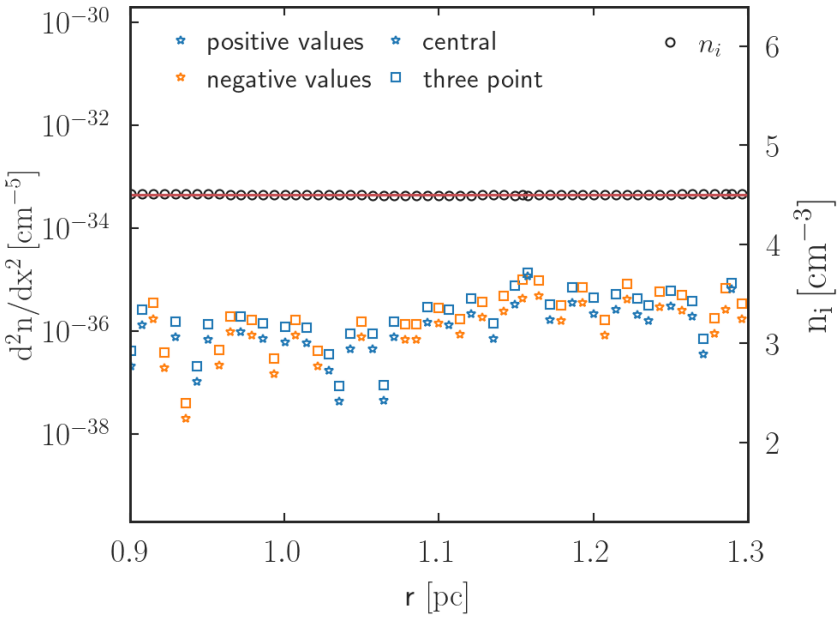


Figure 5.6: Oscillations in the second-order derivative of density at almost constant density regions. Number densities are marked as black circles. A red line is drawn to show that the calculated densities are not identical in almost constant-density regions, leading to small oscillations in the second derivatives. Model parameters: table [3.1] with non-uniform temperature (Figure [3.5]) and $\xi = 1.5$.

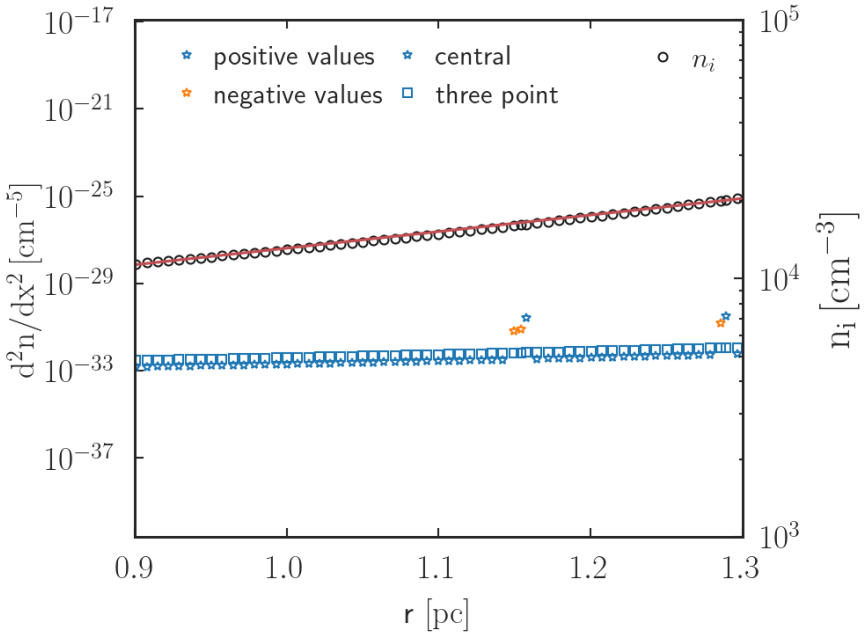


Figure 5.7: Abrupt change in the second-order derivative due to unequal spacing of the shells. Number densities are marked as circles to understand the spatial points calculated in the code. The spatial grid points are not equidistant (see $1.1 \leq r \leq 1.2\,\mathrm{pc}$), leading to abrupt spikes (using a central point) in the otherwise smooth second derivatives. Model parameters: table [3.1] with non-uniform temperature (Figure [3.5]) and $\xi = 1.5$.

On the surface of the cloud, second-order derivative values calculated using the three-point method are higher than the rest of the second-order derivative methods. Towards the center of the cloud, both the central and three-point method shows stable values. However, the three-point method shows fewer oscillations and wiggles in the second-order derivative compared to the rest (Figure [5.5b]) of the second-order derivative methods. Hence, the Lagrange three-point method is more stable in an unequally spaced region to calculate the second-order derivative. As depicted in Figure [5.4], the density of the species is constant at the center of the cloud. This constant density should yield a second-order derivative of zero in these regions. Due to the small oscillations in the density profile due to numerical precision, the second-order derivative exhibits relatively substantial peaks (practically zero). These peaks are further explored in §[5.5.1].

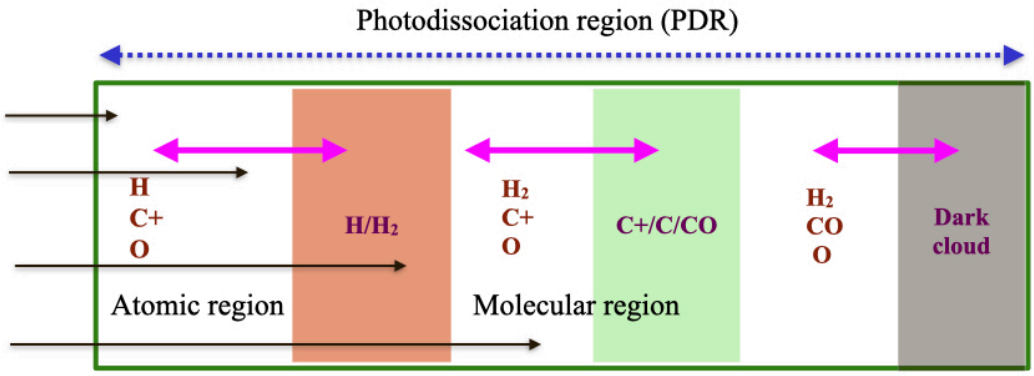


Figure 5.8: Addition of diffusion into the simplified version of the PDR structure. UV field (black arrows) passes through the cloud by ionizing and dissociating the region. Different molecules diffused (double-headed arrows) throughout the cloud.

## 5.4 Addition of diffusion rates into KOSMA-$\tau$

Solving the gas-phase chemistry (eq. [3.6]) is explained in §[3.1.4]. The linearized system of equations to solve the chemical rates,

$$\mathbb{Q} \cdot \delta n = \mathbb{F} \tag{5.27}$$

must be solved at every spatial point to obtain the local conditions. Here vector $\mathbb{F}$ contains the chemical reaction rates, and the matrix $\mathbb{Q}$ is a square matrix of size $NSP \times NSP$ where $NSP$ is the total number of species in the model. By definition, diffusion encompasses the dynamics between previously isolated nearby spatial positions. Consequently, it is essential to model the coupling between adjacent spatial positions.

The diffusion contributions to the $\mathbb{F}$ (eq.[3.7]) and $\mathbb{Q}$ (eq.[3.12]) are,

$$\mathbb{F}^s_{i_\mathrm{d}} = \left[\frac{\partial n^s_i}{\partial t}\right]_\mathrm{d}, \text{and} \quad \mathbb{Q}^s_{i_\mathrm{d}} = -\frac{d\mathbb{F}^s_{i_\mathrm{d}}}{dn^s_i} \tag{5.28}$$

Here onwards, $\mathbb{F}^s_{i_\mathrm{d}} = \mathbb{F}^s_\mathrm{d}$ and $\mathbb{Q}^s_{i_\mathrm{d}} = \mathbb{Q}^s_d$. The calculated diffusion rates, $\mathbb{F}^s_\mathrm{d}$ is added to $\mathbb{F}^s_i$ ($\mathbb{F}^s_i = \mathbb{F}^s_{i,\mathrm{c}} + \mathbb{F}^s_\mathrm{d}$) where $\mathbb{F}^s_{i,c}$ denotes the chemical reaction rates other than diffusion. For diffusion, $\mathbb{F}^s_\mathrm{d}$ depends on the density $n^{s-1}_i, n^s_i$, and $n^{s+1}_i$. Hence the resultant Jacobi matrix element will be added to the diagonal element $\mathbb{Q}(i,i)$. $\mathbb{Q}^s_\mathrm{d}$ is calculated for position $s$. Consequently, the dependence of positions $s-1$ and $s+1$ must be incorporated into $\mathbb{Q}^s_\mathrm{d}$ to complete the coupling between nearest neighboring shells.

The diffusion considers the contribution from left and right shells and the outflow of material from the current shell. These contributions must be added to the corresponding spatial and species position of the $\mathbb{Q}$ and $\mathbb{F}$.

The diffusion equation at shell $s$ can be written from eq.[4.2] and eq.[4.24],

$$\left[\frac{\partial n_i^s}{\partial t}\right]_{\mathrm{d}} = \frac{\partial \phi_i^s}{\partial x} = -K_{\mathrm{turb}}\frac{\partial^2 n_i^s}{\partial x^2} - K_{\mathrm{mol}}\frac{\partial^2 n_i^s}{\partial x^2} + n_\Sigma^s K_{\mathrm{therm}}\frac{\partial}{\partial x}\left(\frac{1}{T^s}\frac{\partial T^s}{\partial x}\right) \quad (5.29)$$

To further simplify, let's consider only molecular diffusion contribution. To find out the numerical solution in a discretized mesh, we can approximate the diffusion rate equation for molecular diffusion at spatial position $s$ as follows,

$$\begin{aligned}\mathbb{F}_{\mathrm{d}}^s = -K_{\mathrm{mol}}\frac{\partial^2 n_i}{\partial x^2}\bigg|_s &= -K_{\mathrm{mol}}\Big[\frac{2n_i^{s-1}}{(x^s - x^{s-1})(x^{s+1} - x^{s-1})} \\ &\quad - \frac{2n_i^s}{(x^s - x^{s-1})(x^{s+1} - x^s)} + \frac{2n_i^{s+1}}{(x^{s+1} - x^{s-1})(x^{s+1} - x^s)}\Big] \\ &= -K_{\mathrm{mol}}\left(n_i^{s-1}L^s + n_i^s C^s + n_i^{s+1}R^s\right) \quad (5.30)\end{aligned}$$

where, the consecutive spatial positions are denoted using $s-1, s$, and $s+1$ and,

$$L^s = \frac{2}{(x^s - x^{s-1})(x^{s+1} - x^{s-1})}, \quad (5.31)$$

$$C^s = \frac{-2}{(x^s - x^{s-1})(x^{s+1} - x^s)}, \quad (5.32)$$

$$R^s = \frac{2}{(x^{s+1} - x^{s-1})(x^{s+1} - x^s)}. \quad (5.33)$$

$L^s, R^s$, and $C^s$ vary depending on the position in the cloud at which we are calculating the diffusion rates.

The diffusion contribution $\mathbb{Q}_{\mathrm{d}}^s$ to the Jacobi matrix $\mathbb{Q}$,

$$\mathbb{Q}_{\mathrm{d}}^s = -\frac{d\mathbb{F}_{\mathrm{d}}^s}{dn_i^s} = K_{\mathrm{mol}}C^s \quad (5.34)$$

This equation only has the contribution from the current shell $s$. However, the coupling term must account for the neighboring shell's contribution, which is not a function of the density of the shell $s$ but the density of $s-1$ and $s+1$ shells. Nevertheless, in the case of diffusion the resultant density of the current shell $s$ is influenced by the density of the shells $s-1$ and $s+1$ due to the interconnected nature of diffusion. Hence, to complete the coupling between different shells, we must add a term $[\mathbb{Q}_{\mathrm{d}}^s]_A$, which is,

$$[\mathbb{Q}_d^s]_A = R^s + L^s, \quad (5.35)$$

which is similar to the contribution from the current shell $s$ to $\mathbb{Q}_{\mathrm{d}}^s$ but includes the information from $s-1$ and $s+1$. Then the diffusion contribution to the

Jacobi matrix can be redefined as,

$$\mathbb{Q}_{\mathrm{d}}^{s} = -\frac{d\mathbb{F}_{\mathrm{d}}^{s}}{dn_{i}^{s}} - K_{\mathrm{mol}}[\mathbb{Q}_{\mathrm{d}}^{s}]_{A} = K_{\mathrm{mol}}(C^{s} + L^{s} + R^{s}) \tag{5.36}$$

The chemical solver is called to solve the chemistry and evaluate the densities at every position, as shown in Figure [3.4]. The module to solve diffusion is called from the chemical solver in the KOSMA-$\tau$ PDR model. The coherence length of turbulent diffusion, position ($s-1, s$, and $s+1$) and corresponding densities and temperature are given as the input parameters to solve diffusion. The module to solve diffusion will calculate the diffusion rates ($\mathbb{F}_{\mathrm{d}}^{s}$) and contributions to the Jacobi matrix ($\mathbb{Q}_{\mathrm{d}}^{s}$) for all species at the current shell $s$ and return these values. These values are then added to the chemical reaction rates as shown in eq. [3.5] and eq. [3.12]. An algorithm for calculating diffusion rates is given alg. [2].

**Algorithm 2:** The algorithm for calculating diffusion rates for all species at position $s$.

**Data:** $L, n, x, s$, and $t$

**Result:** $\mathbb{F}^s_{\rm d}, \mathbb{Q}^s_{\rm d}$

read position: $x_i^{s-1}$,$x_i^s$, and $x_i^{s+1}$ // $x_i^{s+1}$ is the interpolated position

read temperature: $t_i^{s-1}$,$t_i^s$, and $t_i^{s+1}$ // $t_i^{s+1}$ is the interpolated temperature at position $x_i^{s+1}$

calculate $\dfrac{\partial T}{\partial x}, \dfrac{\partial^2 T}{\partial x^2}$ // first and second order derivative of temperature §[5.3]

/* iterate over all species */

**for** *species* $i$ **do**

read density: $n_i^{s-1}$,$n_i^s$, and $n_i^{s+1}$ // $n_i^{s+1}$ is the interpolated density at position $x_i^{s+1}$

calculate $V_t^s$ and $V_i^s$ // turbulent velocity and thermal velocity

calculate $\dfrac{\partial n}{\partial x}, \dfrac{\partial^2 n}{\partial x^2}$ // first and second order derivative of density §[5.3]

calculate $K_{\rm turb}, K_{\rm mol}, K_{\rm therm}$

calculate $C^s, L^s$, and $R^s$

calculate $\dfrac{\partial \phi_{\rm turb}}{\partial x}, \dfrac{\partial \phi_{\rm mol}}{\partial x}, \dfrac{\partial \phi_{\rm therm}}{\partial x}$

$\mathbb{F}^s_d = -\dfrac{\partial \phi_{\rm turb}}{\partial x} - \dfrac{\partial \phi_{\rm mol}}{\partial x} + \dfrac{\partial \phi_{\rm therm}}{\partial x}$ // diffusion rates eq.[5.1]

$\mathbb{Q}^s_{\rm d} = -\dfrac{d\mathbb{F}^s_{\rm d}}{dn^s_i} - K_{\rm mol}[\mathbb{Q}^s_{\rm d}]_A - K_{\rm turb}[\mathbb{Q}^s_{\rm d}]_A - K_{\rm therm}[\mathbb{Q}^s_{\rm d}]_A$

// diagonal element for the Jacobian matrix

**end**

## 5.5 Testing the diffusion model

The diffusion model is tested with different input parameters (table [6.1]), and the results can be found in §[6]. Here the initial tests are done based on the parameters in the table [3.1] and coherence length of $L = 0.2\,\mathrm{pc}$. After adding the diffusion into the KOSMA-$\tau$ PDR model, the calculated second-order derivatives are shown in Figure [5.9] and Figure [5.10]. Figure [5.9] shows the overall behavior

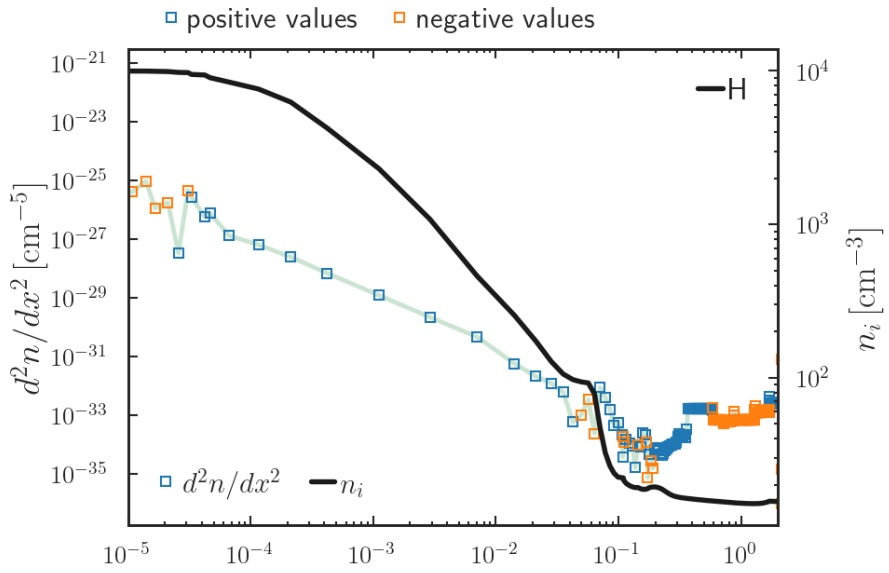


(a) H

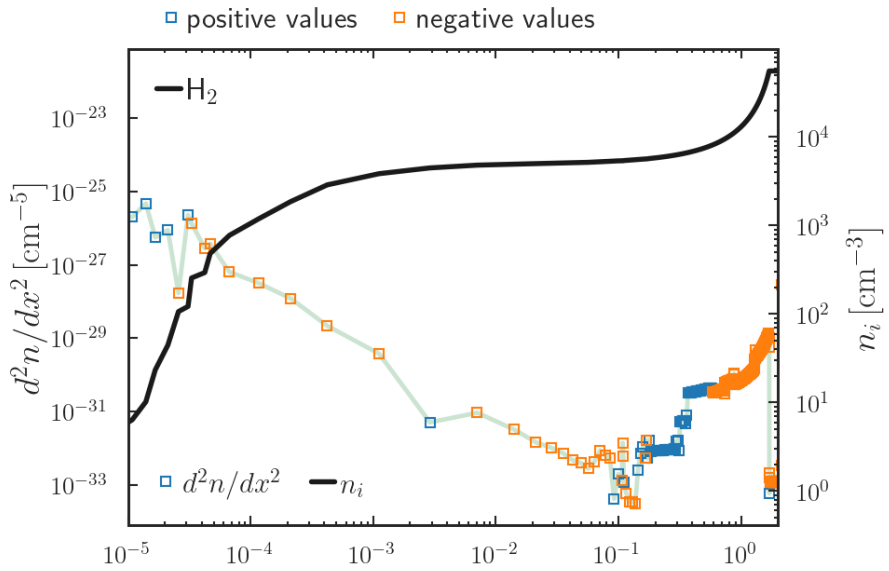


(b) $H_2$

Figure 5.9: Second order derivative of H and $H_2$. Model parameters: reference model (table [3.1]) with coherence length $L = 0.2\,\mathrm{pc}$ and $\xi = 1.5$.

of the second-order derivative of H and $H_2$. The one point where both atomic and molecular hydrogen is shown as positive values between $10^{-3} \leq r \leq 10^{-2}$ in Figure [5.9b ] is due to the slight increase in the density gradient in that region. For atomic hydrogen (upper panel of Figure [5.10a]), the density is almost constant in the shown region, and the second-order derivatives show abrupt changes due to unequal spacing and uncertainty in the interpolated densities. In the case of molecular hydrogen, the second-order derivative (lower panel of Figure [5.10a]) shows an abrupt change in the region $1.6 \leq r \leq 1.8\mathrm{pc}$. This sudden drop in the second-order derivative is attributed to the change in the density of the species

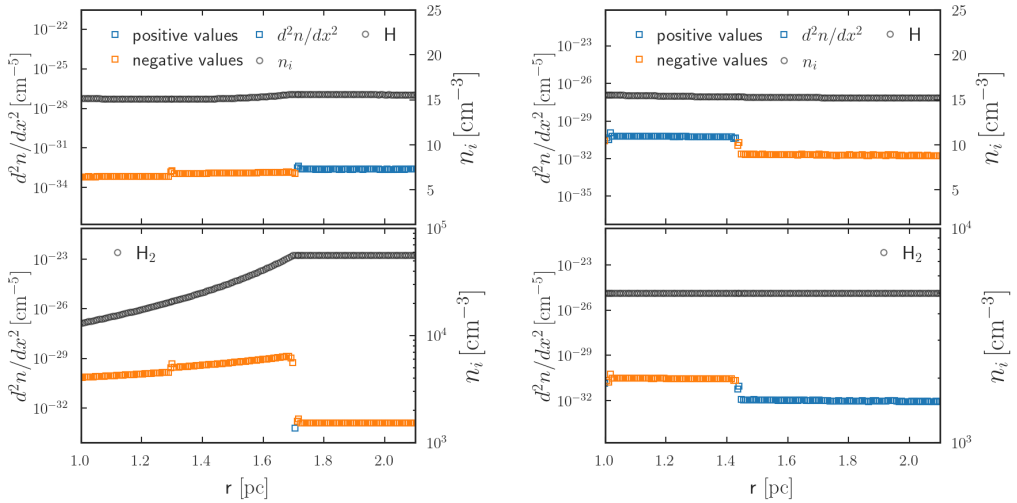


(a) $\xi = 1.5$ (b) $\xi = 0$

Figure 5.10: Second order derivative at constant density regions. When the density of the cloud changes (Figure [3.3]), there is a discontinuity in the second-order profile ($1.6 \leq r \leq 1.8$). Model parameters: reference model with non-uniform temperature and coherence length of turbulent diffusion $L = 0.2\,\mathrm{pc}$.

and needs to be addressed carefully. From Figure [5.10b] it is clear that the second-order derivatives of H and $H_2$ demonstrate abrupt changes due to uneven spacing and the uncertainty in the interpolated values.

From the initial runs, the following problems have to be addressed.

1. **diffusion at almost constant density regions:** When the number densities or temperature are almost constant, the calculated second-order derivative will fluctuate. For example, Figure [5.10b] shows the change in the second-order derivative as the density of the species is constant. Miscalculations of these fluctuations can result in the floating point exception handling issues which later will be treated as Nan in the model. Solving the chemical rates (including diffusion) with Nan values will result in nonphysical densities. Hence, it is necessary to identify these numerical fluctuations from the physical fluctuations.

2. **diffusion at sudden changes in the density:** Sharp gradients in the density impact the second-order derivative (lower panel of Figure [5.10a]). The drop of a few orders of magnitude in the derivatives and the diffusion rates may significantly impact the chemical network and the resultant densities of the species.

3. **sharp changes in the gradient due to unequal intervals or other reasons:** Incorporating diffusion into the chemistry of the KOSMA-$\tau$ PDR model will involve solving for the density while accounting for sudden vari-

ations in the diffusion rates. Consequently, the outcome of the sudden alteration will persist in the cloud (Figure [5.10b]). The rationale behind this is that the outcomes of the present shell are derived from the previous shell. It is imperative to differentiate between sudden changes caused by numerical calculations and those resulting from physical phenomena.

Implementing a flux limiter function in conjunction with Lagrange's three-point interpolation method has the potential to mitigate the effects of uneven intervals and resultant spikes. Also, while trying to reduce the number of spikes, one must be careful about not reducing the spikes due to the diffusion of species. To illustrate, in the lower panel of Figure [5.10a], there is a significant decrease in the second-order derivative within the $1.7 \leq r \leq 1.75$ range due to the density gradient. On the other hand, in the region, $r \geq 1.6$ of Figure [5.10b], the density is almost constant, and the oscillations in the second derivative of density result from numerical precision.

### 5.5.1 Flux limiter

When numerically solving the partial differential equations, high-resolution techniques are used if substantial accuracy is needed due to shocks or discontinuities (Godunov & Bohachevsky 1959). Using flux limiters with a high accuracy scheme will make the solution's total variation diminish (TVD). Flux limiters are numerical schemes that solve problems described by partial differential equations. These limiters help to avoid oscillations (wiggles) in the computational models, which otherwise would result in nonphysical results (Koren 1993). The wiggles or fluctuations may occur due to discontinuities or sharp changes in high-order spatial discretization schemes.

In a 1D semi-discrete scheme,

$$\frac{dn_i}{dt} + \frac{\phi(n_{s+1}) - \phi(n_{s-1})}{\Delta x} = 0 \tag{5.37}$$

where, $\phi(n_{s+1})$ and $\phi(n_{s-1})$ represents the edge fluxes of the $sth$ shell.

$$\phi(n_{s+1}) = f_{s+1}^{low} - \phi(r_i^{s+1})(f_{s+1}^{low} - f_{s+1}^{high}) \tag{5.38}$$

$$\phi(n_{s-1}) = f_{s-1}^{low} - \phi(r_i^{s-1})(f_{s-1}^{low} - f_{s-1}^{high}) \tag{5.39}$$

Where $f^{low}$ is the low-resolution (low accuracy) flux, $f^{high}$ is the high-resolution (high accuracy) flux, $\phi(r_i)$ is the flux limiter function, and $r_i$ represents the ratio

of successive gradients on the solution mesh, ie.

$$r_i = \frac{n_i^{s-1} - n_i^s}{n_i^s - n_i^{s+1}} \tag{5.40}$$

Since our data is sufficiently smooth, we used Koren (1993) as the flux limiter function.

$$\phi(r_i) = max\left[0, min\left(2r_i, min\left(\frac{1+2r_i}{3}, 2\right)\right)\right] \tag{5.41}$$

The flux limiter function is defined as $\phi(r_i) \geq 0$ with a maximum value of 2. When the limiter is equal to zero (opposite slopes or sharp or zero gradients), the flux is represented by a low-resolution scheme. In contrast, a high-resolution scheme is used when the flux limiter is 1 (smooth solution). Using eq. [5.37- 5.41] the flux corrected value of $n_s$ can be evaluated (Koren 1993). If the value of $r_i$ is, $0.25 \leq r_i \leq 2.5$ then $(0.5 \leq \phi(r_i) \leq 2)$,

$$n_1 = n_{in} \tag{5.42}$$

here $n_{in}$ is the input or boundary value at $x = 0$ (surface).

$$n_2 = \frac{1}{2}(n_1 - n_2) \tag{5.43}$$

$$n_{\text{last}+1} = n_{\text{last}} + \frac{1}{2}(n_{\text{last}} - n_{\text{last}-1}), \tag{5.44}$$

where $n_{\text{last}}$ is the boundary value (center of the cloud). The eq. [5.42], eq. [5.43] and eq. [5.44] relations are used at the boundaries. If the shell $s$ is between the boundary values (Koren 1993), then

$$n_s = n_{s-1} + \frac{1}{3}(n_s - n_{s-1}) + \frac{1}{6}(n_{s-1} - n_{s-2}) \quad (k = \frac{1}{3} \text{ relation}) \tag{5.45}$$

$$n_{s+1} = n_s + \frac{1}{2}\phi(r_i)(n_s - n_{s-1}), \tag{5.46}$$

With the corrections, the interpolated density of the species can be improved, as shown in Figure [5.11]. Figure [5.11] illustrates that the flux correction reduced the deviation in the interpolated density from the calculated density. No particular flux limiter is found to address all the problems, and most of the time, the flux limiter is chosen on a trial-and-error basis.

The Figure [5.12] illustrates the behavior of $r_i$. Most values fall in the $0.25 \leq r_i \leq 2.5$ regime, as indicated by the green lines. The spikes in the ratio ($\geq$ 100) coincided with significant variations in the second-order derivatives (Figure [5.12a]) and abrupt changes in the density profile (Figure [5.12b]). Hence, abrupt

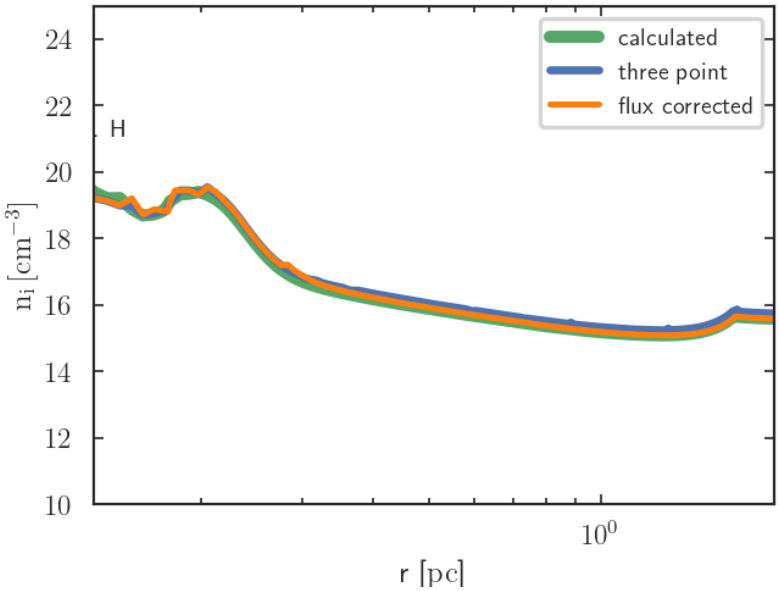


Figure 5.11: Flux corrected interpolated density for H compared to the interpolated density. a) shows the behavior of the ratio of successive gradients and the changes with second-order derivative, and b) shows the behavior of the ratio of successive gradients with density. Model parameters: table [3.1] with $\xi = 1.5, L = 0.2\,\mathrm{pc}$ and non-uniform temperature.

changes in the density can be identified by looking at the value of $r_i$. The small spikes in the ratio ($\leq 100$) can be caused by the unequal spacing between different spatial positions or error in interpolation, which requires further investigation.

Figure [5.13a] and Figure [5.13b] shows that the spikes in the ratio of successive gradients are in the limit $0.25 \leq r \leq 2.5$ for unequal spacing and constant

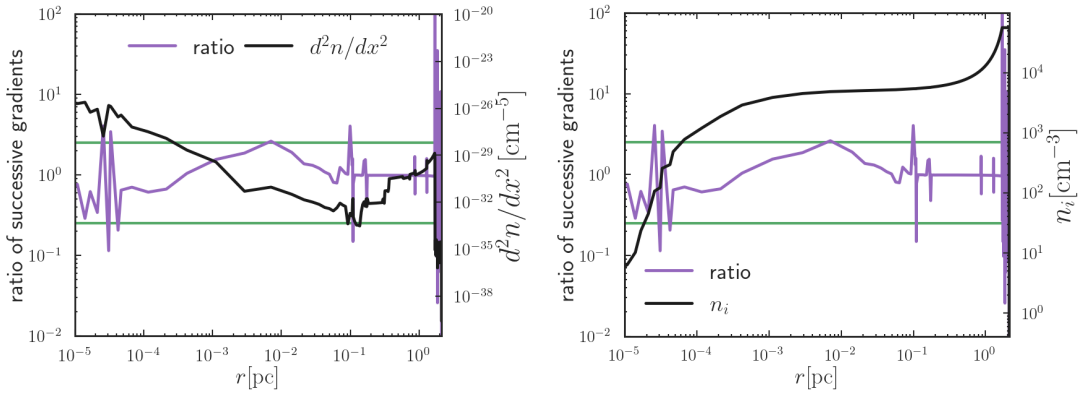


(a) ratio and second-order derivative

(b) ratio and density

Figure 5.12: Ratio of successive gradients for $H_2$. a) shows the behavior of the ratio of successive gradients and the changes with second-order derivative, and b) shows the behavior of the ratio of successive gradients with density. Two green lines are drawn at $r_i = 0.25$ and $r_i = 2.5$.

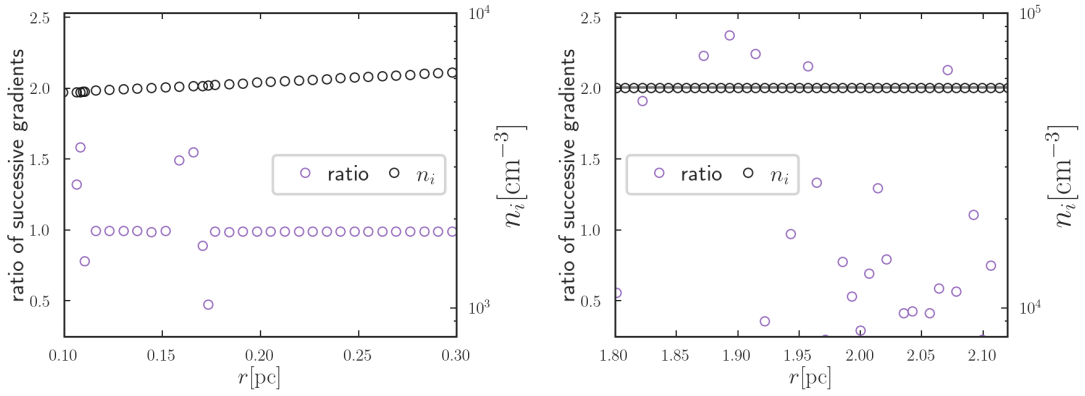


Figure 5.13: Ratio of successive gradients for $H_2$. a) shows the behavior of the ratio of successive gradients when the shells are closer, and b) shows the behavior of the ratio of successive gradients when the densities are almost constant.

density regions. Hence, eq. [5.42-5.46] will solve the problem without dismissing the diffusion rates. When the density of a species at shell $s$ is lower than the neighboring points $s-1$ and $s+1$ ($n_{s-1} > n_s$ and $n_s < n_{s+1}$), then the calculated ratio of successive gradients is $r_i \gg 2.5$ (but less than 100). Similarly, when $n_{s-1} < n_s$ and $n_s > n_{s+1}$, the ratio of successive gradients is $r_i \ll 0.25$ (but greater than 0.001). This is mainly due to the physical characteristics of the cloud. Therefore the resultant value will not be flux-limited.

The flux limiter function mitigated the sharp behavior of the second-order derivative by improving the interpolated density for $\xi = 1.5$ and $\xi = 0$ cases. The flux limiter function is not necessary throughout the cloud due to the smooth density and temperature profile of the modeled molecular cloud. Hence, a ratio of successive second-order derivatives is introduced to determine whether the flux limiter needs to be used. If the ratio of successive second-order derivatives exceeds three orders of magnitude, then the densities and temperatures are improved using flux limiters. The Koren flux limiter function failed to resolve every abrupt change in the second-order derivative due to the uncertainty interpolation. Hence, if the ratio of successive second-order derivatives with flux-limited densities and temperatures exceeds three orders of magnitude, an average value of the last three second-order derivatives is estimated as follows,

$$\left(\frac{\partial^2 n_i^s}{\partial^2 x^s}\right)_{\text{corrected}} = \frac{\left(\frac{\partial^2 n_i^{s-2}}{\partial^2 x^{s-2}}\right) + \left(\frac{\partial^2 n_i^{s-1}}{\partial^2 x^{s-1}}\right) + \left(\frac{\partial^2 n_i^{s}}{\partial^2 x^{s}}\right)}{3} \tag{5.47}$$

By computing the mean value of the second-order derivative of a given species over the two previous shells ($s-2$ and $s-1$) and the current shell ($s$), it is possible to mitigate abrupt variations in the second derivative. This corrected value is

calculated only if the ratio of successive gradients is within limits $0.25 \leq r \leq 2.5$ (no sharp changes in the density). Most of the time, the calculated second-order derivative and the diffusion rate are less than two orders of magnitude different from the last shell.

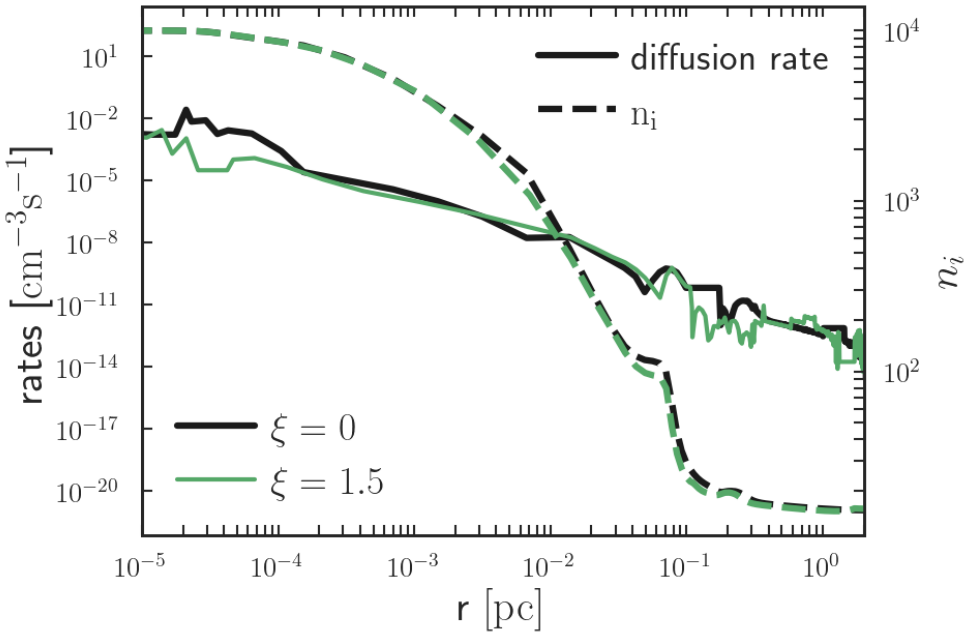


(a) H

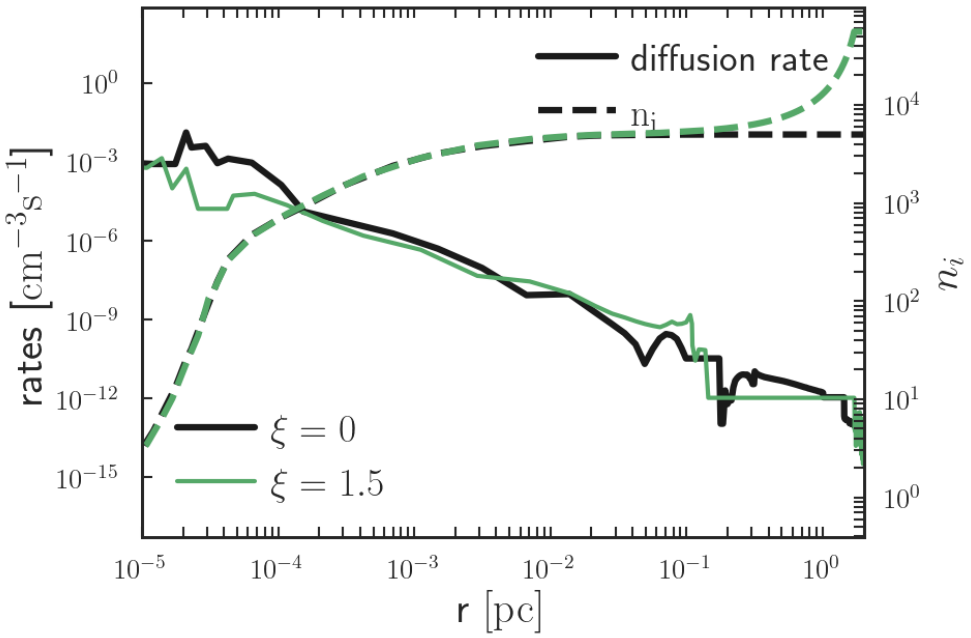


(b) $H_2$

Figure 5.14: Corrected diffusion rates with for H (a) and $H_2$(b). The dashed line indicates the number density. Diffusion rates are smaller for $\xi = 1.5$ case.

### 5.5.2 Limits of diffusion rates

The limits of diffusion coefficients are already explored in §[5.5.2]. The total diffusion rates of $H_2$ and H are shown in Figure [5.14] with different density profiles. The spikes in the total diffusion rates are less than two orders of magnitude change from the previous position, and removing them might remove the diffusion effects. The influence of thermal, molecular, and turbulent diffusion rates on the total diffusion rate is explored in §[6].

For a cloud of size 2.13 pc, the maximum diffusion coefficient will be $K = 10^{23}\,\mathrm{cm^2\,s^{-1}}$ (eq. [4.24]). Considering the maximum second-order derivative for $H_2$ ($\frac{d^2n}{dx^2} = 10^{-21}\,cm^{-5}$ ), the resultant total rates is $10^2\,\mathrm{cm^{-3}s^{-1}}$. Assuming a lowest second order derivative of $\frac{d^2n}{dx^2} = 10^{-70}\,cm^{-5}$ and minimum diffusion coefficient $K = 10^{15}\,\mathrm{cm^2\,s^{-1}}$ (eq. [4.24]), the resultant rates is $10^{-55}\,\mathrm{cm^{-3}s^{-1}}$. In the case of diffusion, $0.0\,\mathrm{cm^{-3}s^{-1}}$ is also a result that indicates that there is little to no concentration gradient. Hence, numerically the diffusion rates only vary between $10^{-55} - 10^2\,\mathrm{cm^{-3}s^{-1}}$ (the upper limit of the diffusion rate depends on the cloud parameters) excluding $0.0\,\mathrm{cm^{-3}s^{-1}}$. If the diffusion rate is $\leq 10^{-40}\ \mathrm{cm^2s^{-1}}$ resultant effect on the number density is negligible because the other chemical reaction rates are higher. Due to the numerical precision, the KOSMA-$\tau$ PDR model considers any value less than $10^{-33}$ as zero. Hence, we can conclude that the lowest diffusion rate is $10^{-40}\ \mathrm{cm^2s^{-1}}$, which removes the wiggles in the almost constant density regions and sets the rates to constant ($10^{-40}\ \mathrm{cm^2s^{-1}}$).

Figure [5.15] shows the formation and destruction reaction of $H_2$ as a function of distance from the surface of the cloud. The diffusion dominates the formation and destruction of the species $H_2$ with a coherence length of $L = 0.2$ pc. A more detailed exploration of diffusion and chemical rates is provided in the §[6].

### 5.5.3 Other simulation details

In the KOSMA-$\tau$ PDR model, the minimum number of global iterations is 2, and the maximum is 60 (Röllig & Ossenkopf-Okada 2022). Most models converge within 30 iterations. The introduction of diffusion reduced the number of iterations. The model converges faster within the parameter space for lower masses than the higher masses, provided the chemical network is the same. Moreover, the inclusion of diffusion reduces the number of global iterations required for the model to converge. The total computation time for a diffusion model takes around two to five minutes, whereas, without diffusion, it takes approximately five to seven minutes using an Intel i5-8500 CPU. If the model does not find a stable converged solution in 60 iterations, the results from the last iteration are saved. Most of the time, the results are good enough to understand the physics

and chemistry of the cloud. If the diffusion causes FPE issues, the diffusion will be turned off (the diffusion contribution to the $\mathbb{F}$ and $\mathbb{Q}$ will be zero), and the chemistry will be allowed to recover. Then, diffusion will turn back on in the following shell. For example, in some cases, it is numerically challenging to solve the chemistry with diffusion to get a stable solution for diffuse clouds ($n_{\text{surf}} \leq 10^2\,\text{cm}^{-3}$) with $L \geq 10\%R$. This is because the higher diffusion rates can result in negative or too low densities ($\leq 10^{33}$), resulting in floating point exception errors(FPE). More of the limits are explored in §[6.1].

Like any other data set, the resultant diffusion rate dataset has outliers and missing data. To process the chemistry correctly, these should be handled appropriately. Therefore, if the diffusion rates are Nan, the contribution to the $\mathbb{F}$ and

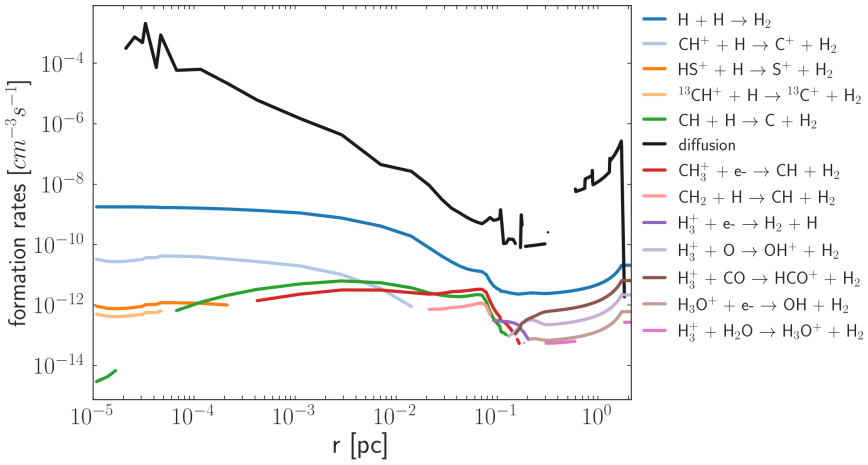


(a) formation rates

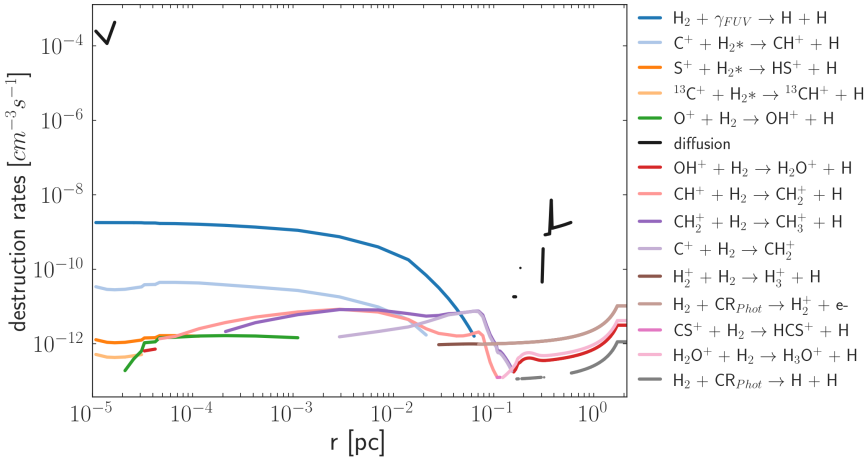


(b) destruction rates

Figure 5.15: Formation and destruction rates with $\xi = 1.5$ for $H_2$. Diffusion and other chemical reactions are shown. Diffusion rates are higher than the rest of the chemical reactions. The gaps in the line profile indicate that the reaction is not a top contributor at that spatial position. Model parameters: table [3.1] with $\xi = 1.5$ and $L = 0.2\,\text{pc}$.

$\mathbb{Q}$ will be zero. During the visualization of the results, Python-pandas handles the missing values.

# Chapter 6

# Results

Dynamic mixing can influence the physical structure and chemistry of a PDR. This study considers the temperature, surface density, mass, clump size, cosmic ray ionization rate, and UV field (table [6.1]) to understand the diffusion effects on the physical structure of the PDR. Sixty-one species are included in the study to comprehend the diffusion effects in the chemistry of the PDR. Including diffusion, these species are formed and destroyed through 812 reactions. The without-diffusion case results (table [3.1]) are used as a reference for comparison.

When including diffusion into the chemistry, solving the chemistry is no longer a local problem because the diffusion depends on the properties of the nearest neighboring shells. Diffusion rates depend on the movement of particles. Hence, it can appear as the formation rate on a shell and the destruction rate of another shell or as the formation/destruction rate on both shells. Therefore, we used scatter plots rather than line plots demonstrating diffusion rates to visualize the results. The resultant variation in abundance from the without-diffusion scenario looks minimal in a steady-state model (compared to the 3-4 orders of magnitude difference in similar studies done on a time-dependent model, e.g., Xie et al. 1995; Lesaffre et al. 2007). Therefore, we provided changes in individual chemical reaction rates and integrated line intensities of different species.

The local conditions are related to the amount of diffusion through the diffusion coefficients. Hence, to understand how diffusion affects the physical and chemical structure of the molecular cloud, it is essential to look at the diffusion coefficients. Moreover, it is crucial to comprehend the interdependence between different diffusion coefficients and the specific roles played by each diffusion coefficient in determining the total diffusion rates. Numerous questions still need to be answered, including the potential correlation between total diffusion rates and unique coherence lengths and whether this correlation is consistently linear. The total diffusion rate is the sum of turbulent, molecular, and thermal diffusion rates. Therefore the relation between coherence length and total diffusion

| Case I : $R = 8\,\mathrm{pc}$ | Case II : $R = 2.13\,\mathrm{pc}$ |
|---|---|
| n = $10^3$, M = $10^6$ $M_\odot$<br>$\chi = 100$<br>$K = 0, 10^{15} - 10^{23}\mathrm{cm}^2\,\mathrm{s}^{-1}$<br>T = dynamic , $\xi = 1.5$ | n = $10^4$, M = $10^4$ $M_\odot$<br>$\chi = 100$<br>$K = 0, 10^{15} - 10^{23}\mathrm{cm}^2\,\mathrm{s}^{-1}$<br>T = dynamic, $\xi = 1.5$ |
| **Case III : $R = 1\,\mathrm{pc}$** | **Case IV : $R = 0.5\,\mathrm{pc}$** |
| n = $10^3$, M = $10^3$ $M_\odot$<br>$\chi = 100$<br>$K = 0, 10^{15} - 10^{23}\mathrm{cm}^2\,\mathrm{s}^{-1}$<br>T = dynamic, $\xi = 1.5$ | n = $10^2$, M = $10^2$ $M_\odot$<br>$\chi = 100$<br>$K = 0, 10^{15} - 10^{23}\mathrm{cm}^2\,\mathrm{s}^{-1}$<br>T = dynamic, $\xi = 1.5$ |

Table 6.1: These cases are considered for the with and without diffusion computations. Case II tested with constant gas temperatures $T = 50, 70$, and 120K to understand the effect of gas temperatures on diffusion. We considered a dust temperature of 20 K unless a dynamic temperature calculation is enabled. $K = 0\,\mathrm{cm}^2\,\mathrm{s}^{-1}$ denotes the without diffusion scenarios.

rates might not be linear (for example, the diffusion rates of CO in Figure [C.5]). Additionally, the relationship between chemical rates and diffusion rates requires further investigation. What is the impact of cloud chemistry on diffusion rates? Do different diffusion coefficients have the same level of impact on the chemical structure of the cloud? The KOSMA-$\tau$ PDR model is tested with different coherence lengths and total diffusion coefficients to answer these questions.

This chapter is organized into three sections. The first section investigates the contribution of molecular, thermal, and turbulent diffusion to the total diffusion rates. The subsequent two sections explore the impact of diffusion on the physical structure and the chemical structure of clouds, respectively. Unless otherwise noted, Case II from the table [6.1] with dynamic temperature, and $\xi = 1.5$ serves as the reference for the discussion.

## 6.1 Diffusion coefficients

As the local conditions of the cloud change, the diffusion coefficient also changes. The total diffusion coefficient $K$ (eq.[4.3]) varies in the range $10^{15}$ -$10^{23}\mathrm{cm}^2\,\mathrm{s}^{-1}$, with the molecular diffusion coefficient serving as the lower threshold. The total diffusion coefficient and individual contribution to the total diffusion coefficients of each species within the cloud are distinguishable. The turbulent diffusion

coefficient ($K_{\rm turb}$) of the cloud has a maximum value of $10^{23}$cm$^2$ s$^{-1}$, which is seven orders of magnitude higher than the molecular diffusion ($K_{\rm mol} \leq 10^{16}$cm$^2$ s$^{-1}$). It is possible to employ different coherence lengths ($L \leq 10\%R$ Xie et al. 1995; Mac Low & Ossenkopf 2000) to comprehend the effects of various turbulent scenarios on the chemistry and physics of the molecular cloud. For instance, if turbulent and molecular diffusion are on the same scale, how does this impact the total diffusion rates? Is thermal diffusion dominant at lower levels of turbulence? To answer these questions, the coherence length of turbulent diffusion is varied.

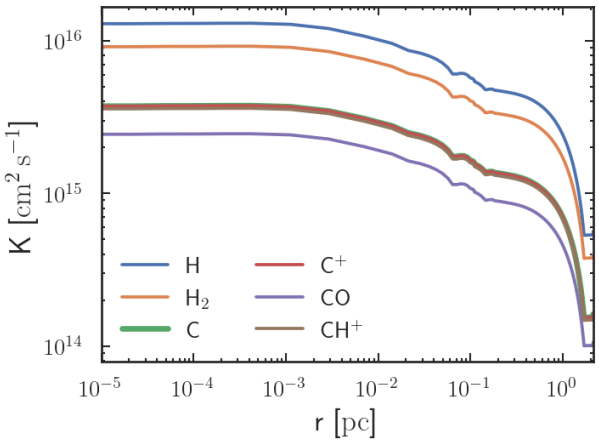


Figure 6.1: Molecular coefficients of selected species. Model parameters: Case II from the table [6.1].

Figure [6.1] shows the behavior of the molecular diffusion coefficient and Figure [6.2] depicts the changes in the thermal diffusion coefficients of various species. The reason for the significant change in the profile of the thermal diffusion coefficient ($K_{\rm therm} = K_{\rm mol} k_T$) from the molecular diffusion coefficient ($K_{\rm mol}$) is due to the fraction $\frac{n_i^s(n_\Sigma - n_i^s)}{n_\Sigma^2}$ (see eq.[4.18]). As a result, the profile of the thermal diffusion coefficient follows the density profile of the species. The coefficient of turbulent diffusion exhibits variations in response to alterations in the coherence length (Figure [6.3]).

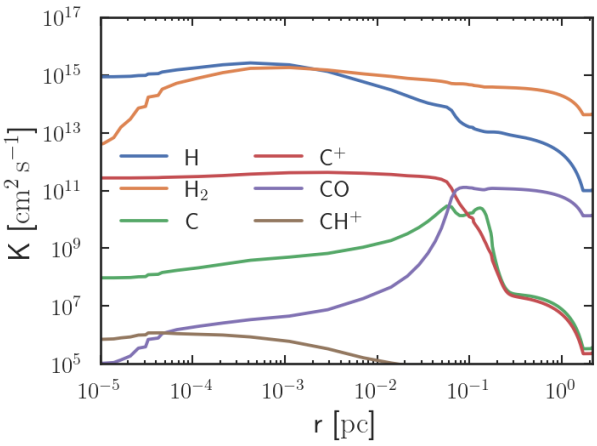


Figure 6.2: Thermal diffusion coefficients for different species. Model parameters: Case II from the table [6.1].

The diffusion velocity (molecular, thermal, and turbulent) will vary as the square root of temperature (eq.[4.23]), as shown in the Figure [6.4]. The turbulent velocity of the species is the sound speed in the atomic gas, which is the same for every species. The thermal and molecular diffusion velocities are the thermal velocity of the individual species, which varies depending on the mass of the species. Figure [6.5] depicts the variation in gas temperature as a function of

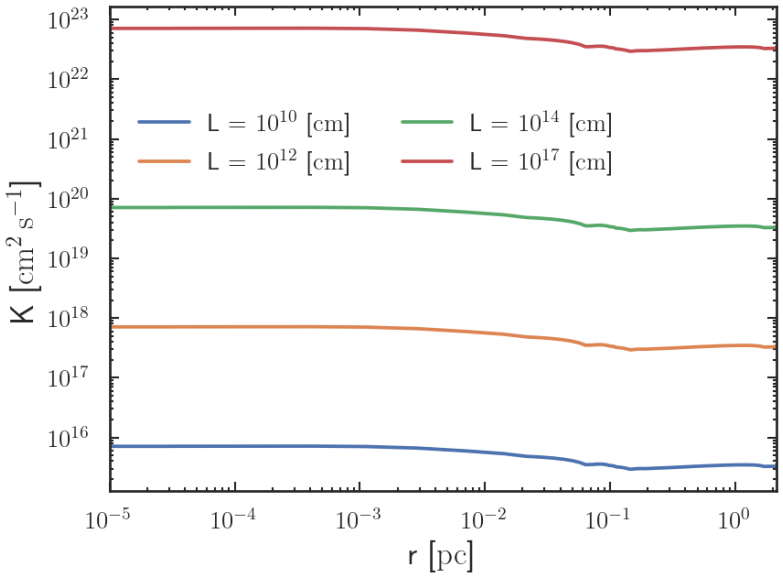


Figure 6.3: Change in the turbulent diffusion coefficient, $K_{\mathrm{turb}}$ as the coherence length $L$ changes. Model parameters and labels are the same as in Figure [6.2].

distance from the surface of the cloud. The blue line denotes the temperature in the absence of diffusion, whereas the other straight line depicts the temperature in the presence of diffusion. The dissimilarity between the two is negligible, albeit

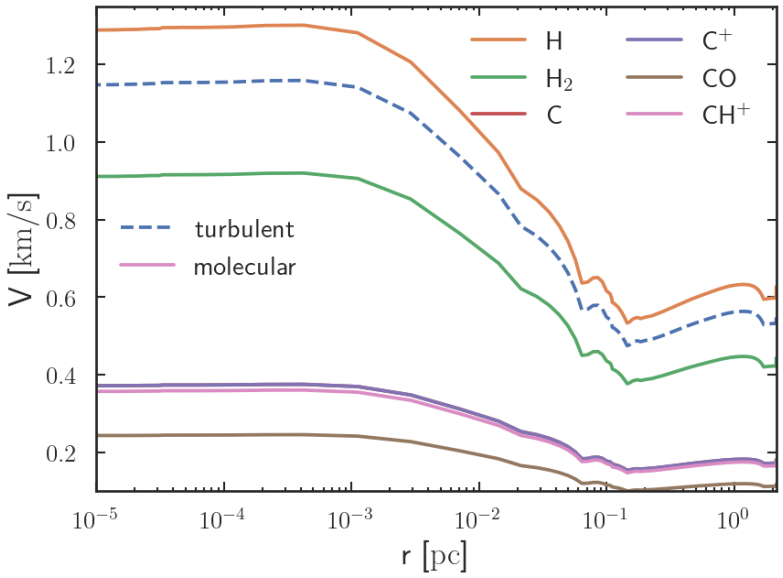


Figure 6.4: Turbulent (dashed lines) and molecular (straight line) diffusion velocities. The turbulent diffusion velocities are the same for all species. The thermal diffusion velocity of each species is the same as the molecular diffusion velocity. Model parameters and labels are the same as in Figure [6.2].

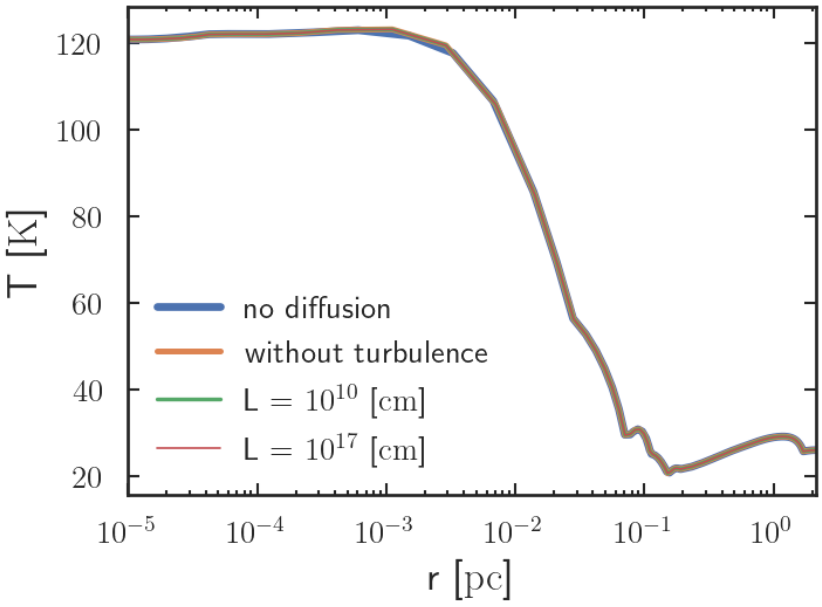


Figure 6.5: Gas temperature as a function of distance from the cloud surface (pc). The difference in temperature between the without diffusion (blue) and with diffusion is small. Compared to the without diffusion case, the cloud is slightly warmer in the region $4 \times 10^{-4} \leq r \leq 3 \times 10^{-3}$ pc when diffusion is added. Different colors indicate different diffusion coefficients, which overlap each other. Model parameters: Case II from the table [6.1].

the diffusive scenario exhibits a marginally higher temperature between $4 \times 10^{-4}$ and $3 \times 10^{-3}$ pc. The different colors on the graph represent varying diffusion coefficients, but they overlap. As evidenced by the data presented in Figure [6.5], it is apparent that introducing diffusion does not yield a substantial alteration in the gas temperature within the cloud compared to the scenario in which diffusion is absent. However, when diffusion is added, the maximum gas temperature shows a 0.2% increase compared to the scenario without diffusion. The following subsections examine the changes in diffusion coefficients and rates when solely the turbulent diffusion coefficient is varied. This section also comprehensively assesses the scenario when the molecular cloud is devoid of turbulent diffusion.

## 6.2 Diffusion rates

As the coherence length of turbulent diffusion increases from $10^9$ cm to $10^{17}$ cm, changes in the diffusion contributions are significant (Figure [6.6]). The graph in the appendix (§.[C]) shows a zoomed-in view of the grid points in the cloud, as they are more tightly spaced in the region $0.1 - 2.13$ pc due to the choice of representation. The individual contribution from molecular, thermal, and turbulent

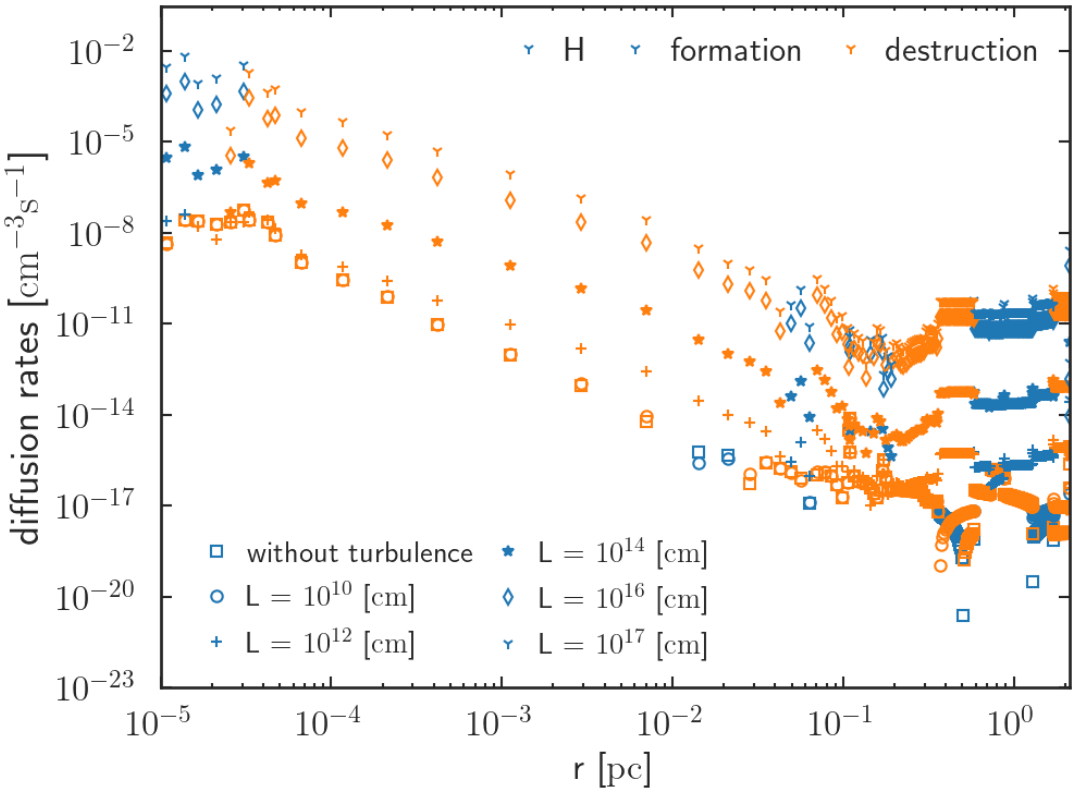


(a) H

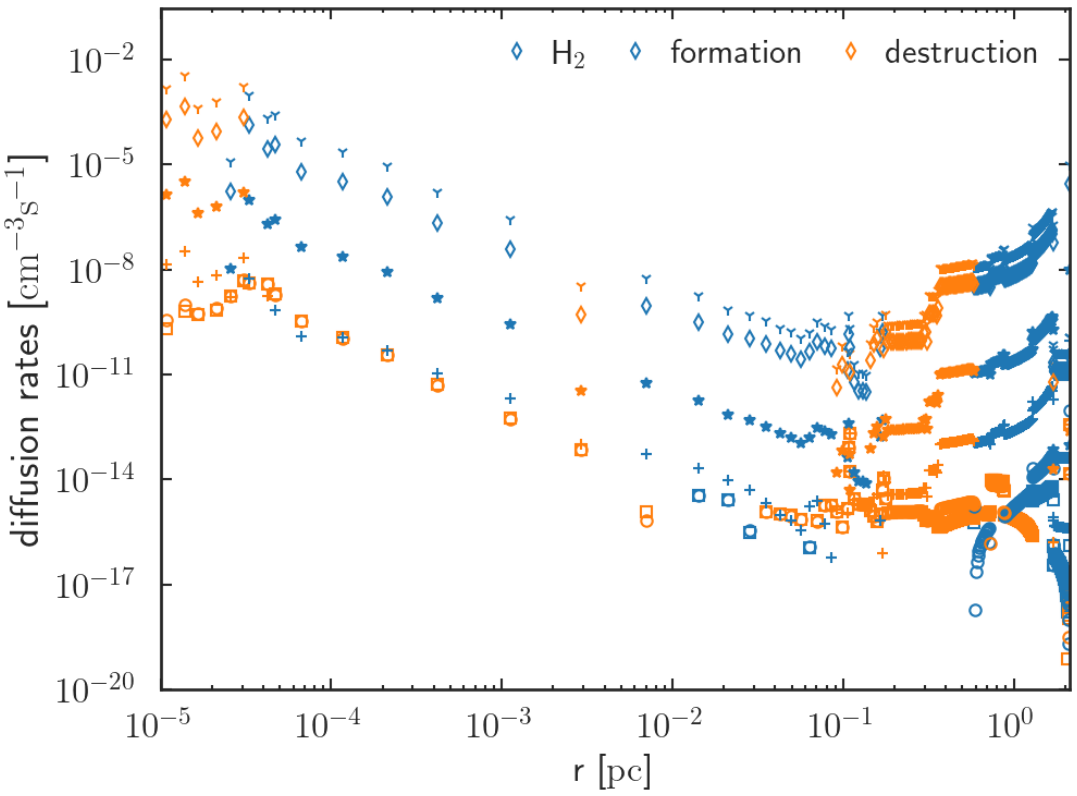


(b) $H_2$

Figure 6.6: Total diffusion rates with different $L$ values. Model parameters: Case II (table [6.1]).

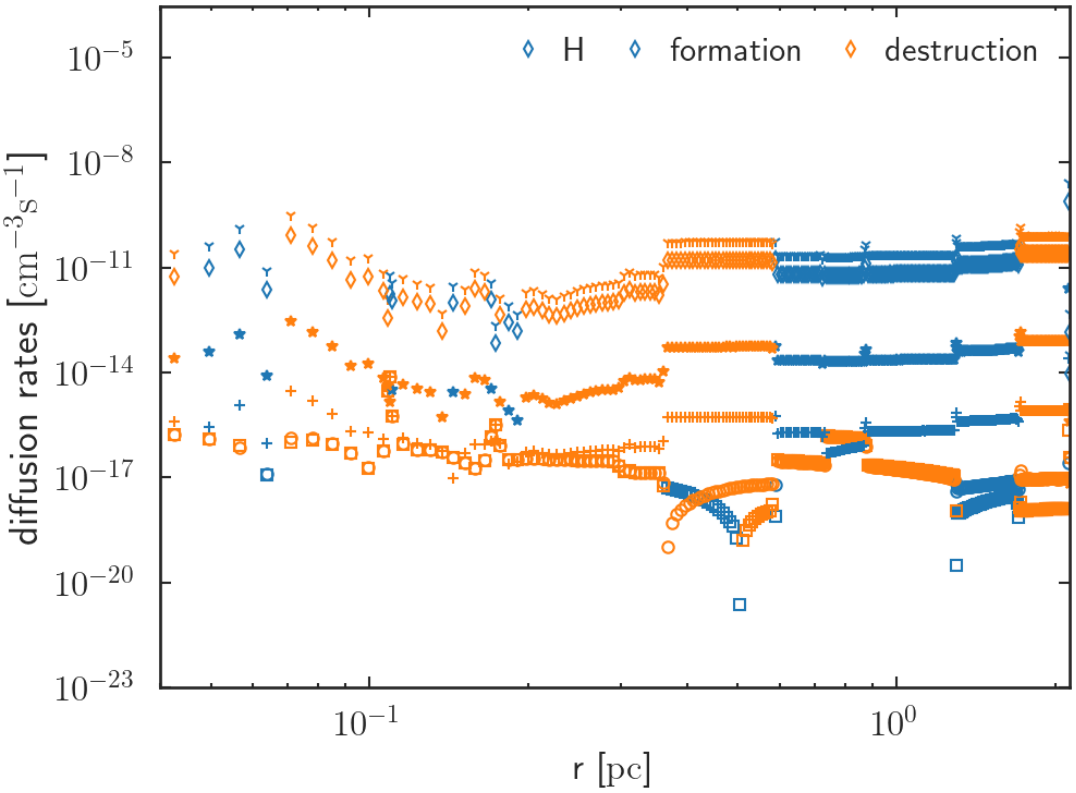


(a) H

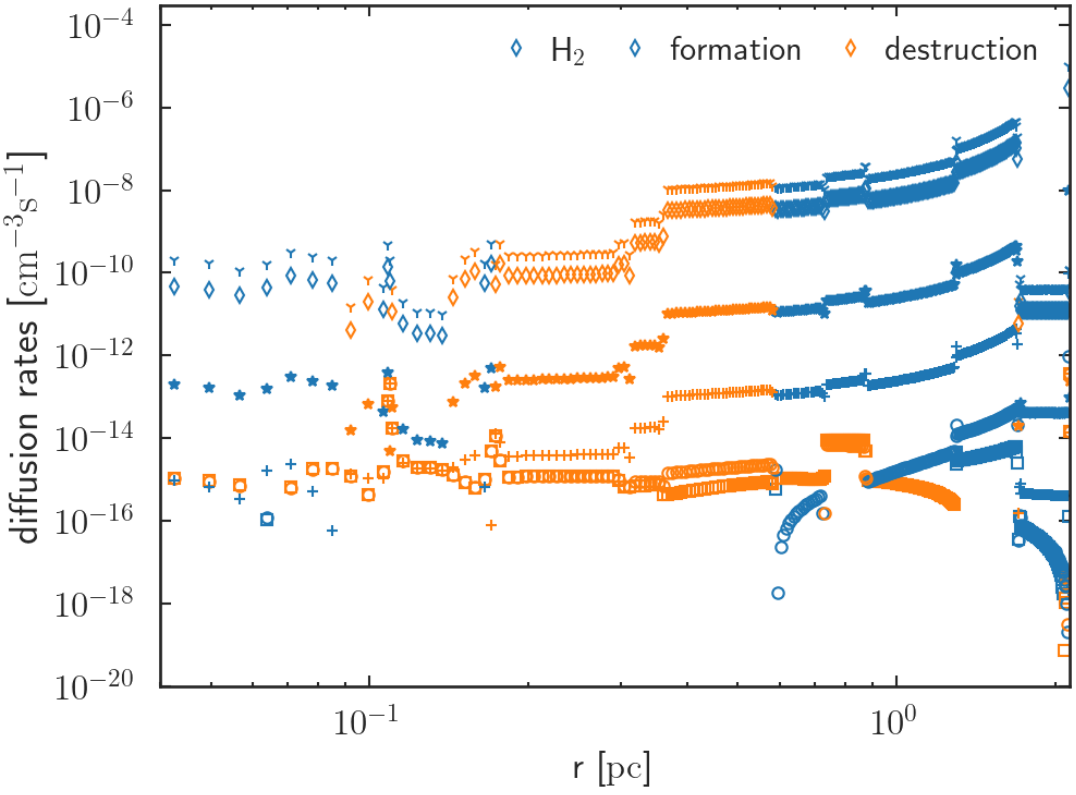


(b) $H_2$

Figure 6.7: Total diffusion rates with different $L$ values. Labels are the same as in Figure [6.6].

diffusion to the total diffusion rate for different coherence lengths ($L$) is shown in the Figures [6.9 - 6.16] and the behavior is explained below.

Figure [6.6] shows the total diffusion rate for atomic and molecular hydrogen as a function of distance from the surface of the cloud with different coherence lengths $L$. Primarily, diffusion is a formation reaction for molecular hydrogen (Figure [6.6b]), whereas it is a destruction reaction for atomic hydrogen (Figure [6.6a]). The contribution from thermal diffusion is higher than the other components for the cases without-turbulence and turbulence with a coherence length of $L \leq 10^{10}$ cm. Therefore diffusion is a destructive reaction for molecular hydrogen in this scenario. Diffusion rates are higher on the surface due to higher diffusion coefficients. Up to $r = 0.08$ pc, the change in total diffusion rates is linear to the change in the coherence length. The diffusion contributions are not linear in the region $0.08 - 0.2$ pc for atomic and molecular hydrogen, as shown in Figure [6.7], due to the difference in the contribution from thermal, molecular, and turbulent diffusion to the total diffusion rate(Figure [6.9-6.16]).

The thermal diffusion process significantly affects the total diffusion rates of CO, as shown in Figure [C.5]. In the region $r \leq 10^{-3}$ pc, the impact of thermal diffusion is observed to be greater than that of turbulent and molecular diffusion, regardless of the coherence length. Thus, the total diffusion rate remains consistent up to $r \leq 10^{-3}$ pc. In the region $r \geq 10^{-3}$ pc, thermal or turbulent diffusion contributes more to the total diffusion depending on the coherence length (Figure [C.5(b-f)]). The same trend applies to $CH^+$. However, when considering C (Figure [C.1]) and $C^+$ (Figure [C.3]), the impact of the turbulent diffusion is less noticeable in the region $r \leq 0.01$ pc, due to the high thermal diffusion contribution at $L \leq 10^{12}$ cm in these areas. The density gradient of C and $C^+$ is minor in these regions compared to the mid-to-center region ($r \geq 0.01$ pc) of the modeled cloud. As a result, the contribution from molecular and turbulent diffusion is smaller than the thermal diffusion rates.

**without-turbulence:** Molecular diffusion considers the concentration gradient between nearby spatial positions, and thermal diffusion acts upon the temperature gradient. In the without-turbulence scenario, the total diffusion rates for atomic and molecular hydrogen are similar to $L \leq 10^{10}$ cm scenario, as shown in Figure [6.6]. This is because the thermal diffusion rates are higher than the contribution from both molecular and turbulent diffusion. The turbulent diffusion rates are significant in the $L \leq 10^{10}$ cm scenario, but not enough to exceed the thermal diffusion contribution in certain regions. Consequently, certain areas within the cloud without-turbulence scenario contribute more than that turbulence with a coherence length of $L \leq 10^{10}$ cm.

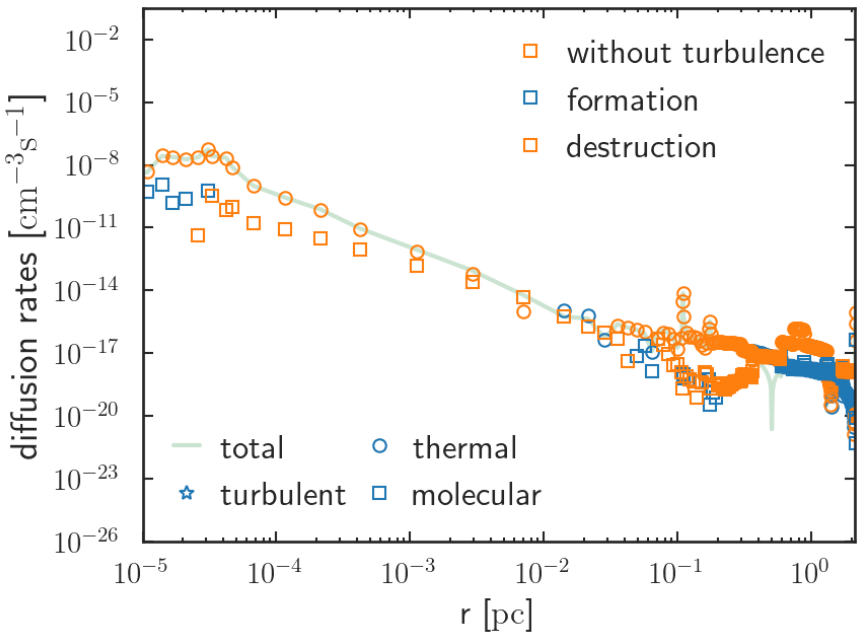


(a) H

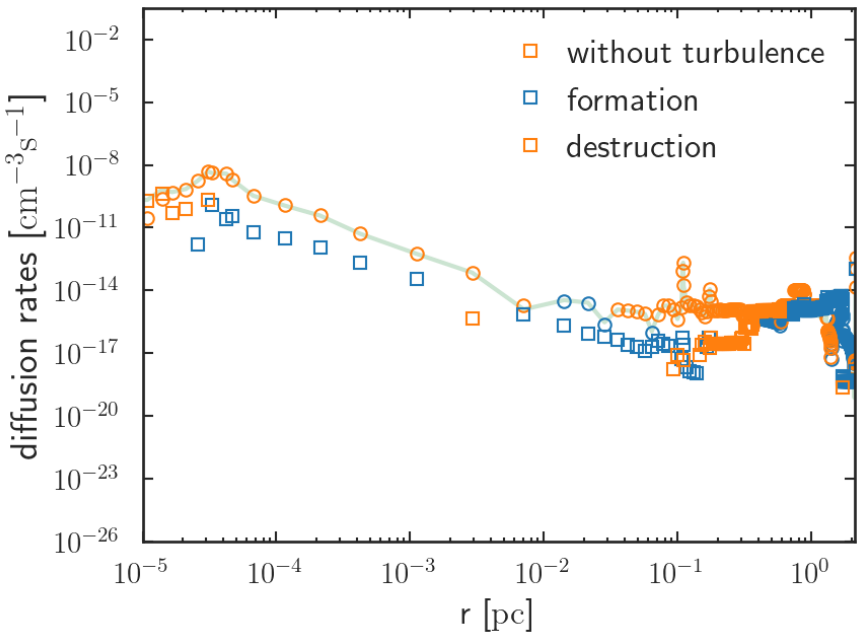


(b) $H_2$

Figure 6.8: Individual contribution to total diffusion rates in a scenario without turbulent diffusion. Model parameters: same as Figure [6.6].

For atomic hydrogen in the region $0.4 - 0.6\,\mathrm{pc}$, molecular (formation) and thermal (destruction) diffusion contribute on the same scale resulting in a reduced total diffusion rate. Unlike higher turbulent coherence lengths, diffusion is a destruction reaction for atomic and molecular hydrogen in the region $10^{-5} \leq r \leq 10^{-2}\,\mathrm{pc}$. This is due to the fact that thermal diffusion, which is a destruction reaction, contributes more to the total diffusion rates than molecular diffusion. In the region $1 \leq r \leq 2.13\,\mathrm{pc}$, the cloud contains mainly cold molecular gas.

Hence, molecular diffusion contributes more than thermal diffusion to the total diffusion rates of molecular hydrogen.

To compensate for the destruction of $H_2$ via diffusion, molecular hydrogen is formed via the reactions $CH + H \longrightarrow C + H_2$, $HS^+ + H \longrightarrow S^+ + H_2$, $^{13}CH^+ + H \longrightarrow {}^{13}C^+ + H_2$, and $CH_3{}^+ + e^- \longrightarrow CH + H_2$. Also, a reduction in the destruction reaction $OH^+ + H_2 \longrightarrow OH^+ + H$ is noted. The destruction reaction $O^+ + H \longrightarrow O + H^+$ shows an increase in the rates for $L \leq 10^{10}$ cm compared to the case without turbulence. Also, the destruction reactions, $HS^+ + H \longrightarrow S^+ + H_2$ and photoionization of H show an increase in the case without-turbulence compared to $L \leq 10^{10}$ cm. A more detailed investigation of the changes in the chemistry is provided in §[6.4].

**L = $10^{10}$ cm :** At $L = 10^{10}$ cm molecular and turbulent diffusion contributes similarly to the total diffusion rates of atomic and molecular hydrogen in the region $10^{-5} \leq r \leq 0.1$ pc (Figure [6.9]). The atomic-to-molecular transition takes place within the range of $0.001 \leq r \leq 0.01$ pc (Figure [6.24a]). Thermal diffusion is at most four orders of magnitude higher than molecular and turbulent diffusion in the atomic region. Hence, the resultant total diffusion rate acts as a destruction reaction for both H and $H_2$. In the region between 0.1 and 0.3 pc, thermal diffusion contributes more to the total diffusion rates due to the slight increase in the temperature profile (Figure [6.10]). In the region, $0.3 \leq r \leq 0.4$ pc, the destruction via turbulent and molecular diffusion and formation via thermal diffusion are on similar scales. Hence, the resultant total diffusion rate is smaller than the individual rates (Figure [6.10a]) for atomic hydrogen. Similarly, molecular hydrogen shows a reduced total diffusion rate in the region $0.5 - 0.7$ pc, as shown in Figure [6.10b]. In the case of CO, $C^+$, C and $CH^+$ (Figure [C.1-C.7]), thermal diffusion contributes more than molecular and turbulent diffusion. Due to the significantly low second-order derivative of density, the total diffusion rate of C (Figure [C.1a]) and $C^+$ (Figure [C.3a]) is dominated by thermal diffusion throughout the cloud. For $CH^+$ (Figure [C.7a]) and CO (Figure [C.5a]), thermal diffusion dominates up to 0.3 pc and in the region $r \geq 1$ pc, turbulent diffusion contributes significantly more than molecular and thermal diffusion.

**L = $10^{12}$ cm :** As the coherence length increases to $L = 10^{12}$ cm, diffusion remains a formation reaction for molecular hydrogen and a destruction reaction for atomic hydrogen (Figure [6.6]). However, the individual contributions of diffusion to the total diffusion rates exhibit notable variations (see Figure [6.11]). On the surface ($r \leq 10^{-4}$ pc), turbulent diffusion is at most four orders of magnitude greater than thermal or molecular diffusion. This constitutes a total diffusion rate

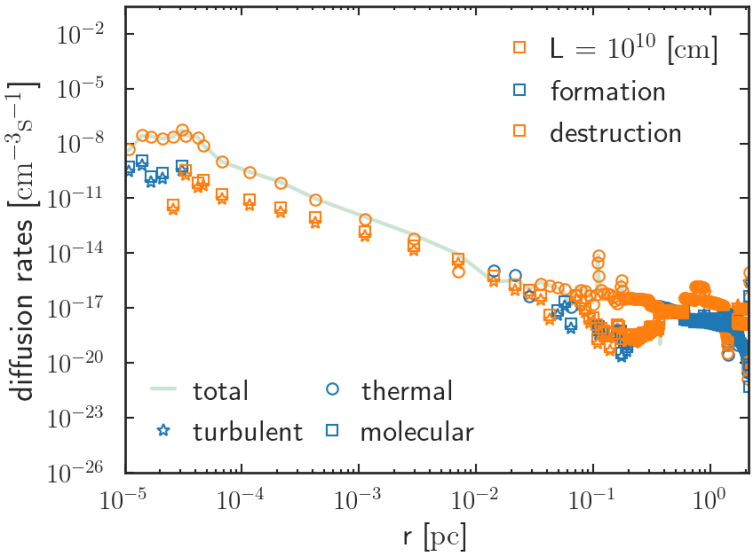


(a) H

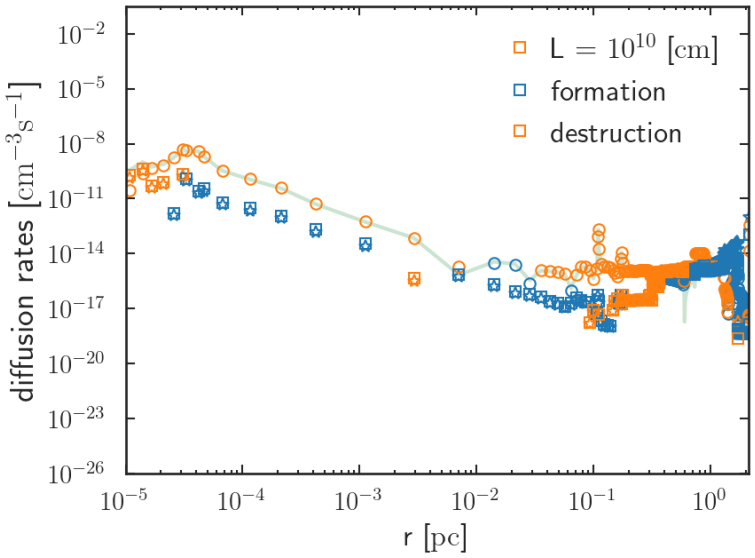


(b) $H_2$

Figure 6.9: Individual contribution to total diffusion rates with $L = 10^{10}$ cm. Formation (blue) and destruction (orange) rates with the total diffusion rate (light green line) are shown. Model parameters: Case II (table [6.1]).

of at least three to four orders of magnitude higher than the without-turbulence scenario.

Turbulent diffusion contributes more to the total diffusion of H and $H_2$ up to $r = 0.1$ pc. The thermal and turbulent diffusion contributions are on the same orders of magnitude for H and $H_2$ in the region $10^{-5} \leq r \leq 10^{-3}$ pc. In the region, $0.1 \leq r \leq 0.3$ pc, thermal diffusion contribution slightly outweighs turbulent diffusion due to the increase in the temperature in this region. Deeper in the cloud ($r \geq 0.3$ pc), turbulent diffusion contributes more than thermal and molecular diffusion. In this region, thermal diffusion contribution is lower than

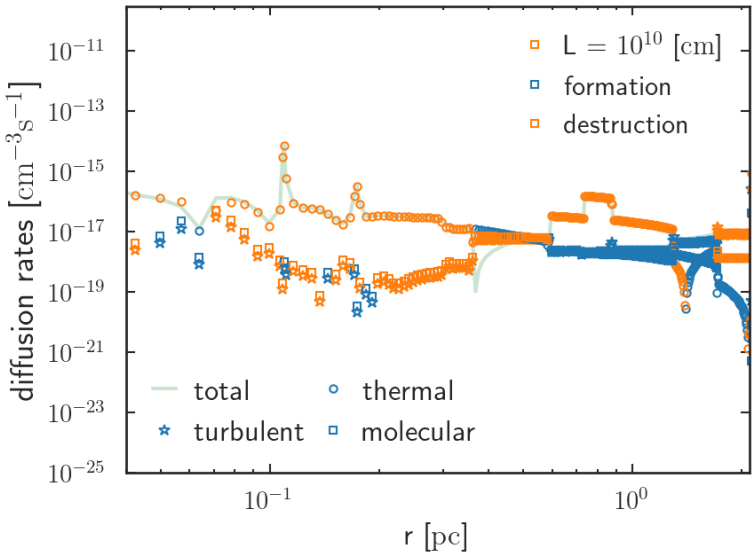


(a) H

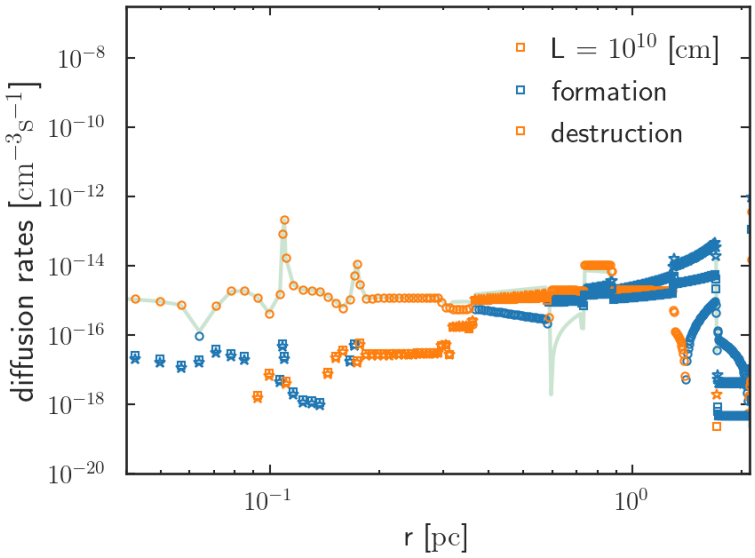


(b) $H_2$

Figure 6.10: Individual contribution to total diffusion rates with $L = 10^{10}$ cm. Formation (blue) and destruction (orange) rates with the total diffusion rate (light green line) are shown. Model parameters: Case II (table [6.1]).

molecular diffusion. It is noteworthy that in the region between 0.1 and 0.2 pc, the total diffusion rates with $L = 10^{12}$ cm are similar to those without-turbulence for both H and $H_2$. This is because thermal diffusion contributes significantly to the total diffusion rates for these species.

**L = $10^{14}$ cm :** As the coherence length of turbulent diffusion is set to $L = 10^{14}$cm, diffusion continues to act as a formation reaction for atomic hydrogen and a destruction reaction for molecular hydrogen, as depicted in Figure [6.6]. Nevertheless, there are notable variations in the individual contributions of dif-

fusion, as illustrated in Figure [6.13]. The turbulent contribution to the total diffusion rates is higher than the thermal and molecular diffusion contributions for atomic and molecular hydrogen. The sudden change in the diffusion rates of molecular hydrogen between $10^{-3}$ pc and $10^{-2}$ pc is due to the error in the interpolated density of molecular hydrogen (§[5]). Over the limited number of points, the density profile of the molecular hydrogen changes significantly, resulting in an

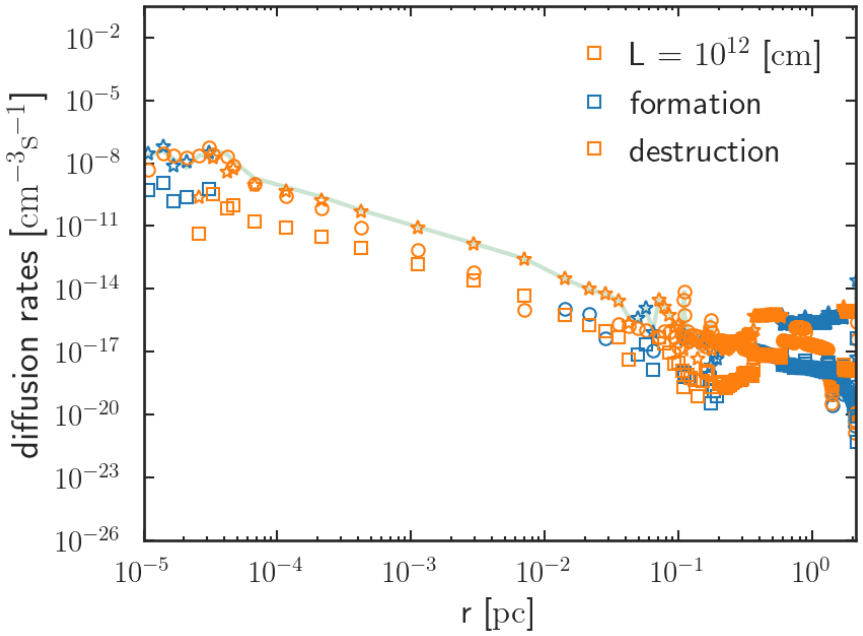


(a) H

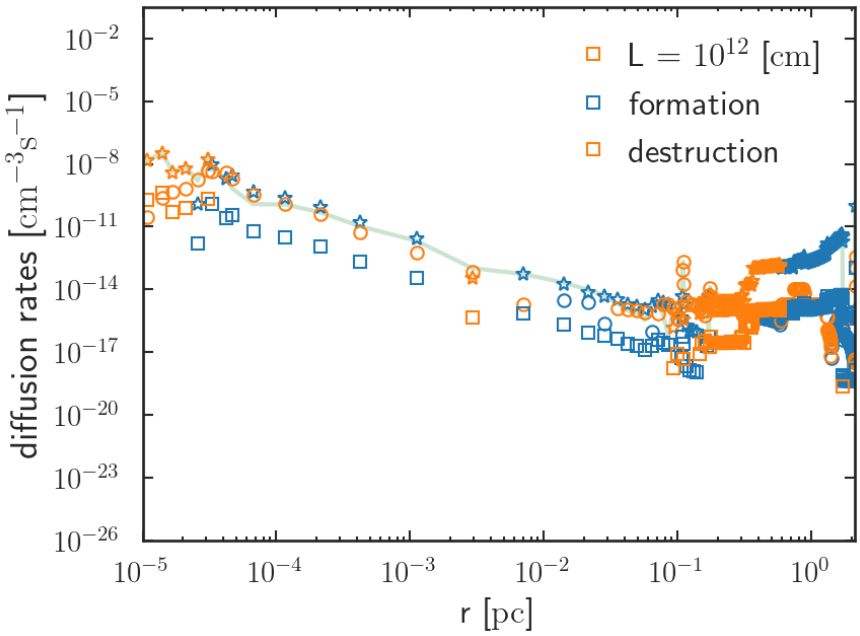


(b) $H_2$

Figure 6.11: Individual contribution to total diffusion rates with $L = 10^{12}$ cm. Labels are similar to Figure [6.9]

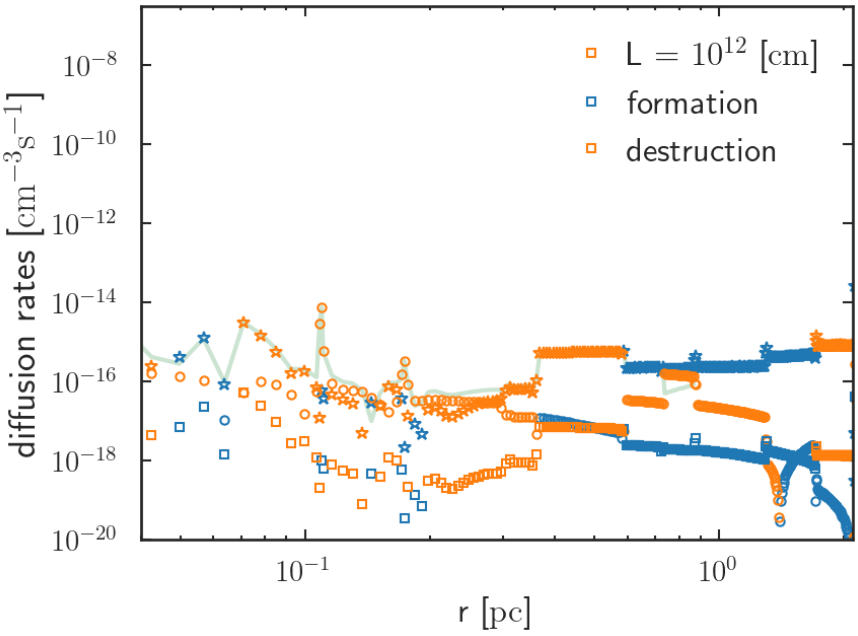


(a) H

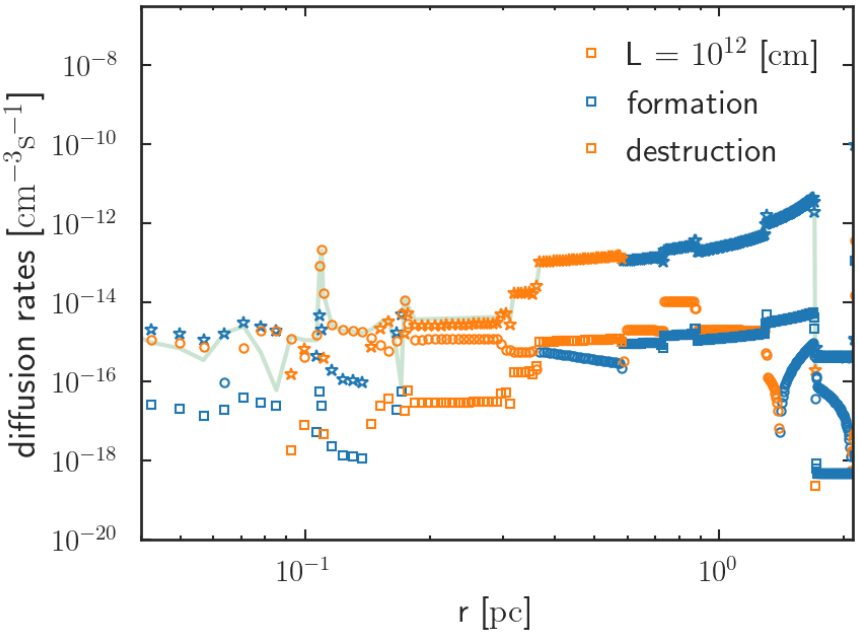


(b) $H_2$

Figure 6.12: Individual contribution to total diffusion rates with $L = 10^{12}$ cm. Labels are similar to Figure [6.9]

interpolation error. The energy balance and chemistry are well resolved in these regions. A detailed explanation is given in §.[5.5.1].

On the surface ($r \leq 10^{-4}$ pc), the contribution from chemical reactions other than diffusion is of the order of $\sim 10^{-9}\,\mathrm{cm^{-3}s^{-1}}$ which is three orders of magnitude lower than the diffusion contribution to the destruction of H. For the formation of $H_2$, the topmost contribution other than diffusion is the reaction $H + H \longrightarrow H_2$ ($\sim 10^{-9}\,\mathrm{cm^{-3}s^{-1}}$) which is four orders of magnitude lower than the diffusion

contribution. Figure [6.14] illustrates that, even at the center of the cloud the turbulent diffusion dominates the total diffusion rates.

**$10^{16} \leq L \leq 10^{17}$cm :** Turbulent diffusion plays a substantial role in the total diffusion rates of atomic and molecular hydrogen when the coherence length ranges from $10^{16} \leq L \leq 10^{17}$cm. Upon initial examination, it is evident from the

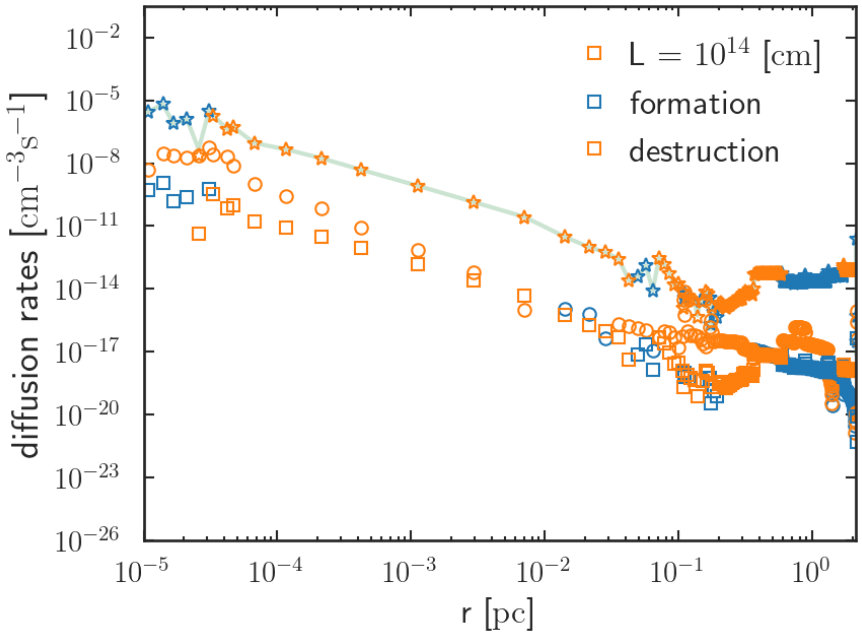


(a) H

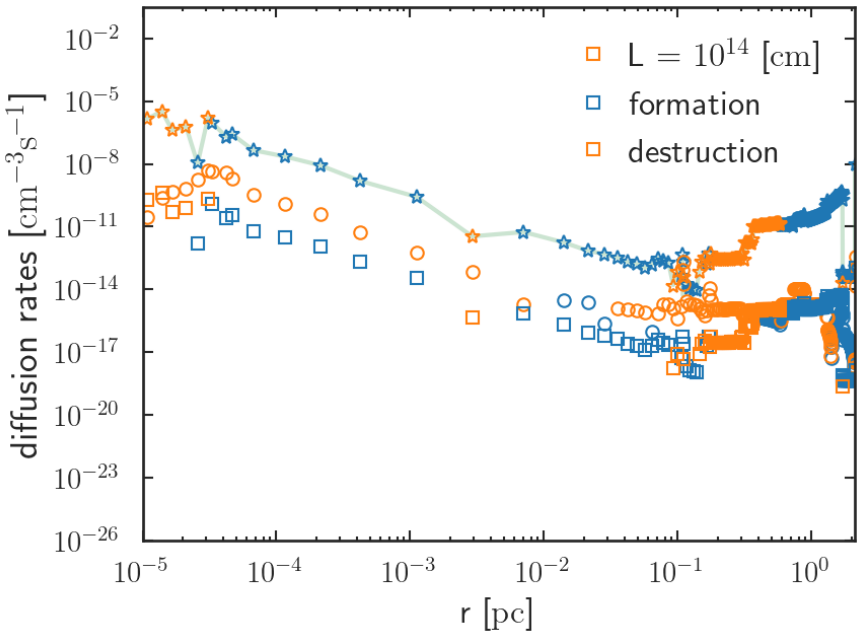


(b) $H_2$

Figure 6.13: Individual contribution to total diffusion rates with $L = 10^{14}$ cm. Labels are similar to Figure [6.9]

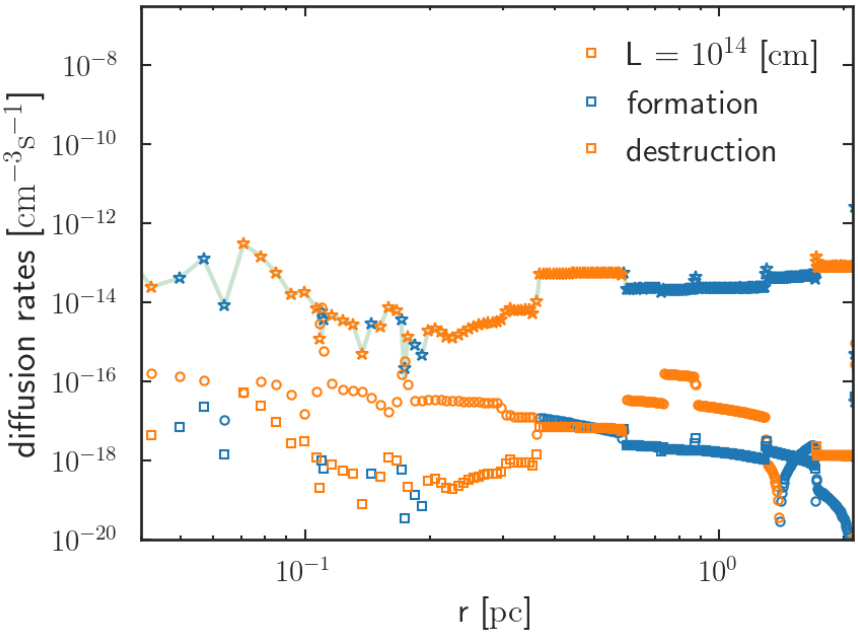


(a) H

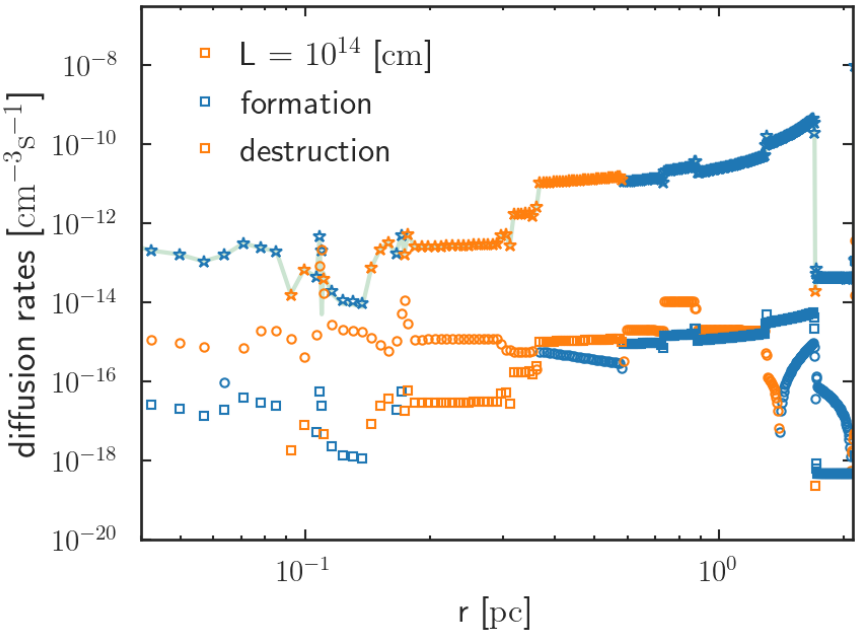


(b) $H_2$

Figure 6.14: Individual contribution to total diffusion rates with $L = 10^{14}$ cm. Labels are similar to Figure [6.9].

figures. [6.15-6.16] that turbulent diffusion exerts a substantial influence (approximately seven to eight orders of magnitude more) in comparison to thermal or molecular diffusion. In the region where $r \geq 0.1$ pc, thermal diffusion rates are significantly higher than molecular diffusion rates by a factor of one to four orders of magnitude (Figure [6.17]). However, turbulence-diffusion dominates in this area, with turbulent diffusion being four orders of magnitude greater than thermal diffusion. The significant difference between the diffusion rates at $L = 10^{16}$ cm and

$L = 10^{17}$ cm is primarily due to the impact of turbulent diffusion. In contrast, no significant changes are observed in the thermal or molecular diffusion rates.

Without turbulence, the maximum diffusion rate for atomic hydrogen is $\sim 10^{-7}\,\mathrm{cm^{-3}\,s^{-1}}$, and for molecular hydrogen $\sim 10^{-8}\,\mathrm{cm^{-3}\,s^{-1}}$. In contrast, with a coherence length of turbulent diffusion $L \sim 10^{17}$ cm, the maximum diffusion rate for atomic and molecular hydrogen is $\sim 10^{-2}\,\mathrm{cm^{-3}\,s^{-1}}$. These are at least six to

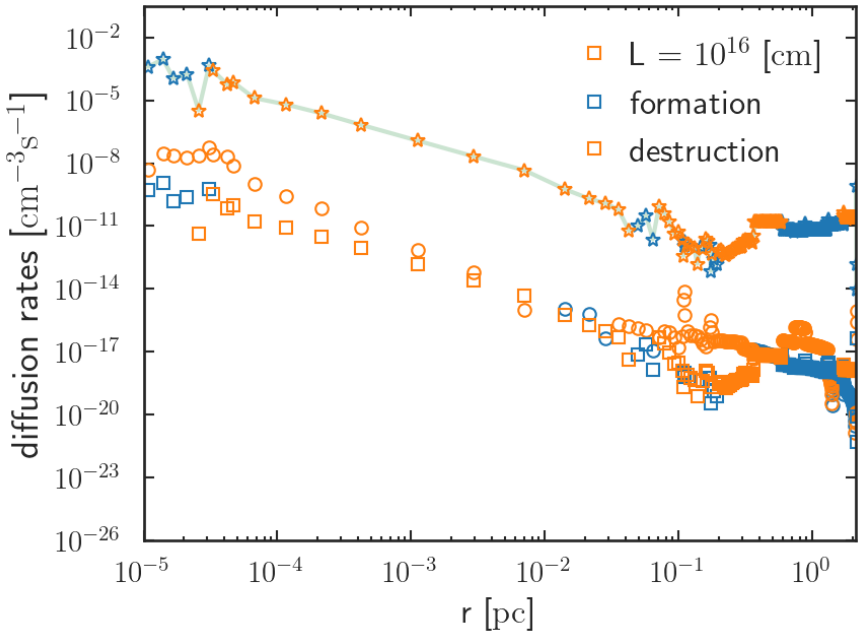


(a) H

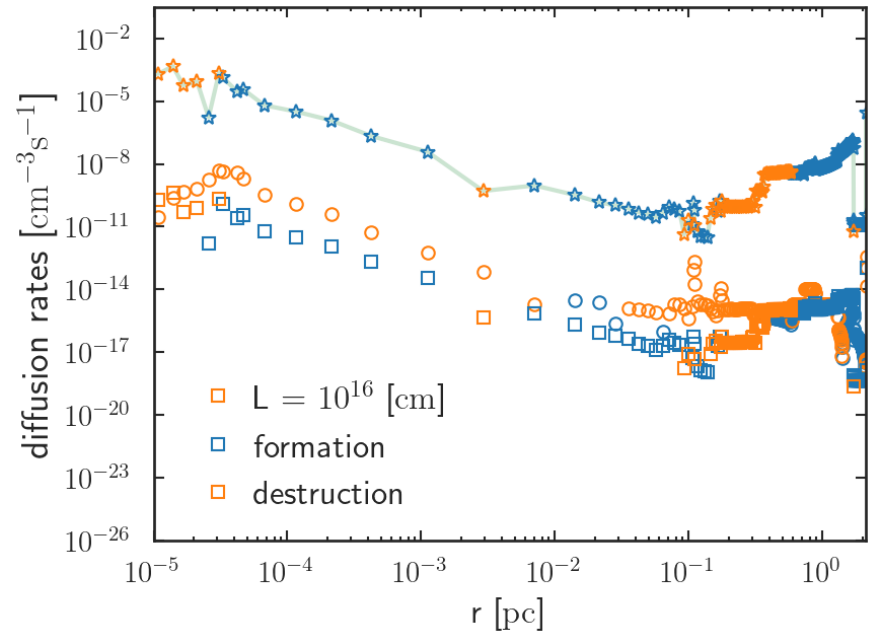


(b) $H_2$

Figure 6.15: Individual contribution to total diffusion rates with $K = 10^{22}$ $\mathrm{cm^2\,s^{-1}}$. Labels are similar to Figure [6.9].

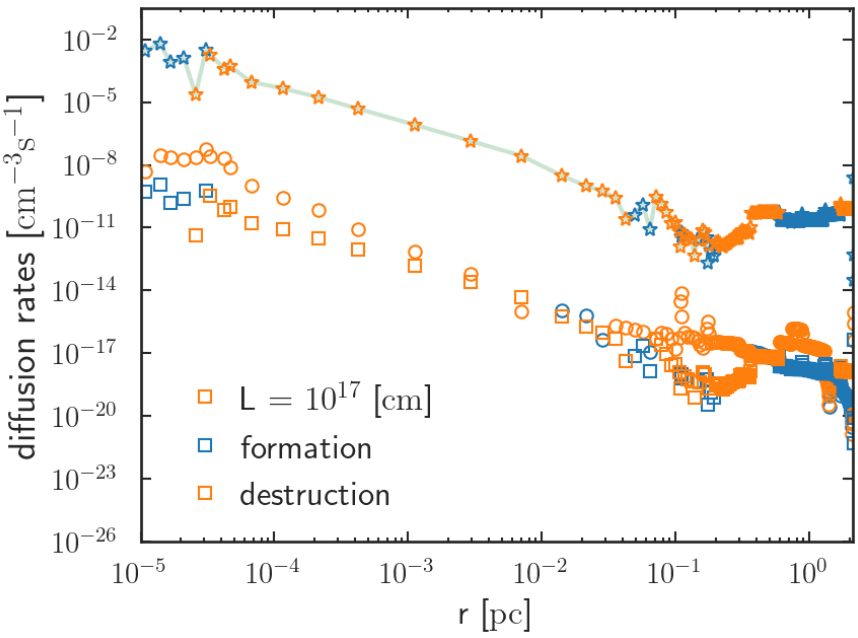


(a) H

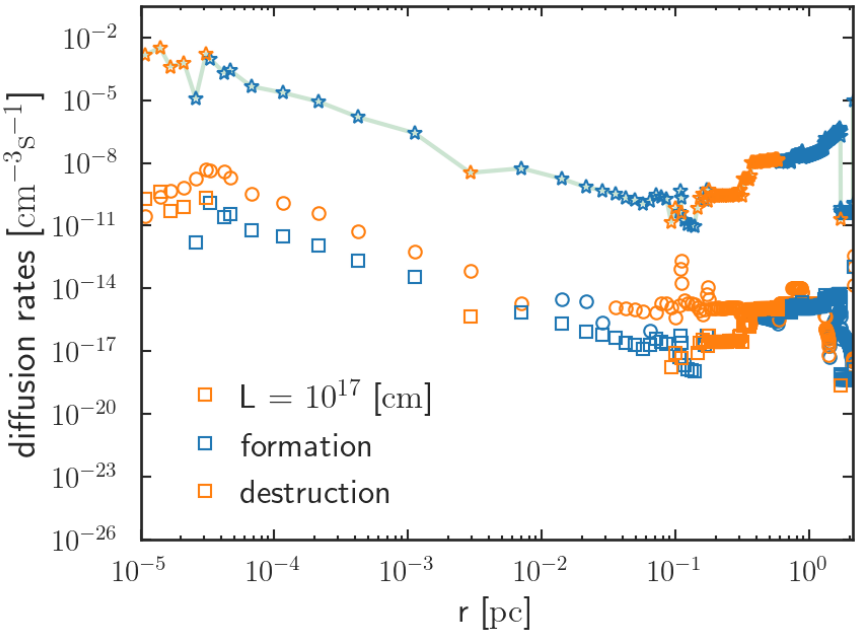


(b) $H_2$

Figure 6.16: Individual contribution to total diffusion rates with $L = 10^{17}$ cm. Labels are similar to Figure [6.9].

seven orders of magnitude higher than the other chemical reactions for H and $H_2$. When the coherence length of turbulent diffusion $L \geq 10^{14}$ cm, the total diffusion rates of most of the species are dominated by turbulent diffusion throughout the cloud. With a coherence length of $10^{11} \leq L \leq 10^{12}$ cm, the total diffusion rates of most of the species are dominated by turbulent diffusion on the surface of the cloud, which can provide insights into the correlation between surface chemistry and its influence on the chemistry of the cloud center. At lower coherence lengths,

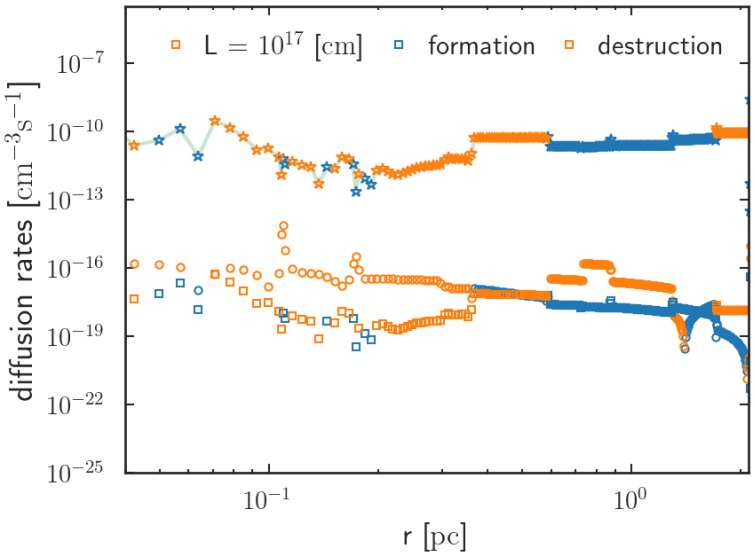


(a) H

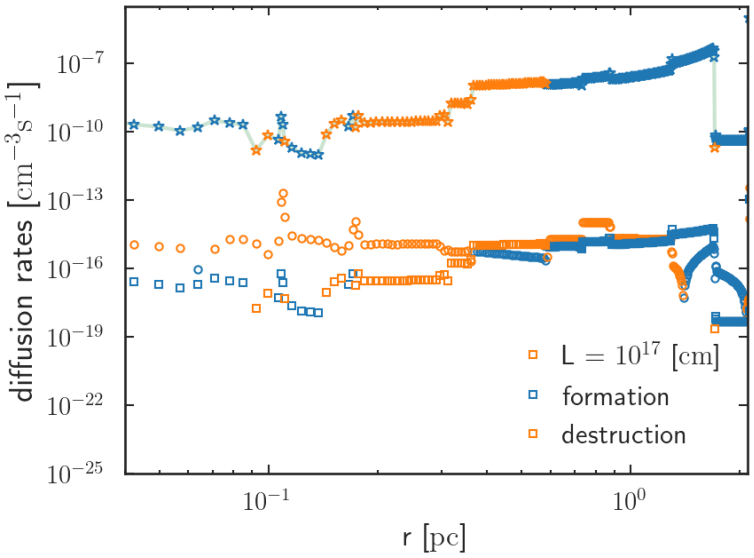


(b) $H_2$

Figure 6.17: Individual contribution to total diffusion rates with $L = 10^{17}$ cm. Labels are similar to Figure [6.9].

the influence of diffusion becomes noteworthy and affects the chemical behavior of species such as H,C, or $C^+$. The diffusion of said species holds significant importance in the chemical processes occurring within the center of the cloud, which can shed light on the impact of surface turbulence on the chemical and physical properties of the center of the cloud. The chemical reactions of different molecules and their response to diffusion are examined in the subsequent sections (§.[6.4]).

## 6.3 Diffusion effects on the physical structure of the cloud

This section looks into the influence of diffusion on the physical characteristics of the cloud, including abundance, column density, and temperature. A detailed analysis of the H−$H_2$ transition and C−$C^+$−CO transition is vital in understanding the chemistry of the cloud. The amount of molecular gas available depends on the location of the photodissociation front or the H−$H_2$ transition region, which facilitates the calculation of the star formation rates.

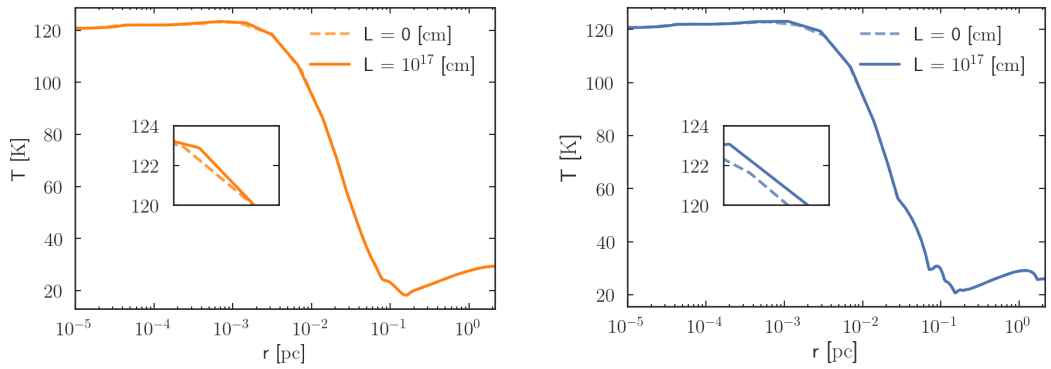


(a) $\xi = 0$ (b) $\xi = 1.5$

Figure 6.18: Changes in the gas temperature with different $\xi$ values. Compared to the constant density profile ($\xi = 0$), the power-law density profile ($\xi = 1.5$) shows an increase in temperature in the mid-depth regions. Model parameters: Case II (table 6.1).

### 6.3.1 Density profile

KOSMA-$\tau$ PDR model can calculate the parameters of the spherical cloud in two different densities, either constant ($\xi = 0$) or varying ($\xi = 1.5$) (see eq.[3.1]). In varying-density scenarios, the cloud is assumed to have a low-density PDR envelope around it, which changes the overall mass of the clump changes as in eq.[3.1], with the difference in the gas and dust temperature profile is shown in Figure [6.18]. The intrinsic change in the density of the clump between constant power-law density profiles will introduce a gradient which in turn increases the temperature. This is clearly evident in the region $r \geq 0.03\,\mathrm{pc}$ of Figure [6.18]. When diffusion is added, there is an increase in the gas temperature at the surface to the mid-depth region compared to the corresponding non-diffusive case (inset of Figure [6.18]). In contrast, dust temperature shows no change in these regions. Consequently, the turbulent, molecular, and thermal diffusion velocities are higher for $\xi = 1.5$ in the region $r \geq 0.2\,\mathrm{pc}$.

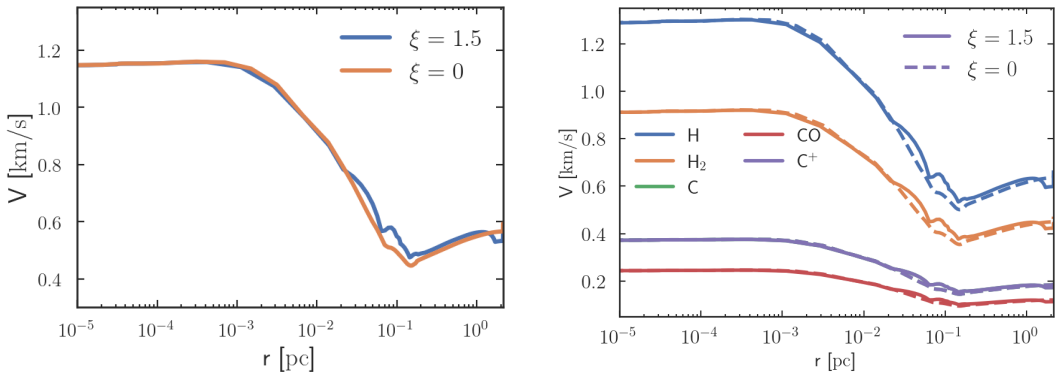


(a) turbulent velocity

(b) molecular velocity

Figure 6.19: Change in diffusion velocities at different density profiles. Model parameters: Case II (table [6.1]) with $L = 10^{17}$ cm and non-uniform temperature.

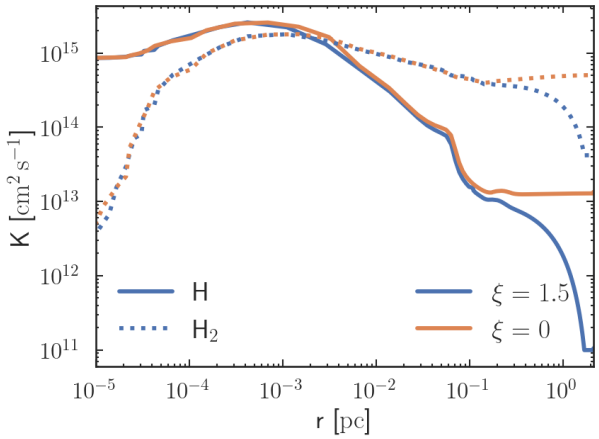


Figure 6.20: Change in the thermal diffusion coefficients as the density profile changes.

In the region $5\times10^{-4} \leq r \leq 0.2$ pc, turbulent and thermal velocities are higher for $\xi = 0$ compared to $\xi = 1.5$. The effect of the density profile on the diffusion coefficients is depicted in Figure [6.20- 6.21]. As shown in Figure [6.21a], the turbulent diffusion coefficient is higher for $\xi = 1.5$ than $\xi = 0$. Thermal diffusion rates of atomic hydrogen with $\xi = 0$ are higher in the region $r \geq 0.08$ pc than $\xi = 1.5$ (Figure [6.23a]). In contrast, turbulent diffusion coefficients with $\xi = 0$ are lower in the region $r \geq 0.08$ pc than $\xi = 1.5$. Figure [6.23] illustrates the variations in the total diffusion rates. The density profile significantly impacts the total diffusion rate of atomic hydrogen in the region where $r \geq 0.1$ pc. In this region, the thermal diffusion rates substantially increase for both atomic and molecular hydrogen. The change in fractional number density due to the density profile considered is shown in Figure [6.22] and Figure.[6.25]. The results of the two scenarios change the number density at the cloud center; however, the influence of diffusion on the H$-$H$_2$ transition and C$-$CO transition are similar. Most of the effects outlined can be attributed to the difference in density at the core of the cloud.

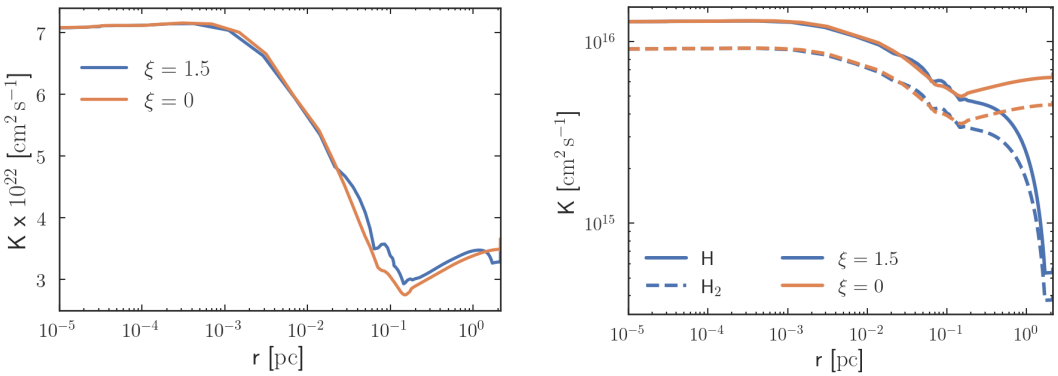


(a) turbulent diffusion coefficient (b) molecular diffusion coefficient

Figure 6.21: Change in diffusion coefficients at different density profiles. Model parameters: Case II (table [6.1]) with $L = 10^{17}$ cm and non-uniform temperature.

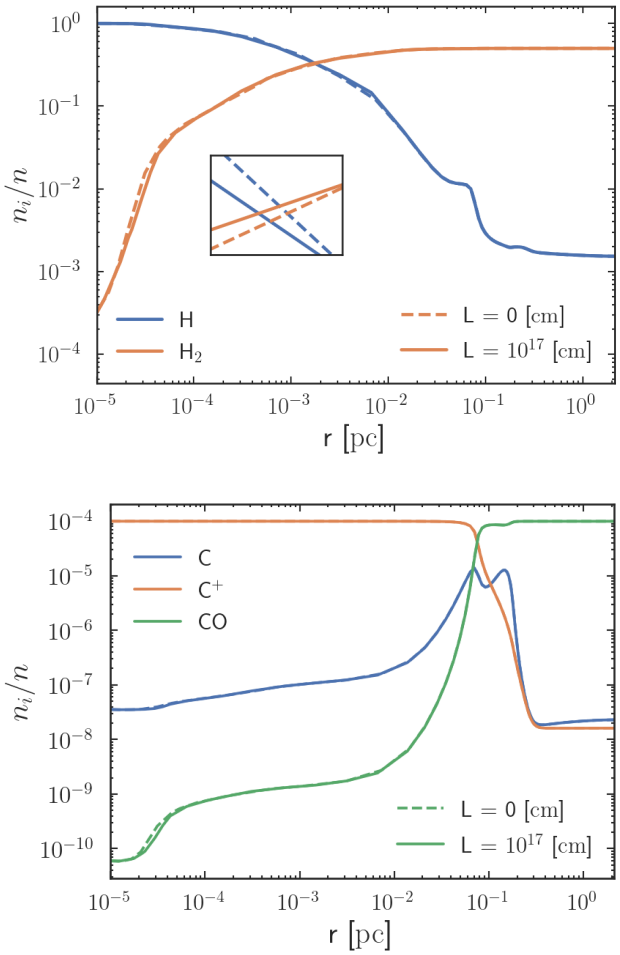


Figure 6.22: Change in abundance due to diffusion. Model parameters: Case II (table [6.1]) with $L = 10^{17}$ cm, $\xi = 0$, and non-uniform temperature.

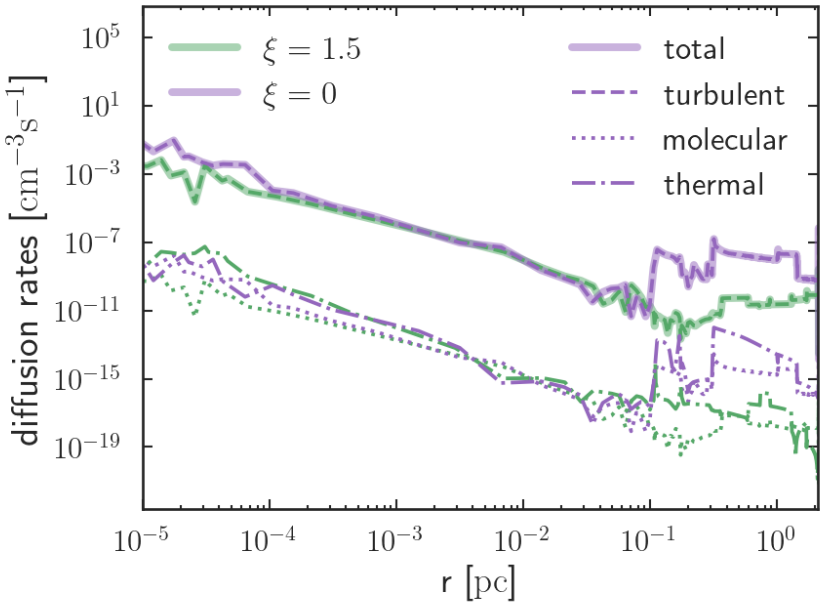


(a) H

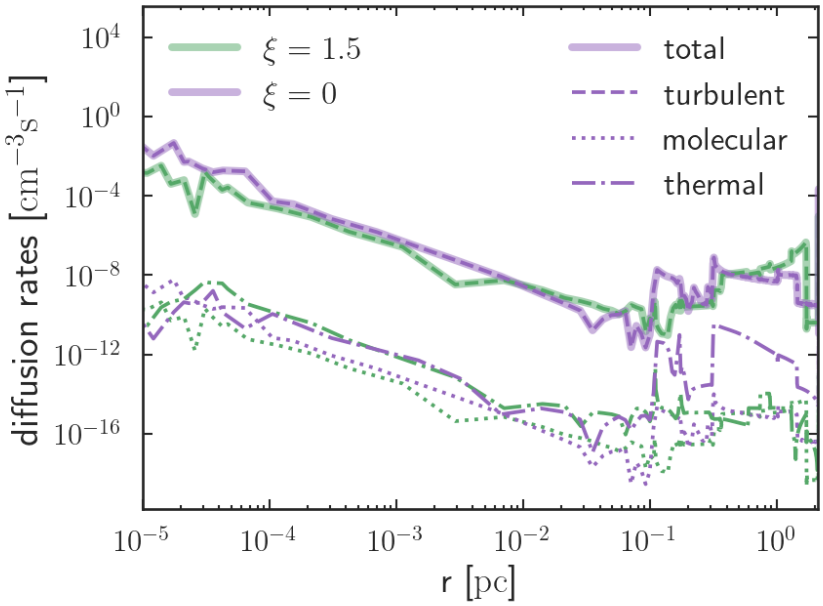


(b) $H_2$

Figure 6.23: Change in the total diffusion rates at different density profiles. Model parameters: Case II (table [6.1]) with $L = 10^{17}$ cm and non-uniform temperature.

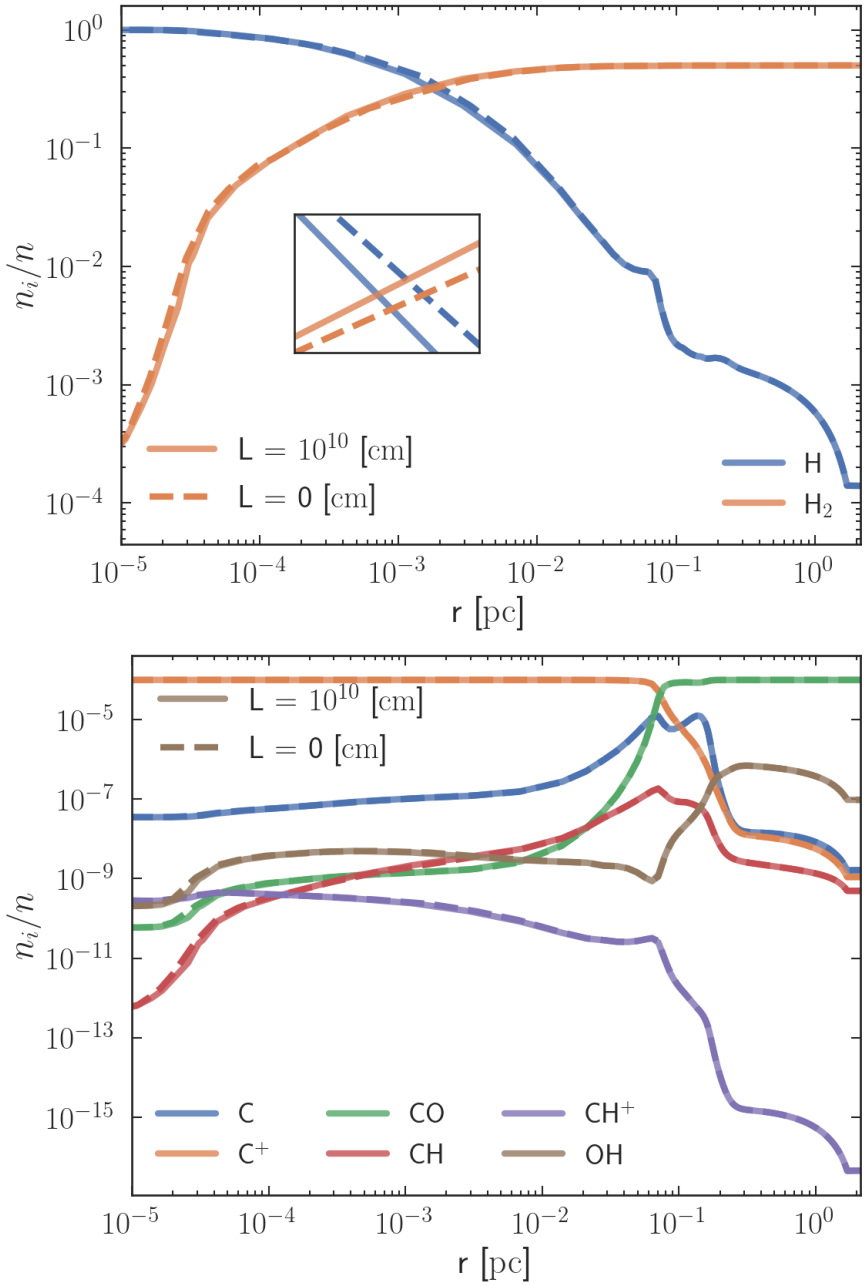


Figure 6.24: Abundance of selected species with $L = 10^{10}$ cm as a function of distance from the cloud surface (pc). H$-$H$_2$ transition shifts towards the surface of the cloud. Model parameters: Case II (table [6.1]) with $\xi = 1.5$.

### 6.3.2 Abundance and column densities

The molecular and turbulent diffusion rate of a species depends on the density gradient. Diffusion increases the surface temperature of the cloud and shifts the atomic-to-molecular region to the surface (Figure [6.25a]). Compared to the without diffusion case, this results in a warmer H$-$H$_2$ transition region. On the surface of the cloud ($r \leq 10^{-4}$ pc), the gas temperature is higher, resulting in higher thermal diffusion rates (compared to the molecular and turbulent counterparts) at

lower coherence lengths (Figure [6.6]). At higher coherence lengths, turbulent diffusion rates (destruction) are much higher than molecular and thermal diffusion rates, resulting in larger total diffusion rates (Figure [6.16]). These larger diffusion rates lead to the destruction of H in these regions resulting in a decrease in the abundance of $H_2$ at the surface (Figure [6.24a] and Figure [6.25a]). When atomic hydrogen has higher diffusion coefficients, its diffusion rates are higher at the surface, causing destruction through diffusion instead of grain catalysis. In these regions, grain catalysis is of the order of $10^{-9}\,\mathrm{cm^{-3}s^{-1}}$. In contrast to

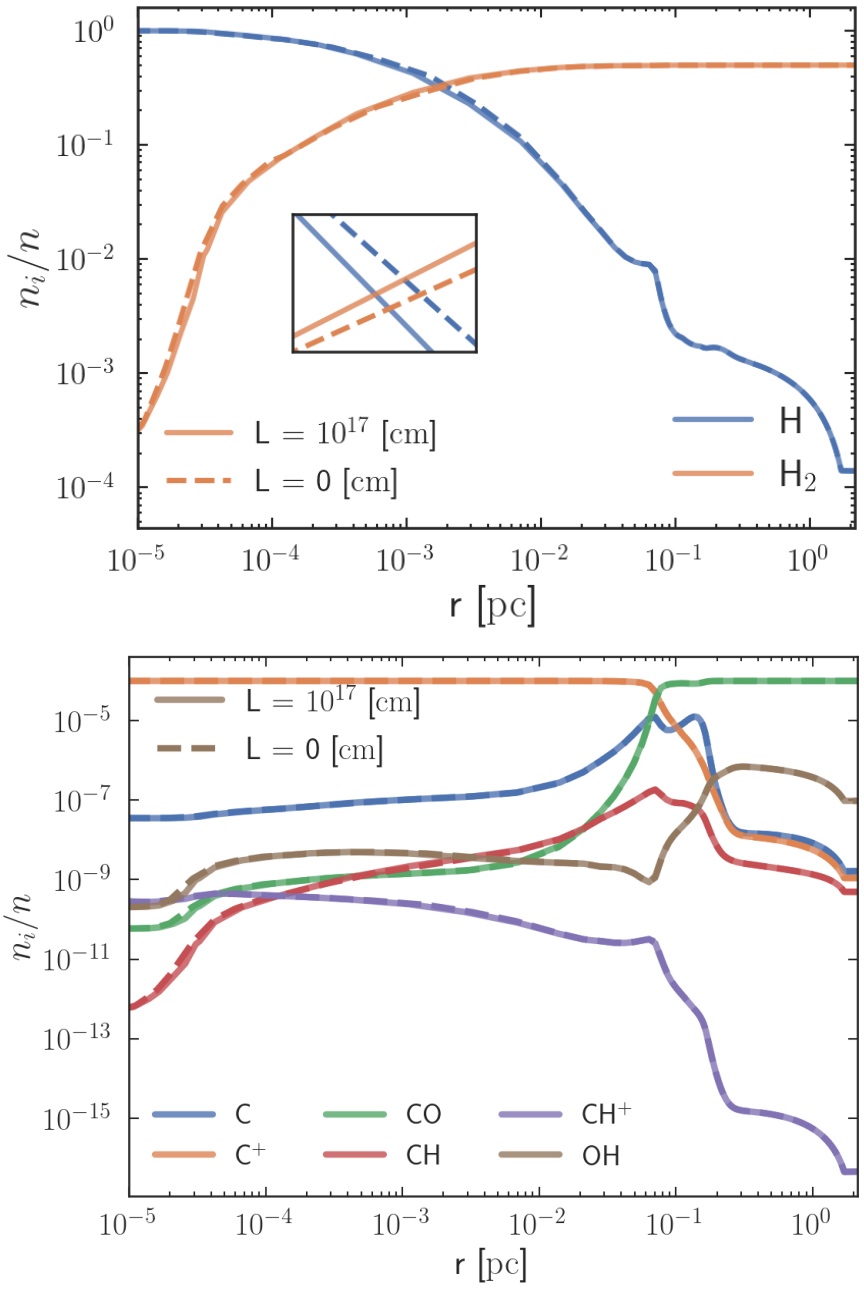


Figure 6.25: Abundance of selected species with $L = 10^{17}\,\mathrm{cm}$. H$-$H$_2$ transition shifts towards the surface of the cloud. Model parameters: same as Figure [6.24].

diffusion rates which are $\leq 10^{-2}\,\mathrm{cm^{-3}s^{-1}}$ (for $L = 10^{17}\,\mathrm{cm}$) which must reduce the abundance of the $H_2$ drastically. However, the diffusion rates of $H_2$ (formation reaction due to high turbulence) is less than or equal to $10^{-2}\,\mathrm{cm^{-3}s^{-1}}$, which replenishes the missing $H_2$, resulting in a significant reduction in abundance from no diffusion, but not drastically. The H is destroyed via diffusion, and in similar scales $H_2$ is formed via diffusion. The other chemical reactions which facilitate the formation and destruction of H and $H_2$ indicate an increase/decrease in their contribution to the formation/destruction of H and $H_2$ (§[6.4]). This change in the chemical network of the PDR results in an equilibrium solution (Figure [6.25]).

The timescale to reach an equilibrium solution for gas-phase chemistry is $\sim 10^6$ years. However, as illustrated in §[7.5], the mixing time scale is inversely proportional to the diffusion rates. For example, the mixing is faster (lower timescale) with higher diffusion rates, and the chemistry will take longer to achieve equilibrium than the diffusion. Consequently, the resultant abundance will not show a significant difference from the scenario without diffusion. At lower diffusion rates, the diffusion mixing takes longer than the chemical timescale, resulting in a minor impact of diffusion in the abundance profiles. The diffusion timescale is species and position specific, and the impact would vary across the cloud.

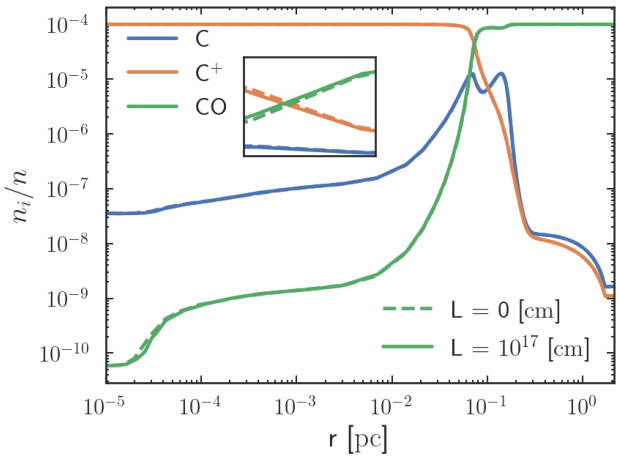


Figure 6.26: $C^+ - C - CO$ transition. Model parameters: Case II (table [6.1]) with $\xi = 1.5$.

The expansion of the molecular region results in a narrower atomic region than the case without diffusion, which changes the abundance profile of many other species (Figure [6.24]- 6.25] and Figure [B.2]). However, the change in the abundance between different diffusion coefficients is insignificant. The $C^+ - C - CO$ transition is shifted towards the surface of the cloud (Figure [6.26]). In the region $0.03 - 0.3\,\mathrm{pc}$ (in the inset of the Figure [6.26]), the abundance of $C^+$ slightly decrease, and CO shows an increase in the abundance compared to the without diffusion scenario. CO and its isotopologue (Figure [B.1]) show a decrease in the abundance at the surface of the cloud ($r \leq 10^{-4}\,\mathrm{pc}$). The abundance of $C^+$ and $S^+$ are not influenced by diffusion in the region $r \leq 0.01\,\mathrm{pc}$.

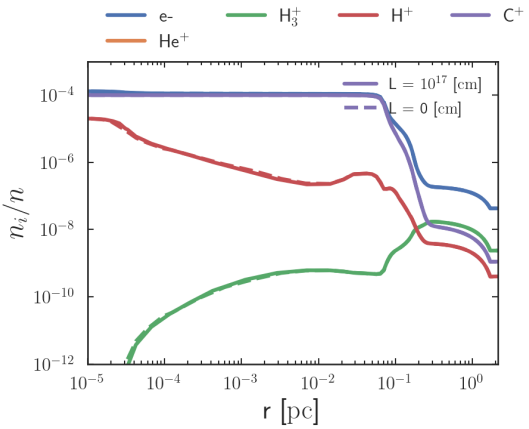


Figure 6.27: Abundance of electrons and ions. Model parameters: Case II (table [6.1]) with $\xi = 1.5$.

Many previous studies (e.g., Xie et al. 1995) found that electron abundance increases in the interior of the cloud due to diffusion. However, this study found that the electron abundance shows a decrease with diffusion in the case with $\zeta_{CR} = 5 \times 10^{-17} s^{-1}$ per H and no change in the case with $\zeta_{CR} = 2 \times 10^{-16} s^{-1}$ per H. On the surface, FUV radiation is the primary source of ion production, while charge transfer reactions play an important role in mid-depth regions. In the interior of the cloud, cosmic ray ionization plays a significant role in ion production. The recombination will depend on the availability of free electrons in the cloud. On the surface, ion production and electron recombination are consistent and linked to the radiation field. If free electrons are available in the UV-shielded interiors of the cloud, the destruction of electrons will be faster than the formation, resulting in a reduced abundance of ions and electrons.

Diffusion can increase the abundance of ions and electrons in the interior of the cloud (Xie et al. 1995) by transporting them from the outer layers. When diffusion is added, the diffusion of electrons is the biggest (about four to nine orders of magnitude higher than the next highest destruction reaction rate) destruction reaction of electrons. As a result, the electron recombination of many ions, such as $C^+, H^+, CH^+, CH_3{}^+$, and $S^+$ are reduced. In addition, the formation of molecules like O, C, and S are reduced in the cloud (table [6.3]). Also, the destruction of ions such as $O^+$, $OH^+$, $CO^+$, and $CH^+$ are reduced in the cloud as illustrated in the table [6.4].

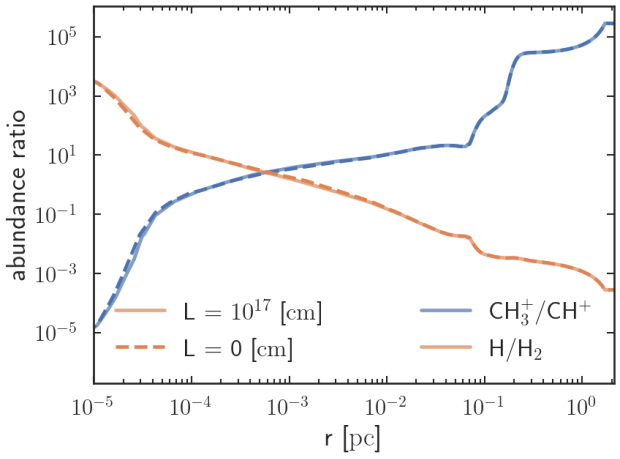


Figure 6.28: Abundance ratio of $CH_3{}^+/CH^+$ with different diffusion coefficients. Model parameters: Case II (table [6.1]) with $\xi = 1.5$.

When diffusion is added, the abundance of $HCO^+$, $HC^{18}O^+$, $H^{13}CO^+$, and $H^{13}C^{18}O^+$ decrease in the region $10^{-5} \leq r \leq 10^{-4}$ pc. In the region $7 \times 10^{-4} -$

0.007 pc, however, the abundance of $^{13}CH, CH_2, CS$, and SO slightly increase. When diffusion is introduced, the abundance of most other species exhibits minimal or no fluctuation. This is because the chemical reaction by which the model achieved equilibrium differs from the scenario without diffusion. The equilibrium solution is obtained by lowering the other formation/destruction reactions. A comprehensive analysis of chemical reactions is presented in §.[6.4].

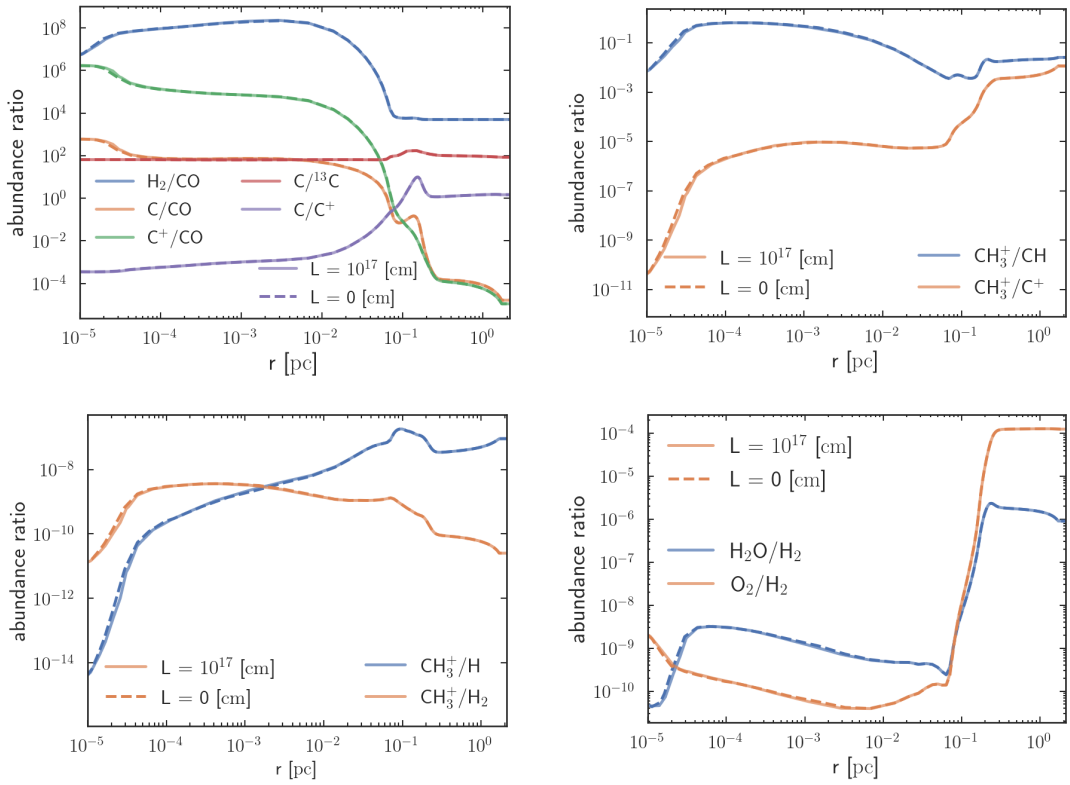


Figure 6.29: Abundance ratio of selected species with different diffusion coefficients. Model parameters: Case II (table [6.1]) with $\xi = 1.5$.

The abundance ratios of different molecules are shown in Figures [6.28-6.29]. With different coherence lengths of diffusion, the abundance profiles of species do not change drastically in steady-state, by extension, the abundance ratios. On the surface of the cloud, diffusion causes a slight increase in the abundance ratios of C/CO, $C^+$/CO, $O_2/H_2$, and $H/H_2$. However, the abundance ratio of $C/C^+$ slightly decreases due to a decrease in the abundance of C. The abundance ratios of $H_2O/H_2$ and $H_2/CO$ show a decrease on the surface for the diffusion scenario. $H_2/CO$ abundance ratio slightly increases in the region $10^{-4} \leq r \leq 0.003$ pc due to the availability of $H_2$.

Similar to the abundance profiles, the resultant change in the column densities due to diffusion is minor (Figures [6.30]). The column densities of electrons show a slight increase in the region $r \leq 0.003$ *pc* whereas $H_3^+$ and $He^+$ show no changes. Ions such as $H_2^+, H_2O^+, H_3O^+$, and $H^{13}CO^+$ show a slight decrease in

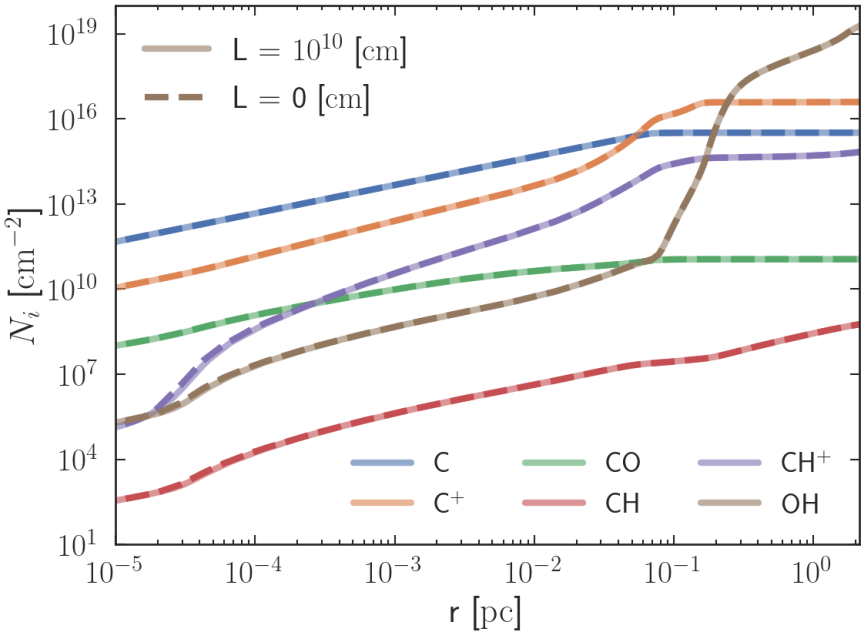


(a) $L = 10^{10}$ cm

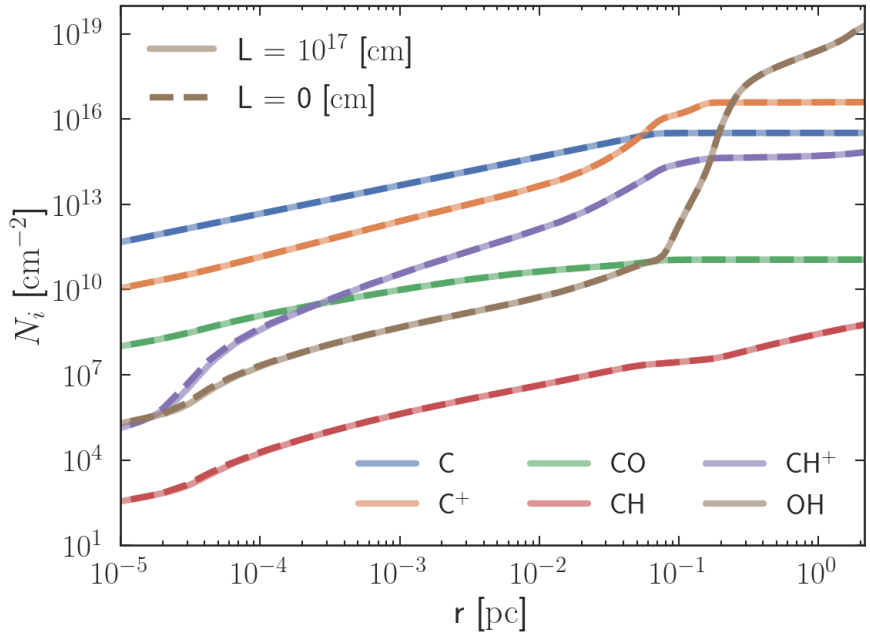


(b) $L = 10^{17}$ cm

Figure 6.30: Column densities of selected species with $L = 10^{10}$ cm and $L = 10^{17}$ cm as a function of distance from the cloud surface (pc). Model parameters: Case II (table [3.1]).

the column densities similar to the corresponding molecules. The column density ratios $H_2/CO$ decrease at the surface of the cloud (Figure [6.31]). The column density ratios $O_2/H_2$, $H_2O/H_2$, $CH_3^+/C^+$, ad $CH_3^+/H_2$ show decrease on the surface.

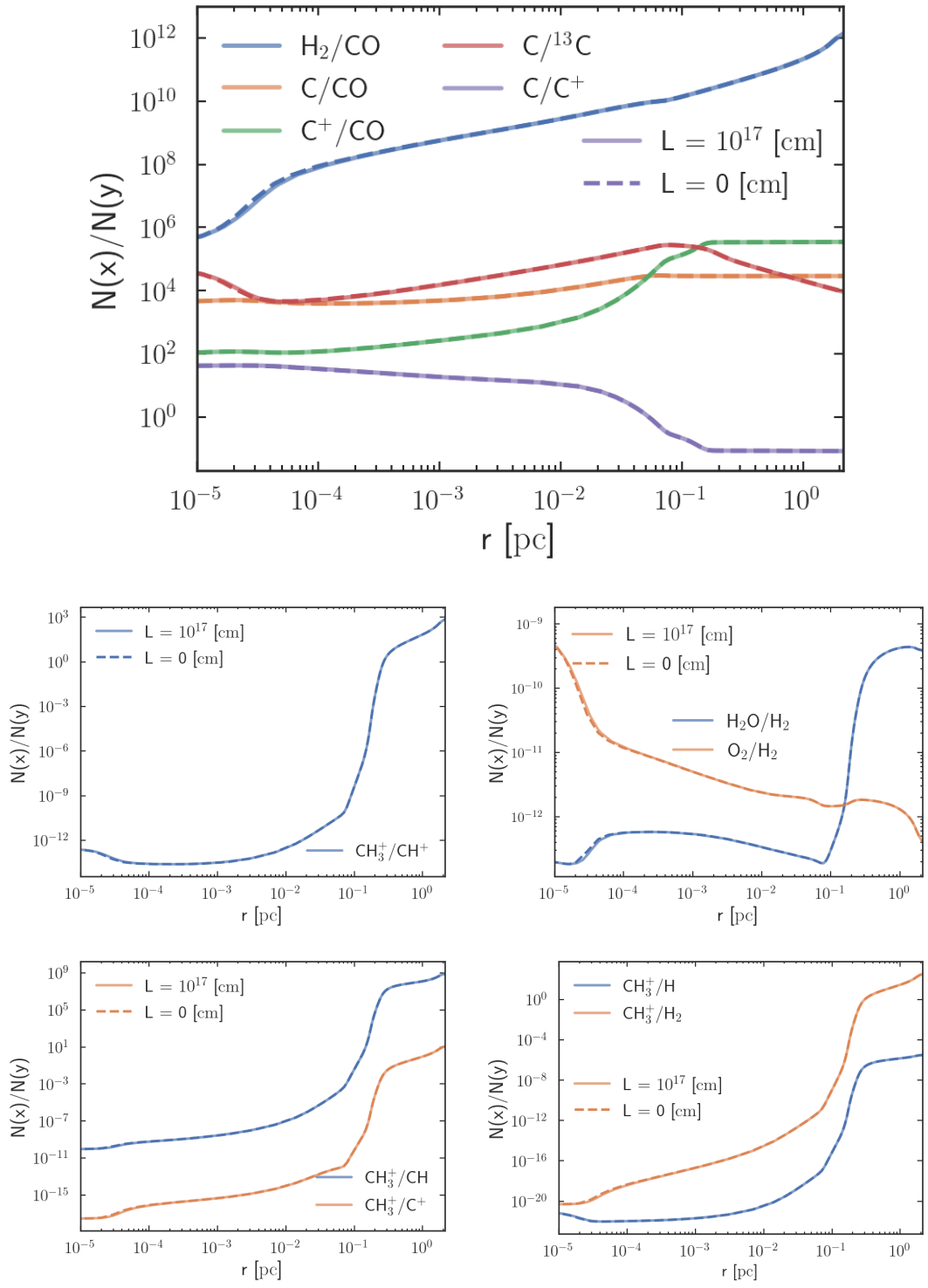


Figure 6.31: Column density ratio of selected species with different diffusion coefficients. Model parameters: Case II (table [6.1]) with $\xi = 1.5$.

### 6.3.3 Temperature

To obtain the temperature, the KOSMA-$\tau$ PDR model tries to solve the heating and cooling rate equations at every shell. Hence, the changes in the local conditions due to diffusion are reflected in the heating and cooling rates and the resultant gas temperatures. With diffusion, the gas temperature only slightly differs from the cases without diffusion (Figure [6.5]), irrespective of the diffusion coefficient. However, when diffusion is added, the maximum temperature increases by at least 0.2 %. Different diffusion coefficients are tested to understand the influence of diffusion on the temperature. Figure [6.5] displays the gas temperature at different $L$ values, from no diffusion ($L = 0\,\mathrm{cm}$) to the highest diffusion ($L = 10^{17}\,\mathrm{cm}$). Although there is a slight increase in surface temperature, the different $L$ values did not significantly affect the gas temperature. Nonetheless, the diffusion effects on the heating and cooling rates are clearly visible (Figure [6.32-6.33]).

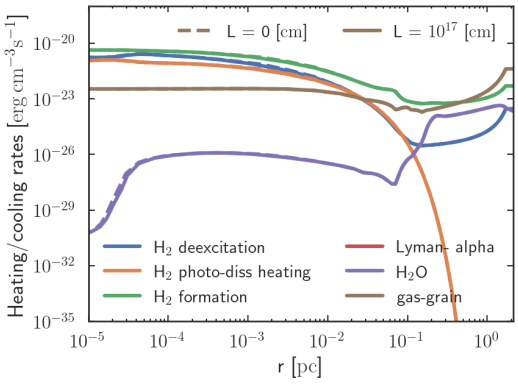


(a)

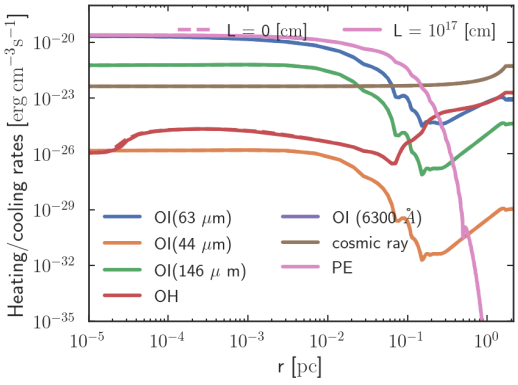


(b)

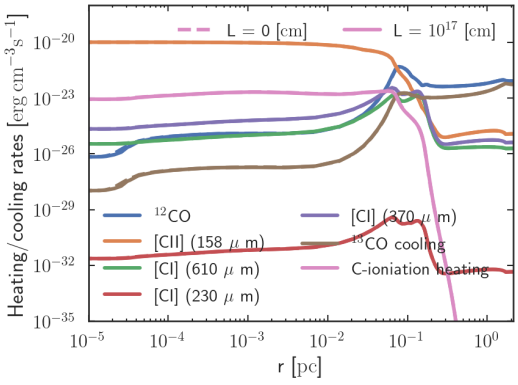


(c)

Figure 6.32: Heating and cooling rates with $L = 10^{17}\,\mathrm{cm}$ (straight) and without diffusion (dashes). Model parameters: Case II (table 6.1) with non-uniform temperature and $\xi = 1.5$.

The heating and cooling rates through $H_2$ photodissociation, $H_2$ formation, and $H_2$ deexcitation reactions show a decrease with diffusion (Figure [6.33]). $H_2$ photodissociation heating shows a slight increase at the surface ($10^{-5} \leq r \leq 10^{-4}\,\mathrm{pc}$) (Figure [6.33]). In contrast, OH, $^{12}$CO and $^{13}$CO show a slight decrease in the rates at the surface ($10^{-5} \leq r \leq 10^{-4}\,\mathrm{pc}$) whereas, [CII](158$\mu$m) cooling line indicates no change in the cooling rate.

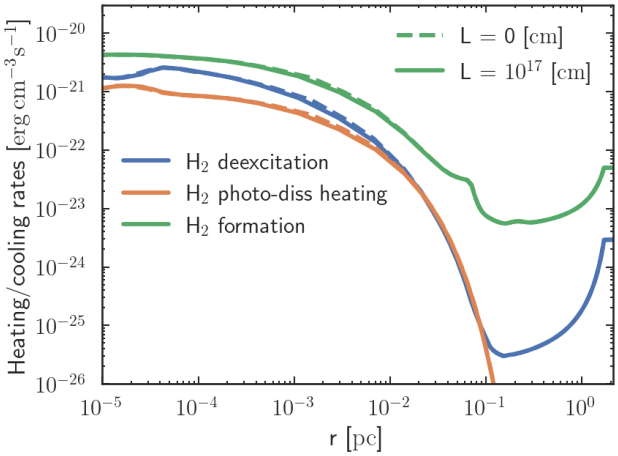


Figure 6.33: $H_2$ formation and destruction heating with $L = 10^{17}$ cm(straight) and without diffusion (dashes). Heating rates show an increase in the rates. Model parameters: Case II (table 6.1) with non-uniform temperature and $\xi = 1.5$.

Changes in the abundance of atomic oxygen due to diffusion are minor. As a result, [O I] $^3P_1 \rightarrow {}^3P_2$ and [O II] $^3P_0 \rightarrow {}^3P_1$ cooling rates are not significantly influenced by diffusion (the effect of [O I] $^3P_0 \rightarrow {}^3P_2$ on the temperature is negligible). Heating due to gas grain collisions is also unaffected. A dynamic temperature calculation always finds a stable solution to the temperature (Röllig & Ossenkopf-Okada 2022). However, it is important to note that this approach could mask the impact of diffusion on temperature. To investigate the correlation between temperature and diffusion, this study examines a case where the gas temperatures remain constant at 30, 50, 70, and 120 K (Figure [6.34]).

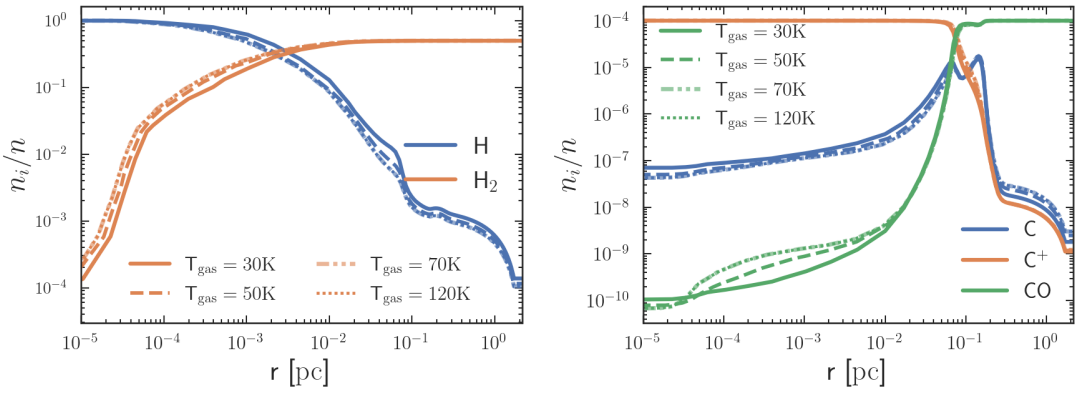


(a) H−$H_2$ (b) C/$C^+$/CO

Figure 6.34: H−$H_2$ transition and C/$C^+$/CO transition at constant temperature. Model parameters: Case II(table [6.1] with uniform gas temperature, $\xi = 1.5$ and $L = 10^{17}$ cm. Dust temperature $T_{\rm dust} = 20K$.

In a constant temperature scenario, the $L = 10^{17}$ cm case shows a significant difference in the abundance of H and $H_2$. As the gas temperature increases from 30 K to 120 K, the abundance of $H_2$ increases on the surface. Deeper in the cloud, the abundance of H decreases as the temperature increases. As a result, the molecular region shifts outwards as the temperature increases (in a dynamic temperature scenario, $H_2$ shifts to the intermediate temperatures). As

the temperature rises, the amount of CO on the surface increases significantly while the amount of C decreases. The abundance of $C^+$ remains unchanged until the $C^+-CO$ transition, after which it increases with higher temperatures.

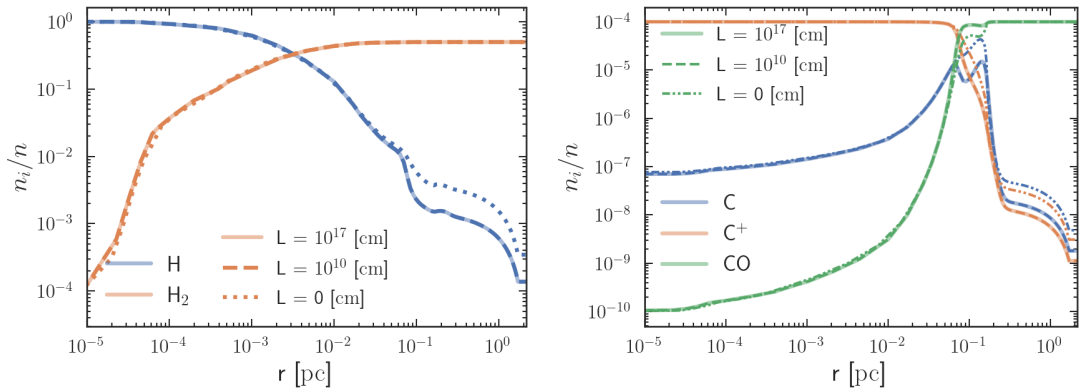


(a) $H-H_2$ (b) $C/C^+/CO$

Figure 6.35: $H-H_2$ transition and $C/C^+/CO$ transition at $T_{gas} = 30\,K$. Model parameters: Case II(table [6.1] with uniform gas temperature, $\xi = 1.5$ and $L = 10^{17}\,cm$. Dust temperature $T_{dust} = 20K$.

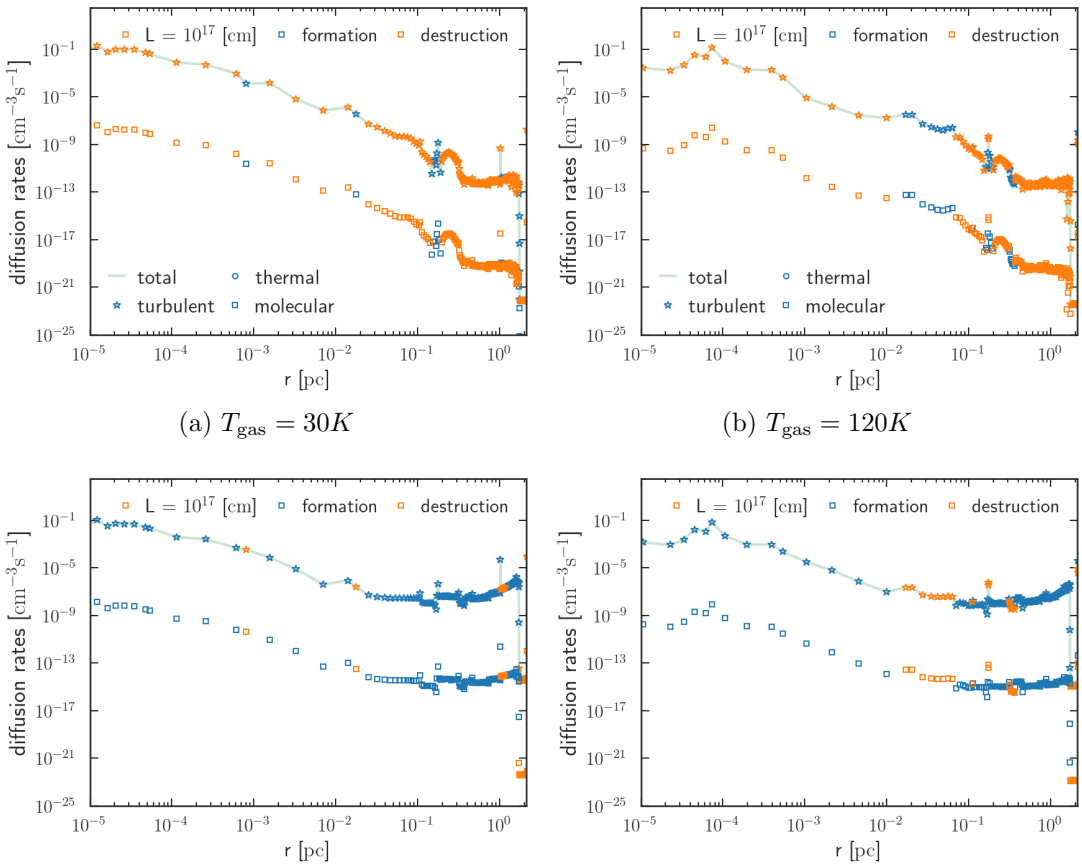


(a) $T_{gas} = 30K$ (b) $T_{gas} = 120K$

(c) $T_{gas} = 30K$ (d) $T_{gas} = 120K$

Figure 6.36: diffusion rates of atomic hydrogen at different temperatures. Model parameters: Case II(table [6.1] with uniform gas temperature, $\xi = 1.5$ and maximum diffusion coefficient $L = 10^{17}\,cm$. Dust temperature $T_{dust} = 20K$.

Figure [6.35] shows the $H-H_2$ and $C^+-C-CO$ transition with a uniform temperature of 30 K. Neither the heating-cooling rate nor the abundance profiles show any changes when comparing different coherence lengths at the same temperature. However, diffusion decreases the atomic hydrogen abundance in the interior of the cloud at lower temperatures. Similarly, the abundance of the C and $C^+$ significantly decreases when diffusion is added.

In a constant temperature scenario, the turbulent and molecular velocities for a species are constant throughout the cloud and, by extension, the diffusion coefficients. Furthermore, the thermal diffusion contribution to the total diffusion rate is zero due to the lack of temperature gradient. Hence, a constant turbulent and molecular diffusion scenario is created. In addition, unlike a dynamic temperature scenario, diffusion of atomic hydrogen is a destruction reaction in the interior of the cloud, resulting in a reduced abundance (Figure [6.16]). To test the different diffusion coefficients, turbulence length scales are varied. The diffusion rates modify as the length scale changes; however, the resultant abundance does not. The changes in the diffusion rates for atomic (Figure [6.36(a-b)]) and molecular (Figure [6.36(c-d)]) hydrogen with different temperatures are shown.

Evaluating the diffusion effects in an isothermal scenario might result in overestimating diffusion effects. Since the temperature of the molecular cloud varies over the depth, it is necessary (and advised) to consider a dynamical temperature calculation to understand the local conditions accurately. The changes in the temperature profile due to diffusion are minor in a steady-state scenario. However, the changes in the chemistry, together with diffusion in the isothermal scenario, are significant.

## 6.4 Diffusion effects on chemistry

Chemical reaction rates alter in response to variations in the diffusion coefficient. As already mentioned, the entire chemical network has 812 reactions and 61 different species (table [3.2]), the analysis of which is impossible to fit into the thesis. Hence, five substantial contributors to the formation/destruction of the species are chosen to be analyzed. The chemistry is solved at equilibrium, meaning the total number of particles formed and destroyed stays the same. The chemical network is analyzed using chemchkanalyser.

The additional formation/destruction reaction pathway created by adding diffusion into the chemistry of the KOSMA-$\tau$ PDR model reduced or wholly removed some reactions from the top five contributors compared to $L = 0\,\mathrm{cm}$ scenario. Table [6.2] shows the reactions which become top contributors (other than diffusion) when diffusion is added to the chemistry. Table [6.4] shows the destruction reactions, which decreased significantly (compared to the scenario without diffusion) such that it no longer contributes considerably to the destruction of species with diffusion scenarios. Table [6.3] shows the formation reactions, which decreased significantly (relative to the scenario without diffusion) such that it no longer notably contributes to the formation of species with diffusion scenarios. Some of the reactions, for example, formation reactions of $S^+, S, HS$, and CS reduced only at higher turbulent diffusion scenarios ($L \geq 10^{17}\mathrm{cm}$). In contrast, the formation reaction of O and He are reduced at all coherence length scenarios. From table [6.3] and table [6.4], it is clear that species involving sulfur such as $CS^+, S, SO$, and $S^+$ have reduced rates with diffusion.

The subsequent subsections demonstrate the impacts of different turbulent diffusion length scales, namely lower ($L = 10^{10}\,\mathrm{cm}$) and upper ($L = 10^{17}\,\mathrm{cm}$) bounds, in comparison to the scenario where diffusion is absent. The effect of other coherence lengths is shown if they differ from what has already been covered. In addition, atomic and molecular hydrogen, $C, C^+, CO$, $CH, CH^+$, and OH are chosen to examine the impact of diffusion on the chemistry.

| Formation/destruction reactions | | |
|---|---|---|
| species | reaction | note |
| H | $H_2 + CR_{phot} \longrightarrow H + H$ | formation |
| C | $C + O^{18}O \longrightarrow CO + {}^{18}O$ | destruction |
| $CH^+$ | $CH^+ + H \longrightarrow CO + C^+ + H_2$ | destruction |

Table 6.2: Missing reactions other than diffusion of species. Unlike scenarios with diffusion, these formation or destruction reactions are not among the top five contributors for $L = 0\,\mathrm{cm}$.

| Formation reactions | | |
|---|---|---|
| species | reaction | missing from |
| He | $He^+ + C^{18}O \rightarrow {}^{18}O + C^+ + He$ | $L = 10^{14} - 10^{17}$[cm] |
| O | $He^+ + {}^{13}CO \rightarrow O + {}^{13}C^+ + He$ | $L = 10^{10} - 10^{17}$[cm] |
| O | $H_2O^+ + e^- \rightarrow O + H_2$ | $L = 10^{14} - 10^{17}$[cm] |
| O | $CO^+ + e^- \rightarrow O + C$ | $L = 10^{14} - 10^{17}$[cm] |
| C | $CS + \gamma_{FUV} \longrightarrow S + C$ | $L = 10^{17}$[cm] |
| C | $CH_2{}^+ + e^- \longrightarrow C + H_2$ | $L = 10^{17}$[cm] |
| OH | $He^+ + H_2O \longrightarrow OH + He + H^+$ | $L = 10^{17}$[cm] |
| CO | $C^+ + SO \longrightarrow S^+ + CO$ | $L = 10^{14} - 10^{17}$[cm] |
| CO | $C + OH \longrightarrow CO + H$ | $L = 10^{17}$[cm] |
| $S^+$ | $He^+ + CS \longrightarrow S^+ + C + He$ | $L = 10^{17}$[cm] |
| S | $H_2S^+ + e^- \longrightarrow S + H + H$ | $L = 10^{17}$[cm] |
| HS | ${}^{18}OH + CS \longrightarrow C^{18}O + HS$ | $L = 10^{17}$[cm] |
| CS | $C + OCS \longrightarrow CO + CS$ | $L = 10^{17}$[cm] |
| $^{18}O$ | $C^{18}O^+ + e^- \longrightarrow {}^{18}O + C$ | $L = 10^{14} - 10^{17}$[cm] |
| $^{18}O$ | $H_2{}^{18}O^+ + e^- \longrightarrow {}^{18}O + H_2$ | $L = 10^{17}$[cm] |
| $H^{13}CO^+$ | $H_2{}^+ + {}^{13}CO \longrightarrow H^{13}CO^+ + H$ | $L = 10^{17}$[cm] |

Table 6.3: Compared to the scenario without-diffusion, these formation reactions are no longer in the top five contributors.

| Destruction reactions | | |
|---|---|---|
| species | reaction | missing from |
| $e^-$ | $OH^+ + e^- \longrightarrow O + H$ | $L = 10^{14} - 10^{17}$[cm] |
| $e^-$ | $H_2O^+ + e^- \longrightarrow O + H$ | $L = 10^{14} - 10^{17}$[cm] |
| $O^+$ | $O^+ + H_2^{18}O \longrightarrow H_2^{18}O^+ + O$ | $L = 10^{10} - 10^{17}$[cm] |
| C | $C + OH^+ \longrightarrow O + CH^+$ | $L = 10^{10} - 10^{12}$[cm] |
| $^{13}C^+$ | $^{13}C^+ + SO \longrightarrow S + {}^{13}CO^+$ | $L = 10^{17}$[cm] |
| $^{13}C$ | $^{13}C + OH^+ \longrightarrow O + {}^{13}CH^+$ | $L = 10^{10} - 10^{17}$[cm] |
| $OH^+$ | $OH^+ + OH \longrightarrow H_2O^+ + O$ | $L = 10^{10} - 10^{17}$[cm] |
| $OH^+$ | $OH^+ + S \longrightarrow S^+ + OH$ | $L = 10^{10} - 10^{14}$[cm] |
| $CO^+$ | $CO^+ + S \longrightarrow S^+ + CO$ | $L = 10^{12} - 10^{17}$[cm] |
| CO | $OH^+ + CO \longrightarrow HCO^+ + O$ | $L = 10^{10} - 10^{14}$[cm] |
| $CH^+$ | $CH^+ + S \longrightarrow CS^+ + H$ | $L = 10^{10} - 10^{17}$[cm] |
| CH | $CH + S \longrightarrow CS + H$ | $L = 10^{14} - 10^{17}$[cm] |
| $^{13}CO^+$ | $^{13}CO^+ + S \longrightarrow S^+ + {}^{13}CO$ | $L = 10^{14} - 10^{17}$[cm] |
| $^{13}CO$ | $OH^+ + {}^{13}CO \longrightarrow H{}^{13}CO^+ + O$ | $L = 10^{10} - 10^{17}$[cm] |
| $^{13}CH^+$ | $^{13}CH^+ + S \longrightarrow HS^+ + {}^{13}C$ | $L = 10^{10} - 10^{17}$[cm] |
| $^{13}CH^+$ | $^{13}CH^+ + H_2O \longrightarrow H{}^{13}CO^+ + H_2$ | $L = 10^{10} - 10^{17}$[cm] |
| $^{13}CH^+$ | $^{13}CH^+ + S \longrightarrow S^+ + {}^{13}CH$ | $L = 10^{10} - 10^{17}$[cm] |
| $H_2O^+$ | $C + H_2O^+ \longrightarrow OH + CH^+$ | $L = 10^{17}$[cm] |
| $^{13}CH_2{}^+$ | $^{13}CH_2{}^+ + {}^{18}O \longrightarrow H{}^{13}C{}^{18}O^+ + H$ | $L = 10^{10} - 10^{17}$[cm] |
| $^{18}O$ | $CH_2{}^+ + {}^{18}O \longrightarrow HC{}^{18}O^+ + H$ | $L = 10^{10} - 10^{12}$[cm] |
| $^{18}OH^+$ | $^{18}OH^+ + OH \longrightarrow H_2^{18}O^+ + H$ | $L = 10^{10} - 10^{17}$[cm] |
| $^{18}OH^+$ | $CH + + {}^{18}OH^+ \longrightarrow {}^{18}O + CH_2{}^+$ | $L = 10^{10} - 10^{12}$[cm] |
| $^{18}OH^+$ | $^{13}C + + {}^{18}OH^+ \longrightarrow {}^{18}O + {}^{13}CH^+$ | $L = 10^{10} - 10^{17}$[cm] |
| $C^{18}O^+$ | $C^{18}O^+ + S \longrightarrow S + C^{18}O$ | $L = 10^{10} - 10^{17}$[cm] |
| $C^{18}O$ | $OH^+ + C^{18}O \longrightarrow HC^{18}O^+ + O$ | $L = 10^{10} - 10^{17}$[cm] |
| $^{13}C^{18}O^+$ | $^{13}C^{18}O^+ + S \longrightarrow S^+ + {}^{13}C^{18}O$ | $L = 10^{10} - 10^{17}$[cm] |

Table 6.4: Compared to the scenario without-diffusion, these destruction reactions are no longer in the top five contributors in diffusion cases.

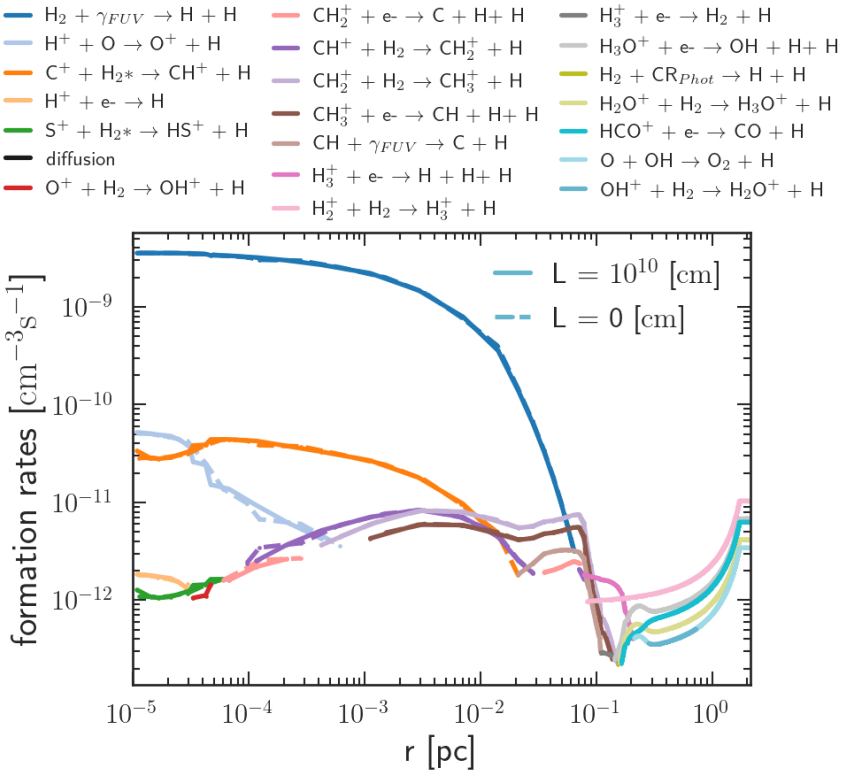


Figure 6.37: Diffusion effects on the formation reactions of H. If diffusion does not affect chemical reaction rates, then chemical reaction rates with $L = 10^{10}$ cm will overlap with $L = 0$ cm. Model parameters: Case II (table [6.1]) with non-uniform temperature, and $\xi = 1.5$.

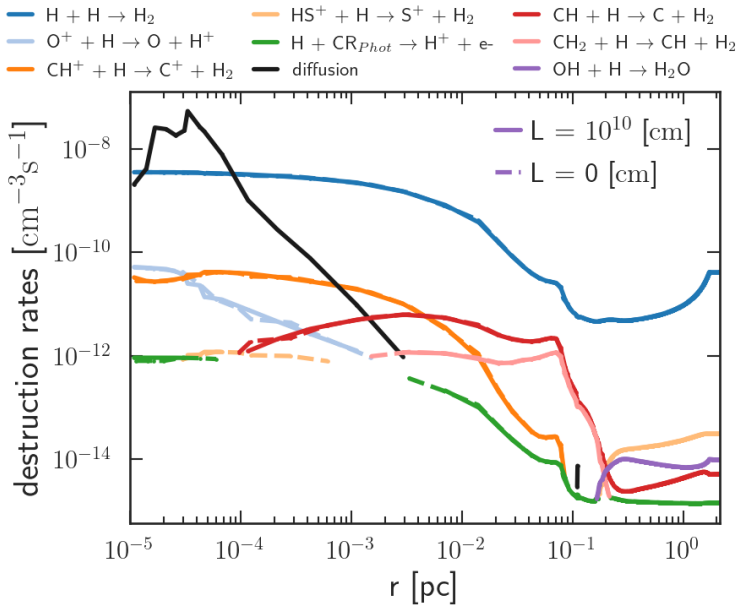


Figure 6.38: Diffusion effects on the destruction reactions of H. Without-diffusion (dot) is compared with $L = 10^{10}$ cm(straight-dot). Model parameters: Case II (table [6.1]) with non-uniform temperature, and $\xi = 1.5$.

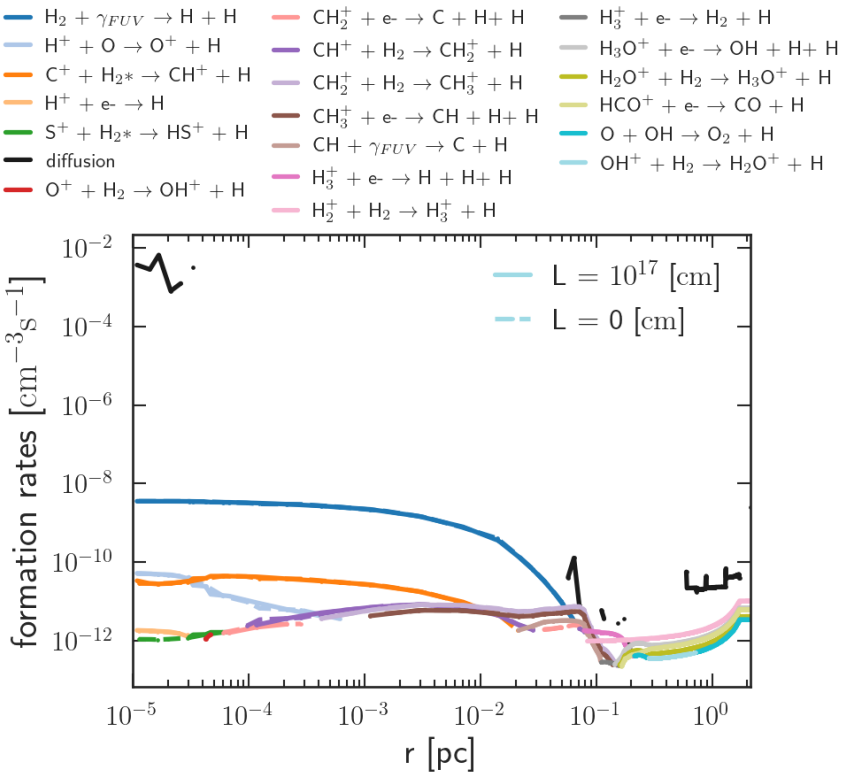


Figure 6.39: Diffusion effects on the formation reactions of H. Without-diffusion (dash-dot) is compared with $L = 10^{17}$ cm (straight-dot). Model parameters: Case II (table [6.1]) with non-uniform temperature, and $\xi = 1.5$.

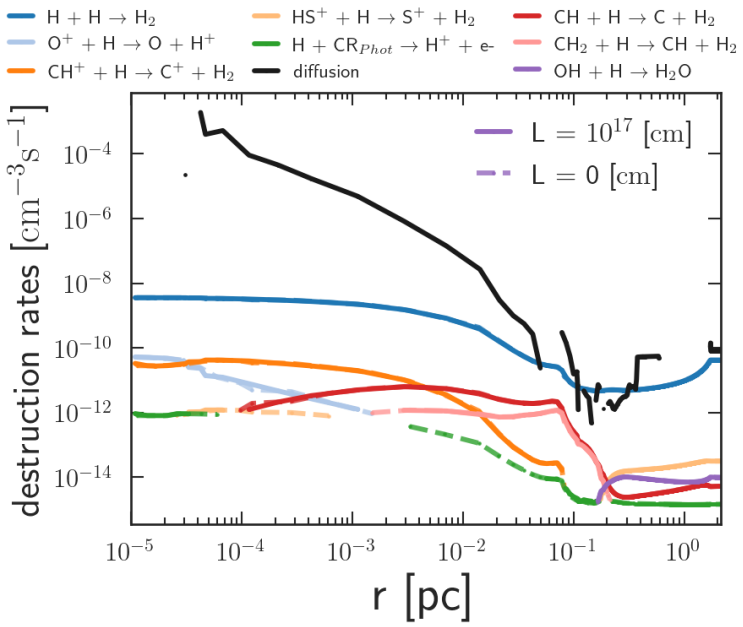


Figure 6.40: Diffusion effects on the destruction reactions of H. Without-diffusion (dot) is compared with $L = 10^{17}$ cm (straight-dot). Model parameters: Case II (table [6.1]) with non-uniform temperature, and $\xi = 1.5$.

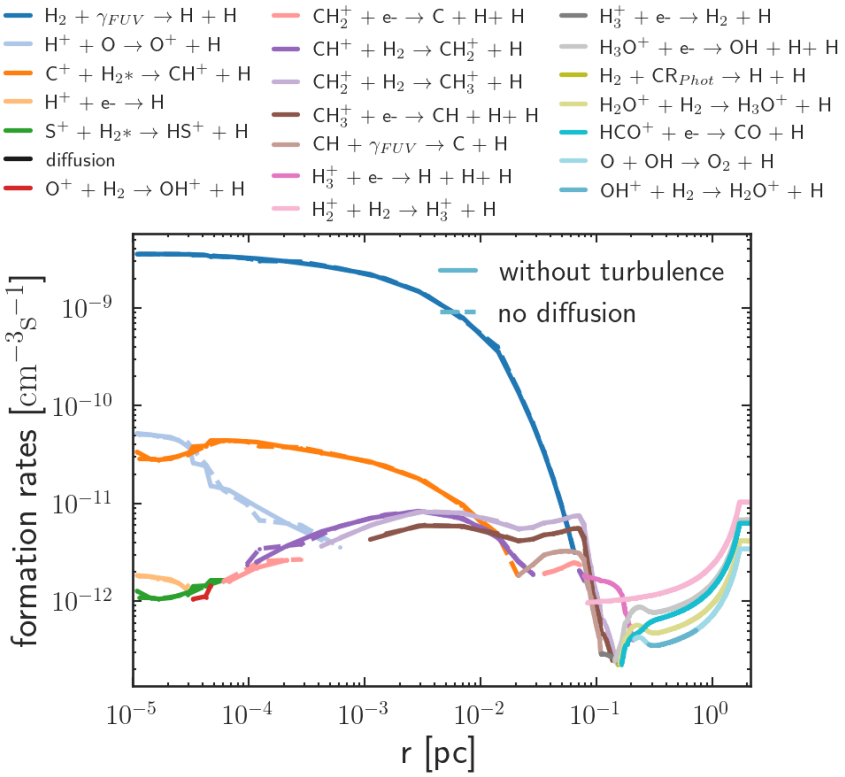


(a) formation

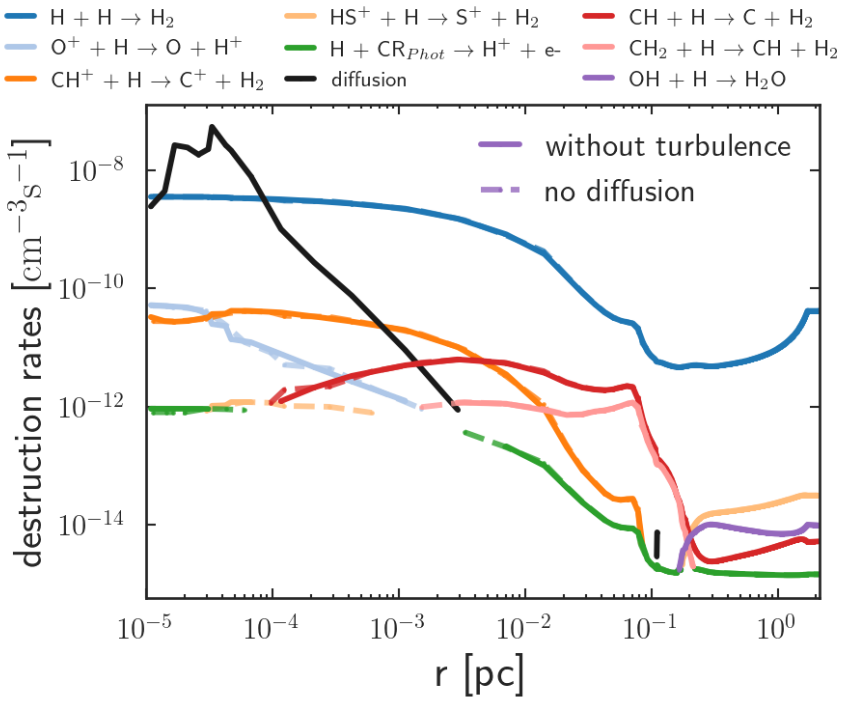


(b) destruction

Figure 6.41: Formation and destruction reactions of H in a scenario without turbulence (straight-dot) compared $L = 0$ cm scenario (dash-dotted line). Model parameters: Case II (table [6.1]) with non-uniform temperature, and $\xi = 1.5$.

### 6.4.1 H and $H_2$

The principal process for the formation of atomic hydrogen is the photodissociation of molecular hydrogen, while the primary mechanism for its destruction is via grain catalysis. At a distance of $r \gtrsim 0.1\,\mathrm{pc}$ (exact position depends on the surface density and intensity of incident radiation), the contribution of photodissociation of $H_2$ diminishes considerably owing to the decreased accessibility of far-ultraviolet (FUV) photons. Molecular hydrogen is formed through the interaction between hydrogen atoms and dust grains, while its destruction is through photodissociation. The formation of $H_2$ in the inner regions of the cloud involves chemical reactions such as $C^+ + H_2 \longrightarrow {CH_2}^+$, ${CH_2}^+ + H_2 \longrightarrow {CH_3}^+ + H$, and cosmic ray ionization of $H_2$. Figure [2.5] illustrates the top five reactions responsible for forming and destroying molecular hydrogen without diffusion. The formation and destruction of atomic hydrogen with two different coherence lengths are shown in figures [6.37-6.40].

Diffusion is one of the primary destructive reactions for atomic hydrogen (Figure [6.38]). As the diffusion coefficient increases to $L = 10^{17}\,\mathrm{cm}$ (Figure [6.40]), diffusion rates exceed the grain catalysis reaction by at least four orders of magnitude in the region $r \leq 0.001\,\mathrm{pc}$.

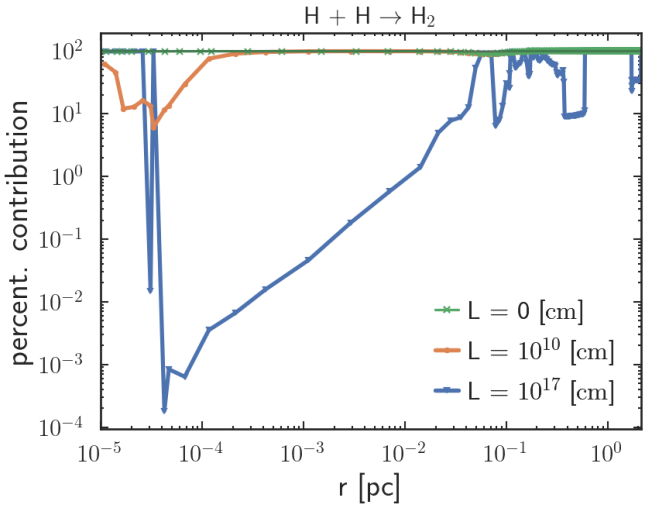


Figure 6.42: Percentage of contribution from the $H_2$ formation on the dust grain to the total destruction rate of atomic hydrogen. Model parameters: same as Figure [6.49].

The photodissociation of $H_2$ (Figure [6.37]) and the formation of $H_2$ on dust grains (Figure [6.38]) show minor variations in the rates when diffusion is added. However, the percentage of contribution to the total destruction reaction (Figure [6.42]) varies as the coherence length increases. A straight black line is drawn to show the 100% contribution. The abrupt change in the contribution from grain catalysis in the region $10^{-5} \leq r \leq 10^{-4}\,\mathrm{pc}$ (Figure [6.42]) coincides with the diffusion contribution to the formation of atomic hydrogen (Figure [6.37]). At lower coherence lengths, the contribution from the grain catalysis is reduced by an order of magnitude in the region $r \leq 10^{-4}\,\mathrm{pc}$. With a coherence length of $L = 10^{17}\,\mathrm{cm}$, diffusion contributes $\gtrsim 90\%$ to the total destruction of atomic hydrogen. Consequently, the contribution from

grain catalysis has decreased to $\lesssim 0.001\%$ (Figure [6.42]).

The diffusion contribution to the formation of atomic hydrogen is significant in the region $r \leq 3 \times 10^{-5}$ pc; as a result, the contribution from the photodissociation of $H_2$ has only decreased significantly in this region (Figure [6.43]). At lower coherence lengths of turbulent diffusion, the diffusion of H is not comparable to the photodissociation of $H_2$ as illustrated in Figure [6.37]. The photodissociation of molecular hydrogen with $L = 10^{10}$ cm and $L = 0$ cm, therefore, contributes equally to the total formation rate (Figure [6.43]).

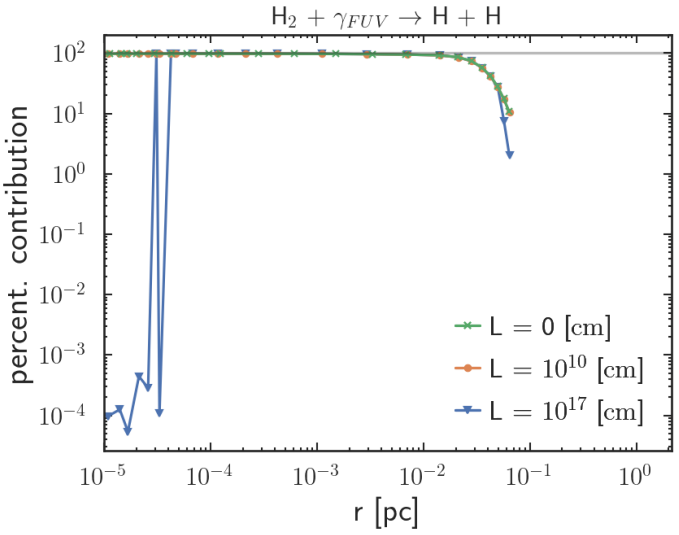


Figure 6.43: Percentage of contribution from the photodissociation of $H_2$ to the total formation rate of atomic hydrogen. Model parameters: same as Figure [6.49].

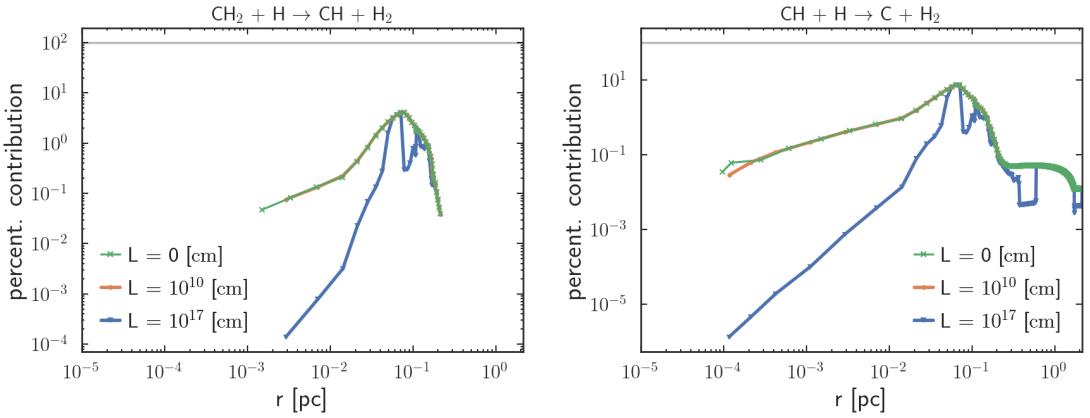


(a) (b)

Figure 6.44: Percentage of contribution from individual reaction to the total destruction rate of atomic hydrogen. Model parameters: same as Figure [6.49].

As diffusion takes a significant role in the chemistry of atomic hydrogen, the following reactions show significant variations:

$$\text{formation of H}: \begin{cases} S^+ + H_2{}^\star \longrightarrow HS^+ + H \\ H^+ + O \longrightarrow O^+ + H, \\ C^+ + H_2{}^\star \longrightarrow CH^+ + H \\ CH^+ + H_2 \longrightarrow CH_2{}^+ + H \end{cases}$$

$$\text{destruction of H}: \begin{cases} \mathrm{H} + \mathrm{CR_{phot}} \longrightarrow \mathrm{H^+} + \mathrm{e^-}, \\ \mathrm{O^+} + \mathrm{H} \longrightarrow \mathrm{O} + \mathrm{H^+}, \\ \mathrm{HS^+} + \mathrm{H} \longrightarrow \mathrm{S^+} + \mathrm{H_2}, \\ \mathrm{CH_2} + \mathrm{H} \longrightarrow \mathrm{CH} + \mathrm{H_2} \end{cases}$$

At a coherence length of $L = 10^{17}$ cm, the destruction reaction $\mathrm{CH^+} + \mathrm{H} \longrightarrow \mathrm{C^+} + \mathrm{H_2}$ decreased its contribution to the total destruction rate significantly in the region $10^{-4} \leq r \leq 0.002$ pc (Figure [6.42]). Similarly, the reaction $\mathrm{CH_2} + \mathrm{H} \longrightarrow \mathrm{CH} + \mathrm{H_2}$ decreases its contribution to the total destruction rate of H in the region $0.002 \leq r \leq 0.04$ pc as illustrated in Figure [6.42a]. In a $L = 0$ cm scenario, the destruction of atomic hydrogen via cosmic ray ionization contributes significantly between $r \geq 0.003$ pc and 2.13 pc. Deeper in the cloud ($r \geq 0.2$ pc), the cosmic ray ionization of atomic hydrogen is a dominant reaction when diffusion is not a dominant destruction reaction (Figure [6.40]). As the turbulent coherence length increases to $L = 10^{17}$ cm, the contribution from the aforementioned reaction is significant only in the region $r \geq 0.08$ pc.

The diffusion of molecular hydrogen from the colder regions to the warmer region is the primary formation reaction of $H_2$ at higher ($10^{12} \leq L \leq 10^{23}$ cm) coherence lengths (Figure [6.50]). At lower coherence lengths, the thermal diffusion contributes more to the total diffusion rate, resulting in the destruction of molecular hydrogen (§[6.2]). In the region with $3 \times 10^{-5} \leq r \leq 0.01$ pc, the contribution to the formation of molecular hydrogen through grain catalysis decreases by more than 90% due to the diffusion of atomic hydrogen (Figure [6.45]). However, the missing $H_2$ is replenished through the diffusion of $H_2$ to the warmer regions from colder regions as depicted in Figure [6.50].

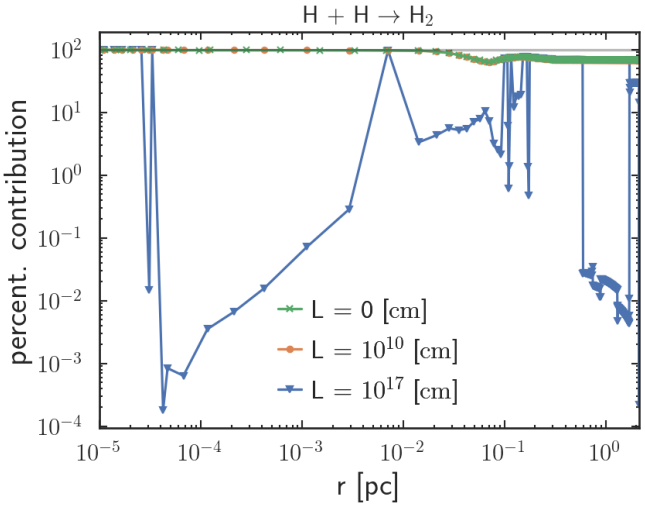


Figure 6.45: Percentage of contribution from the formation of molecular hydrogen on the grains to the total formation rate of molecular hydrogen. Model parameters: same as Figure [6.49].

Figure [6.41] and Figure [6.46] illustrates the formation and destruction reactions in a scenario without turbulence. It is noteworthy that the alterations in the chemical reactions of atomic and molecular hydrogen, apart from diffusion, are significantly visible in the atomic regions of the cloud and not in the molecular

region. This is because, at lower diffusion coefficients, the chemistry in the molecular region is dominated by chemical reactions other than diffusion. Compared

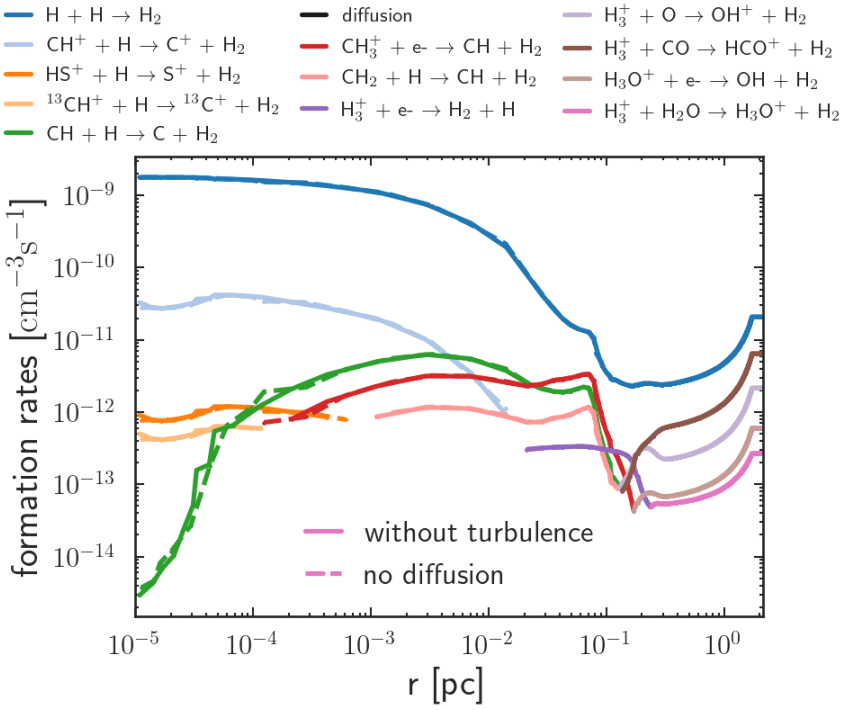


(a) formation

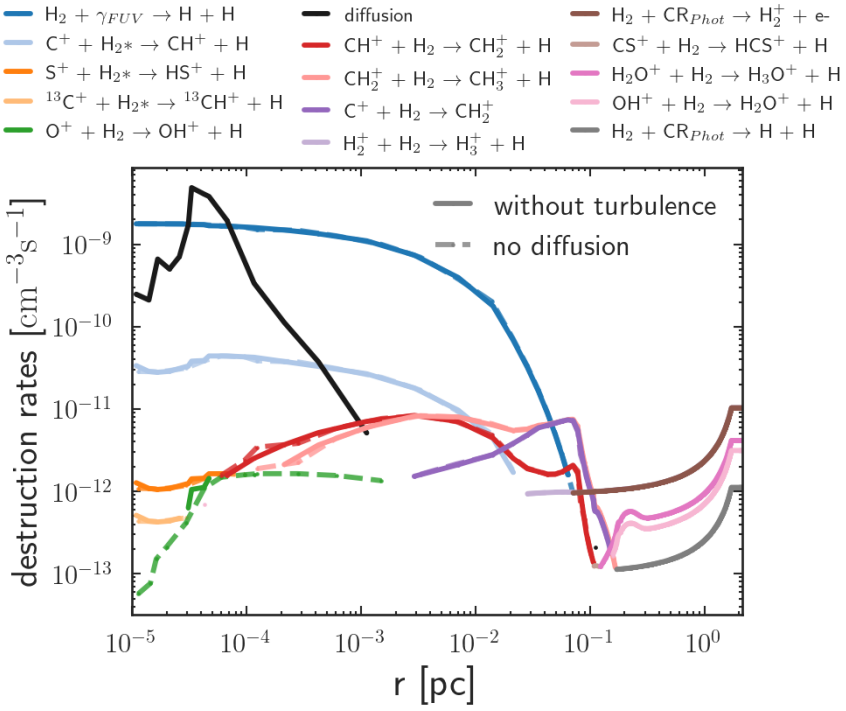


(b) destruction

Figure 6.46: Formation and destruction reactions of $H_2$ in a scenario without turbulence (straight-dot) compared with scenario without diffusion (dash-dotted line).

to the scenario without turbulence, the scenario with turbulence significantly impacts the chemistry of the molecular region. For example, the formation reaction $H_3^+ + H_2O \longrightarrow H_3O^+ + H_2$ is a significant reaction in the region $r \geq 0.2\,\mathrm{pc}$. As the coherence length increases to $L = 10^{17}\,\mathrm{cm}$, the reaction only contributes where the diffusion contribution is significantly low (Figure [6.50]).

The $H_2$ formation reaction $CH + H \longrightarrow C + H_2$ contributed throughout the cloud up to $r \leq 0.1\,\mathrm{pc}$ in a scenario without diffusion (Figure [6.47]). With diffusion, the reaction does not contribute significantly in the region $2 \times 10^{-5} \leq r \leq 6 \times 10^{-5}\,\mathrm{pc}$ because diffusion reduces the availability of the reactants (Figure [6.50]). Nevertheless, formation reaction through the diffusion of $H_2$ contributes significantly in these regions to compensate. The reaction $CH_3^+ + e^- \longrightarrow CH + H_2$ does not contribute to the formation of $H_2$ in the region $10^{-4} - 3 \times 10^{-4}\,\mathrm{pc}$ when diffusion is added. In a non-diffusion scenario, this reaction contributed in the region $10^{-4} - 0.2\,\mathrm{pc}$. The formation reaction $CH_2 + H \longrightarrow CH + H_2$ contributes significantly in the region $0.9 \times 10^{-3} - 0.1\mathrm{pc}$ without diffusion. However, as the coherence length increases to $L = 10^{17}\,\mathrm{cm}$, the reaction only contributes significantly in the region $0.02 - 0.09\,\mathrm{pc}$. Similarly, the reaction $H_3^+ + e^- \longrightarrow H_2 + H$ also reduces its contribution from the region $0.02 - 0.2\,\mathrm{pc}$ to the region $0.09 - 0.1\,\mathrm{pc}$ as the coherence length of turbulent diffusion increases from $L = 0\,\mathrm{cm}$ to $L = 10^{17}\,\mathrm{cm}$. The formation reactions involving $H_3^+$, such as $H_3^+ +$

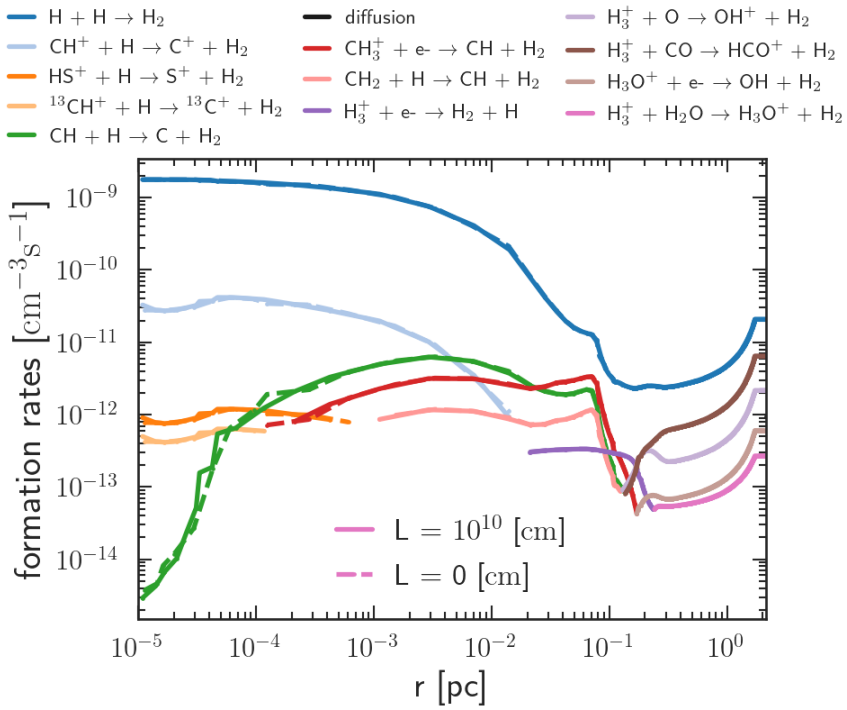


Figure 6.47: Formation reactions of $H_2$. Model parameters: Case II (table [6.1]) with non-uniform temperature, $\xi = 1.5$ and $L = 10^{10}\,\mathrm{cm}$.

$e^- \longrightarrow H_2 + H$, $H_3^+ + O \longrightarrow OH^+ + H_2$, $H_3^+ + CO \longrightarrow HCO^+ + H_2$, $H_3O^+ + e^- \longrightarrow OH + H_2$, and $H_3^+ + H_2O \longrightarrow H_3O^+ + H_2$ shows a decrease in their contribution as the coherence length (in extension diffusion coefficient) increases to $L = 10^{17}$ cm. Diffusion of $H_2$ is at most six orders of magnitude higher than the rest of the chemical reactions deeper in the cloud, resulting in the reduction of other reactions. Consequently, the abundance of $H_2$ does not change drastically in these regions.

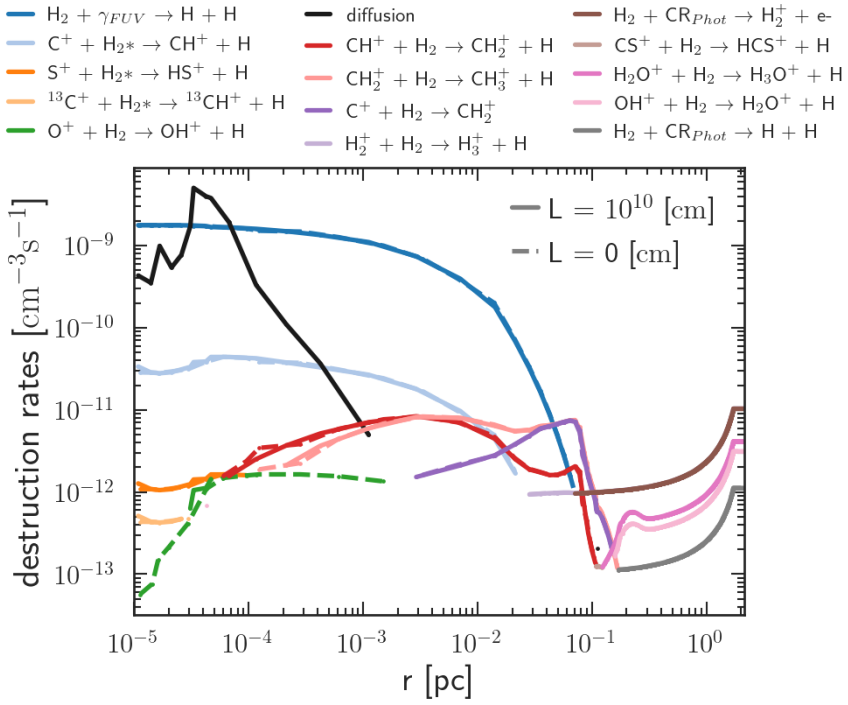


Figure 6.48: Destruction reactions of $H_2$. Model parameters: Case II (table [6.1]) with non-uniform temperature, $\xi = 1.5$ and $L = 10^{10}$ cm.

While looking at the destruction reaction of $H_2$, the diffusion contributions are significant but limited to certain regions of the cloud. At higher coherence lengths, the destruction via diffusion (Figure [6.40]) is at most five orders of magnitude higher than the rest of the chemical reactions and lower coherence lengths, the diffusion rates are on similar scales of other chemical destruction reactions (Figure [6.38]). The destruction reactions $S^+ + H_2\star \longrightarrow HS^+ + H$, and $^{13}C^+ + H_2\star \longrightarrow {}^{13}CH^+ + H$ show a significant increase in the rate at the surface of the cloud with diffusion. In contrast, the reaction $O^+ + H_2 \longrightarrow OH^+ + H$ shows a significant reduction in the rates. In the scenario devoid of diffusion, the reaction $O^+ + H_2 \longrightarrow OH^+ + H$ contributes significantly to the destruction of $H_2$ in the region $10^{-5} - 2 \times 10^{-3}$ pc. As the diffusion increases, the reaction contribution should either reduces or increase if there is any change. However, with $L = 10^{10}$ cm the reaction only contributes in the region $2\times10^{-5} - 4\times10^{-3}$ pc and $10^{-4} - 6\times10^{-4}$ pc and with $L = 10^{17}$ cm the reaction contributes in the region

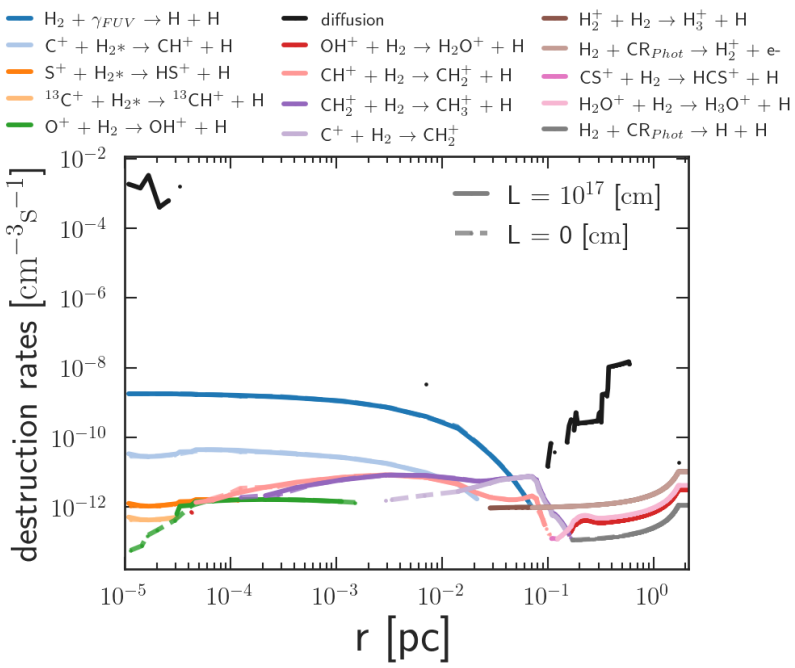


Figure 6.49: Destruction reactions of $H_2$. Model parameters: Case II (table [6.1]) with non-uniform temperature, $\xi = 1.5$ and $L = 10^{17}$ cm.

$2 \times 10^{-5} \leq r \leq 0.8 \times 10^{-4}$ pc. This change in contribution coincides with the diffusion of $H_2$. The reaction $CS^+ + H_2 \longrightarrow HCS^+ + H$ shows a significant reduction in its contribution when diffusion is added.

The observed alterations in the chemical reactions between H and $H_2$ indicate that diffusion significantly impacts the atomic region more than the molecular region. This is due to the higher diffusion velocities at the surface compared to the interior of the cloud. Higher turbulent diffusion on the surface has secondary effects throughout the cloud. Consequently, PDR models should include diffusion to explain the chemistry and physics of the ISM.

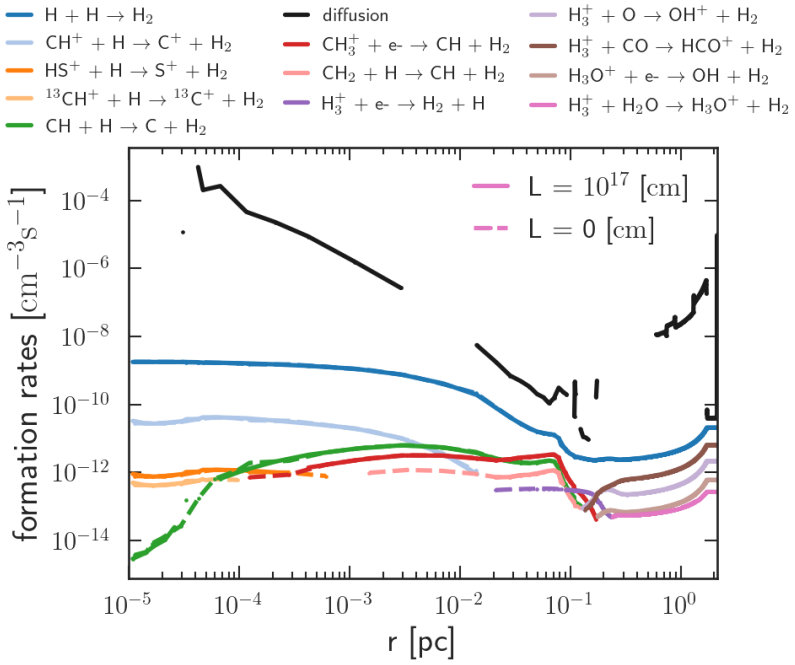


Figure 6.50: Formation reactions of $H_2$. Model parameters: Case II (table [6.1]) with non-uniform temperature, $\xi = 1.5$ and $L = 10^{17}$ cm.

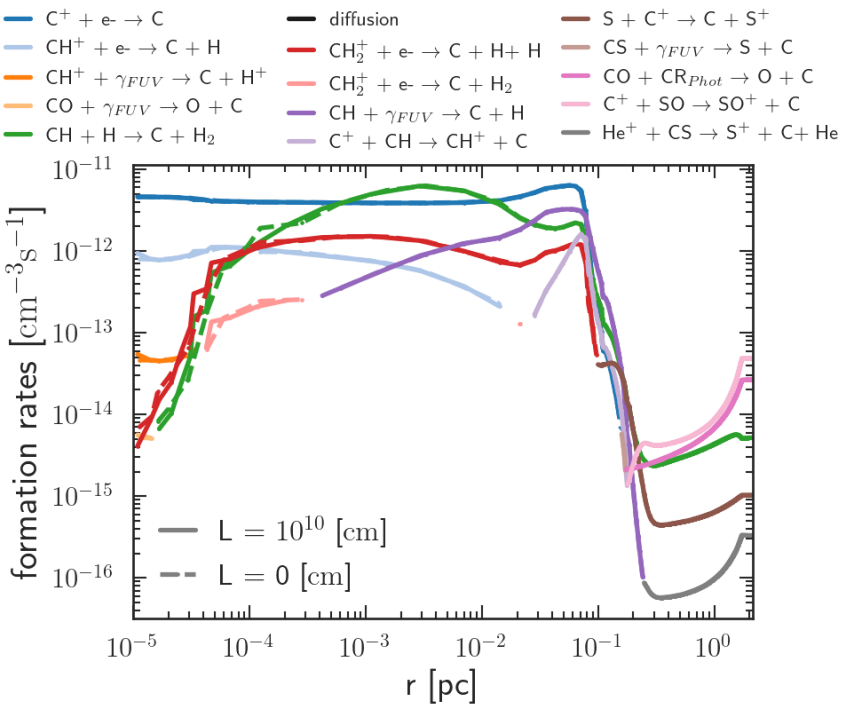


Figure 6.51: Atomic carbon formation reactions with $L = 10^{10}$ cm and without diffusion. The top five reactions contributing to the carbon formation at each shell are shown. Model parameters: Case II (table [6.1]).

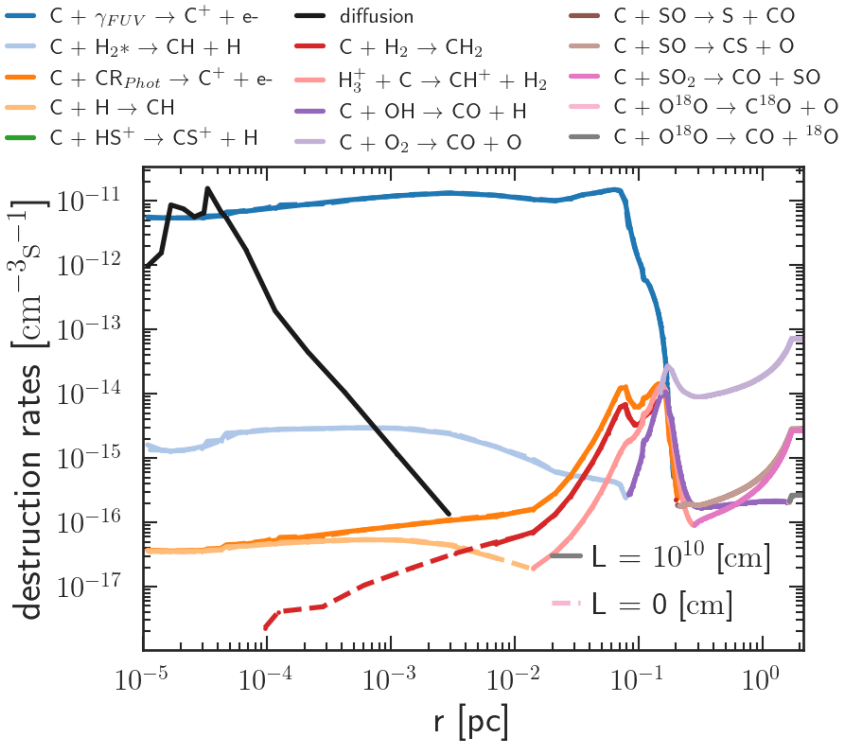


Figure 6.52: Comparison of the destruction reactions of C with $L = 10^{10}$ cm(straight-dot) and no diffusion (dash-dotted line) cases. Model parameters: Case II (table [6.1]).

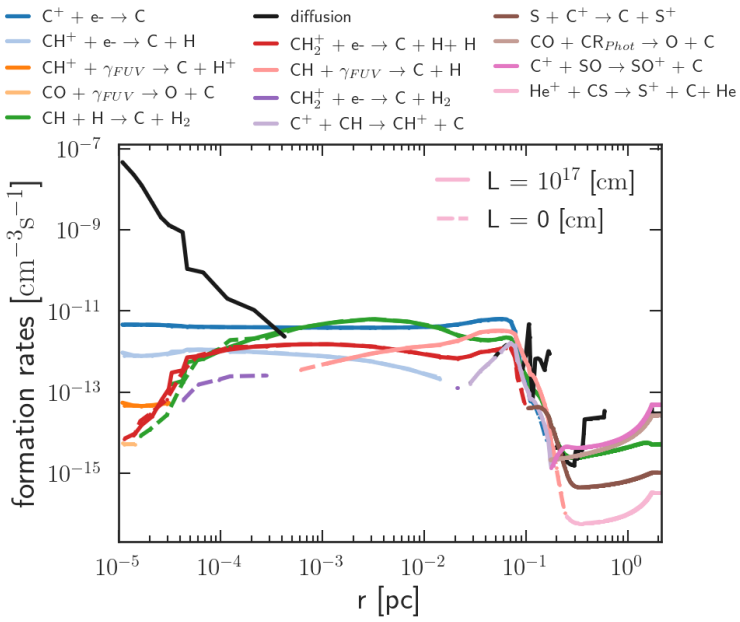


Figure 6.53: Formation reactions of C in a $L = 10^{17}$ cm scenario (straight-dot) compared to a scenario without diffusion (dash-dotted line). Model parameters: same as the Figure [6.52].

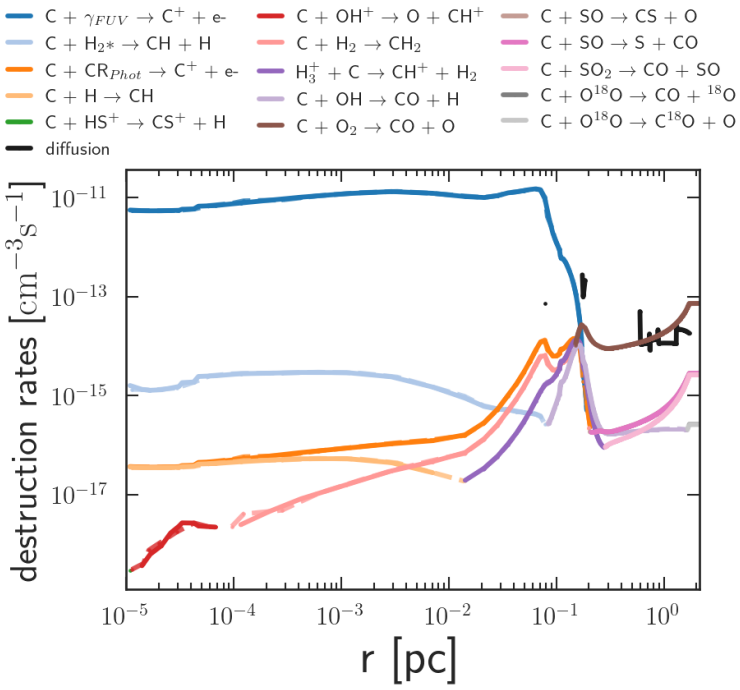


Figure 6.54: Comparison of the destruction reactions of C with $L = 10^{17}$ cm (straight-dot) and the cases with no diffusion (dash-dotted line). The top five contributors to the destruction of C at any given shell are plotted. Model parameters: same as the Figure [6.52].

### 6.4.2 C, $C^+$, and CO

At the surface of the clump, the carbon photo-ionized to form $C^+$. While moving to the inner regions of the cloud, $C^+$ recombines to form carbon. Once the self-shielding of CO is active, the cloud will be dominated by CO. C is sandwiched between $C^+$ and CO regions in a PDR. As Röllig & Ossenkopf (2013), this study considers the carbon transition region when the density of $C^+$ and CO are equal ($n(C^+) = n(CO)$). The change in abundance of C, $C^+$, and CO are shown in the Figure [6.24] and Figure [6.25]. The carbon transition region shifts towards the surface of the cloud as the molecular region expands with diffusion (Figure [6.26]). The abundance of CO shows an increase with $L = 10^{17}$ cm, whereas the $C^+$ abundance shows a decrease.

#### C

Without diffusion, electron recombination of $C^+$ and $CH + H \longrightarrow C + H_2$ are the primary formation reactions for C (Figure [6.55]).

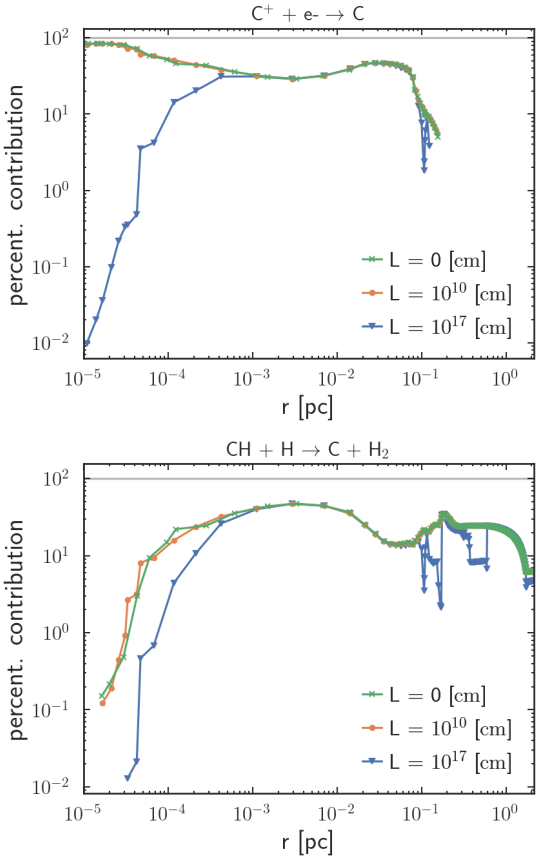


Figure 6.55: Percentage of contribution from individual reactions to the total formation rate of atomic carbon. Model parameters: Case II (table [6.1]) with non-uniform temperature, and $\xi = 1.5$.

The electron recombination of C does not significantly change reaction rates when diffusion is added (Figure [6.51]). However, as the coherence length increases to $L = 10^{17}$ cm, the electron recombination of $C^+$ shows at most four orders of magnitude (Figure [6.55]a) decrease in the region $10^{-5} \leq r \lesssim 3 \times 10^{-4}$ pc. As the coherence length of diffusion $L$ increases to $10^{17}$ cm, the top contributor $CH + H \longrightarrow C + H_2$ shows a significant variation on the surface of the cloud ($10^{-5} \leq r \leq 5 \times 10^{-4}$pc). The percentage of contribution from the reaction $CH + H \longrightarrow C + H_2$ dropped at least an order of magnitude in the region $2 \times 10^{-5} - 5 \times 10^{-4}$ pc when coherence length of diffusion increased to $L = 10^{17}$ cm (Figure [6.53]). The diffusion removes atomic hydrogen and CH from the surface. However, the diffusion of $H_2$

and other reactions replenishes the abundance of H. Consequently, the reaction rate shows minor variation in the rates in the region $r \geq 5 \times 10^{-4}$pc.

Several other formation reactions exhibit notable modifications, including the reaction $CH_2^+ + e^- \longrightarrow C + H + H$, the photodissociation of $CH^+$, and the reaction $CH_2^+ + e^- \longrightarrow C + H_2$. Without diffusion, the aforementioned reaction $CH_2^+ + e^- \longrightarrow C + H + H$ accounts for a fraction of around $0.1 - 1\%$ of the total formation of atomic carbon. The contribution from the aforementioned reaction only shows minor variations when diffusion is added at lower coherence lengths. At $L = 10^{17}$ cm the contribution was reduced by four orders of magnitude in the region $r \leq 10^{-5}$ pc. The photodissociation of $CH^+$ exhibited a significant decrease in its impact on the total formation rates, with a reduction of four orders of magnitude. In a scenario without diffusion and diffusion with $L = 10^{10}$ cm, reaction $CH_2^+ + e^- \longrightarrow C + H_2$ contributes significantly in the region $4 \times 10^{-5} - 3 \times 10^{-4}$ pc. In the $L = 10^{17}$ cm case, the reaction does not substantially contribute to the formation of atomic carbon. This is primarily due to the reduced availability of $CH_2^+$. With a coherence length of $L = 10^{17}$ cm, the contribution of photodissociation of CS to the total formation rate is also negligible. Diffusion contributes significantly to the formation of the atomic carbon at the surface of the cloud at $L = 10^{17}$ cm. In other cases, the contribution of diffusion fails to rank among the top five formation reactions.

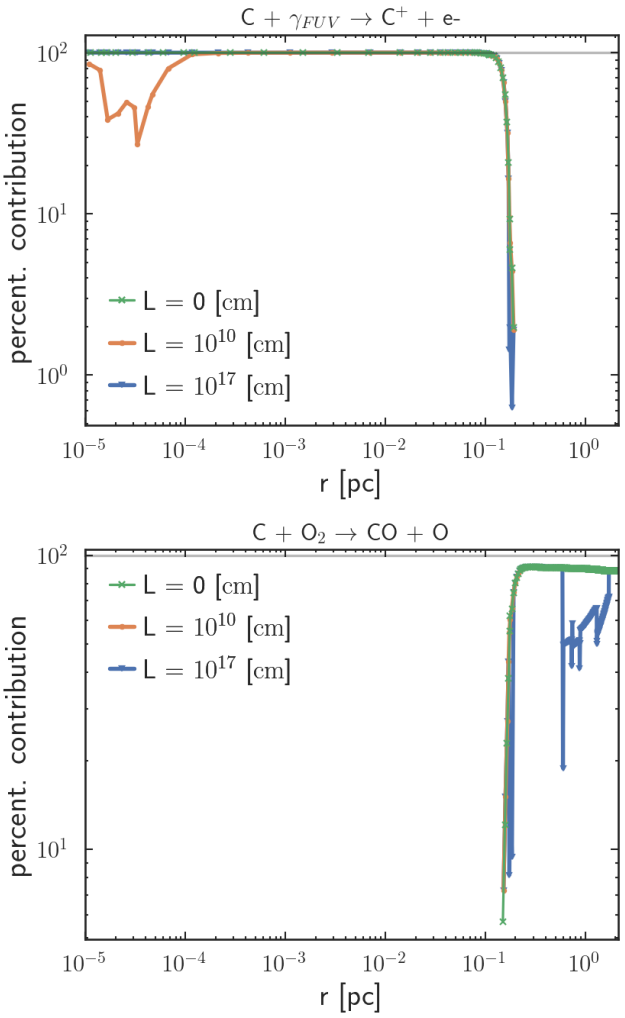


Figure 6.56: Percentage of contribution from individual reaction to the total destruction rate of atomic carbon. Model parameters: Case II (table [6.1]) with non-uniform temperature, and $\xi = 1.5$.

With a coherence length of $L = 10^{10}$ cm, the diffusion and photodissociation of C contribute on the same scale to the total destruction reaction (Figure [6.52]).

As the coherence length increases to $L = 10^{17}$ cm, diffusion contribution is limited to the interior of the cloud (Figure [6.54]). The destruction reactions, $C + H_2 \longrightarrow CH_2$, and $C + H \longrightarrow CH$ show variations spatially at which the reactions are significant. Also, when diffusion is added ($L = 10^{10}$ cm), the reaction $C + OH^+ \longrightarrow O + CH^+$ does not contribute significantly to the destruction of the atomic carbon (table [ 6.4]). At coherence length, $L = 10^{17}$ cm, the abovementioned reaction only contributes (Figure [6.54]) in the region $2 \times 10^{-5} \leq r \leq 5 \times 10^{-5}$ pc. Without diffusion, the reaction $C + H \longrightarrow CH$ contributes up to the $H - H_2$ transition region. Nevertheless, as in Figure [6.54], the contribution from the reaction $C + H \longrightarrow CH$ is reduced when diffusion is added. As the coherence length increases to $L = 10^{10}$ cm, the reaction contributes up to 0.008pc. With a coherence length of $L = 10^{17}$ cm, the contribution diminishes up to the region $2 \times 10^{-3}$pc. Similarly the destruction reaction $C + H_2 \longrightarrow CH_2$ contributes significantly in the region $10^{-4} \leq r \leq 0.1$ pc. As the coherence length increases from $L = 10^{10}$ cmto $L = 10^{17}$ cm, the contribution changes spatially $3 \times 10^{-4} \leq r \leq 0.1$ pc to $7 \times 10^{-3} \leq r \leq 0.1$ pc. As the $H - H_2$ transition region shifts towards the surface of the cloud, the contribution from $C + H_2 \longrightarrow CH_2$ shifts deeper into the cloud.

The destruction reaction ${H_3}^+ + C \longrightarrow CH^+ + H_2$ shifts from $0.02 - 0.4$ pc to $0.05 - 0.4$ pc as the coherence length increases from no diffusion to $L = 10^{17}$ cm. With a coherence length of $L = 10^{10}$ cm, the reaction shows an extended contribution in the region $0.01 - 0.4$ pc. The reaction $C + O^{18}O \longrightarrow C^{18}O + O$ reduces the contribution deeper in the cloud as the coherence length increases. This reduction in the destruction is compensated by introducing the reaction $C + O^{18}O \longrightarrow CO + {}^{18}O$.

### $C^+$

The addition of diffusion does not result in any alteration to the abundance of $C^+$ in the region $r \leq 0.06\,\mathrm{pc}$(Figure [6.24] and Figure [6.25]). As the coherence length of turbulent diffusion increases to $L = 10^{17}\,\mathrm{cm}$, the total diffusion rates increases linearly (Figure [C.3]). At lower coherence lengths ($L \leq 10^{12}\,\mathrm{cm}$) the thermal diffusion rates are higher than the molecular and turbulent contributions. Consequently, diffusion is a destruction reaction in the region $r \lesssim 0.003\,\mathrm{pc}$. For other coherence lengths, ($10^{12} \lesssim L \leq 10^{17}\,\mathrm{cm}$), the diffusion is a destruction reaction in the region $r \leq 0.05\,\mathrm{pc}$. The formation and destruction of $C^+$,

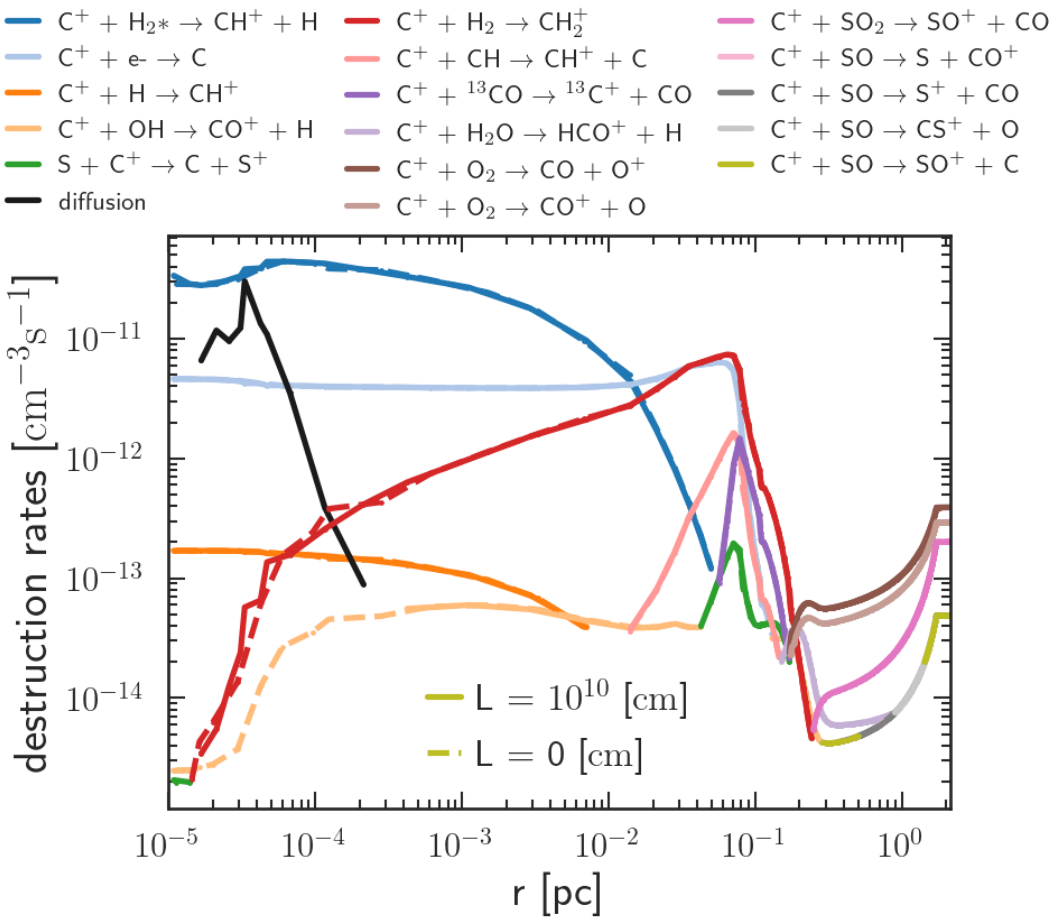


Figure 6.57: Destruction reactions of $C^+$ in a $L = 10^{10}\,\mathrm{cm}$ scenario (straight-dot) compared with a scenario without diffusion (dash-dotted line). Model parameters: Case II from the table [6.1].

with $L = 10^{10}\,\mathrm{cm}$ and $L = 10^{17}\,\mathrm{cm}$ are shown in figures [6.57-6.54]. With $L = 10^{10}\,\mathrm{cm}$, the diffusion rates are lower than the highest destruction reaction $C^+ + H_2^\star \longrightarrow CH^+ + H$. Figure [6.58] indicates that in a scenario without diffusion (dash-dotted line), the destruction reaction $C^+ + OH \longrightarrow CO^+ + H$ contributes significantly in the region $10^{-5} \leq r \leq 0.04\,\mathrm{pc}$. However, with $L = 10^{10}\,\mathrm{cm}$, the reaction contributes similarly except in the region $10^{-5} \leq r \leq 3 \times 10^{-4}\,\mathrm{pc}$. This is

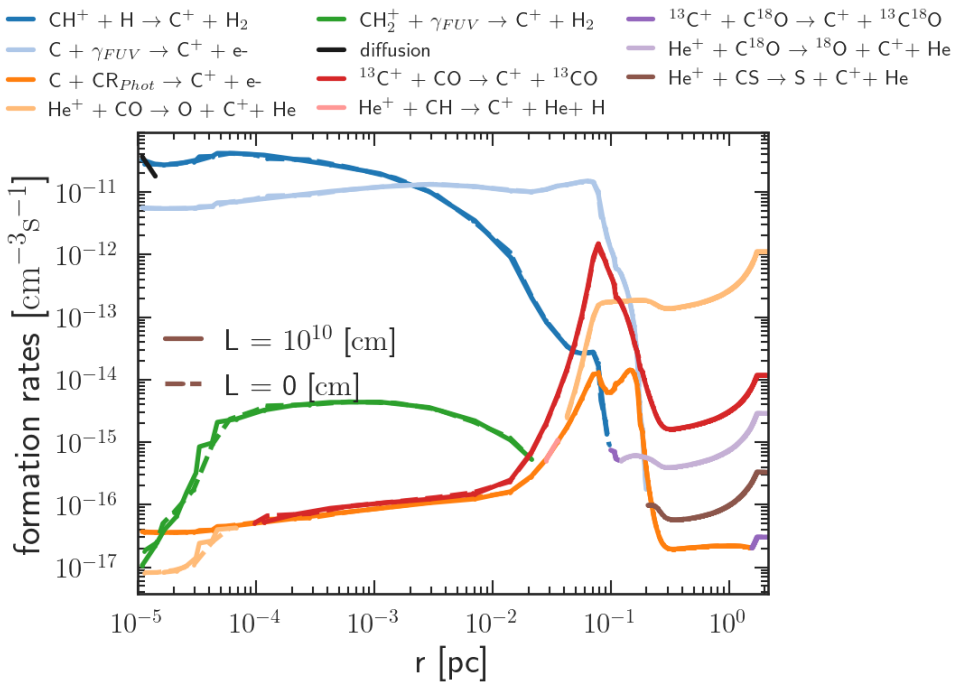


Figure 6.58: Formation reactions of $C^+$ in a $L = 10^{10}$ cm scenario (straight-dot) compared with $L = 0$ cm (dash-dotted line). Model parameters: same as the Figure [6.57].

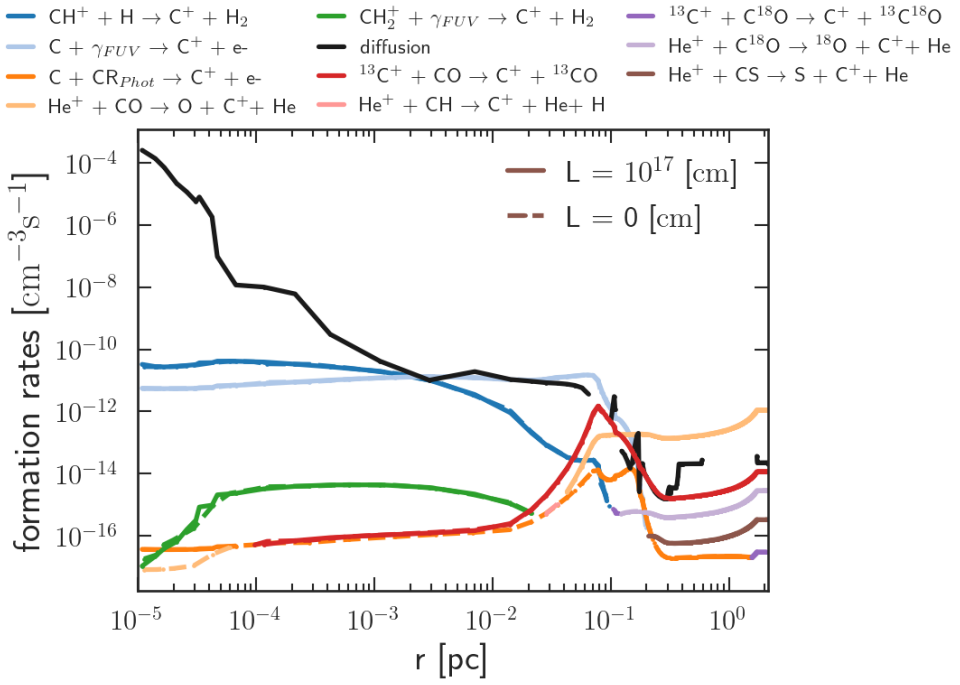


Figure 6.59: Formation reactions of $C^+$ in a $L = 10^{17}$ cm scenario (straight-dot) compared with scenario without diffusion (dash-dotted line). Model parameters: same as the Figure [6.57].

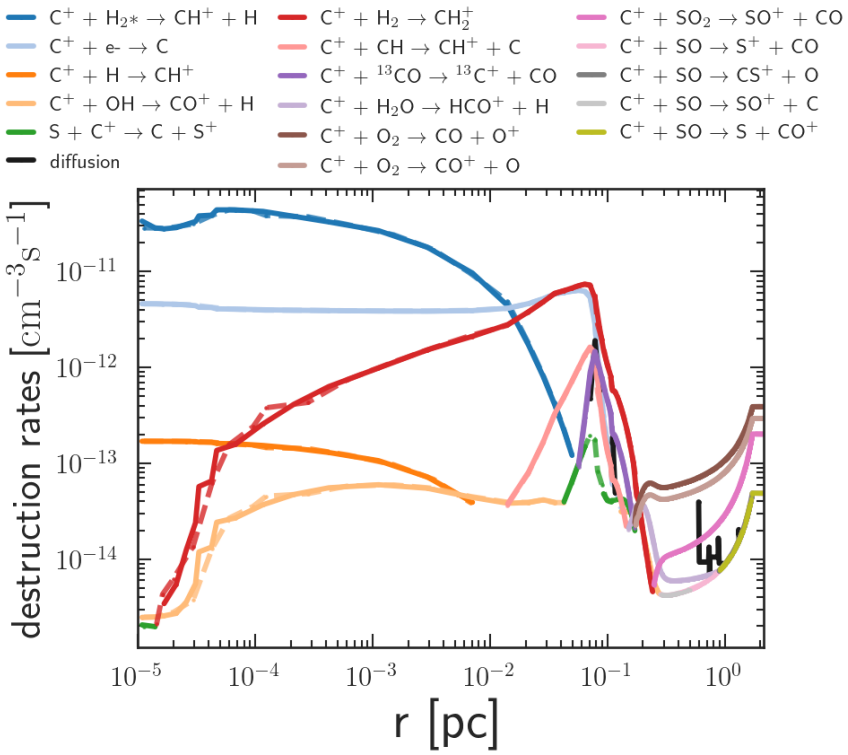


Figure 6.60: Destruction reactions of $C^+$ in a $L = 10^{17}$ cm scenario (straight-dot) compared with a scenario without diffusion (dash-dotted line). Model parameters: same as the Figure [6.57].

because the primary destruction reaction in this region is diffusion. The behavior of diffusion and $C^+ + OH \longrightarrow CO^+ + H$ at $L = 10^{17}$ cm in Figure [6.60] supports this argument. The reaction $C^+ + H_2 \longrightarrow {CH_2}^+$ shows significant variations in the reaction rates at the surface.

### CO

The main formation reactions of CO are:

$$CO^+ + H \longrightarrow CO + H^+, \qquad HCO^+ + e^- \longrightarrow CO + H, \tag{6.1}$$

$$CH + O \longrightarrow CO + H, \qquad C^+ + {}^{13}CO \longrightarrow {}^{13}C^+ + CO. \tag{6.2}$$

When diffusion is added, the reactions $C^+ + SO \longrightarrow S^+ + CO$ and $C + OH \longrightarrow CO + H$ do not contribute significantly to the formation of CO as illustrated in table [6.3]. Also, the reaction $OH^+ + S \longrightarrow S^+ + OH$ does not contribute significantly to the destruction of CO (table [6.4]). Figure [6.61] illustrates the changes in the formation reactions by comparing the $L = 0$ cm case with $L = 10^{10}$ cm. Diffusion is not a dominant formation reaction at lower coherence lengths because thermal diffusion contributes more to the total diffusion rate, which is

a destruction reaction (Figure [C.5]). Consequently, up to $r \leq 2 \times 10^{-3}$ pc, the diffusion rates are similar irrespective of the turbulence coherence length used (see §[6.2] and Figure [C.5a]). For all cases other than $L = 10^{17}$ cm, the diffusion is a destruction reaction in the region $r \leq 2 \times 10^{-3}$ pc.

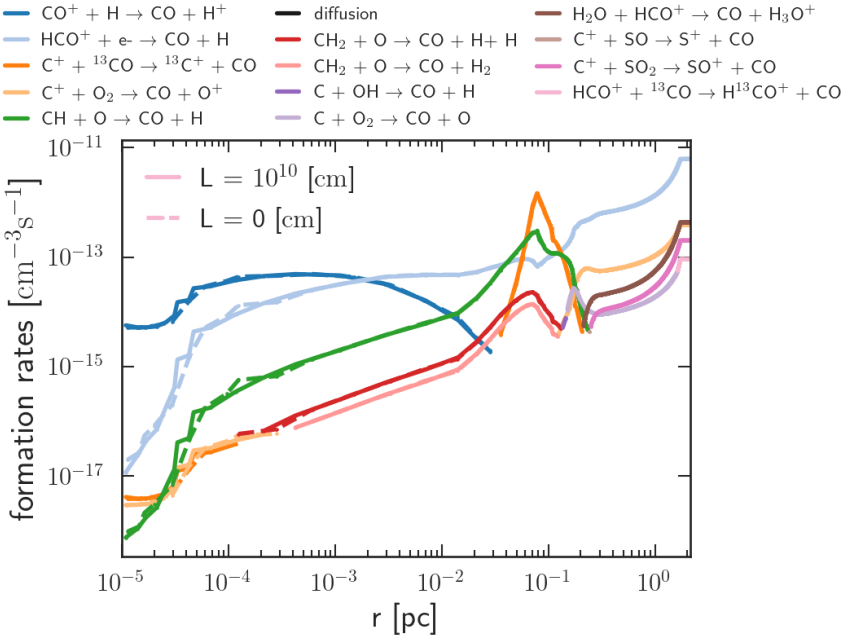


Figure 6.61: Formation reactions of CO in a $L = 10^{10}$ cm scenario (straight-dot) compared with a scenario without diffusion (dash-dotted line). Model parameters: same as the Figure [6.52].

At $L = 10^{10}$ cm, the contribution from diffusion is not significant in the formation or destruction of CO. At the surface, the formation reactions show significant variations in their rates after adding diffusion.

$$\mathrm{CH + O \longrightarrow CO + H} \qquad \mathrm{C^+ + O_2 \longrightarrow CO + O^+}$$
$$\mathrm{C^+ + O_2 \longrightarrow CO + O^+} \qquad \mathrm{C^+ + {}^{13}CO \longrightarrow {}^{13}C^+ + CO}$$

As a result of diffusion, the abundance of O and $O_2$ shows a slight decrease, as shown in Figure [B.1b]. Consequently, the aforementioned reactions exhibit fluctuations; however, the variation in the percentage of contributions to the total formation reaction rates is minor (Figure [6.63]).

At $L = 10^{17}$ cm, diffusion is a prominent formation and destruction reaction (Figure [6.62]). With $L = 10^{17}$ cm, the turbulent diffusion rates are higher than the thermal diffusion rates, resulting in the formation of the CO at the surface as shown in Figure [C.5f] and Figure [6.62]. In the region $0.005 \lesssim r \lesssim 0.4$pc, the turbulent diffusion contribution is higher than the thermal or molecular diffusion (Figure [C.5]), resulting in the formation of CO via diffusion. The formation reaction $\mathrm{C^+ + {}^{13}CO \longrightarrow {}^{13}C^+ + CO}$ contributed significantly in the region $r \leq$

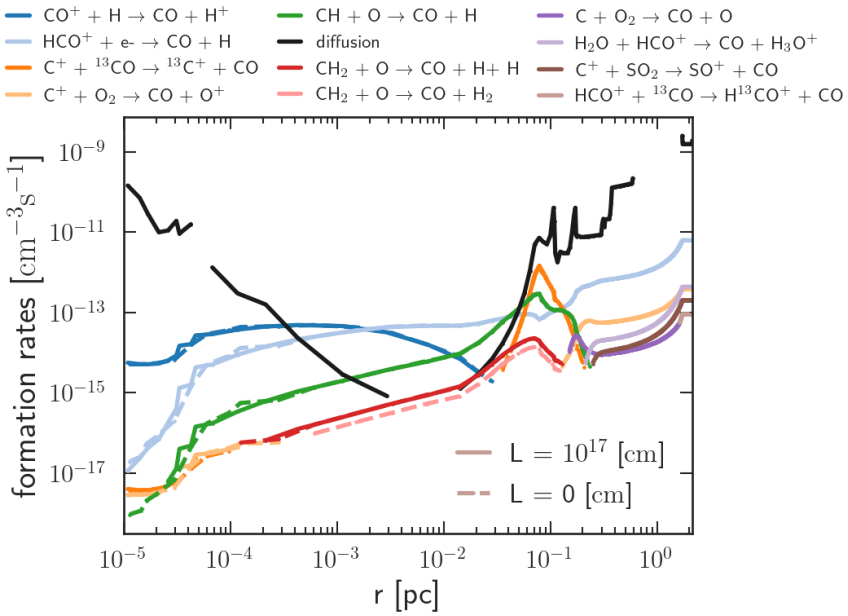


Figure 6.62: Formation reactions of CO in a $L = 10^{17}$ cm scenario (straight-dot) compared with a scenario without diffusion (dash-dotted line). Model parameters: same as the Figure [6.52].

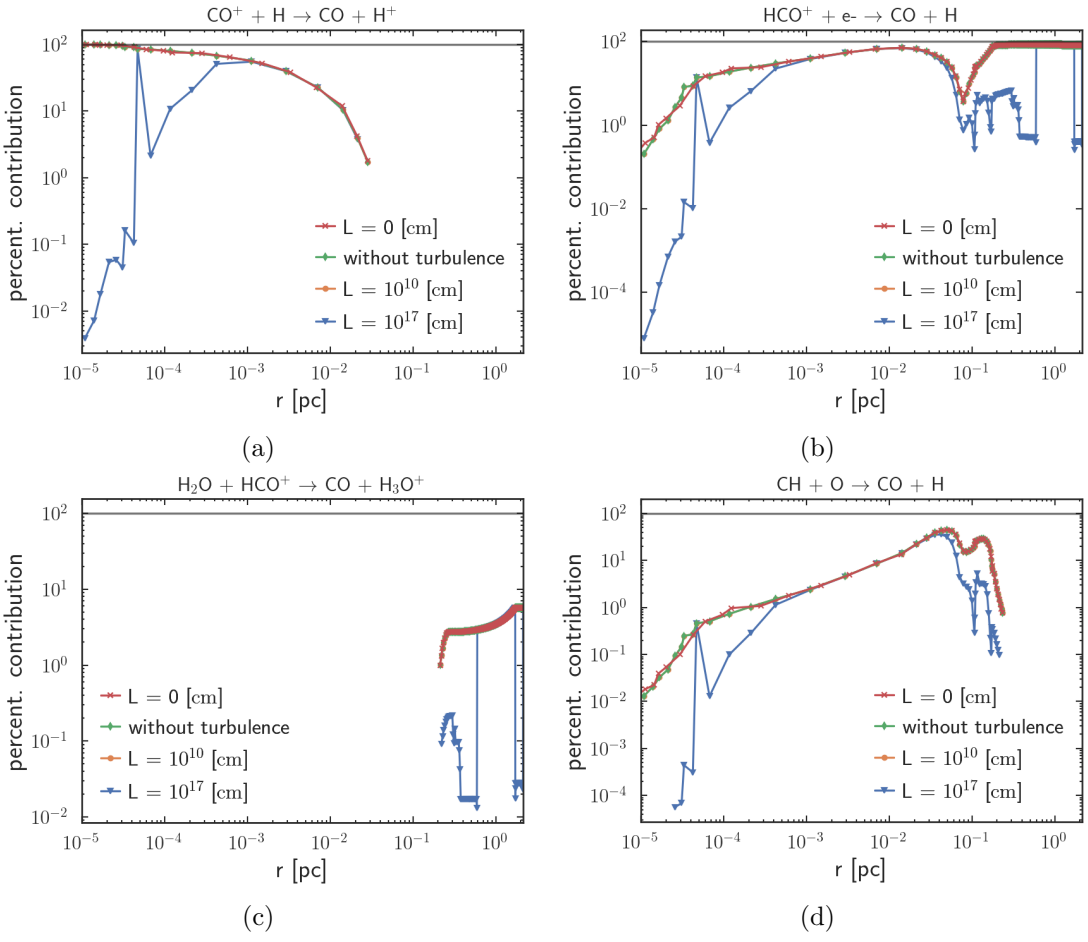


Figure 6.63: Percentage of contributions to the formation reactions of CO in different diffusion scenarios. Model parameters: same as the Figure [6.61].

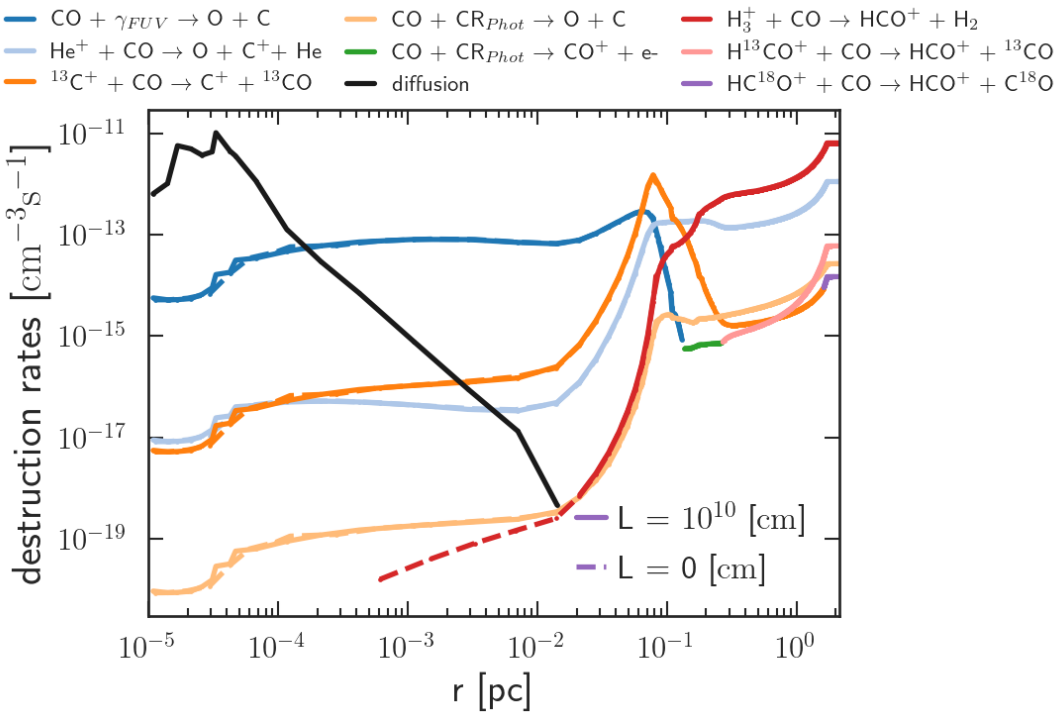


Figure 6.64: Destruction reactions of CO in a $L = 10^{10}$ cmscenario (straight-dot) compared with a scenario without diffusion (dash-dotted line). Model parameters: same as the Figure [6.52].

$10^{-4}$ pc. However, as the coherence lengths of turbulent diffusion increased to $L = 10^{17}$ cm, the contribution from this reaction to the total formation reaction was reduced by two orders of magnitude in the region $r \leq 4\times10^{-5}$ pc. Also, in the region $0.03-0.2$ pc, the contribution from the aforementioned reaction is reduced by one order of magnitude. With $L = 10^{17}$ cm, diffusion contributes significantly to the total formation, reducing the contribution from other reactions (Figure [6.63]). On the surface, the reactions $CO^+ + H \longrightarrow CO + H^+$, $HCO^+ + e^- \longrightarrow CO + H$, and $CH + O \longrightarrow CO + H$ show two to four orders of magnitude (Figure [6.63]) decrease in the contribution. Deeper in the cloud, $H_2O + HCO^+ \longrightarrow CO + H_3O^+$ shows an order of magnitude reduction (Figure [6.63]) in the contribution to the total formation rate.

At $L = 10^{10}$ cm, the diffusion of CO is the dominant destruction factor, with a contribution of up to three orders of magnitude greater than that of other chemical reactions (Figure [6.64]). At $L = 10^{17}$ cm, the diffusion contribution to the total destruction reaction is significant only in the region $r \geq 0.5$ pc (Figure [6.65]). The diffusion contribution is significant in the region $3\times10^{-5} - 6\times10^{-5}$ pc and $5\times10^{-3}-8\times10^{-3}$ pc (denoted by a black dot in Figure [6.64]). The dashed-dotted line is employed to identify points within the cloud where the diffusion rates are destruction/formation at one shell but formation/destruction at neighboring

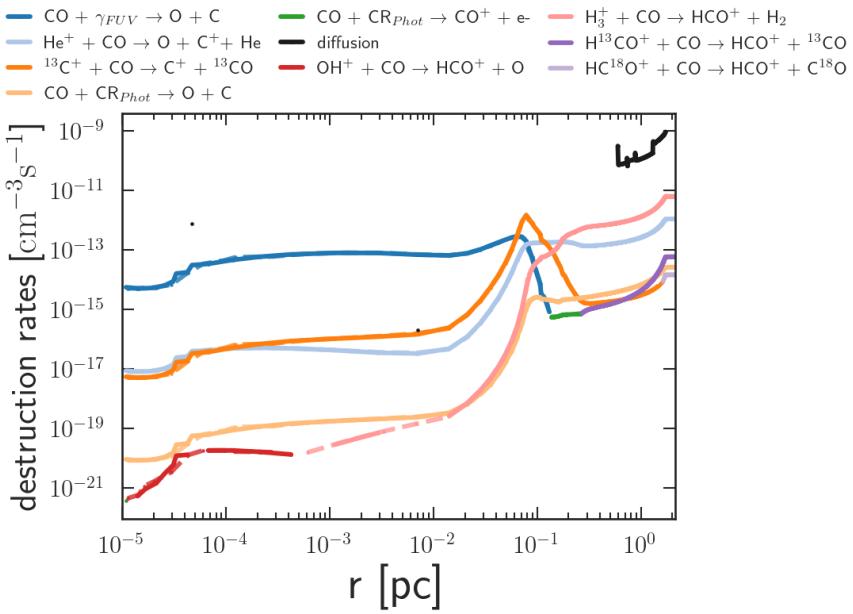


Figure 6.65: Destruction reactions of CO in a $L = 10^{17}$ cm scenario (straight-dot) compared with a scenario without diffusion (dash-dotted line). Model parameters: same as the Figure [6.52].

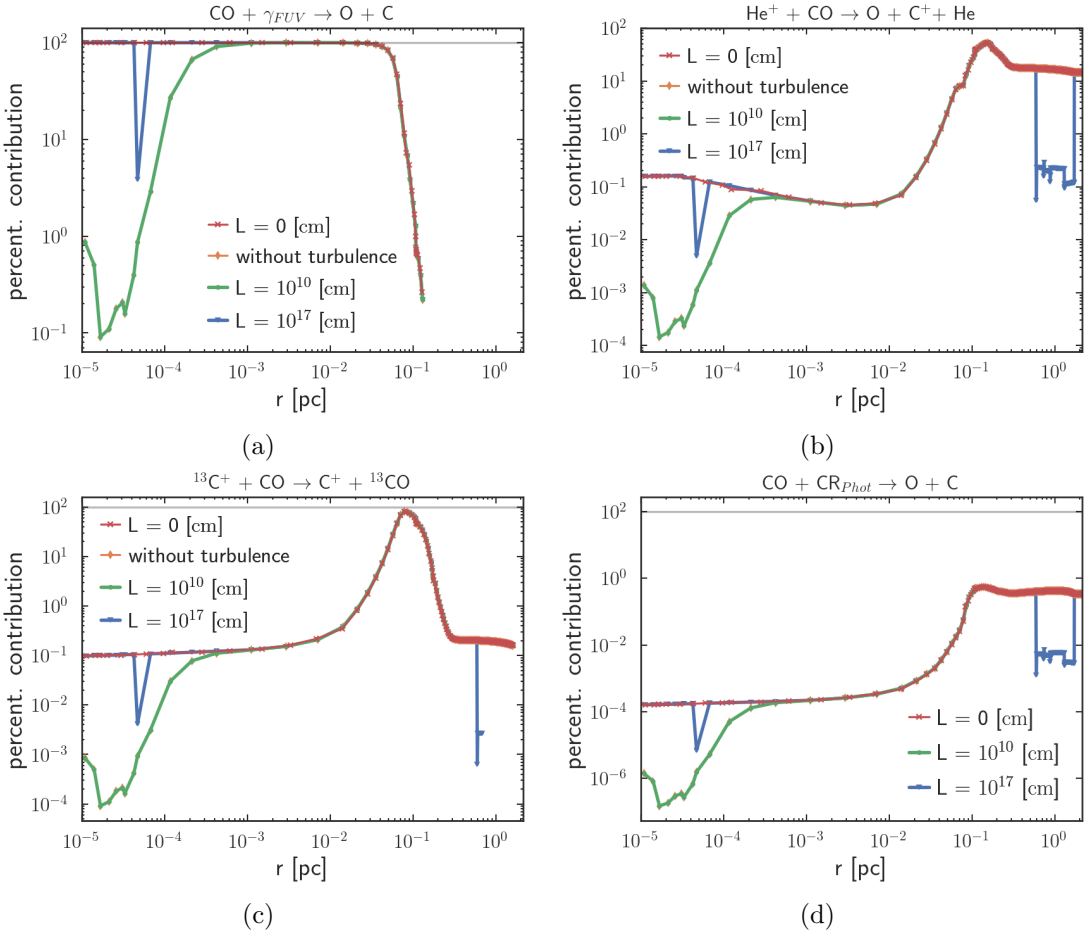


Figure 6.66: Percentage of contributions to the destruction reactions of CO in different diffusion scenarios. Model parameters: same as the Figure [6.61].

shells.

The destruction reactions, photodissociation of CO, and $^{13}C^+ + CO \longrightarrow C^+ + {}^{13}CO$ shows higher contribution in the region $2 \times 10^{-5} \leq r \leq 6 \times 10^{-5}$ pc than scenario without diffusion (Figure [6.62]). At lower coherence lengths of turbulent diffusion, the contribution from the photodissociation of CO to the total destruction of CO reduced down to 0.1% and then increased up to 100% (Figure [6.66a]). At higher coherence lengths of turbulent diffusion, the contribution from this reaction only reduced at a particular shell in the cloud due to the diffusion contribution in the region. Similarly, the contribution from the reaction, $^{13}C^+ + CO \longrightarrow C^+ + {}^{13}CO$ reduced down to $10^{-4}$% at lower coherence lengths of turbulent diffusion (Figure [6.66c]) and then increased up to 1%. In the absence of diffusion, the reaction $H_3{}^+ + CO \longrightarrow HCO^+ + H_2$ contributes significantly in the region $r \geq 5 \times 10^{-4}$ pc. However, it can be observed that when the coherence length is $L = 10^{17}$ cm, the reaction starts to make a substantial contribution in the region where $r \geq 0.001$ pc. The observed phenomenon can be attributed to the notable impact of diffusion in the specified areas.

### 6.4.3 $CH^+$ and CH

The main formation reactions of CH in the cloud are $CH_3^+ + e^- \longrightarrow CH + H + H$ and $CH_3^+ + e^- \longrightarrow CH + H_2$. The destruction of CH is through the reaction $CH + H \longrightarrow C + H_2$. Diffusion influenced the destruction of CH significantly (Figure [6.68]), especially on the surface; the diffusion is at least four orders of magnitude higher than the rest of the chemistry. The diffusion of H also impacted the destruction of CH via the reaction $CH + H \longrightarrow C + H_2$.

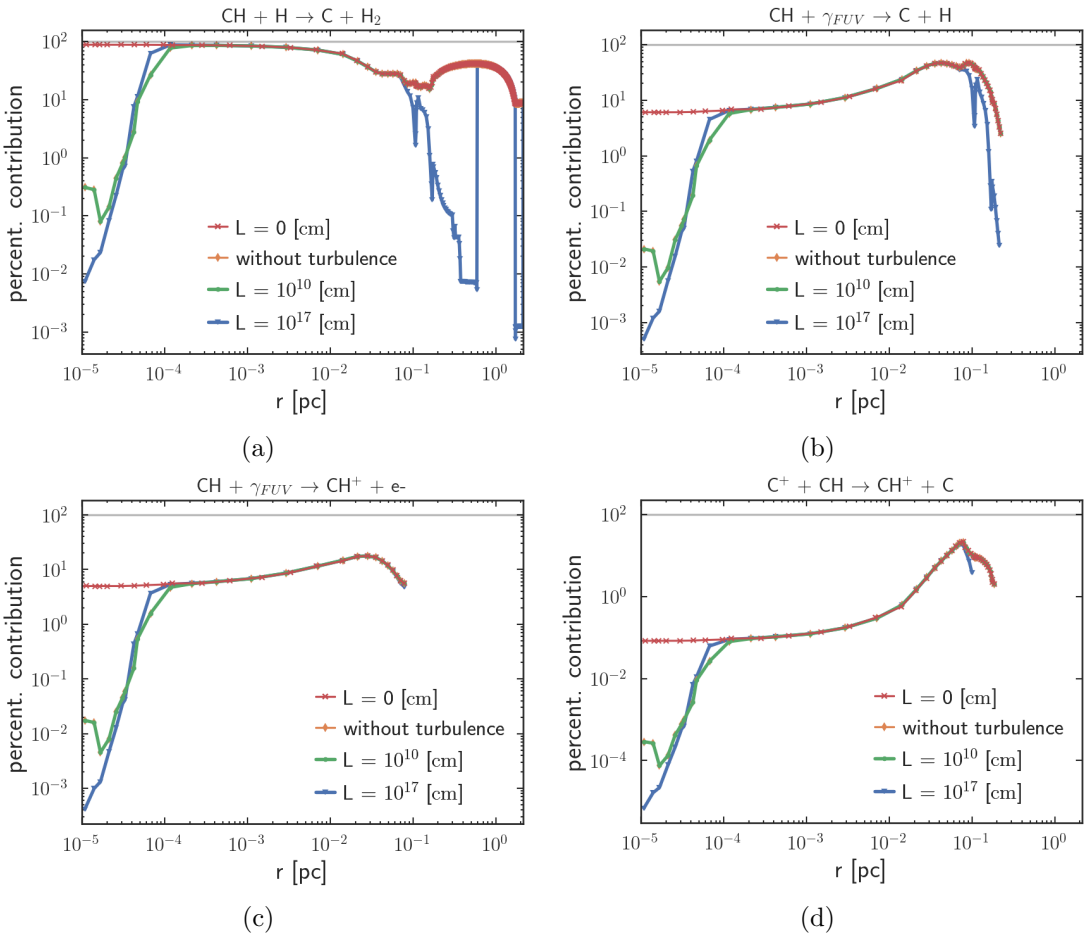


Figure 6.67: Percentage of contributions to the destruction reactions of CH in different diffusion scenarios. Model parameters: case II (table [6.1]).

Figure [6.67] illustrates the change in the percentage of contribution to the total destruction rate of CH as the coherence length increases. In the absence of turbulence, the reaction $CH + H \longrightarrow C + H_2$ exhibits negligible deviation in its contribution compared to the scenario without diffusion. The photodissociation and photoionization of CH show a significant change in the rates at the surface (Figure [6.68]). The destruction reaction $H^+ + CH \longrightarrow CH^+ + H$ is a significant contributor in a scenario without diffusion, which did not contribute significantly in a scenario with diffusion (green dash-dotted line in the Figure [6.68b] and Figure [6.70b]).

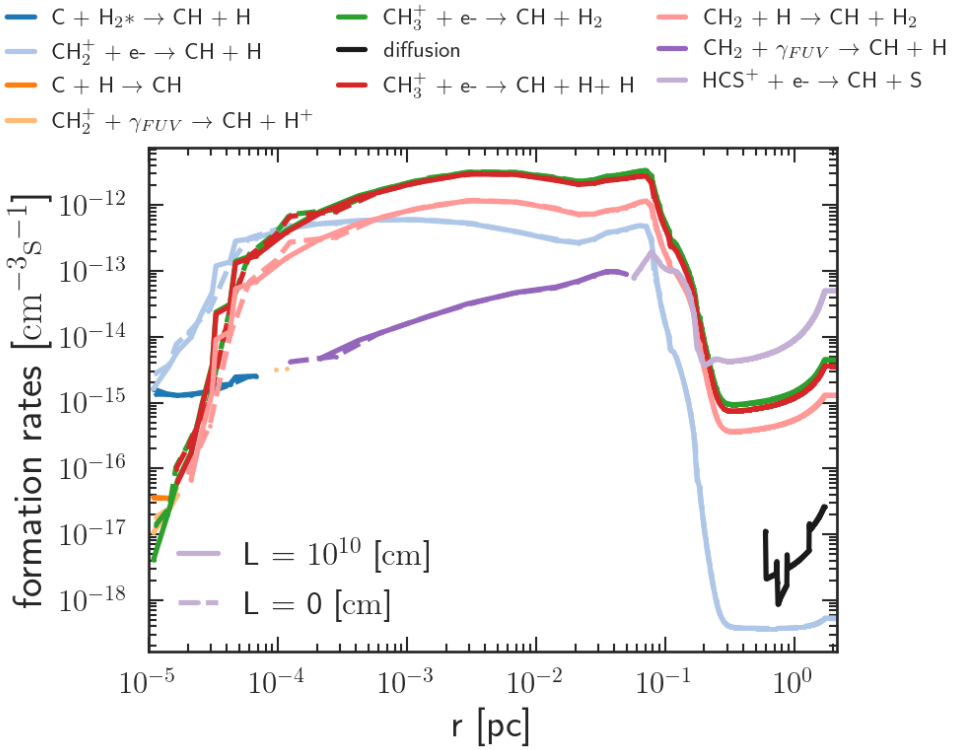


(a) formation reactions

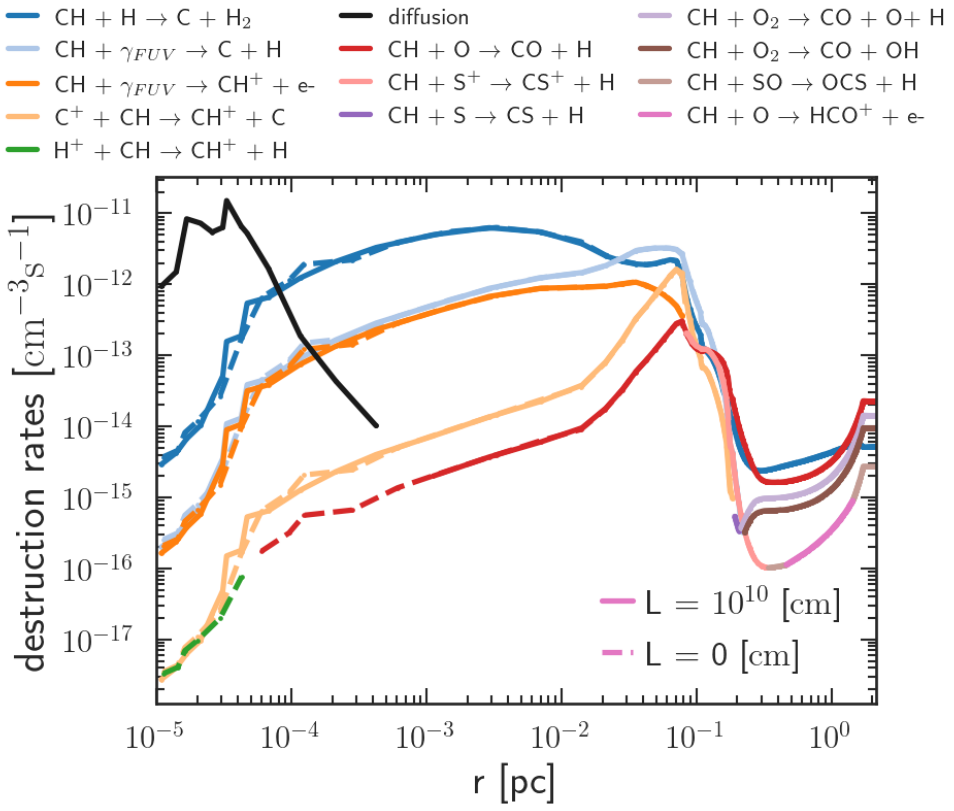


(b) destruction reactions

Figure 6.68: Formation and destruction rates for CH with $L = 10^{10}$ cm. Model parameters: same as the Figure [6.61].

With $L = 0\,\text{cm}$, the reaction $\text{CH} + \text{O} \longrightarrow \text{CO} + \text{H}$ is a significant contributor to the total destruction in the region $6 \times 10^{-5} \leq r \leq 2.13\,\text{pc}$. With $L = 10^{10}\,\text{cm}$, the aforementioned reaction contributes less on the surface than the $L = 0\,\text{cm}$ scenario (Figure [6.68b]). Also, the reaction $\text{C}^+ + \text{CH} \longrightarrow \text{CH}^+ + \text{C}$ contributes less as the coherence lengths of turbulent diffusion increases to $L = 10^{17}\,\text{cm}$ in the region $r \geq 0.1\,\text{pc}$ (Figure [6.70]). Figure [6.67d] illustrates that when turbulent diffusion is included, the percentage of contribution from the above-mentioned reaction reduces significantly in the region $r \leq 2 \times 10^{-4}\,\text{pc}$.

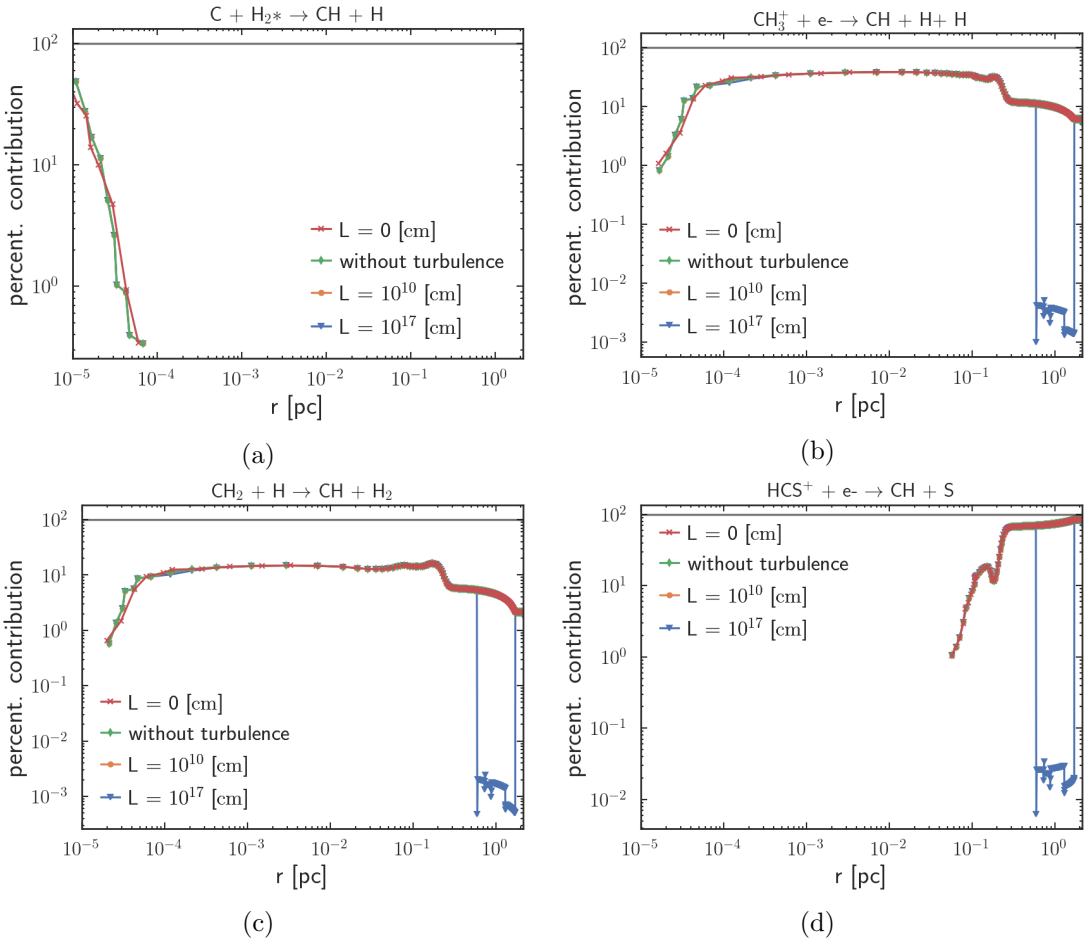


Figure 6.69: Percentage of contributions to the formation reactions of CH in different diffusion scenarios. Model parameters: same as the Figure [6.71].

Diffusion is not a top contributor to the formation or destruction of CH in the mid-depth regions, $10^{-3} \leq r \leq 0.1\,\text{pc}$. This is because the diffusion rates in this region are lower than the rest of the chemical reaction rates, as illustrated in §[C.5]. As a result, the chemical reaction rates of the with-diffusion scenario in this region closely resemble those of the without-diffusion scenario. With a coherence length of $L = 10^{10}\,\text{cm}$, diffusion rates are about two orders of magnitude lower than the top contributor reaction $\text{HCS}^+ + \text{e}^- \longrightarrow \text{CH} + \text{S}$ in the region $r \geq 0.6\,\text{pc}$ (Figure [6.68a]). Whereas with a coherence length of $L = 10^{17}\,\text{cm}$, the

diffusion rates are about three orders of magnitude higher than the top contributor reaction $HCS^+ + e^- \longrightarrow CH + S$ in the region $r \geq 0.6\,pc$ (Figure [6.70a]). Without turbulence, the contribution from diffusion to the formation/destruction of CH is negligible.

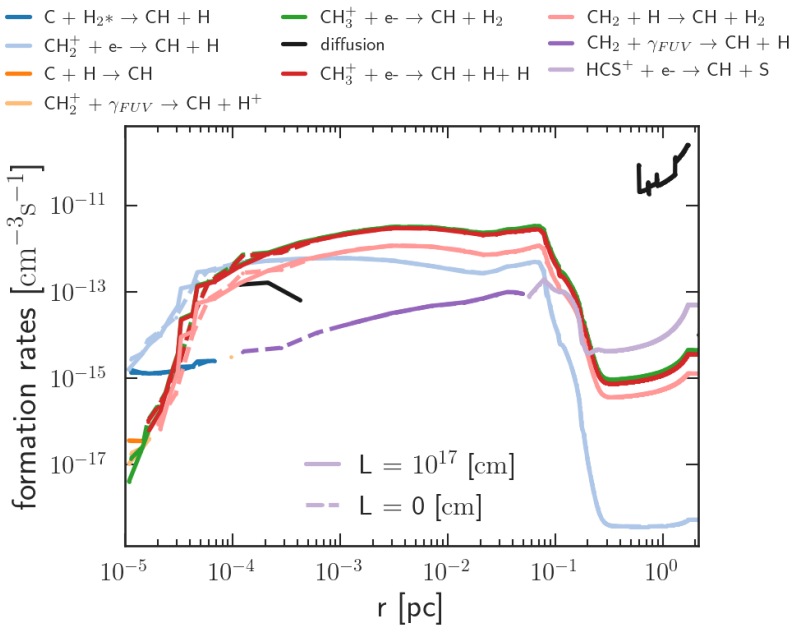


(a) Formation reaction

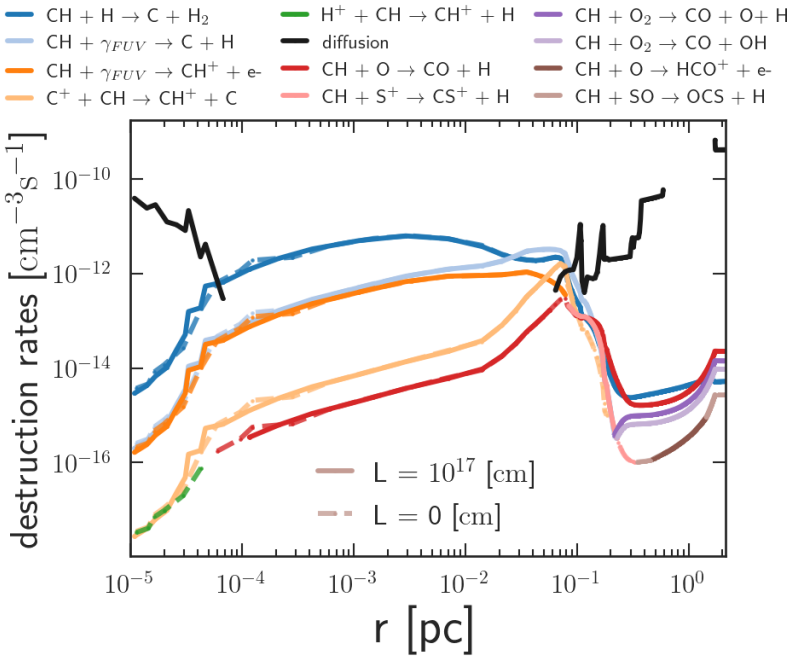


(b) Destruction

Figure 6.70: Formation and destruction rates for CH with $L = 10^{17}\,cm$. Model parameters: same as the Figure [6.71].

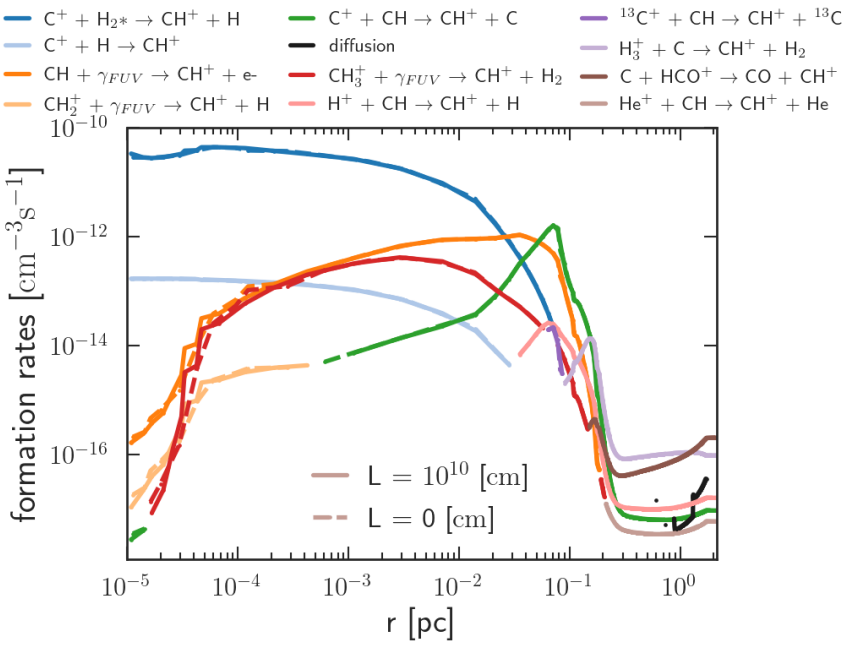


(a)

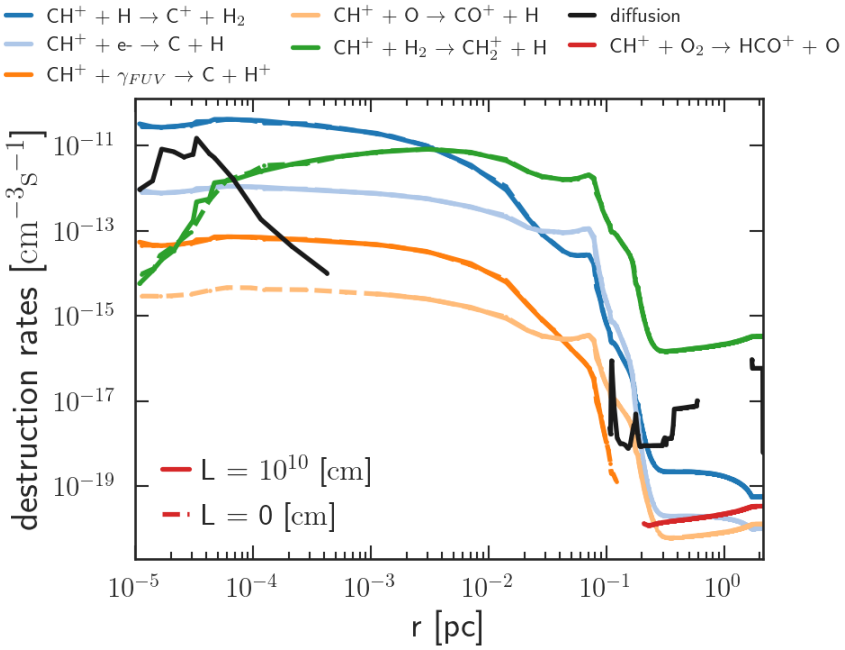


(b)

Figure 6.71: Formation (a) and destruction (b) rates for $CH^+$ with $L = 10^{10}$ cm. Model parameters: same as the Figure [6.68].

Similar to CH, the formation and destruction of $CH^+$ are also influenced by diffusion. Figure [C.7a] demonstrates that diffusion rates are similar in scenarios with and without turbulence in the region of $3 \times 10^{-5} \lesssim r \lesssim 10^{-3}$ pc because thermal diffusion rates are higher than turbulent and molecular diffusion rates. In the scenario with a turbulent coherence length, $L = 10^{16}$ cm, the turbulent and

thermal diffusion rates are on the same scale, leaving the resultant total diffusion rates different from the other diffusion scenarios in the region $r \lesssim 3 \times 10^{-5}$ pc. Similarly, for $L = 10^{17}$ cm, the turbulent diffusion rates are higher than the thermal diffusion rates, resulting in higher total diffusion rates in the region $r \lesssim 3 \times 10^{-5}$, deviating from the other diffusion scenarios. As the coherence length increases to $L = 10^{17}$ cm, the total diffusion rates exhibit a linear rise in relation to the coherence length within the region $r \geq 10^{-3}$ pc.

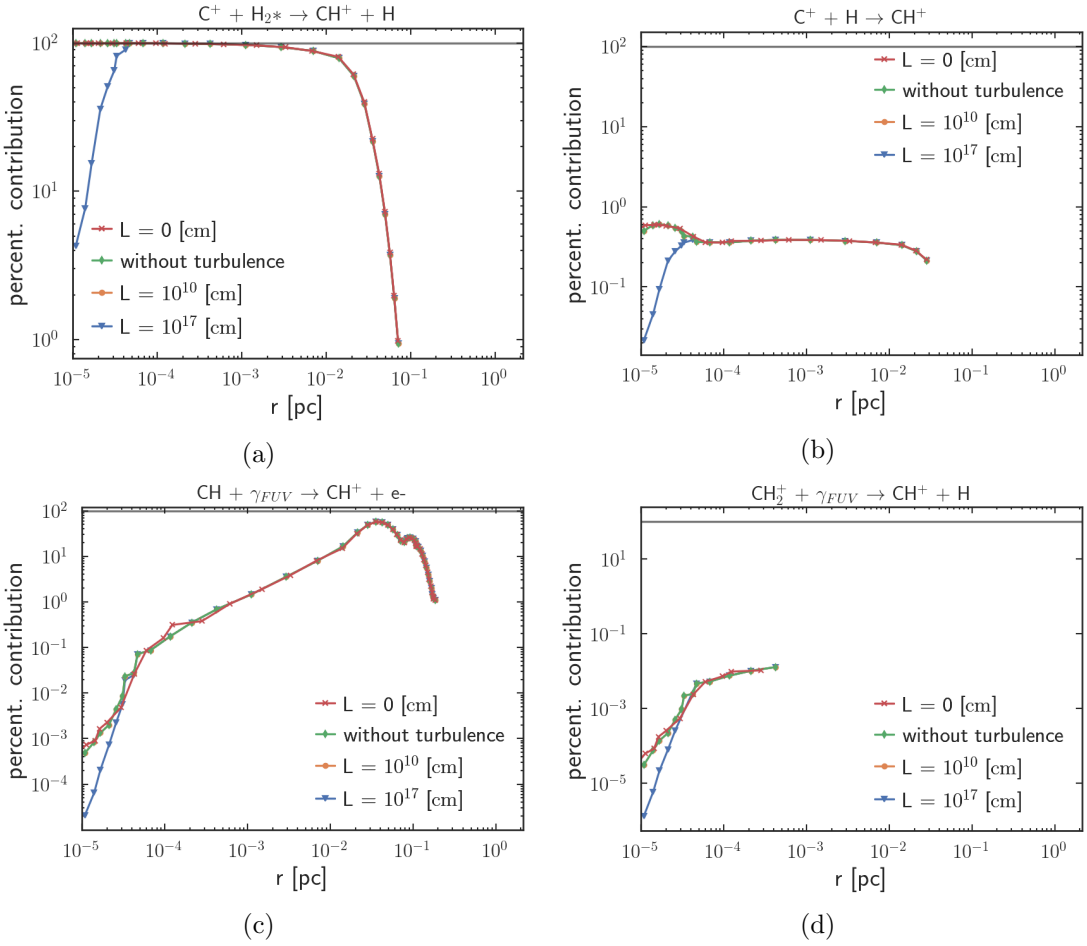


Figure 6.72: Percentage of contributions to the formation reactions of $CH^+$ in different diffusion scenarios. Model parameters: same as the Figure [6.71].

With $L = 10^{10}$ cm, diffusion of $CH^+$ is a prominent destruction reaction on the surface (Figure [6.71b]). Destruction via $CH^+ + H \longrightarrow C^+ + H_2$ is the top contributor throughout the cloud in all the scenarios except for $L = 10^{17}$ cm as depicted in Figure [6.74a]. In the destruction of $CH^+$, the reaction $CH^+ + O \longrightarrow CO + H$ contributes significantly throughout the cloud the in a $L = 0$ cm scenario. With diffusion, the reaction only contributes significantly from $r \gtrsim 9 \times 10^{-4}$ pc. The destruction reaction $CH^+ + H_2 \longrightarrow {CH_2}^+ + H$ significantly contributes to the destruction of $CH^+$ in all scenarios except $L = 0$ cm(Figure [6.74e]). Formation via $C^+ + H_2\star \longrightarrow CH^+ + H_2$ is the leading contributor in all the (with and without

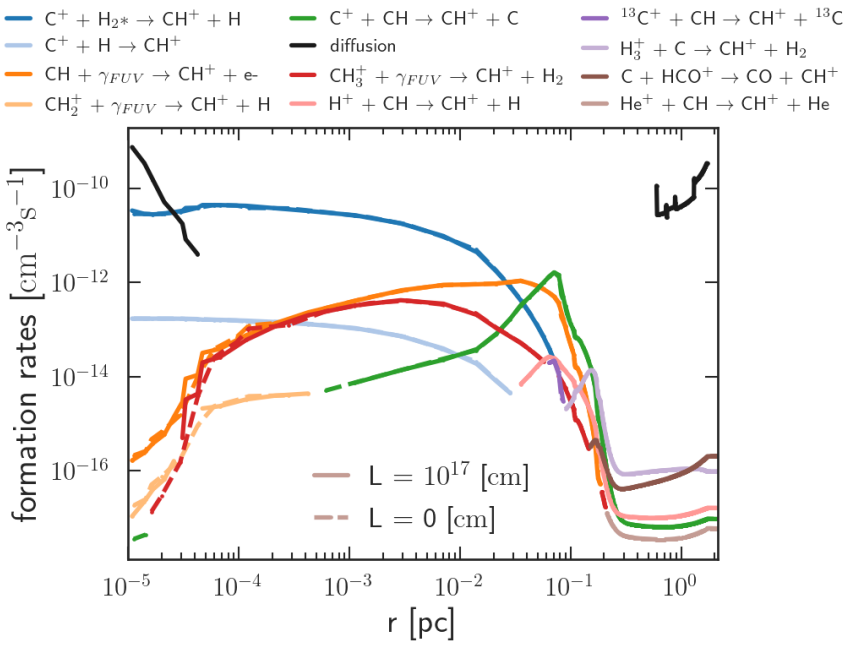


(a)

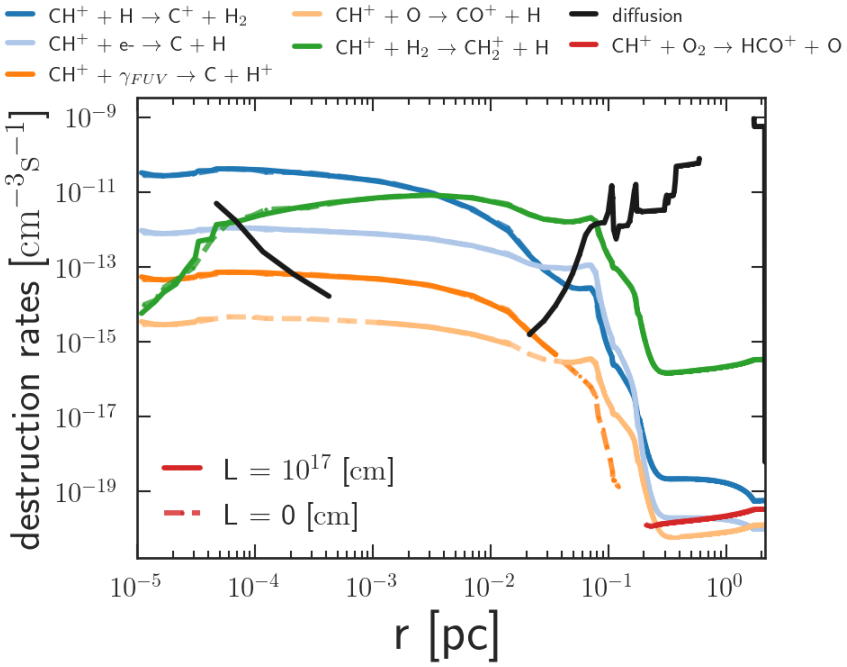


(b)

Figure 6.73: Formation (a) and destruction (b) rates for $CH^+$ with $L = 10^{17}$ cm. Model parameters: same as the Figure [6.68].

diffusion) scenarios. However, formation via photoionization of CH, photodissociation of $CH_2^+$ and $CH_3^+$ shows significant changes on the surface of the cloud. As the coherence lengths of turbulent diffusion increase to $L = 10^{17}$ cm, the contribution from diffusion to the formation is five orders of magnitude higher than the second highest reaction $H_3^+ + C \longrightarrow CH^+ + {}^{13}C$ in the region $r \geq 0.1$ pc.

The chemical structure of CH and $CH^+$ are significantly impacted by diffusion. As illustrated in Figure [B.2a], the abundance of CH and $CH^+$ only shows a negligible deviation from the $L = 0\,\mathrm{cm}$ scenario. Since H, $H_2$, C, CH, and $CH^+$ are the precursor of species, such as $CH_2{}^+$, $CH_3{}^+$, diffusion has a secondary impact on the chemical structure of these species. The $CH_2{}^+$, $CH_3{}^+$ and $CH_2$ show a

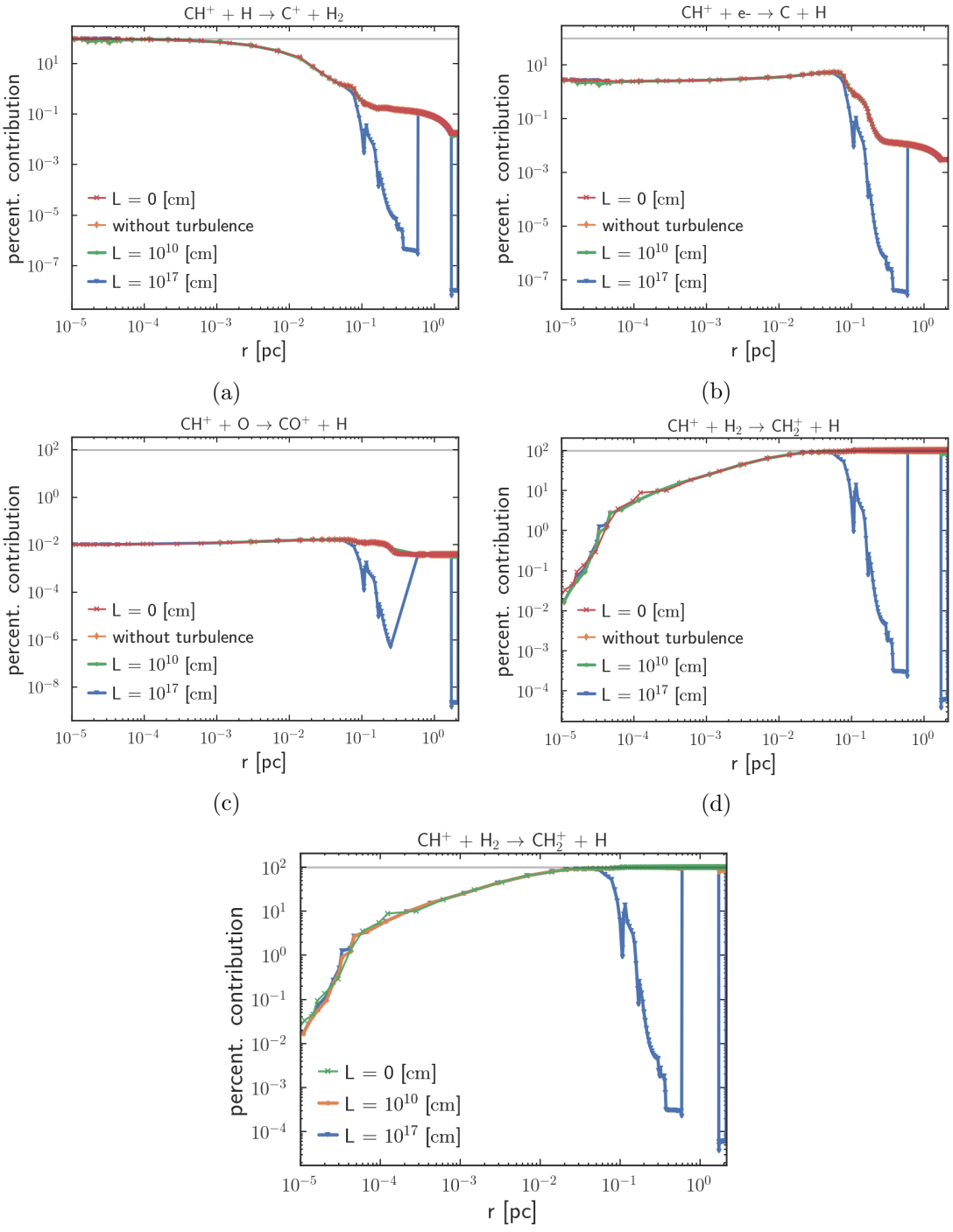


Figure 6.74: Percentage of contributions to the destruction reactions of $CH^+$ in different diffusion scenarios. Model parameters: same as the Figure [6.71].

slight decrease in the abundance in the region $r \lesssim 10^{-4}\,\mathrm{pc}$ and a slight increase in the region $10^{-4} \lesssim r \lesssim 10^{-3}\,\mathrm{pc}$. The abundance of $CH_2{}^+$, $CH_3{}^+$ and $CH_2$ seems to follow the abundance profile of molecular hydrogen.

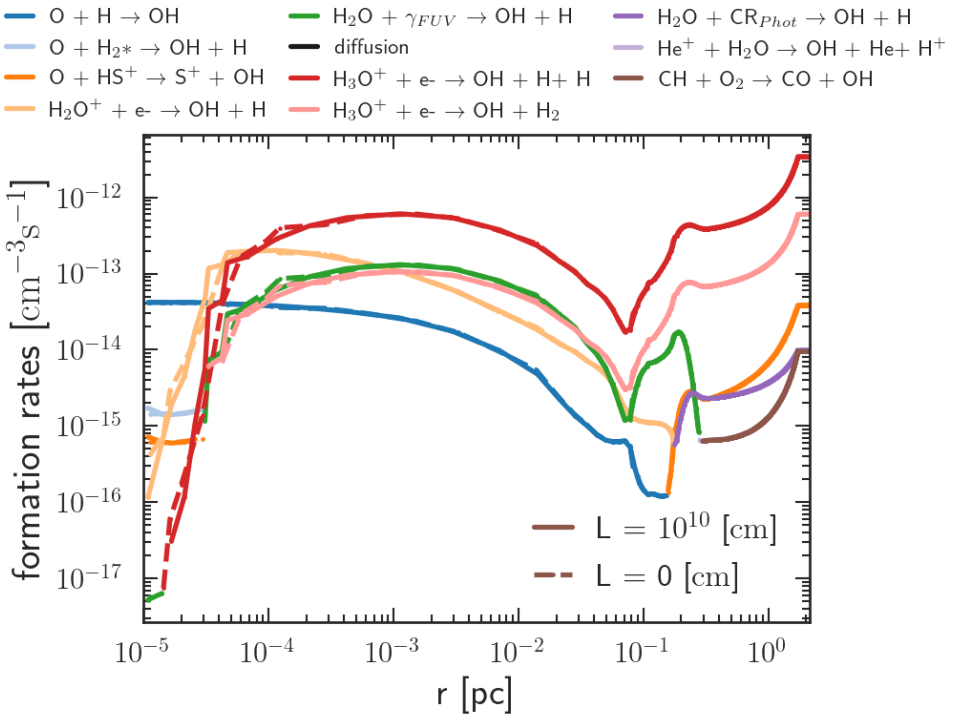


Figure 6.75: Formation reactions of OH with (straight-dot) and without (dashed line) diffusion. A turbulent coherence length of $10^{10}$ cm is used. Model parameters: Case II from table [6.1]

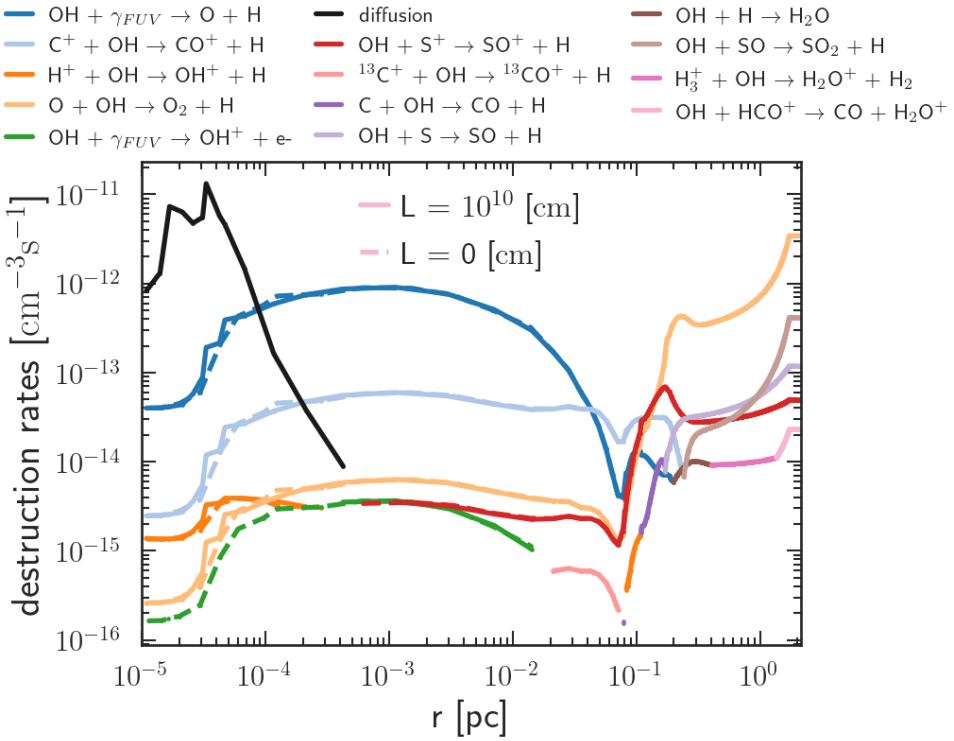


Figure 6.76: Destruction reactions of OH with (straight-dot) and without (dashed line) diffusion. Model parameters: same as Figure [6.75].

### 6.4.4 OH

As illustrated in Figure [B.2f], the abundance of OH does not change significantly when diffusion is added to the chemistry. However, the small variations in the abundance are visible, resulting from chemical reaction changes. The primary formation reactions of OH without diffusion are:

$$\begin{cases} O + H \longrightarrow OH \\ H_3O^+ + e^- \longrightarrow OH + H + H \\ H_2O^+ + e^- \longrightarrow OH + H \end{cases} \tag{6.3}$$

Photodissociation and $O + OH \longrightarrow O_2 + H$ are the primary destruction reactions in a scenario without diffusion.

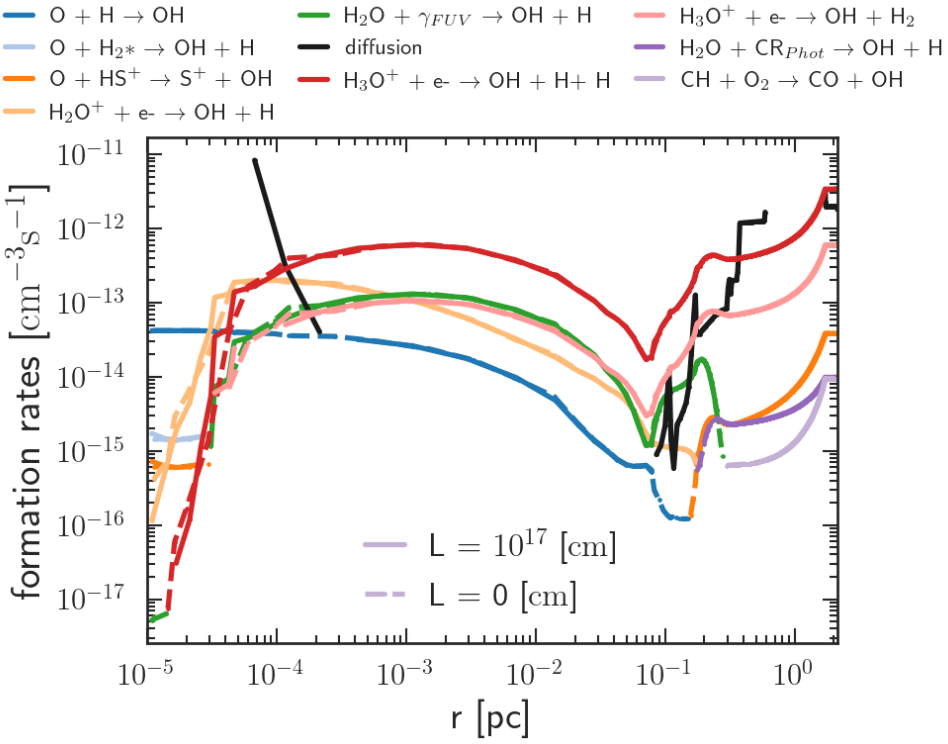


Figure 6.77: Formation reactions of OH with (straight-dot) and without (dashed line) diffusion.

Within the region of $10^{-5} \leq r \leq 0.4\,\mathrm{pc}$, the contribution of thermal diffusion to total diffusion rates with $L = 10^{10}\,\mathrm{cm}$ is at least three orders of magnitude higher than molecular or turbulent diffusion contributions (as depicted in Figure [C.6b]). Due to high thermal diffusion contribution, total diffusion rates remain comparable within the region of $10^{-5} \leq r \leq 0.002\,\mathrm{pc}$, regardless of coherence length (Figure [C.6a]). Similar to CH, contributions from $L = 10^{16}\,\mathrm{cm}$ and $L = 10^{17}\,\mathrm{cm}$ deviate from this trend within the region of $10^{-5} \leq r \leq 4 \times 10^{-5}\,\mathrm{pc}$ due to the higher turbulent diffusion rates than molecular and thermal diffusion rates.

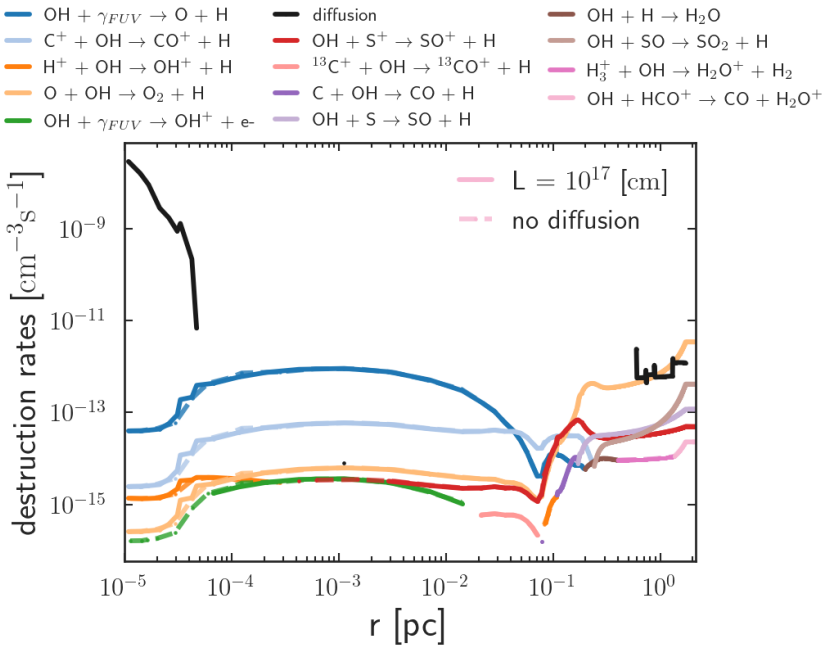


Figure 6.78: Destruction reactions of OH with (straight-dot) and without (dashed line) diffusion.

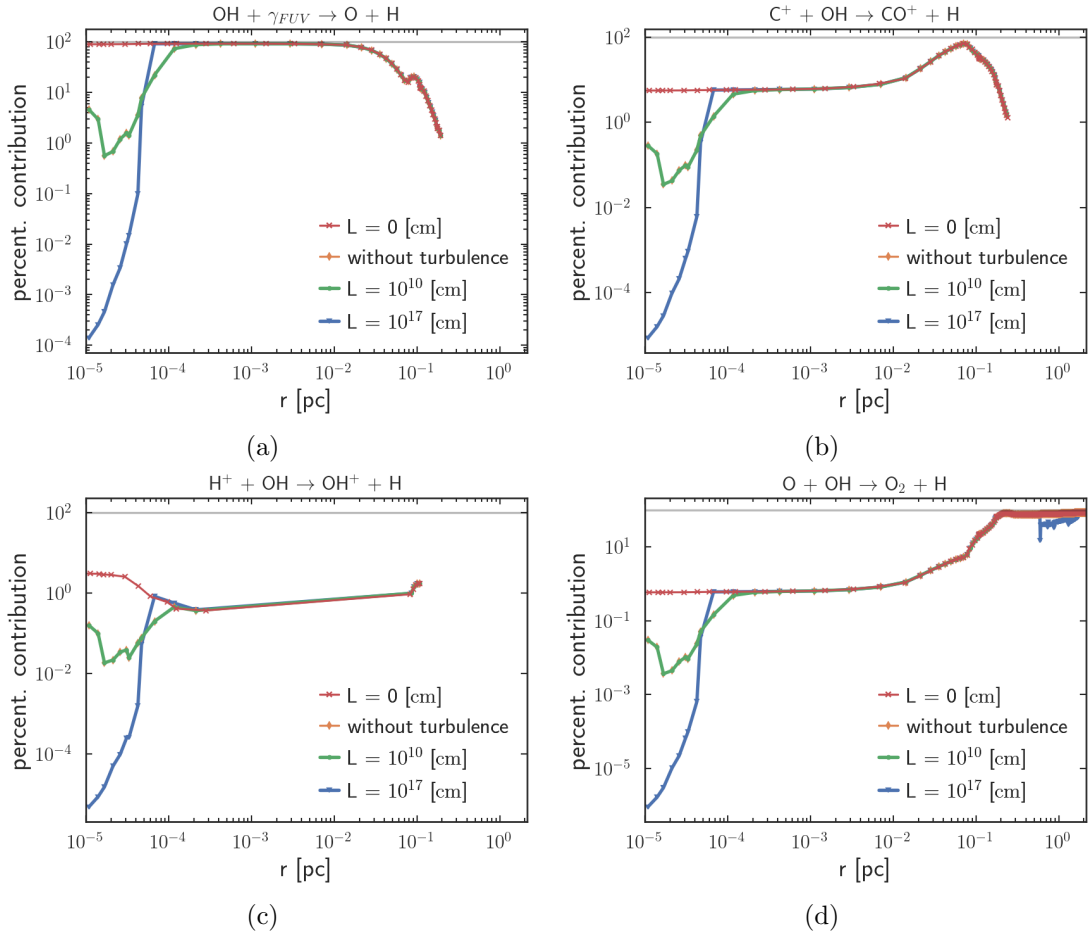


Figure 6.79: Percentage of contributions to the destruction reactions of OH in different diffusion scenarios. Model parameters: same as the Figure [6.76].

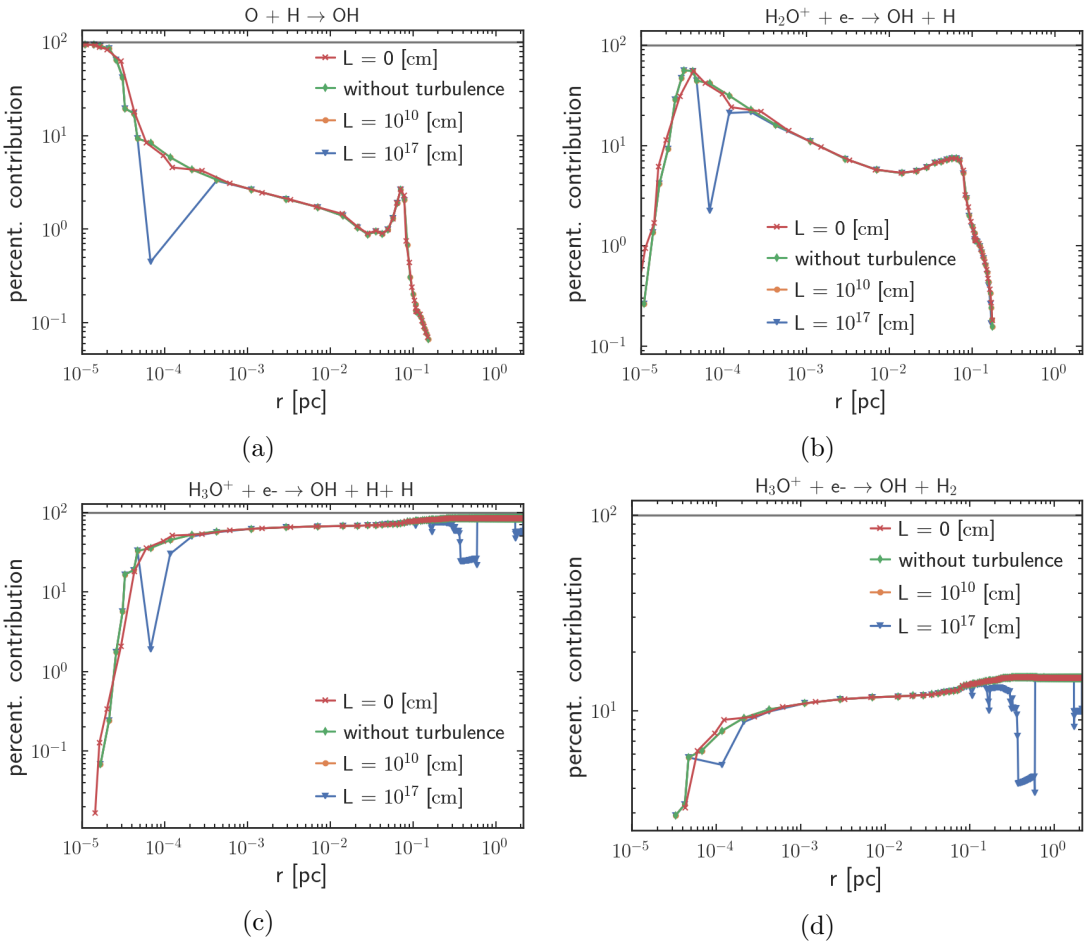


Figure 6.80: Percentage of contributions to the formation reactions of OH in different diffusion scenarios. Model parameters: same as the Figure [6.75].

In the region of $10^{-5} \leq r \leq 4 \times 10^{-4}$ pc, diffusion with $L = 10^{10}$ cm is a destruction reaction, and at most, it is two orders of magnitude higher than photodissociation of OH (Figure [6.76]). With a turbulent coherence length of $10^{17}$ cm, diffusion becomes a destruction reaction within the region of $10^{-5} \leq r \leq 5 \times 10^{-5}$ pc and $r \geq 0.6$ pc. Diffusion and photodissociation of OH and $O + OH \longrightarrow O_2 + H$ are the primary destruction reactions with $L = 10^{17}$ cm. As the coherence lengths of turbulent diffusion increase, the diffusion rates increase up to $\sim 10^{-9}\text{cm}^{-3}\text{s}^{-1}$, which is four orders of magnitude higher than the next highest destruction reaction rate of OH. Consequently, the percentage of contribution from the other destruction reactions to the total destruction rate of OH reduces significantly, as illustrated in Figure [6.79]. The scenario without turbulence shows a minor impact on the chemistry of the of OH.

The formation reaction rates of $H_2O^+ + e^- \longrightarrow OH + H$ and $H_3O^+ + e^- \longrightarrow OH + H + H$ exhibit deviations from the scenario without diffusion on the surface ($r \leq 3 \times 10^{-4}$ pc). At lower coherence lengths, the diffusion is not a significant formation reaction of OH; however, with $L = 10^{17}$ cm diffusion contributes

significantly in the region $6 \times 10^{-5} \leq r \leq 2 \times 10^{-4}\,\mathrm{pc}$ and $0.08 \lesssim r \lesssim 0.5\,\mathrm{pc}$. As the diffusion contribution to the total formation rate increases in the above-mentioned regions, the percentage of contribution from other chemical reactions reduces correspondingly (Figure [6.80]). With $L = 10^{17}\,\mathrm{cm}$ , formation reaction $\mathrm{He}^+ + \mathrm{H_2O} \longrightarrow \mathrm{OH} + \mathrm{He} + \mathrm{H}^+$ is no longer a significant contributor to the total formation of OH compared to other scenarios with and without diffusion.

# Chapter 7

# Discussion

To comprehend the impact of diffusion on the physical and chemical composition of molecular clouds, it is imperative to analyze the diffusion coefficients that are subject to local conditions. This study included energy balance, cosmic ray ionization, $H_2$ formation, photodestruction process, CO and $H_2$ self-shielding, gas-dust interactions, and dust surface chemistry. This study explores the correlation between different diffusion coefficients and their contributions to total diffusion rates. Additionally, it delves into the impact of cloud temperature on diffusion rates, the potential non-linearity of coherence length correlations, and the relationship between chemistry and diffusion. With this work, the diffusion scenario has incorporated the chemistry of the KOSMA-$\tau$ PDR model, and different input parameters and diffusion coefficients have been tested to evaluate different limits. The effects on the observable line emissions are also assessed.

## 7.1 Initial conditions

The four cases used in this model are in the table [6.1]. Case II is evaluated in detail and presented in §[6]. All other test cases are tested and compared to the corresponding non-diffusion case. The comparison did not reveal qualitatively any significant change in the abundances or column density (compared to the corresponding case without diffusion) other than demonstrated using Case II. However, testing with different surface densities, masses, and radii of the cloud revealed the following limits.

The minimum size of the KOSMA-$\tau$ spherical cloud is $10^{-2}$pc. A minimum surface density of $10^3\,\mathrm{cm}^{-3}(M = 10^4 M_\odot)$ is needed to calculate the higher diffusion ($10^{12} \leq L \leq 10^{17}$cm) cases. Otherwise, the equilibrium chemistry solver will give negative or too low ($\leq 10^{-33}$) densities. In this case, diffusion will be switched off to recover the chemistry and solve for a steady-state solution. When the diffusion is switched off, the contribution to the $\mathbb{F}$ and $\mathbb{Q}$ from diffusion is

set to zero. The interpolated positions, densities, temperature, and calculated diffusion rate prior to deactivation will be documented for debugging.

### 7.1.1 Coherence length and diffusion coefficients

As already discussed, the diffusion coefficients in a multi-component plasma are poorly known. A detailed discussion of the limits of the diffusion coefficients is given in §[4.4].

The study by Lesaffre et al. (2007) considers that the electrostatic force binds the ions and electrons to have the same diffusion coefficients for the ion-electron fluid. Considering the same diffusion coefficients for ions and electrons will result in a lower thermal diffusion coefficient for electrons. The presence of free electrons is crucial for the mixing of various phases within the interstellar medium. Due to their relatively lower mass, electrons exhibit faster diffusion velocities than other species (Figure [7.1]). Consequently, collisions between electrons and other species can result in the heating of the gas. $C^+$ and $H_3{}^+$ are shown to compare the velocities of ions with electrons (Figure [7.1]). The thermal velocity of the electron is calculated using eq.[4.8] with $\mu = m_e$. Even though the diffusion velocity of electrons is one order of magnitude higher than the ions, the medium will remain neutral. Because the thermal energy is lower than the electrostatic energy between the ions and electrons. For example, the thermal energy of a particle with a temperature

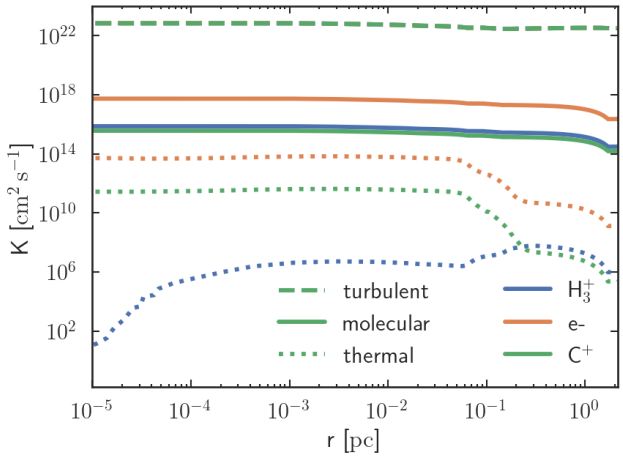


(a) diffusion coefficients

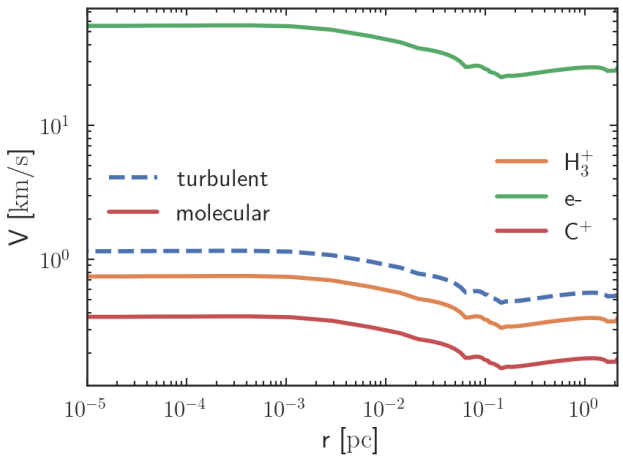


(b) diffusion velocities

Figure 7.1: Variation of individual diffusion coefficients (a) and velocities (b) with $L = 10^{17}$ cm for $e^-$, $C^+$, and $H_3{}^+$. Model parameters: Case II (table 6.1).

of 120 K will be,

$$E = \frac{3}{2}kT = \frac{3}{2} \times 1.38 \times 10^{-23} \times 120\, J/K\, K = 2.484 \times 10^{-21} J \tag{7.1}$$

Considering the step size (width of a shell in the KOSMA-$\tau$ PDR model) ($\sim$ 0.001pc) as the distance between the ion and the electron, electrostatic energy between electrons and the singly ionized atom will be,

$$E = \frac{1}{4\pi\,\epsilon_0}\frac{q_1 q_2}{r} = 8.99 \times 10^9 \frac{(-1.602 \times 10^{-19}\mathrm{C})^2}{0.001\mathrm{pc}} \mathrm{Nm^2/C^2} \approx 7 \times 10^{-18}\mathrm{J} \tag{7.2}$$

The distance between the electrons and ions is usually smaller than 0.001 pc. From the above equations, it is clear that the thermal motion of the electrons is not strong enough to surpass the electrostatic force between them. As a result, the medium will remain neutral.

KOSMA-$\tau$ is a 1D PDR model that cannot generate turbulent diffusion self-consistently. Hence, the maximum diffusion coefficient and the coherence length of diffusion should also be considered input parameters. For a cloud of radius, 2.13 pc, the largest turbulent eddy will be the size of 0.213 pc ($L \leq 10\%R$ Xie et al. 1995; Mac Low & Ossenkopf 2000). With transonic turbulence ($\sim$ 1 km/s), the highest diffusion coefficient of $10^{22} \leq K \leq 10^{23}\mathrm{cm^2\,s^{-1}}$ can be achieved. Suppose the turbulent coherence length is $L = 10^{14}$ cm ($K = 10^{19}\,\mathrm{cm^2\,s^{-1}}$), a cloud with a radius of 2.13 pc can have a considerable turbulent diffusion contribution (higher than thermal and molecular diffusion) to the total diffusion rate for most species. In this case, the chemistry of most of the species is significantly influenced by diffusion throughout the cloud. When the coherence length is $10^{10} \leq L \leq 10^{14}$ cm, the turbulent or thermal diffusion contributes significantly to the total diffusion rates of most of the species. In this case, the diffusion contribution to the chemistry is significant in the warmer atomic region of the cloud (see §[6.4]).

The total diffusion rate combines thermal, molecular, and turbulent diffusion rates. For species such as $\mathrm{C, CO, C^+}$, OH or CH, the thermal diffusion rates are higher than the molecular and turbulent diffusion rates at lower coherence lengths ($L \leq 10^{14}$ cm) (Figure [C.1-C.7]). This implies that the total diffusion rates of a species depend heavily on thermal diffusion rates, density gradient, and coherence length of turbulent diffusion. Hence, the total diffusion rate does not always have a linear relation with the turbulent coherence length. Instead, the total diffusion rates of a species have a non-linear relation with the turbulent coherence length and the temperature and density gradient.

The underlying assumption of the model is that the turbulence is in a tran-

sonic state, meaning that the velocity of the gas varies proportionally to the square root of its temperature. In an isothermal gas environment, the diffusion coefficient remains uniform across the entirety of the gas clump. The chemistry is strongly affected by turbulent diffusion at lower coherence lengths (see §[6.2]). The chemical structure can exhibit considerable variation based on factors such as the coherence length and gas temperature. Therefore, selecting the coherence length becomes crucial for interpreting observational findings in the context of isothermal cold molecular clouds.

## 7.2 Impact of diffusion on the H-$H_2$ transition

The previous studies (Xie et al. 1995; Willacy et al. 2002; Lesaffre et al. 2007) pointed out that when diffusion is added, the abundance of $H_2$ and hence CH is reduced at the interface between WNM and CNM compared to a scenario without diffusion. They also noted the enhancement in the production of $CO, OH$ and $H_2O$ due to diffusion. Diffusion pumps $H_2$ from the cold cloud (Lesaffre et al. 2007) to the warmer regions, and as a result, the abundance of $H_2$ has increased at intermediate temperatures, as shown in §[6.3.2]. As a result of mixing between the diffused H from the warmer region with the diffused $H_2$ from the colder region, the $H-H_2$ transition occurs at slightly warmer temperatures compared to the scenario without diffusion. Diffusion of H towards the center of the cloud reduces the formation of $H_2$ through grain catalysis, which reduces the abundance of $H_2$ on the surface ($r \leq 10^{-4}$ pc) compared to the scenario without diffusion. However, the diffusion of $H_2$ contributes comparably to the primary formation reaction $H + H \longrightarrow H_2$, replenishing the missing $H_2$. Thus, the resultant abundance of H and $H_2$ does not show drastic variation compared to the scenario without diffusion, and $H-H_2$ transition region shifted towards the surface of the cloud. In other words, an expansion of the molecular region is observed.

As the coherence length varies, the diffusion contribution to the total formation or destruction of the species changes. However, the contribution from other chemical reactions to the total formation or destruction reaction alters in such a way that the resultant equilibrium abundance is similar to the scenario without diffusion. As a result, this study failed to see any difference in the abundance when tested with different $L$ values in the steady state. However, the impact of different coherence lengths might be visible in a time-dependent chemistry model.

The $H-H_2$ conversion plays a vital role in the properties of the giant molecular cloud (GMC) and, therefore, the initial conditions of star formation (Lee et al. 2012). The $H-H_2$ conversion is mainly investigated in the PDRs where an atomic envelope bounds the dense molecular region. But the GMC is surrounded by an HI envelope embedded in the radiation field from stars and stellar clusters (Lee et al. 2012), which makes the angular dependence of the radiation, depth dependence of $H_2$ formation, and the prediction of $H-H_2$ transition region important. The study by Lee et al. (2012) used a model created by Krumholz et al. (2008, 2009) and discussed that turbulence might play a role in the $H_2$ formation. From the diffusion and chemical reaction rates, it is clear that the transonic turbulent diffusion accelerates the $H_2$ formation in the PDR, which can have a significant impact on the GMCs. By incorporating the diffusion into the steady-state spherical KOSMA-$\tau$ PDR model, an accurate prediction of $H-H_2$

| Species | integrated line intensity ratio | |
|---|---|---|
| | $\xi = 1.5$ | $\xi = 0$ |
| $[^{12}\mathrm{CI}]/[^{13}\mathrm{CI}]$ | 68 (71) | 66 (71) |
| $[^{12}\mathrm{CI}]/^{12}\mathrm{CO}\,(1 \to 0)$ | 0.12 (0.10) | 0.15 (0.10) |
| $[^{12}\mathrm{CII}]/^{12}\mathrm{CO}\,(1 \to 0)$ | 0.5 (0.4) | 0.5 (0.4) |
| $^{13}\mathrm{CO}(1 \to 0)/^{12}\mathrm{CO}(1 \to 0)$ | 0.4 (0.3) | 0.4 (0.3) |
| $^{12}\mathrm{CO}(2 \to 1)/^{12}\mathrm{CO}(1 \to 0)$ | 0.5 (0.4) | 0.5 (0.4) |

Table 7.1: Impact of diffusion on the integrated line intensity ratio of different species. Corresponding without diffusion values are given in the bracket. Model parameters: Case II from the table [6.1] with $L = 10^{17}$ cm.

transition can be made. Further studies are required to analyze the results in stationary and time-dependent models.

## 7.3 Impact of diffusion on the carbon transition

[CII] has a lower ionization potential (11.3 eV) than HII (13.6 eV) and can be ionized by lower-energy photons. [CII] line can originate from different phases of the ISM: dense PDRs, cold/warm neutral medium, or warm ionized medium (Tarantino et al. 2018). In most galaxies in the local universe, [CII] originates from neutral regions (Pabst et al. 2021), and it is the brightest FIR line in the spectrum of the Milky Way (Pabst et al. 2022). Hence, $C^+$ is one of the most important species in astronomy to understand the local conditions.

With diffusion, the $C^+ - C - CO$ transition shifts towards the surface of the

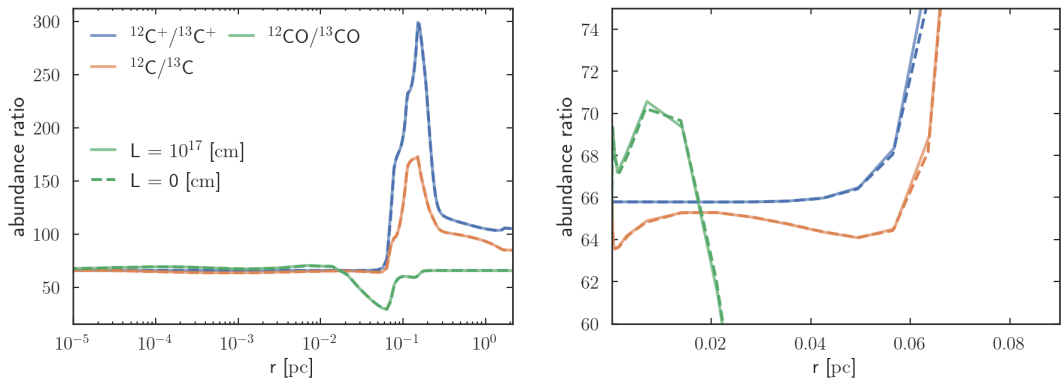


Figure 7.2: Impact of diffusion on the isotopic abundance ratio. The behavior of abundance ratio in the entire cloud (left) and zoomed-in (right). Both subfigures have the same labels.

cloud (Figure [6.26]), increasing the CO abundance and decreasing the $C^+$ abundance compared to the scenario without diffusion. Consequently, the isotopic abundance ratios of $C^+$ and CO (Figure [7.2]) and integrated line intensity ratios of these species show significant deviations with diffusion (table [7.1]).

The isotopic fractionation of carbon is driven by the reaction (Ossenkopf et al. 2013),

$$^{13}C^+ + CO \rightleftharpoons C^+ + {}^{13}CO + 34.8\ \mathrm{K}, \tag{7.3}$$

and it indicates that at colder ($T_{\mathrm{gas}} \leq 35\,\mathrm{K}$) molecular regions, the abundance of $^{13}C^+$ and CO reduces, and the abundance of $^{12}C^+$ and $^{13}CO$ increases. Consequently, the isotopic abundance ratio $^{12}C^+/^{13}C^+$ increases and the $^{12}CO/^{13}CO$ decreases.

The addition of diffusion results in a decrease in the isotopic integrated line intensity ratio of $[^{12}CI]/[^{13}CI]$ from 71 to 68 (table [7.1]). In contrast, the integrated line intensity ratio of $^{12}CO\,(2 \rightarrow 1)/\,^{12}CO(1 \rightarrow 0)$ shows a $\sim 33\%$ increase and $^{13}CO\,(1 \rightarrow 0)/\,^{12}CO(1 \rightarrow 0)$ demonstrates a $\sim 25\%$ increase when compared to scenarios without diffusion. In addition, the integrated line intensity ratio of $[^{12}CII]/^{12}CO(1 \rightarrow 0)$ shows a $\sim 25\%$ and $[^{12}CI]/^{12}CO(1 \rightarrow 0)$ shows a 20% increase. Nevertheless, no apparent disparity in the ratio between the two distinct turbulence coherence lengths is detected.

The reported variations in the integrated line intensity ratio are due to a combination of diffusion, optical depth effects, and fractionation. Further investigation is required to understand how diffusion impacts the optical depth effects. Many previous studies (for example, Ossenkopf et al. 2013; Okada et al. 2019; Guevara et al. 2020) have attempted to explain the observed column density of [CII] and its isotopic integrated line intensity ratios by exploring the effects of fractionation, self-absorption, and optical depth. However, most of these investigations have concluded that PDR models do not accurately reproduce line and continuum emissions. The introduction of turbulent mixing into the PDR models, in addition to the above-mentioned effects, might be the answer to explain these observations.

## 7.4 Integrated line intensities

Using the ONION shell radiative transfer code, we analyzed the PDR code results to understand the effect of diffusion on the line profiles. The change in the integrated line intensities compared to the no diffusion scenario is shown in the table [7.2]. The effect of cosmic ray ionization rate and radial density profile are also indicated. The integrated line intensities do not vary significantly between various

| Species | $\Delta T_{mb}(\%)$ | |
|---|---|---|
| | $\xi = 1.5$ | $\xi = 0$ |
| $C^+$ ($^2P_{3/2} \rightarrow ^2 P_{1/2}$) | +.54 | −1.41 |
| C ($^3P_1 \rightarrow ^3 P_0$) | +2.11 | −.07 |
| C ($^3P_2 \rightarrow ^3 P_1$) | +5.07 | +.8 |
| $^{13}$C ($^3P_{1,3/2} \rightarrow ^3 P_{0,1/2}$) | +7.55 | +3.86 |
| $^{13}$C ($^3P_{2,5/2} \rightarrow ^3 P_{1,3/2}$) | +13.54 | +5.68 |
| $^{13}C^+$ ($^2P_{3/2,2} \rightarrow ^2 P_{1/2,1}$) | +.66 | −2.61 |
| CO ($1 \rightarrow 0$ ) | −12.12 | +7.38 |
| CO ( $2 \rightarrow 1$ ) | +15.96 | +0.49 |
| CO ($3 \rightarrow 2$ ) | +6.77 | +0.32 |
| $C^{18}O$ ($1 \rightarrow 0$) | +0.04 | +0.0 |
| $C^{18}O$ ($2 \rightarrow 1$) | +0.12 | −0.14 |
| $C^{18}O$ ($3 \rightarrow 2$) | +0.12 | −0.11 |
| $C^{18}O$ ($4 \rightarrow 3$) | +0.07 | −0.06 |
| CS ($1 \rightarrow 0$) | −11.36 | −7.46 |
| CS ($2 \rightarrow 1$) | +0.11 | −23.3 |
| CS ($3 \rightarrow 2$) | +3.92 | −8.24 |
| $H^{13}CO^+$ ($1 \rightarrow 0$) | −5.88 | −7.35 |
| $H^{13}CO^+$ ($2 \rightarrow 1$) | −9.42 | −11.92 |
| $H^{13}CO^+$ ($3 \rightarrow 2$)) | +0.41 | +0.43 |
| $H^{13}CO^+$ ($4 \rightarrow 3$) | −0.02 | +0.13 |
| $CH^+$ ($1 \rightarrow 0$) | −4.45 | +2.56 |
| $CH^+$ ($2 \rightarrow 1$) | +5.17 | +19.62 |
| $CH^+$ ($3 \rightarrow 2$) | +6.48 | +24.66 |
| $CH^+$ ($4 \rightarrow 3$) | +9.16 | +33.09 |
| O ($^3P_1 \rightarrow ^3 P2$) | −.120 | +2.879 |
| O ($^3P_0 \rightarrow ^3 P_1$) | −2.54 | −5.55 |
| O ($^3P_0 \rightarrow ^3 P_2$) | −2.70 | −8.06 |
| $HC^{18}O^+$ ($1 \rightarrow 0$) | −2.7 | −10.84 |
| $HC^{18}O^+$ ($2 \rightarrow 1$) | −2.99 | −5.55 |
| $HC^{18}O^+$ ($3 \rightarrow 2$) | +0.21 | +0.75 |
| $HC^{18}O^+$ ($4 \rightarrow 3$) | −0.0 | +0.05 |

Table 7.2: Percentage of change in the integrated line intensities. Positive signs indicate an increased integrated line intensity compared to the without-diffusion scenario. A decrease in the integrated intensity is indicated using a negative sign. $20-40\%$ changes are highlighted using green. Less than 10% changes are denoted by black, and $10-20\%$ changes are denoted by blue color. Model parameters: Case II from the table [6.1] with $L = 10^{17}$ cm.

diffusion coefficients. The changes $\leq 0.03\%$ are omitted due to the uncertainty in the results and cannot provide observational confirmations. Two digits after the decimal points are provided to understand the results better. An increase in the integrated intensity is indicated using a positive sign, and a decrease in the integrated intensity is indicated using a negative sign. Depending on the radial density profile, many species show increased and decreased integrated intensities.

The CO $(1 \rightarrow 0\ )$ line shows a $\sim 12\%$ decrease in the integrated intensity when diffusion is added whereas CO$(2 \rightarrow 1\ )$ shows a $\sim 16\%$ decrease. In addition, CS $(1 \rightarrow 0\ )$ shows a $\sim 11\%$ decrease in the integrated intensity. Furthermore, the diffusion effects are notably visible in the higher $J(J \geq 8)$ transitions compared to the lower $J(J \leq 8)$ transitions for $^{13}$CO, C$^{18}$O, CH$^+$, CO, CS, H$^{13}$CO$^+$, and HC$^{18}$O$^+$ (Figure [7.3]).

The effects of diffusion on the integrated intensities of species are not strong enough to be detected. However, with the recent advances in astronomical observations, subtle variations in the lines could be detected. In that case, CS, CO, C, HCO$^+$, and $^{13}$C are the best tracers of the diffusion effects. Ions like H$^{13}$CO$^+$ and HC$^{18}$O$^+$ are significantly abundant at lower cosmic ray ionization rates due to the

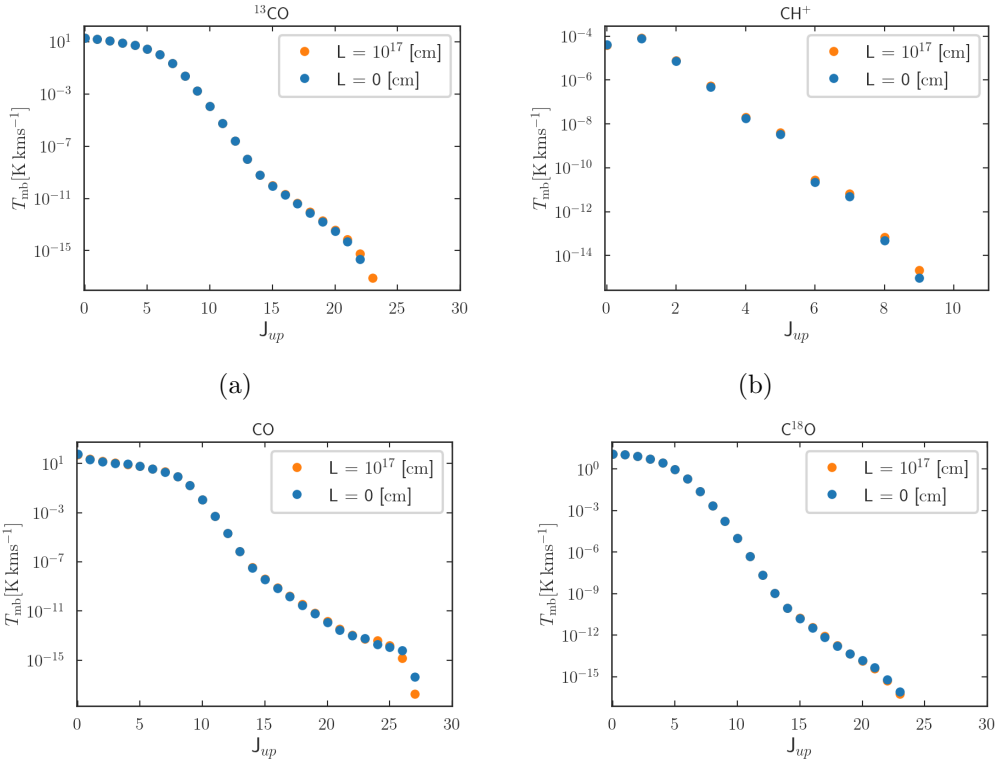


Figure 7.3: Integrated line intensity of selected species showing the impact of diffusion on the higher J lines. The upper J transition is shown on the x-axis.Model parameters: case II(table [6.1].

availability of their precursors, which can be used as excellent tracers of diffusion. The effect of subsonic diffusion on abundance profiles is largely dissipated within the lifetime of a cloud. Hence, the observational effects of some species are only observable with deep-integration time.

## 7.5 Mixing timescale

The local conditions of a PDR vary over the cloud due to the intensity of the incident radiation. Therefore, diffusion could not be understood as the mixing between the surface and the center of the cloud. Diffusion depends on the density gradient between the neighboring shells. As long as the chemical timescale is comparable or larger than the diffusion time scale, the chemistry will be coupled with the diffusion (Xie et al. 1995). The time constant $\frac{R^2}{K}$ (Xie et al. 1995) may give a rough estimate of the upper limits, where $R$ is the radius of the cloud and $K$ is the diffusion coefficient. For example, if a 2 pc cloud has a higher diffusion coefficient such as $K = 10^{23}\,\mathrm{cm^2\,s^{-1}}$, the timescale is,

$$\tau_d^s = \frac{(2\mathrm{pc})^2}{10^{23}\mathrm{cm^2\,s^{-1}}} \approx 10^7 \text{ years.} \tag{7.4}$$

and at a lower diffusion coefficient ($K = 10^{15}\,\mathrm{cm^2\,s^{-1}}$),

$$\tau_d^s = \frac{(2\mathrm{pc})^2}{10^{15}\mathrm{cm^2\,s^{-1}}} \approx 10^{22}\ \mathrm{s} \approx 10^{15} \text{ years.} \tag{7.5}$$

Here, 1 year $= 3.156 \times 10^7$s (Draine 2011). The diffusion time scale ($\tau_d^s$) varies between $10^7 - 10^{15}$ years and comparable or larger than the gas-phase chemical time scale ($\sim 10^6$ years Xie et al. 1995). Considering diffusion as mixing between the surface layer and the center of the cloud is incomplete. Hence, instead of the radius of the cloud, the length over which the density changes by about a hundred percent should go into the calculation of the timescale. For example, the abundance of atomic hydrogen change over a distance of $10^{-3}$ pc (size of the atomic region in the Figure [6.24a]). Then the timescale will be,

$$\tau_d^s = \frac{(10^{-3}\mathrm{pc})^2}{10^{23}\mathrm{cm^2\,s^{-1}}} \approx 3 \text{ years.} \tag{7.6}$$

The diffusion timescale largely depends on the abundance gradient of the species and position. Unlike Xie et al. (1995), this study considers a varying diffusion coefficient rather than a constant one. Therefore, the diffusion timescale should factor in the diffusion coefficient and the local conditions. The timescale to change

the abundance of a species $i$ is,

$$\tau_i = \left[\frac{1}{n_i^s}\frac{dn}{dt}\right]^{-1} \tag{7.7}$$

Here, $\frac{dn}{dt}$ denotes the reaction rates, which are inversely proportional to the time scale. In other words, the higher the rates, the smaller the time scale will be. Using the above equation, the diffusion timescale of the species,

$$\tau_d^s = \left[\frac{1}{n_i^s}\frac{dn_i^s}{dt}\right]^{-1} = \left[\frac{n_i^s}{\frac{d\phi_i}{dx}}\right] \Rightarrow \quad \tau_d^s \propto \frac{1}{K}, \tau_d^s \propto \frac{1}{L} \tag{7.8}$$

where, $\frac{d\phi_i}{dx}$ denotes the diffusion flux. The diffusion timescale is inversely proportional to the coherence length. Hence, the lower limit of the diffusion timescale is proportional to $[10\% R_{\rm pc}]^{-1}$.

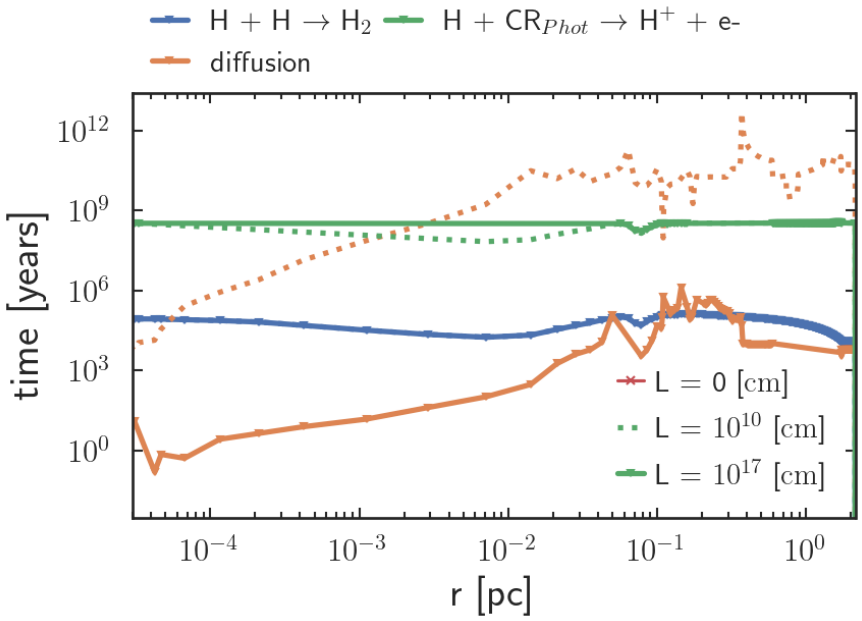


Figure 7.4: Mixing timescale compared to the chemical time scale for H. Model parameters: Case II (table [6.1]) with non-uniform temperature, and $\xi = 1.5$.

To compare the diffusion time scale with the chemical timescale, a detailed solution of the eq.[3.5] is needed. Figure [7.4] shows the diffusion timescale compared to the chemical time scale. The diffusion time scale is calculated using eq.[7.8]. The two or three chemical reactions from the topmost chemical reaction are chosen to calculate the chemical time scale. At lower coherence lengths, the diffusion timescale is larger than the chemical timescale (Figure [7.4]) in the cold molecular gas. However, the diffusion and chemical timescales are comparable in the warmer atomic gas. The diffusion time scale at lower coherence lengths

exceeds the steady-state chemical timescale. At higher coherence lengths, the diffusion timescale is smaller than the chemical timescale by at least three orders of magnitude in the warmer atomic gas. Mixing different PDR layers might be inefficient if the diffusion time scale is much larger than the chemical time scale. As a result, the effects of diffusion on the chemistry may be insignificant. When the diffusion timescale is comparable to the chemical time scale, diffusion and chemistry are coupled, and the impact of diffusion on the chemistry becomes evident.

The diffusion timescale is higher in colder regions than in warmer regions due to the lower diffusion coefficients in colder regions. This is not a direct effect of temperature but rather a mixed effect of temperature, the density of the species, and diffusion coefficient (length scales). Considering the chemical and diffusion rate equations, the time constant proposed by Xie et al. (1995) is not far off. Hence, the upper limit of the diffusion timescale is $10^{15}$ years. However, the lower limit of the diffusion timescale depends on the density of species at the current shell and the neighboring shells. In addition, the temperature and other local conditions also impact the lower limit of the diffusion timescale.

## 7.6 Numerical modeling

The KOSMA-$\tau$ PDR model uses an adaptive mesh to solve chemistry and physics instead of a pre-determined grid. A detailed explanation is provided in §[3.1]. The utilization of adaptive stepping techniques allows the spatial grid to change in each iteration and model, thereby offering an adaptable resolution that facilitates the understanding of the physics and chemistry of the medium. Nevertheless, the utilization of this particular approach for determining the subsequent position complicates the calculation of the diffusion rates (§[5.3]). Consequently, interpolation techniques which provide stable solutions are necessary. A method to limit the interpolation errors during computation is required as well. This study tested a couple of these methods (see §[5]), although there exists a plethora of interpolation and error-constraining approaches that can be explored.

Since the thermal and chemical balance is not always obtained in the same position (adaptive mesh) in the cloud for various models, comparing the physical and chemical properties of different models can diminish some of the diffusion effects. Interpolating the model to a single spatial grid before comparing will fetch further errors from the interpolation methods. So while comparing the results, one must keep this in mind. The steady-state method solves the chemistry to obtain a local equilibrium solution, which might diminish the diffusion effects. Hence it is advised to use a time-dependent solver for the chemistry, which will

provide the solution at a particular time step.

# Chapter 8

# Summary and Outlook

To thoroughly understand the impact of diffusion on the chemical and physical properties of molecular clouds, it is necessary to analyze diffusion coefficients susceptible to local conditions. The objective of this study was to examine the correlation between different diffusion coefficients and their impact on the physical and chemical structure of the PDR. Moreover, this research examined the impact of gas temperature on diffusion rates and explored the potential non-linear correlation between coherence length and overall diffusion rate. The KOSMA-$\tau$ PDR model with diffusion is created with 61 different species formed and destroyed through 812 reactions, including photodestruction process, $H_2$ formation, CO and $H_2$ self-shielding, gas-dust interactions, dust surface chemistry, and cosmic ray ionization. The diffusion model contains thermal, molecular, and turbulent diffusion.

The diffusion coefficient is varied between $10^{15}\,\mathrm{cm^2\,s^{-1}}$ and $10^{23}\,\mathrm{cm^2\,s^{-1}}$. Here the lower limit is taken from the molecular diffusion coefficient of atomic hydrogen. As the coherence length of turbulence diffusion varies, so do the total diffusion rate and the influence of diffusion on chemistry. The maximum coherence length is $L = 10^{17}\,\mathrm{cm}$ ($L \sim 10\%R$), which is supported by observations (Xie et al. 1995; Mac Low & Ossenkopf 2000).

The choice of the coherence length does not significantly influence the resulting abundance in a steady-state PDR model. Hence, understanding the influence of individual coherence length in a steady-state scenario is challenging. Individual choice of coherence length influenced the formation and destruction of chemical reactions. As the diffusion coefficients are higher on the surface, the impact on the chemistry is also evident at the surface of the cloud. The addition of diffusion removed at least one destruction reaction from the top five contributors of 34% of the species in the chosen chemical network. However, at least one of the formation reactions of 18% of the species was eliminated from the top contributors in the chosen chemical network. Chemistry of $H, H_2$, $C, C^+, CH^+, CH, OH$, CO and its

isotopes ($^{13}$CO, C$^{18}$O) are highly influenced by the addition of diffusion. With higher turbulent coherence lengths, diffusion becomes a major contributor to the formation/destruction of different species. As a result, when diffusion is added, the contribution from the other reactions shows up to six orders of difference in the percentage of contribution to the total formation/destruction rates.

The diffusion of electrons and ions facilitates the acceleration of chemistry within a cloud, as this process ensures an adequate supply of electrons deeper in the cloud. The CO $(1 \rightarrow 0)$ ($\sim$ 12%), CO $(2 \rightarrow 1)$ ($\sim$ 16%) and CS $(1 \rightarrow 0)$ ($\sim$ 11%) shows decrease in the integrated line intensities. In addition, diffusion effects are more pronounced in the integrated line intensities of higher $J(J \geq 8)$ transitions for $^{13}$CO, C$^{18}$O, CH$^+$, CO, CS, H$^{13}$CO$^+$, and HC$^{18}$O$^+$ than in the lower $J(J \leq 8)$ transitions. The utilization of CS$^+$ together with isotopes such as C, C$^+$, CO, and HCO$^+$ has proven to be a good tracer of diffusion effects in the PDR. The isotopic line ratios, namely the ratios of [$^{12}$CI]/[$^{13}$CI] and [$^{12}$CII]/[$^{13}$CII], exhibit substantial influence due to diffusion and can serve as effective tracers. Furthermore, the integrated line intensity ratio of $^{12}$CO $(2 \rightarrow 1)$/ $^{12}$CO$(1 \rightarrow 0)$, $^{13}$CO $(1 \rightarrow 0)$/ $^{12}$CO$(1 \rightarrow 0)$, [$^{12}$CII]/$^{12}$CO$(1 \rightarrow 0)$ and [$^{12}$CI]/$^{12}$CO$(1 \rightarrow 0)$ demonstrates a $\leq 25\%$ increase when compared to scenarios without diffusion.

Adaptive-mesh refinement technique is well suited for calculating diffusion effects due to its ability to resolve the regions where it is required. However, as the spatial position of the modeled cloud is not predetermined, the chemistry and physics of different models are not evaluated on the same point, which increases the chance of overlooking the diffusion effects on the chemical and physical structure of the PDR.

Diffusion significantly impacted the contribution to the total formation or destruction of the species as illustrated in the §[6.4]. With higher diffusion rates, dramatic changes in the density structure are expected, which is not visible in the steady state. Different diffusion coefficients did not reveal significant changes in the local quantities in the steady-state. To fully understand the influence of diffusion on the chemical and dynamic evolution of the molecular cloud, it is imperative to consider the time-dependent chemistry solver. The immediate next step will be to test the diffusion model with time-dependent chemistry. Once the time-dependent chemical solver is incorporated, the advection and mass loss from the surface of the cloud can be modeled. The diffusion-advection model and the mass-loss will help to understand the dynamic mixing between different phases of ISM. The diffusion-advection model can explain multiple scenarios like champagne flow, streamer, etc. This study could be expanded to understand the impact of diffusion on sticking parameters and freeze-out processes to comprehend

the influence of diffusion on dust grains. This study found that the H$-$H$_2$ transition and C$^+-$C$-$CO transition regions shift towards the surface of the cloud, which can impact the hydrogen and carbon fractionation. To understand the observations, it is also worth investigating the impact of diffusion on the cosmic ray ionization rates, optical depth, and fractionation effects.

While modeling diffusion and advection, it is worth investigating different interpolation routines to understand the error it creates when calculating the next position, density, and temperature in an AMR grid. With machine learning advancements, it is interesting to look into a decision forest, at least while using the KOSMA-$\tau$ 1D results in `kosmatau3d`. Interstellar clouds have a complex clumpy structure that is organized in filaments (Röllig & Ossenkopf-Okada 2022). These highly turbulent clouds are neither plane-parallel nor spherical in reality. One method to model the complex geometries of interstellar clouds is to use the superposition of KOSMA-$\tau$ clumps as in `kosmatau3d` (Andree-Labsch et al. 2017; Yanitski et al. 2023). By assuming the ISM is composed of a dense clumpy ensemble and a diffuse interclump ensemble, `kosmatau3d` can reproduce the dynamic and chemical structure of molecular clouds in 3D.

A better understanding of the cosmic ray ionization rate is essential in studying photodissociation regions. A detailed parametric study of cosmic ray ionization would help to understand its effects on diffusion and advection and vice versa. A precise measurement of the cosmic ray ionization rate is advised to quantify the diffusion effects further. A detailed investigation of this should be done in future studies.

# Appendix A

# Molecular weight

The molecular weight per hydrogen molecule, $\mu_{\mathrm{H_2}}$ is (Kauffmann et al. 2008)

$$\mu_{\mathrm{H_2}} = \frac{M}{m_{\mathrm{H}} N(\mathrm{H_2})} \tag{A.1}$$

where $m_{\mathrm{H}}$ is the H-atom mass, and $M$ is the total mass contained in a volume with $N(\mathrm{H_2})$ hydrogen molecules. From (Cox 2000), the mass ratios of hydrogen, helium, and metals are

$$\frac{M(H)}{M} \approx 0.71,\ \frac{M(He)}{M} \approx 0.27, \text{and } \frac{M(Z)}{M} \approx 0.02 \tag{A.2}$$

where $M = M(H) + M(He) + M(Z)$. This would give,

$$\mu_{\mathrm{H_2}} = \frac{M}{m_{\mathrm{H}} N(\mathrm{H_2})} = 2.8 \tag{A.3}$$

where,$N(H) = 2N(\mathrm{H_2}), M(H) = m_H N(H)$

Mean molecular weight per free particle $\mu_p$ is (Kauffmann et al. 2008)

$$\mu_p = \frac{M}{m_{\mathrm{H}} N} \tag{A.4}$$

where $N = N(\mathrm{H_2}) + N(\mathrm{He})$ for all gas with H in molecules.

$N(\mathrm{H_2}) = \frac{M(H_2)}{2m_H}$ and $N(\mathrm{He}) = \dfrac{M(He)}{4m_H}$. Hence,

$$\mu_p = \frac{M}{m_H\left[N(\mathrm{H_2}) + N(\mathrm{He})\right]} = \frac{M}{m_H\left[\frac{M(H)}{2m_H} + \dfrac{M(He)}{4m_H}\right]} = \frac{M/M(H)}{\dfrac{1}{2} + \dfrac{1}{4}\dfrac{M(He)}{M(H)}}$$
$$= \frac{(1/0.71)}{\dfrac{1}{2} + \dfrac{1}{4}\dfrac{0.27}{0.71}} = 2.366 \tag{A.5}$$

If the metals are taken into account,

$$\mu_p = \frac{M}{m_{\rm H} N} \tag{A.6}$$

where $N = N(\mathrm{H_2}) + N(\mathrm{He}) + N(Z)$ for all gas with H in molecules and $Z$ denotes metals. $N(\mathrm{H_2}) = \frac{M(H_2)}{2m_H}$ , $N(\mathrm{He}) = \dfrac{M(He)}{4m_H}$ and $N(\mathrm{Z}) = \dfrac{M(Z)}{5\times10^{-2}m_H}$. Hence,

$$\begin{aligned}\mu &= \frac{M}{m_H\left[N(\mathrm{H_2}) + N(\mathrm{He}) + N(Z)\right]} \\ &= \frac{M}{m_H\left[\frac{M(H)}{2m_H} + \dfrac{M(He)}{4m_H} + \dfrac{M(Z)}{5\times10^{-2}m_H}\right]} \\ &= \frac{M/M(H)}{\left[\frac{1}{2} + \dfrac{M(He)/M(H)}{4} + \dfrac{M(Z)/M(H)}{5\times10^{-2}}\right]} = \frac{1/0.71}{\left[\frac{1}{2} + \dfrac{0.27/0.71}{4} + \dfrac{0.02/0.71}{5\times10^{-2}}\right]} = 1.21\end{aligned} \tag{A.7}$$

With recent abundance ratios $Z = 0.0122 (Z/X = 0.0165)$ (Asplund et al. 2006) molecular weight is 1.5

Molecular weight is calculated as $\mu = 1.26 m_{\rm H} = 2.11 \times 10^{-24}$g typical for purely atomic gas (Klessen & Glover 2016). This value is used in calculating the turbulent velocity in this model.

# Appendix B

# Abundance

Fractional abundance of all the species used in the diffusion model. Since the fractional abundance of a species did not show significant variation with different coherence lengths, results from the $L = 10^{17}$ cm is provided here.

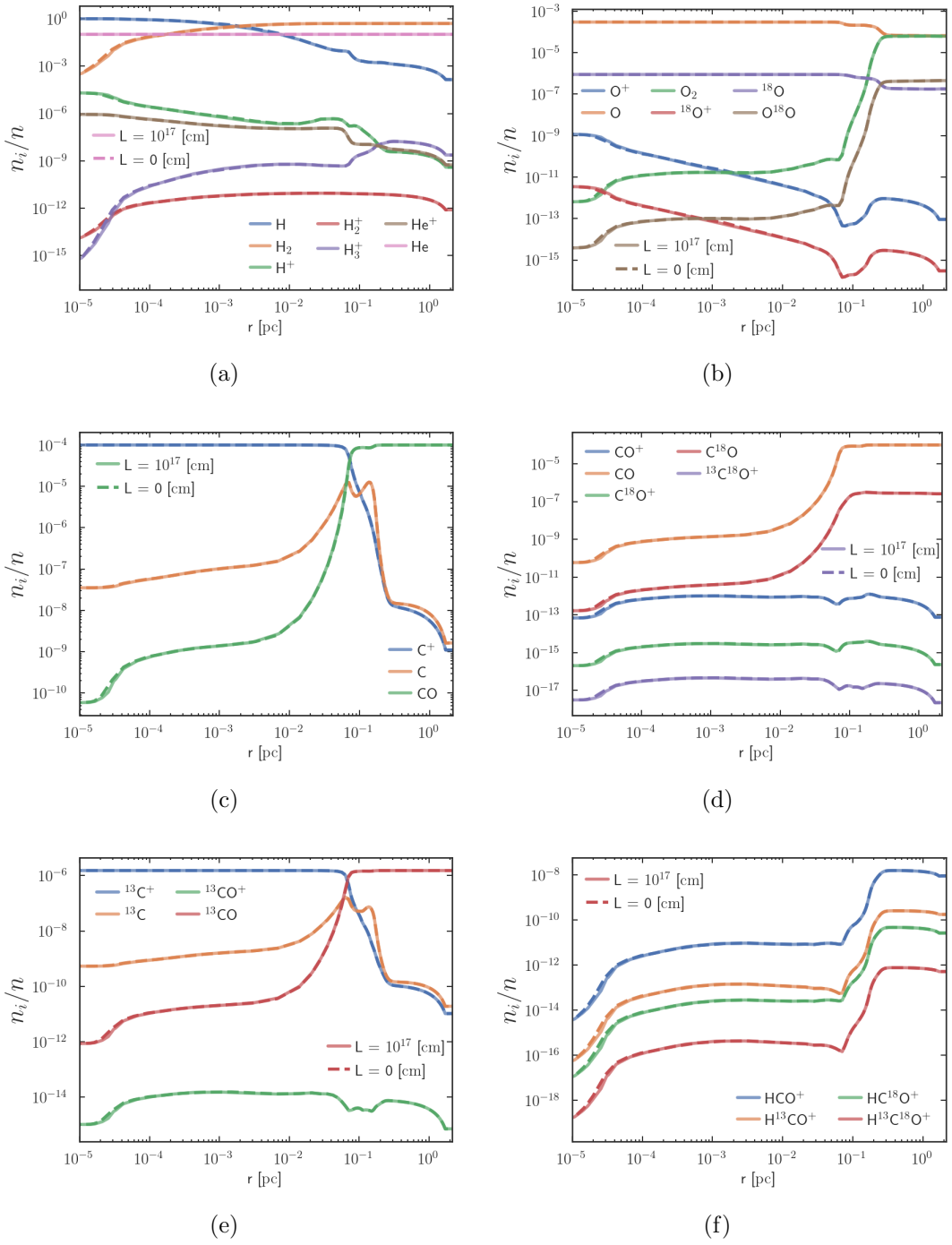


Figure B.1: Fractional abundance of species with and without diffusion. Model parameters: Case II (table [6.1] with non-uniform gas temperature, $\xi = 1.5$ and coherence length of $L = 10^{17}$ cm.

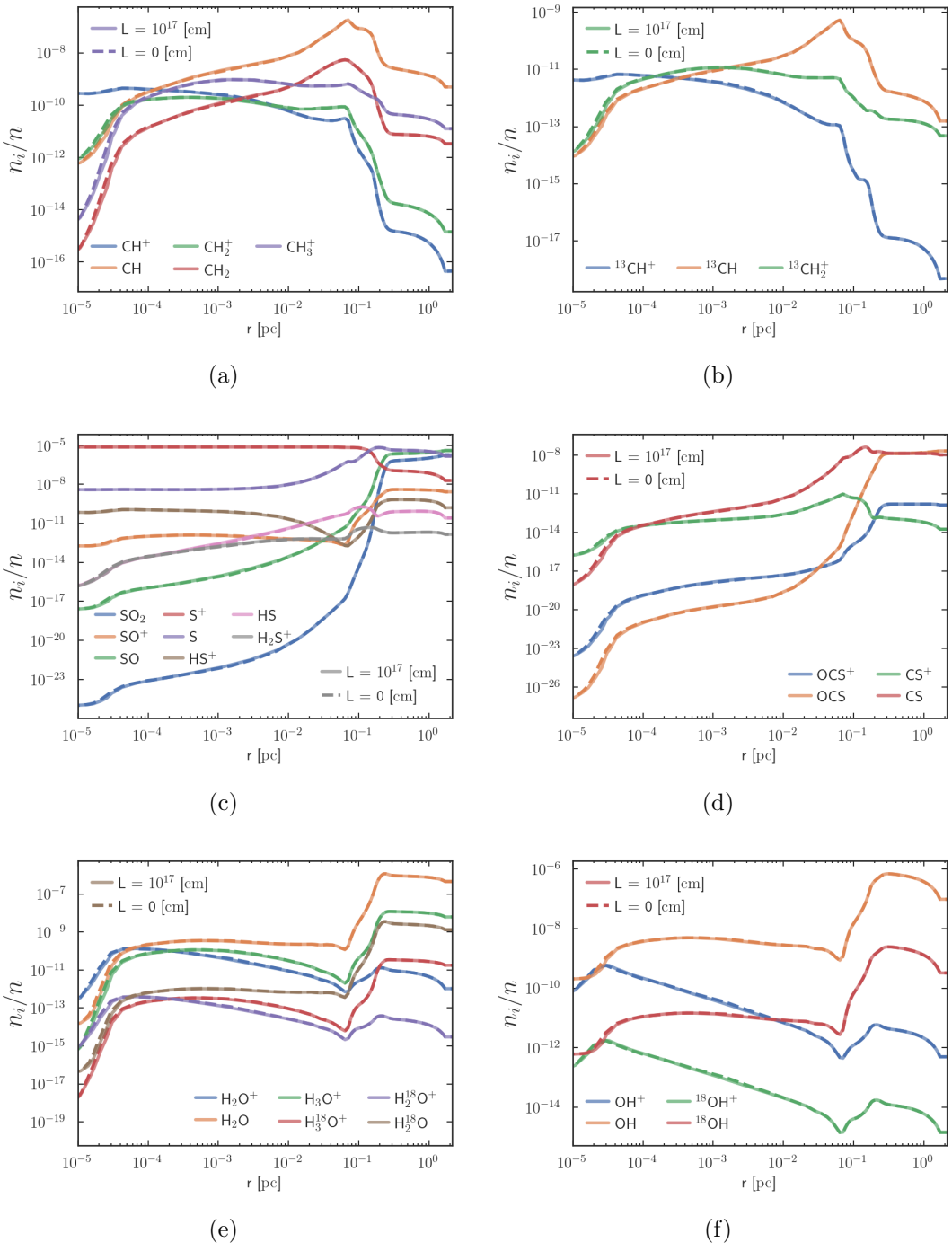


Figure B.2: Fractional abundance of species with and without diffusion. Model parameters: Case II(table [6.1] with non-uniform gas temperature, $\xi = 1.5$ and coherence length of $L = 10^{17}$ cm.

# Appendix C

# Diffusion rates

Diffusion rates of $C, C^+, CO, CH, CH^+$ and OH are provided. Each species has a plot that shows how its total diffusion rate changes as the coherence length varies. The data also indicates the contributions of thermal, molecular, and turbulent diffusion to the total diffusion rates. The region $0.4 - 2.13\,\mathrm{pc}$ has been zoomed in to understand the diffusion rates in colder molecular regions.

# C.1 Diffusion rates of C

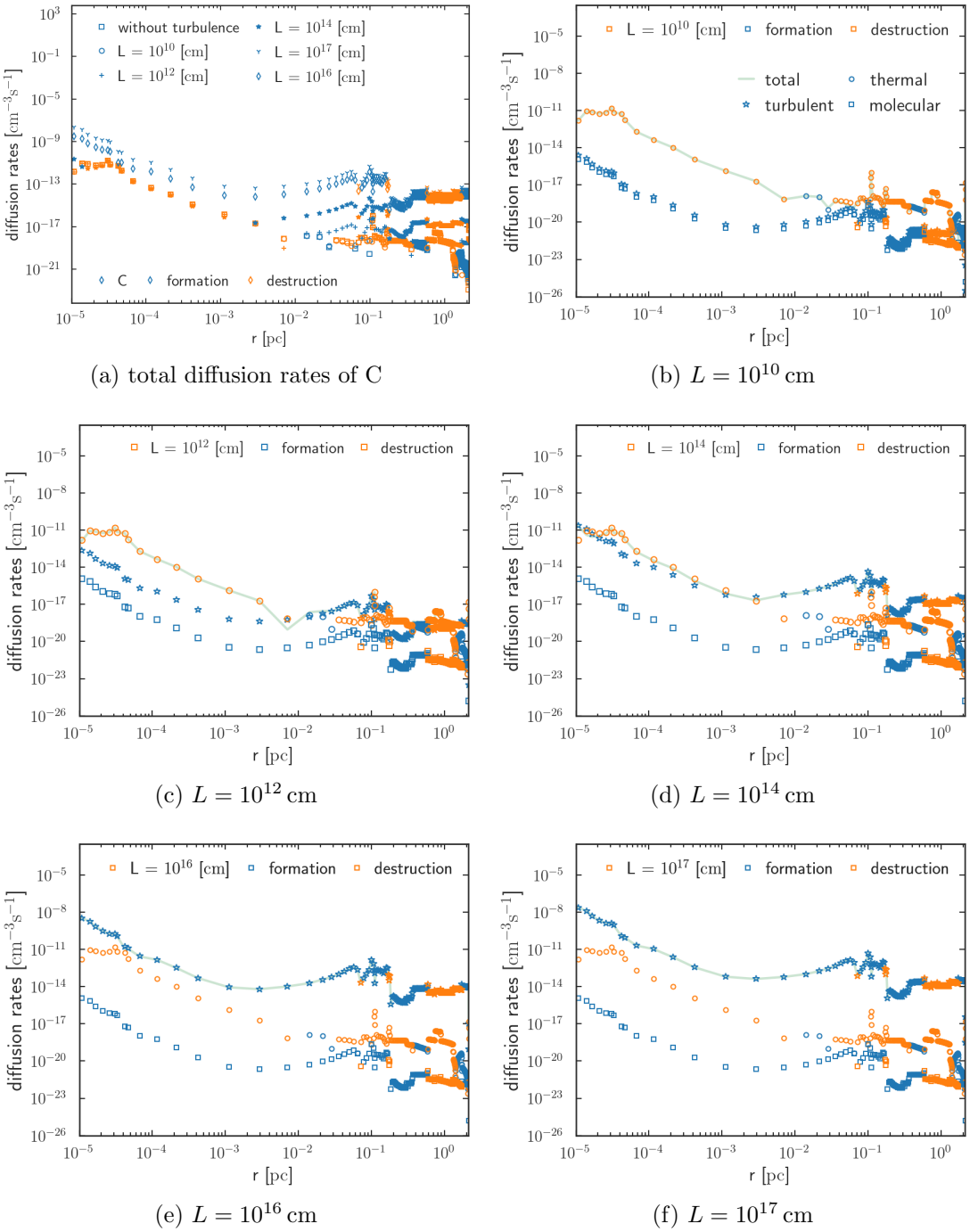


(a) total diffusion rates of C

(b) $L = 10^{10}$ cm

(c) $L = 10^{12}$ cm

(d) $L = 10^{14}$ cm

(e) $L = 10^{16}$ cm

(f) $L = 10^{17}$ cm

Figure C.1: Diffusion rates (a) and contribution from thermal, molecular, and turbulent diffusion to the total diffusion rates (b-f) as the coherence length varies. Labels of subfigures (c-f) are the same as (b). Model parameters: case II (table [6.1]).

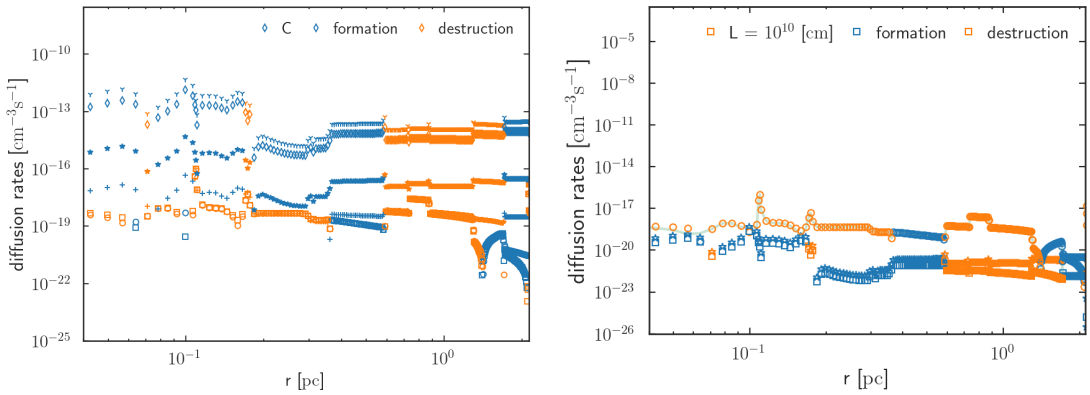


(a) total diffusion rates of C




(b) $L = 10^{10}$ cm

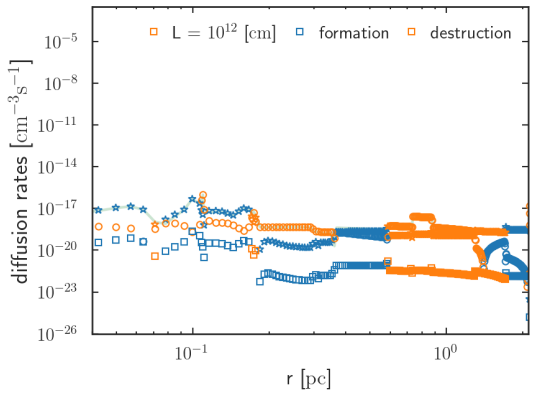


(c) $L = 10^{12}$ cm

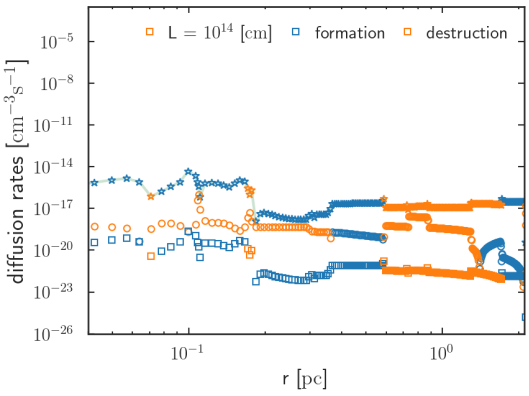


(d) $L = 10^{14}$ cm

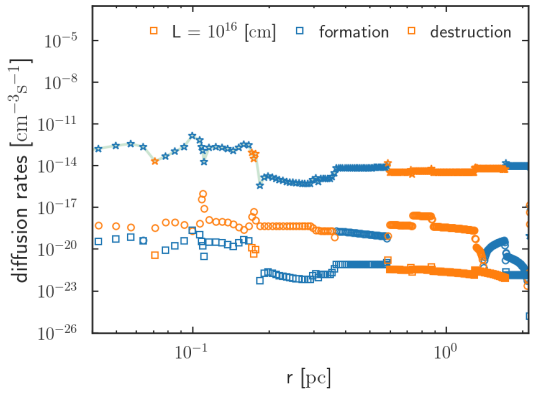


(e) $L = 10^{16}$ cm

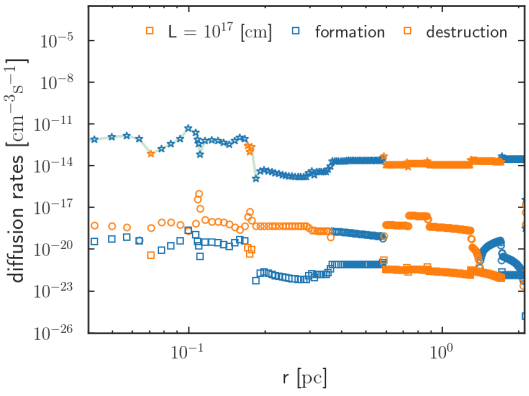


(f) $L = 10^{17}$ cm

Figure C.2: Diffusion rates (a) and contribution from thermal, molecular, and turbulent diffusion to the total diffusion rates (b-f) as the coherence length varies. Model parameters are labels are the same as Figure [C.1].

## C.2 Diffusion rates of $C^+$

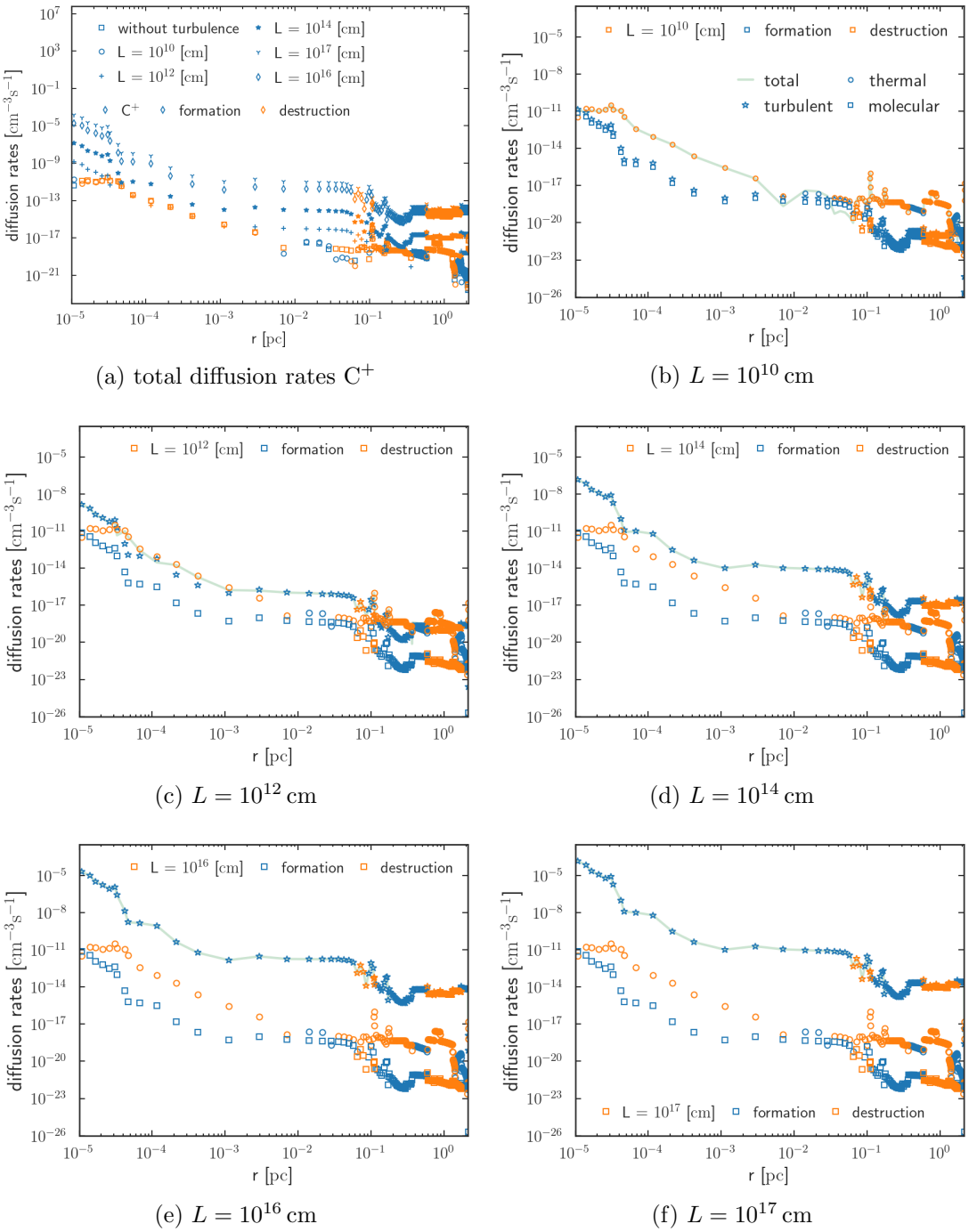


(a) total diffusion rates $C^+$

(b) $L = 10^{10}$ cm

(c) $L = 10^{12}$ cm

(d) $L = 10^{14}$ cm

(e) $L = 10^{16}$ cm

(f) $L = 10^{17}$ cm

Figure C.3: Diffusion rates (a) and contribution from thermal, molecular, and turbulent diffusion to the total diffusion rates (b-f) as the coherence length varies. Labels of subfigures (c-f) are the same as (b). Model parameters: case II (table [6.1]).

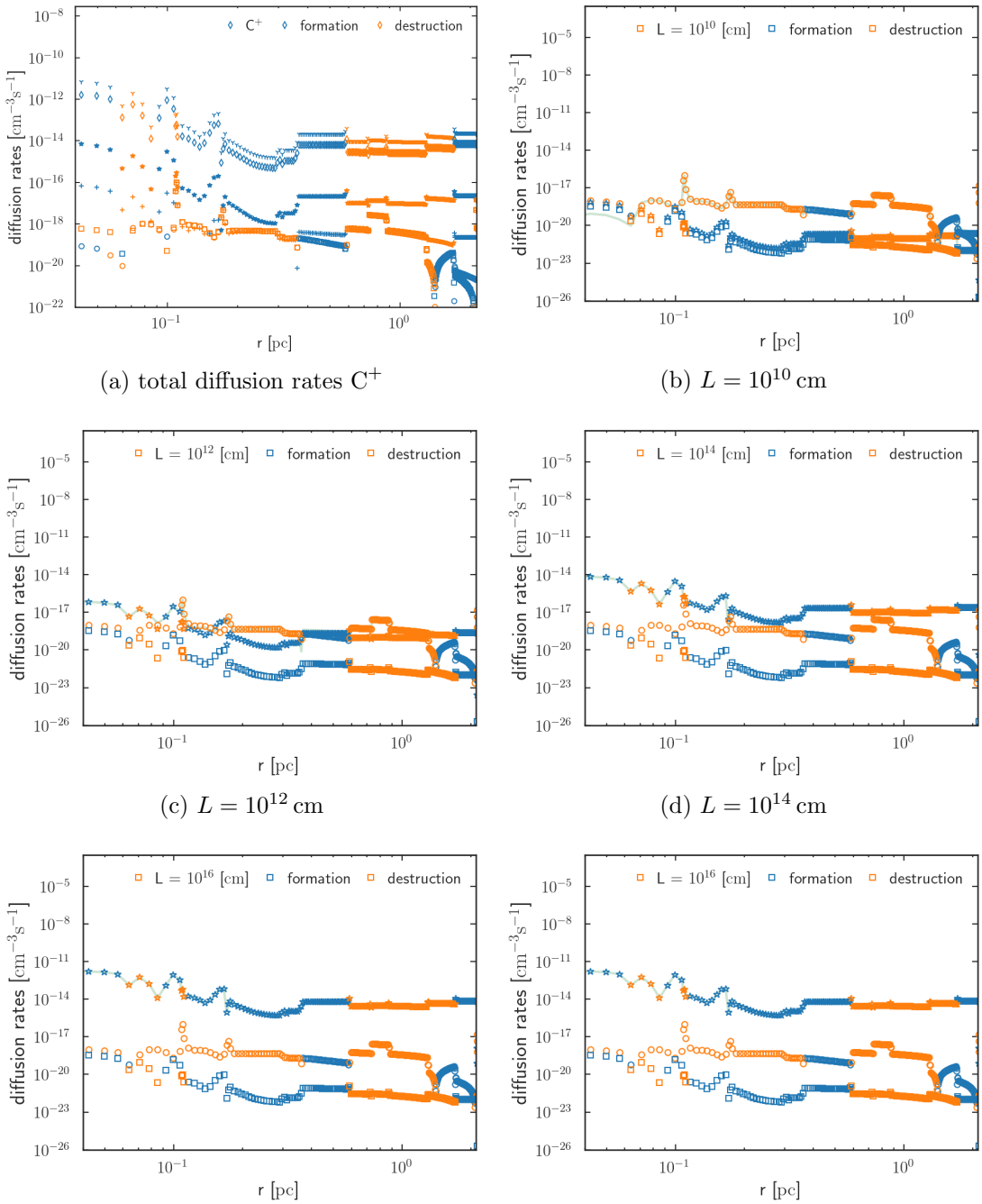


(a) total diffusion rates $C^+$

(b) $L = 10^{10}$ cm

(c) $L = 10^{12}$ cm

(d) $L = 10^{14}$ cm

(e) $L = 10^{16}$ cm

(f) $L = 10^{17}$ cm

Figure C.4: Diffusion rates (a) and contribution from thermal, molecular, and turbulent diffusion to the total diffusion rates (b-f) as the coherence length varies. Model parameters are labels are the same as Figure [C.3].

## C.3 Diffusion rates of CO

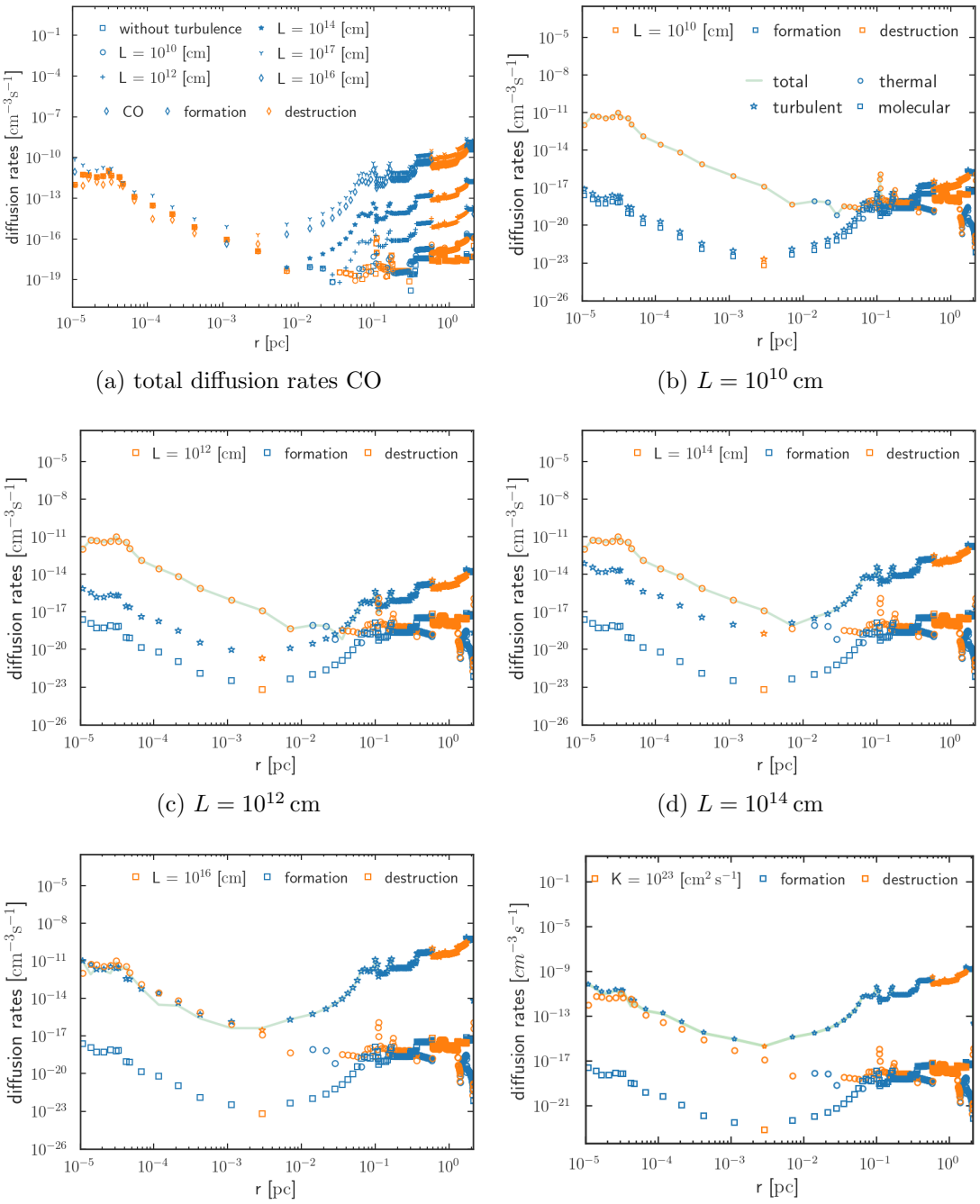


(a) total diffusion rates CO

(b) $L = 10^{10}$ cm

(c) $L = 10^{12}$ cm

(d) $L = 10^{14}$ cm

(e) $L = 10^{16}$ cm

(f) $L = 10^{17}$ cm

Figure C.5: Diffusion rates (a) and contribution from thermal, molecular, and turbulent diffusion to the total diffusion rates (b-f) as the coherence length varies. Labels of subfigures (c-f) are the same as (b). Model parameters: case II (table [6.1]).

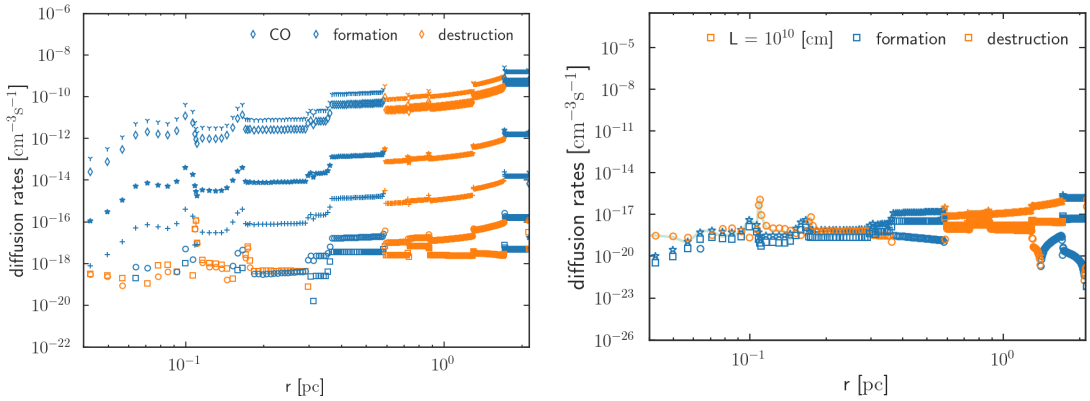


(a) total diffusion rates CO




(b) $L = 10^{10}$ cm

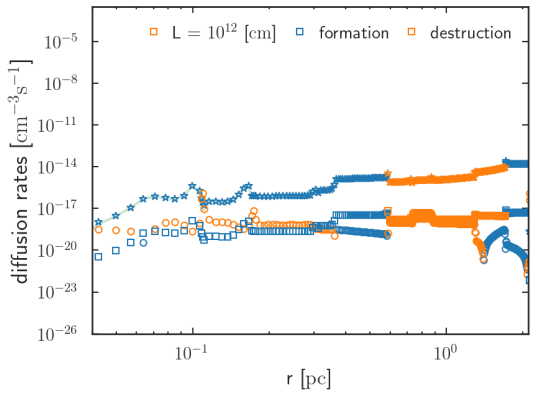


(c) $L = 10^{12}$ cm

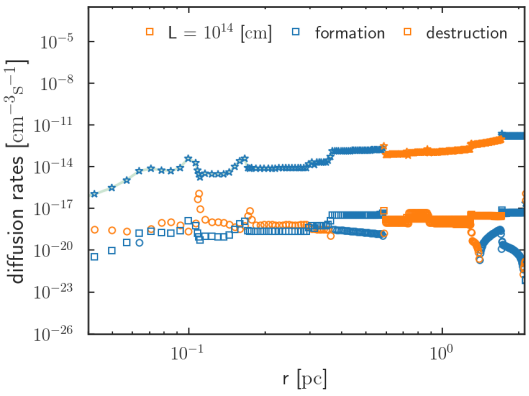


(d) $L = 10^{14}$ cm

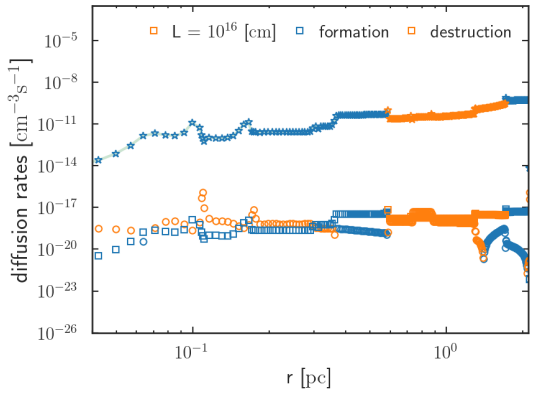


(e) $L = 10^{16}$ cm

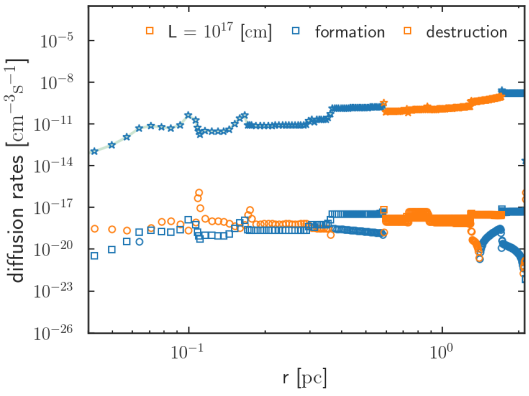


(f) $L = 10^{17}$ cm

Figure C.6: Diffusion rates (a) and contribution from thermal, molecular, and turbulent diffusion to the total diffusion rates (b-f) as the coherence length varies. Model parameters are labels are the same as Figure [C.5].

## C.4 Diffusion rates of $CH^+$

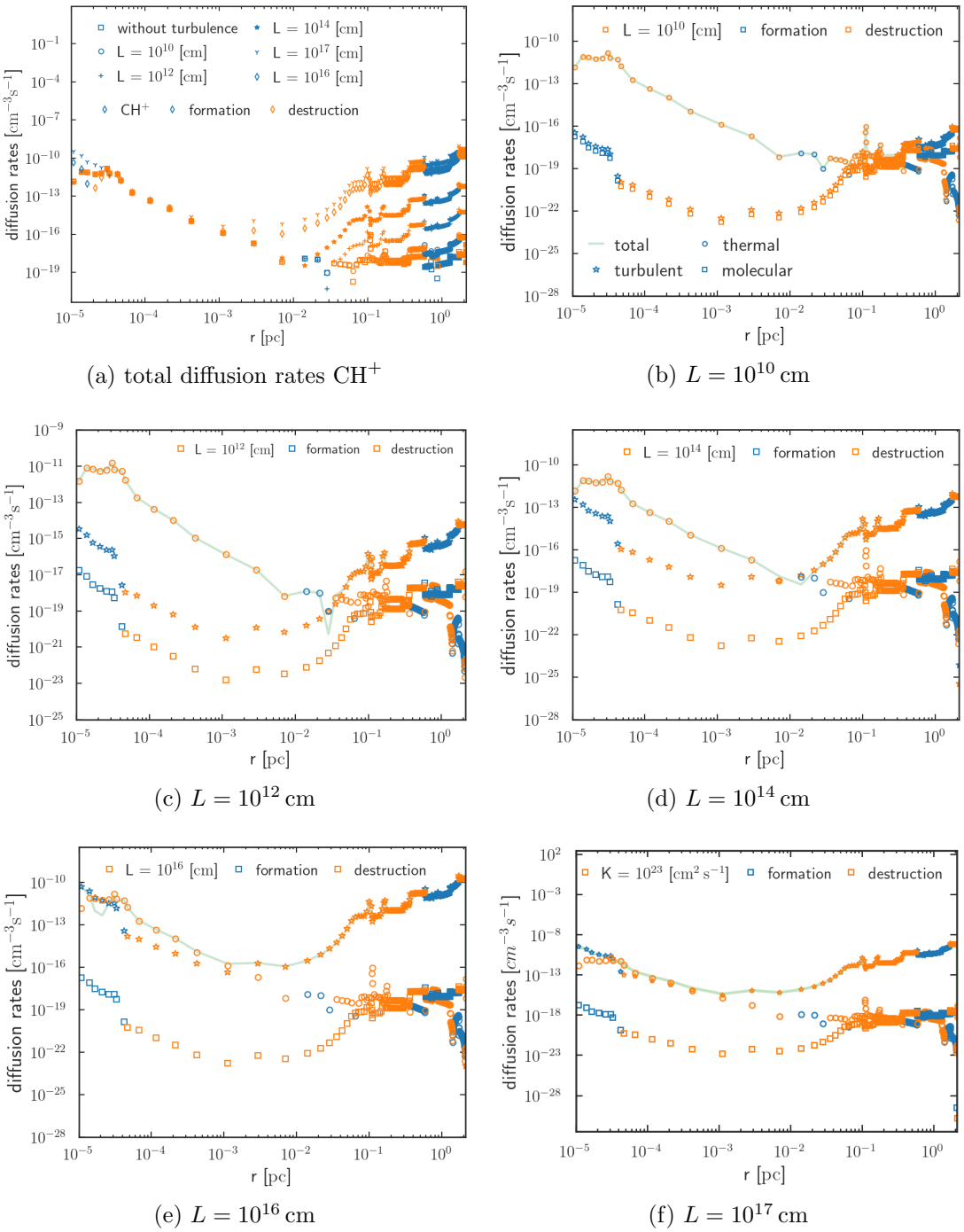


(a) total diffusion rates $CH^+$

(b) $L = 10^{10}$ cm

(c) $L = 10^{12}$ cm

(d) $L = 10^{14}$ cm

(e) $L = 10^{16}$ cm

(f) $L = 10^{17}$ cm

Figure C.7: Diffusion rates (a) and contribution from thermal, molecular, and turbulent diffusion to the total diffusion rates (b-f) as the coherence length varies. Labels of subfigures (c-f) are the same as (b). Model parameters: case II (table [6.1]).

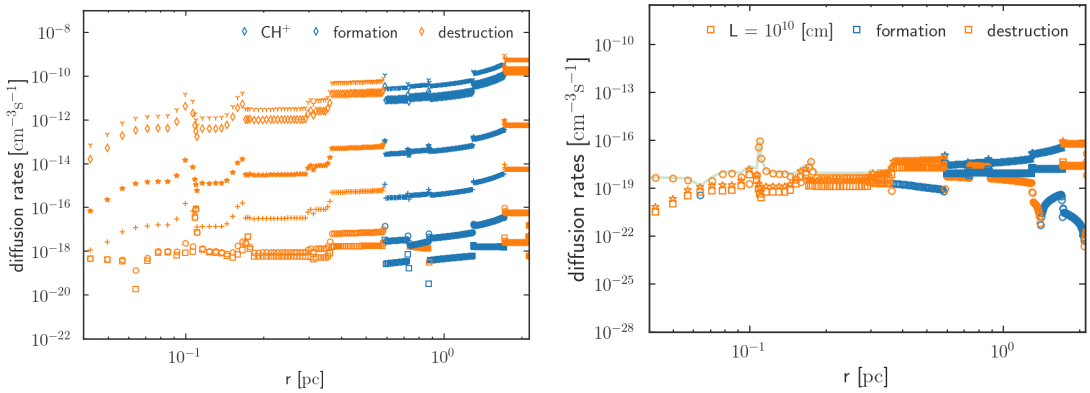


(a) total diffusion rates $CH^+$




(b) $L = 10^{10}$ cm

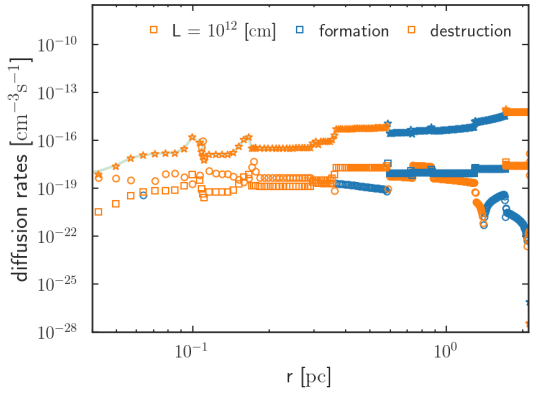


(c) $L = 10^{12}$ cm

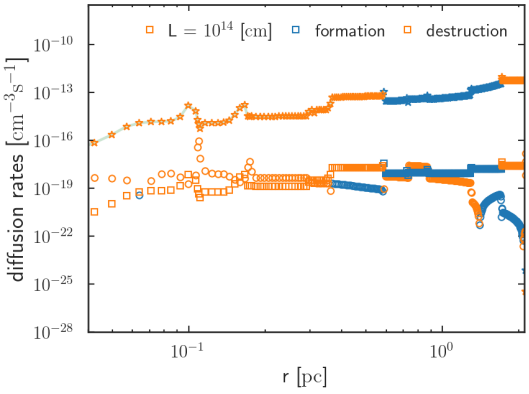


(d) $L = 10^{14}$ cm

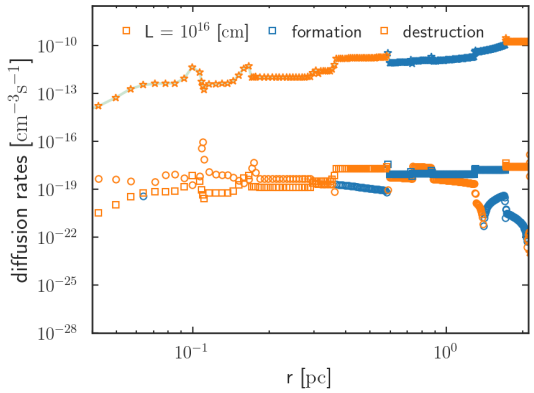


(e) $L = 10^{16}$ cm

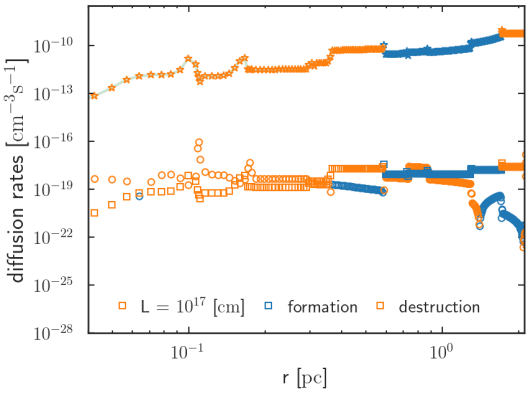


(f) $L = 10^{17}$ cm

Figure C.8: Diffusion rates (a) and contribution from thermal, molecular, and turbulent diffusion to the total diffusion rates (b-f) as the coherence length varies. Model parameters are labels are the same as Figure [C.7].

## C.5 Diffusion rates of CH

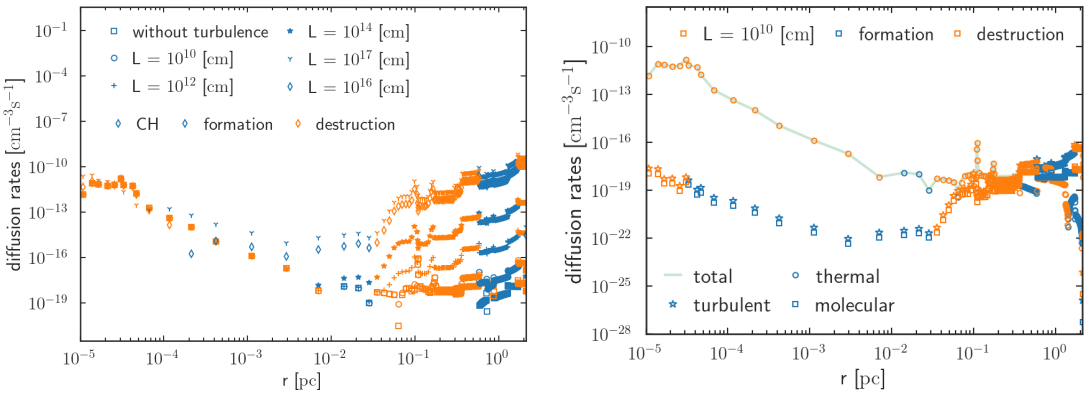


(a) total diffusion rates CH




(b) $L = 10^{10}$ cm

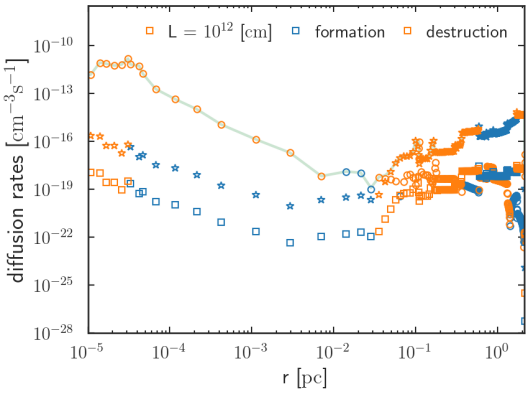


(c) $L = 10^{12}$ cm

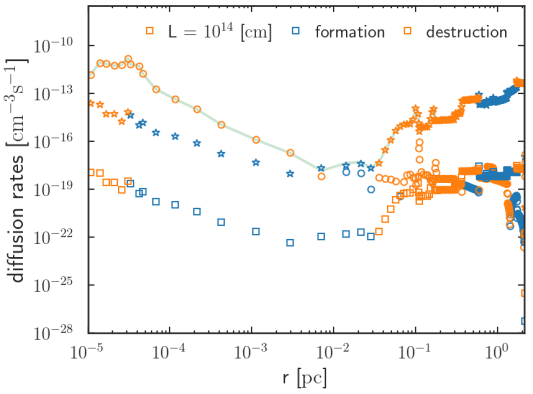


(d) $L = 10^{14}$ cm

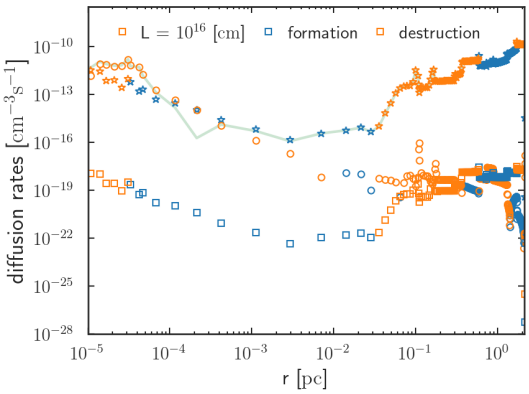


(e) $L = 10^{16}$ cm

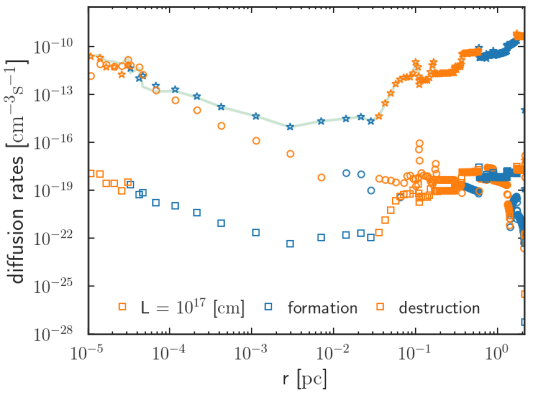


(f) $L = 10^{17}$ cm

Figure C.9: Diffusion rates (a) and contribution from thermal, molecular, and turbulent diffusion to the total diffusion rates (b-f) as the coherence length varies. Labels of subfigures (c-f) are the same as (b). Model parameters: case II (table [6.1]).

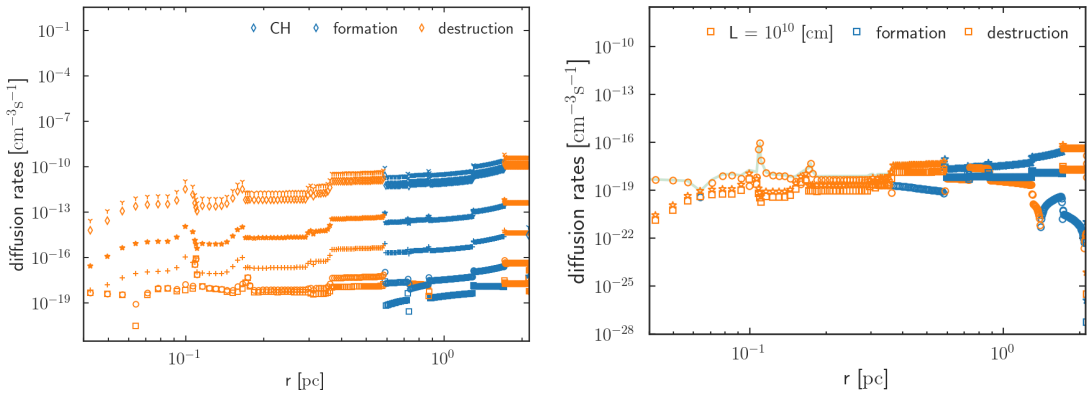


(a) total diffusion rates CH




(b) $L = 10^{10}$ cm

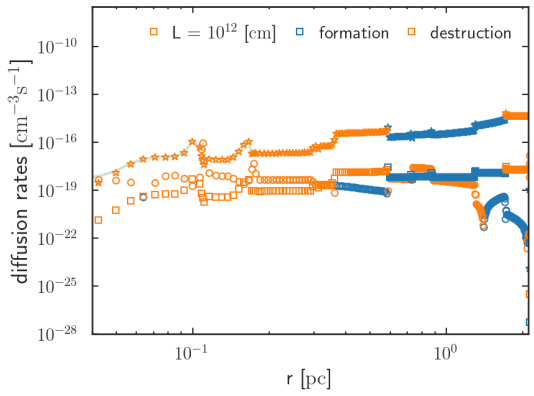


(c) $L = 10^{12}$ cm

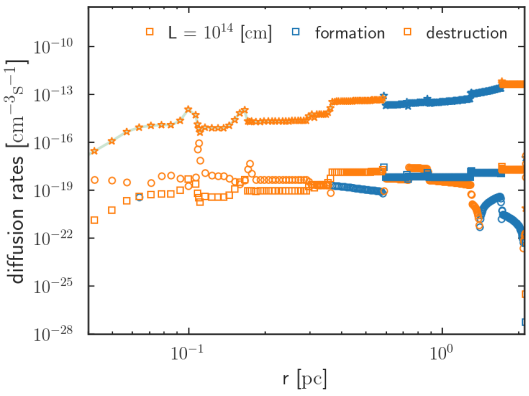


(d) $L = 10^{14}$ cm

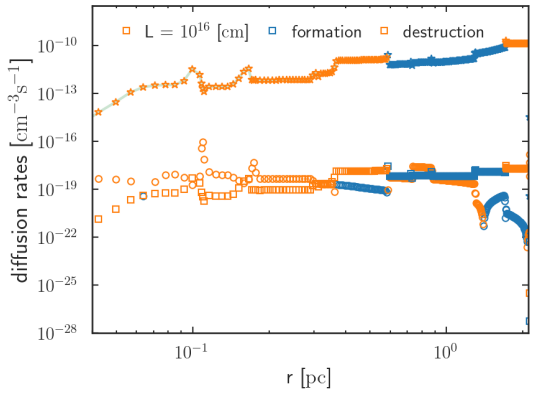


(e) $L = 10^{16}$ cm

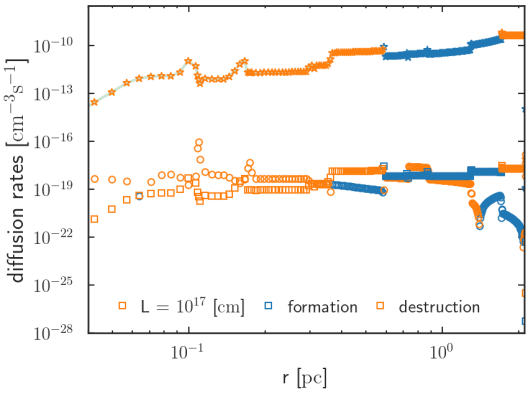


(f) $L = 10^{17}$ cm

Figure C.10: Diffusion rates (a) and contribution from thermal, molecular, and turbulent diffusion to the total diffusion rates (b-f) as the coherence length varies. Model parameters are labels are the same as Figure [C.9].

## C.6 Diffusion rates of OH

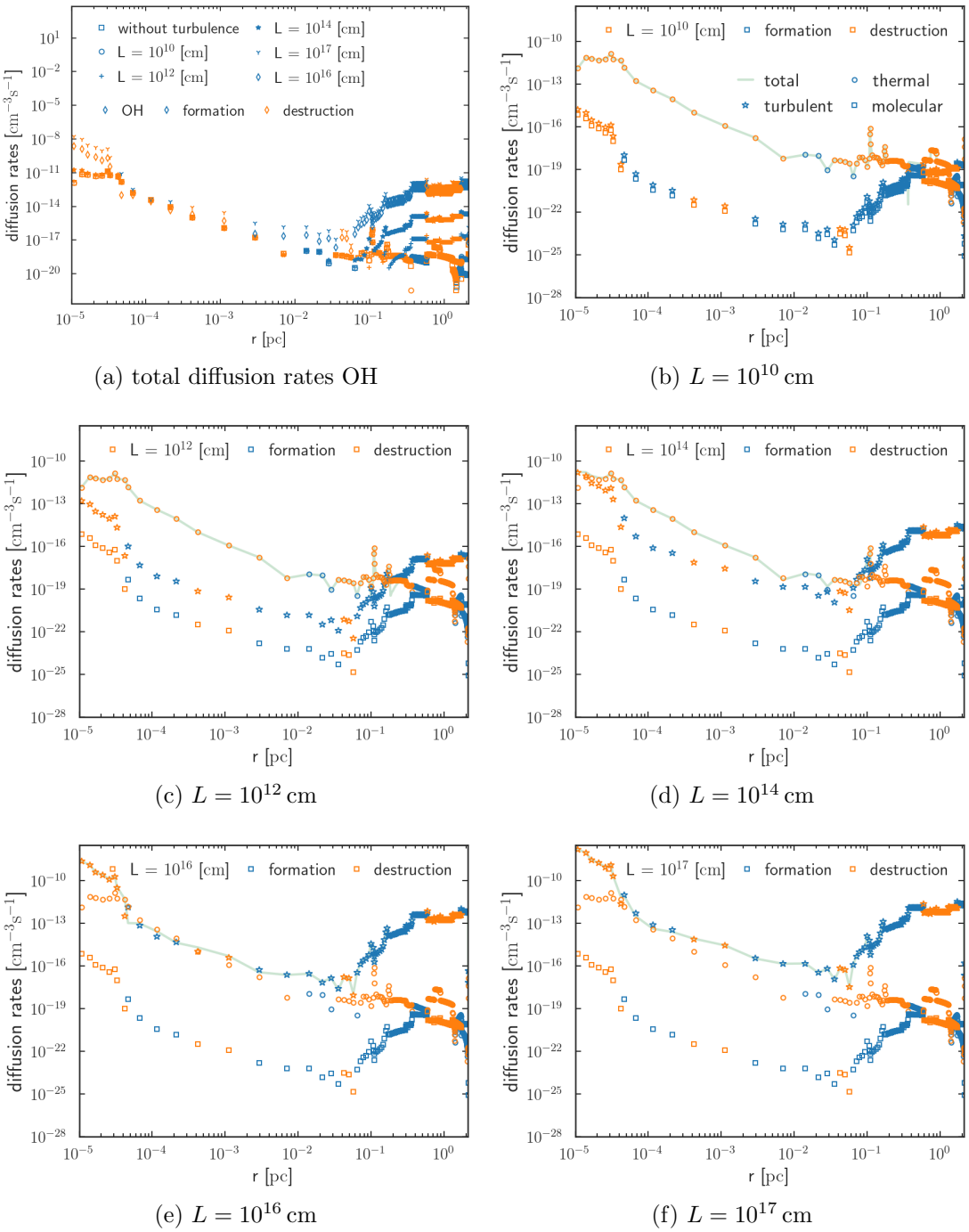


(a) total diffusion rates OH

(b) $L = 10^{10}$ cm

(c) $L = 10^{12}$ cm

(d) $L = 10^{14}$ cm

(e) $L = 10^{16}$ cm

(f) $L = 10^{17}$ cm

Figure C.11: Diffusion rates (a) and contribution from thermal, molecular, and turbulent diffusion to the total diffusion rates (b-f) as the coherence length varies. Labels of subfigures (c-f) are the same as (b). Model parameters: case II (table [6.1]).

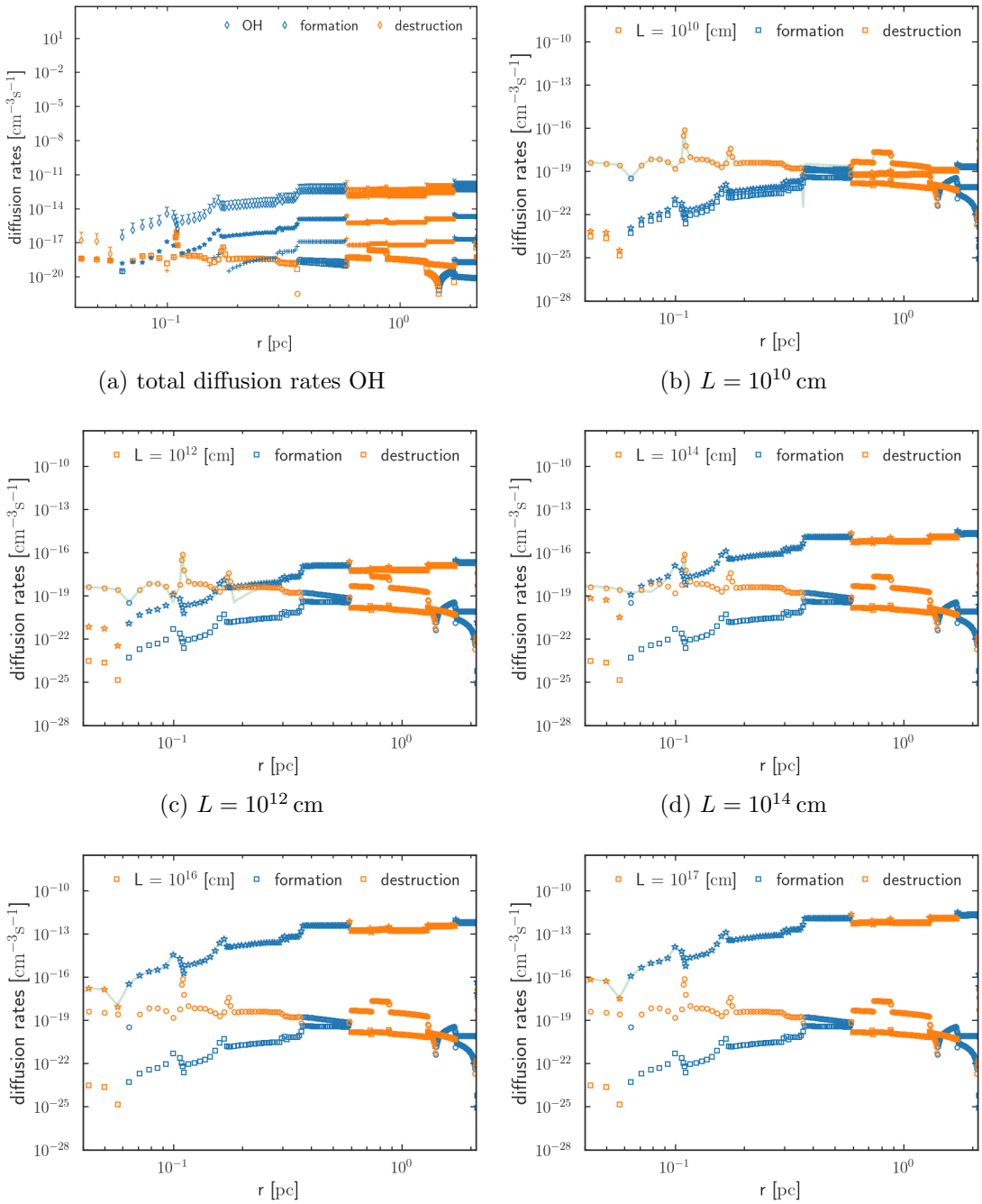


(a) total diffusion rates OH

(b) $L = 10^{10}$ cm

(c) $L = 10^{12}$ cm

(d) $L = 10^{14}$ cm

(e) $L = 10^{16}$ cm

(f) $L = 10^{17}$ cm

Figure C.12: Diffusion rates (a) and contribution from thermal, molecular, and turbulent diffusion to the total diffusion rates (b-f) as the coherence length varies. Model parameters are labels are the same as Figure [C.11].

# Bibliography

Andree-Labsch, S., Ossenkopf-Okada, V., & Röllig, M. 2017, Astronomy and Astrophysics, 598, A2

Arab, H., Abergel, A., Habart, E., et al. 2012, Astronomy and Astrophysics, 541

Asplund, M., Grevesse, N., & Jacques Sauval, A. 2006, Nuclear Physics A, 777, 1

Bakes, E. L. O. & Tielens, A. G. G. M. 1994, The Astrophysical Journal, 427, 822

Bakes, E. L. O. & Tielens, A. G. G. M. 1998, The Astrophysical Journal, 499, 258

Ballesteros-Paredes, J., Klessen, R. S., Low, M. M. M., & Vazquez-Semadeni, E. 2006, Molecular Cloud Turbulence and Star Formation

Bell, T. A., Hartquist, T. W., Viti, S., & Williams, D. A. 2006, Astronomy and Astrophysics, 459, 805

Bell, T. A., Viti, S., Williams, D. A., Crawford, I. A., & Price, R. J. 2005, Monthly Notices of the Royal Astronomical Society, 357, 961

Bell, T. A., Willacy, K., Phillips, T. G., Allen, M., & Lis, D. C. 2011, Astrophysical Journal, 731, 48

Bisbas, T. G., Bell, T. A., Viti, S., Yates, J., & Barlow, M. J. 2012, Monthly Notices of the Royal Astronomical Society, 427, 2100

Blake, G. A. 1988, in Molecular Clouds in the Milky Way and External Galaxies, ed. R. L. Dickman, R. L. Snell, & J. S. Young, Vol. 315 (Springer Berlin Heidelberg), 132–150

Bulirsch, R. & Stoer, J. 1964, Numerische Mathematik, 6, 413

Cazaux, S. & Tielens, A. G. G. M. 2004, The Astrophysical Journal, 604, 222

Chapman, S. 1940, Proceedings of the Royal Society of London. Series A. Mathematical and Physical Sciences, 177, 38

Chapman, S. 1958, Proceedings of the Physical Society, 72, 353

Chapman, S. & Dootson, F. W. 1917, The London, Edinburgh, and Dublin Philosophical Magazine and Journal of Science, 33, 248

Cheng, A. H.-D. & Cheng, D. T. 2005, Engineering Analysis with Boundary Elements, 29, 268

Chevance, M., Kruijssen, J. M., Vazquez-Semadeni, E., et al. 2020, Space Science Reviews, 216, 50

Cox, A. N. 2000, Allen's astrophysical quantities, 4th edn. (New York: AIP Press; Springer)

Cubick, M., Stutzki, J., Ossenkopf, V., Kramer, C., & Röllig, M. 2008, Astronomy & Astrophysics, 488, 623

Draine, B. T. 1978, The Astrophysical Journal Supplement Series, 36, 595

Draine, B. T. 2011, Physics of the Interstellar and Intergalactic Medium (Princeton University Press)

Enskog, D. 1917, PhD thesis, Inaugural Dissertation, Uppsala, Sweden, Uppsala, Sweden

Ferland, G. J., Chatzikos, M., Guzmán, F., et al. 2017, The 2017 release of Cloudy

Ferland, G. J., Porter, R. L., Van Hoof, P. A., et al. 2013, Revista Mexicana de Astronomia y Astrofisica, 49, 137

Ferrière, K. M. 2001, Reviews of Modern Physics, 73, 1031

Fick, A. 1855, Annalen der Physik, 170, 59

Fischer, J., Klaassen, T., Hovenier, N., et al. 2004, Applied Optics, 43, 3765

Fuente, A., Rodríguez-Franco, A., García-Burillo, S., Martin-Pintado, J., & Black, J. H. 2003, Astronomy and Astrophysics, 406, 899

Gierens, K. M., Stutzki, J., & Winnewisser, G. 1992, Astronomy and Astrophysics, 259, 271

Glassgold, A. E., Galli, D., & Padovani, M. 2012, The Astrophysical Journal, 756, 157

Glover, S. C., Federrath, C., Low, M. M., & Klessen, R. S. 2010, Monthly Notices of the Royal Astronomical Society, 404, 2

Glover, S. C. O. & Mac Low, M. 2007, The Astrophysical Journal, 659, 1317

Godunov, S. K. & Bohachevsky, I. 1959, Matematičeskij sbornik, 47, 271

Gong, Y., Liu, S., Wang, J., et al. 2022, Astronomy & Astrophysics, 663, A82

Goodman, A. A., Barranco, J. A., Wilner, D. J., & Heyer, M. H. 1998, The Astrophysical Journal, 504, 223

Gruzinov, A. V., Isichenko, M. B., & Kalda, Y. L. 1990, Zh. Eksp. Teor. Fiz., 97, 476

Guevara, C., Stutzki, J., Ossenkopf-Okada, V., et al. 2020, Astronomy and Astrophysics, 636, A16

Herbst, E. 1995, Annual Review of Physical Chemistry, 46, 27

Hollenbach, D. 1988, Astrophysical Letters and Communications, 26, 191

Hollenbach, D., Kaufman, M. J., Neufeld, D., Wolfire, M., & Goicoechea, J. R. 2012, Astrophysical Journal, 754

Hollenbach, D. J. & Tielens, A. G. 1999, Reviews of Modern Physics, 71, 173

Hutomo, G. D., Kusuma, J., Ribal, A., Mahie, A. G., & Aris, N. 2019, Journal of Physics: Conference Series, 1180, 012009

Kauffmann, J., Bertoldi, F., Bourke, T. L., Evans, N. J., & Lee, C. W. 2008, Astronomy & Astrophysics, 487, 993

Kaufman, M. J., Wolfire, M. G., & Hollenbach, D. J. 2006, The Astrophysical Journal, 644, 283

Kaufman, M. J., Wolfire, M. G., Hollenbach, D. J., & Luhman, M. L. 1999, The Astrophysical Journal, 527, 795

Kazandjian, M. V., Meijerink, R., Pelupessy, I., Israel, F. P., & Spaans, M. 2012, Astronomy and Astrophysics, 542, A65

Kincaid, J. M., Cohen, E. G. D., de Haro, M., López De Haro, M., & de Haro, M. 1986, The Journal of Chemical Physics, 86, 963

Klessen, R. S. & Glover, S. C. O. 2016, in Saas-Fee Advanced Course, Vol. 43, Saas-Fee Advanced Course, ed. Y. Revaz, P. Jablonka, R. Teyssier, & L. Mayer, 85

Kolmogorov, A. 1991a, Proc. Roy. Soc. London Ser. A, 434, 15

Kolmogorov, A. N. 1991b, Proceedings: Mathematical and Physical Sciences, 434, 15

Kolmogorov, A. N. 1991c, Proceedings of the Royal Society of London. Series A: Mathematical and Physical Sciences, 434, 9

Koren, B. 1993, in Numerical Methods for Advection-Diffusion Problems, ed. C. Vreugdenhil & B. Koren (Germany: Vieweg), 117–138

Kritsuk, A. G., Ustyugov, S. D., & Norman, M. L. 2017, New Journal of Physics, 19, 065003

Krumholz, M. R., McKee, C. F., & Tumlinson, J. 2008, The Astrophysical Journal, 689, 865

Krumholz, M. R., McKee, C. F., & Tumlinson, J. 2009, The Astrophysical Journal, 693, 216

Larson, R. B. 1981, Monthly Notices of the Royal Astronomical Society, 194, 809

Le Petit, F., Nehme, C., Le Bourlot, J., & Roueff, E. 2006, The Astrophysical Journal Supplement Series, 164, 506

Lee, M.-Y., Stanimirović, S., Douglas, K. A., et al. 2012, The Astrophysical Journal, 748, 75

Lepp, S. & Shull, J. M. 1983, The Astrophysical Journal, 270, 578

Lesaffre, P., Gerin, M., & Hennebelle, P. 2007, Astronomy & Astrophysics, 469, 949

Levrier, F., Le Petit, F., Hennebelle, P., et al. 2012, Astronomy and Astrophysics, 544, A22

Mac Low, M.-M. & Klessen, R. S. 2004, Reviews of Modern Physics, 76, 125

Mac Low, M. M. & Ossenkopf, V. 2000, Astronomy and Astrophysics, 353, 339

Maillard, V., Bron, E., & Le Petit, F. 2021, Astronomy & Astrophysics, 656, A65

Mathis, J. S., Rumpl, W., & Nordsieck, K. H. 1977, The Astrophysical Journal, 217, 425

McKee, C. F. & Ostriker, E. C. 2007, Annual Review of Astronomy and Astrophysics, 45, 565

McKee, C. F. & Zweibel, E. G. 1992, The Astrophysical Journal, 399, 551

Neufeld, D. A. & Melnick, G. J. 1987, The Astrophysical Journal, 322, 266

Offner, S. S. R., Bisbas, T. G., Viti, S., & Bell, T. A. 2013, The Astrophysical Journal, 770, 49

Okada, Y., Güsten, R., Requena-Torres, M. A., et al. 2019, Astronomy & Astrophysics, 621, A62

Ossenkopf, V. & Low, M. M. 2002, Astronomy and Astrophysics, 390, 307

Ossenkopf, V., Röllig, M., Neufeld, D. A., et al. 2013, Astronomy & Astrophysics, 550, A57

Pabst, C. H. M., Goicoechea, J. R., Hacar, A., et al. 2022, Astronomy & Astrophysics, 658, A98

Pabst, C. H. M., Hacar, A., Goicoechea, J. R., et al. 2021, Astronomy & Astrophysics, 651, A111

Padoan, P. & Nordlund, Å. 2011, The Astrophysical Journal, 730, 40

Pan, L. & Padoan, P. 2009, Astrophysical Journal, 692, 594

Peñaloza, C. H., Clark, P. C., Glover, S. C., & Klessen, R. S. 2018, Monthly Notices of the Royal Astronomical Society, 475, 1508

Pilbratt, G. L., Riedinger, J. R., Passvogel, T., et al. 2010, Astronomy and Astrophysics, 518, L1

Pound, M. W. & Wolfire, M. G. 2008, Astronomical Data Analysis Software ..., 394, 654

Pound, M. W. & Wolfire, M. G. 2011, PDRT: Photo Dissociation Region Toolbox

Prandtl, L. 1904, Verh. d. III. Intern. Mathem. Kongresses, 2, 484

Press, W. H., Teukolsky, S. A., Vetterling, W. T., & Flannery, B. P. 2007, Numerical recipes 3rd edition: The art of scientific computing (Cambridge university press)

Priestley, F. D., Barlow, M. J., & Viti, S. 2017, Monthly Notices of the Royal Astronomical Society, 472, 4444

Roberts, P. H. 1961, Journal of Fluid Mechanics, 11, 257

Röllig, M., Abel, N. P., Bell, T., et al. 2007, Astronomy & Astrophysics, 467, 187

Röllig, M. & Ossenkopf, V. 2013, Astronomy & Astrophysics, 550, A56

Röllig, M. & Ossenkopf-Okada, V. 2022, Astronomy and Astrophysics, 664, A67

Röllig, M., Szczerba, R., Ossenkopf, V., & Glück, C. 2013, Astronomy and Astrophysics, 549, A85

S. Chapman. 1916, Proceedings of the Royal Society of London. Series A, Containing Papers of a Mathematical and Physical Character, 93, 1

Shu, F. H., Adams, F. C., & Lizano, S. 1987, Annual Review of Astronomy and Astrophysics, 25, 23

Singh, A. K. & Bhadauria, B. S. 2009, International Journal of Mathematical Analysis, 3, 815

Sternberg, A. & Dalgarno, A. 1995, The Astrophysical Journal Supplement Series, 99, 565

Stoerzer, H., Stutzki, J., & Sternberg, A. 1996, Astronomy & Astrophysics, 310, 592

Stutzki, J., Bensch, F., Heithausen, A., Ossenkopf, V., & Zielinsky, M. 1998, A&A, 336, 697

Sun, J., Leroy, A. K., Schruba, A., et al. 2018, The Astrophysical Journal, 860, 172

Sydney, C. & Cowling., T. G. 1954, The Mathematical Gazette, 38, 63

Szűcs, L., Glover, S. C. O., & Klessen, R. S. 2014, Monthly Notices of the Royal Astronomical Society, 445, 4055

Tarantino, E., Bolatto, A., & Herrera-Camus, R. 2018, in American Astronomical Society Meeting Abstracts, Vol. 231, American Astronomical Society Meeting Abstracts #231, 130.07

Thongmoon, M. & Mckibbin, R. 2006, Res. Lett. Inf. Math. Sci, 10, 49

Tielens, A. G. G. M. & Hollenbach, D. 1985, The Astrophysical Journal, 291, 722

Valdivia, V., Godard, B., Hennebelle, P., et al. 2017, Astronomy & Astrophysics, 600, A114

Valdivia, V., Hennebelle, P., Gérin, M., & Lesaffre, P. 2016, Astronomy and Astrophysics, 587, A76

Văsaru, G. 1967, Fortschritte der Physik, 15, 1

Wakelam, V., Bron, E., Cazaux, S., et al. 2017, Molecular Astrophysics, 9, 1

Wang, Y., Bihr, S., Beuther, H., et al. 2020, Astronomy and Astrophysics, 634, A139

Weingartner, J. & Draine, B. 2001, The Astrophysical Journal, 548, 296

Willacy, K., Langer, W. D., & Allen, M. 2002, The Astrophysical Journal, 573

Wolfire, M. G., Vallini, L., & Chevance, M. 2022, Annual Review of Astronomy and Astrophysics, 60, 247

Xie, T. 1997, IAU Symposium, 170, 131

Xie, T., Allen, M., & Langer, W. D. 1995, in The Astrophysical Journal, ed. D. P. Clemens & Barvainis Richard, Vol. 440, 674

Yanitski, C. N., Ossenkopf-Okada, V., & Röllig, M. 2023, in Physics and Chemistry of Star Formation: The Dynamical ISM Across Time and Spatial Scales, 265

Yate, C. J. & Millar, T. J. 2003, Astronomy and Astrophysics, 399, 553

Young, E. T., Becklin, E. E., Marcum, P. M., et al. 2012, The Astrophysical Journal, 749, L17

Zuckerman, B. & Evans, N. J., I. 1974, The Astrophysical Journal, 192, L149

# List of Figures

# List of Tables

# List of Algorithms

# Erklärung zur Dissertation

gemäß der Promotionsordnung vom 12. März 2020
„Hiermit versichere ich an Eides statt, dass ich die vorliegende Dissertation selbstständig und ohne die Benutzung anderer als der angegebenen Hilfsmittel und Literatur angefertigt habe. Alle Stellen, die wörtlich oder sinngemäß aus veröffentlichten und nicht veröffentlichten Werken dem Wortlaut oder dem Sinn nach entnommen wurden, sind als solche kenntlich gemacht. Ich versichere an Eides statt, dass diese Dissertation noch keiner anderen Fakultät oder Universität zur Prüfung vorgelegen hat; dass sie - abgesehen von unten angegebenen Teilpublikationen und eingebundenen Artikeln und Manuskripten - noch nicht veröffentlicht worden ist sowie, dass ich eine Veröffentlichung der Dissertation vor Abschluss der Promotion nicht ohne Genehmigung des Promotionsausschusses vornehmen werde. Die Bestimmungen dieser Ordnung sind mir bekannt. Darüber hinaus erkläre ich hiermit, dass ich die Ordnung zur Sicherung guter wissenschaftlicher Praxis und zum Umgang mit wissenschaftlichem Fehlverhalten der Universität zu Köln gelesen und sie bei der Durchführung der Dissertation zugrundeliegenden Arbeiten und der schriftlich verfassten Dissertation beachtet habe und verpflichte mich hiermit, die dort genannten Vorgaben bei allen wissenschaftlichen Tätigkeiten zu beachten und umzusetzen. Ich versichere, dass die eingereichte elektronische Fassung der eingereichten Druckfassung vollständig entspricht.“

Teilpublikationen:
Aleena, B., Ossenkopf-Okada, V., & Röllig, M. 2023, in Physics and Chemistry of Star Formation: The Dynamical ISM Across Time and Spatial Scales, 139

13.08.2023 Aleena Baby 
Datum, Name und Unterschrift

**Declaration:** The figures in Appendix [C] are updated after finding an error in the submitted thesis.